Characterization
Of The
MIC Photon Counting Detector

A Thesis submitted for the Degree

of

Doctor of Philosophy of the University of London

by

Michael Kenneth Oldfield

Department of Physics & Astronomy
University College London
University of London

1993

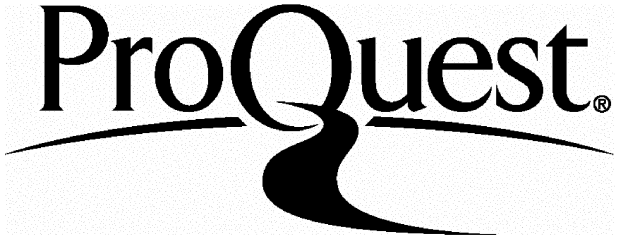

Abstract

A new photon counting detector, MIC, has been developed at UCL and is an enhanced performance version of the highly successful IPCS in use at a number of large ground based optical telescopes throughout the world. This detector is light weight, compact and has a low power consumption making it suitable for Space as well as ground based applications. In particular, a prototype version of the MIC detector, XMM-MIC, has been developed for the Optical Monitor (OM) that is to be included in the ESA 'Horizon 2000' X-Ray Multi-Mirror Mission (XMM).

In this thesis details of the detector system are given along with the theory of operation. A description of those components which limit the detector performance in terms of resolution, image quality, dynamic range and detective quantum efficiency is presented. The performance is characterized both under laboratory and telescope conditions and compared against theoretical data. In addition, computer simulations have been used to compare the detector performance with other types of photon counting detector thus defining the scientific applications to which MIC can most usefully be put. Finally, future developments of the MIC detector are discussed in terms of both Space and ground based applications.

Within the context of this thesis the author has been responsible for the theoretical modelling of a number of detector characteristics, analysis of data and its comparison with theoretical predictions. Computer models were also developed by the author in order to simulate the dynamic range performance of other types of photon counting detector. In addition the author has contributed towards the software development of the detector system and participated fully in all the observing and laboratory trials.

Acknowledgements

Firstly, I would like to give special thanks my supervisor, John Fordham, for all his help and encouragement with both my work and my golf swing. I would also like to thank David Bone for all his guidance and undying optimism no matter what the circumstance. Thanks should also go to Tim Norton for sharing his great insight into MCP intensifiers, and also to Hajime Kawakami for help in carrying out the DQE tests at MSSL.

Secondly, I would like to thank all my family for both their moral and financial support over the last six years especially my parents and most importantly Flukey Dukey.

Finally, I would like to thank my friends Jon 'Lardy' Bellis, Graham 'Fat Boy' Rose, Jane, John 'The Boss' Deacon, Martin 'The Sloath' Clayton, Fishy, PACMAN, Mike.G.

Contents

List Of Figures

List Of Tables

Chapter 1

Introduction

The human eye can gaze upon stars, planets and other galaxies but is unable to either store or quantify most of the detailed information it receives. As far back as 2000 BC the Chinese were the first people to make an indirect record of an astronomical phenomenon by drawing what is thought to be the representation of a lunar eclipse. Then, with the introduction of photographic plates in the 18^{th} century, man has been able to make a direct record of what he saw. Today, modern astronomy relies upon increasingly sophisticated detectors to both collect and accurately represent data from astronomical objects in order that it can be permanently recorded and subsequently analysed.

Successive generations of detector have been able to capture and record astronomical data with both greater sensitivity and accuracy but there is no such thing as an 'ideal' detector. A detector which comes close to fulfilling this ideal should:

- be *efficient* in the sense that it is able to record a high proportion of the photons incident on it, over as broad a wavelength range as possible. A measure of the detectors efficiency in registering the presence of photons is given by its *Detective Quantum Efficiency* (DQE).

- be *accurate* in the sense that the input signal can be derived reliably and precisely from the detectors output signal. Ideally the output signal should be directly proportional to the input signal in which case the detector is said to be counting in a *linear* manner.

- operate over a wide range of input signal intensities without suffering from saturation (where the input signal intensity is very high) or be swamped by detector noise

(where the input signal intensity is dominated by the detector noise). In either of these extremes the detector will no longer count in a linear manner. The intensity range over which the detector counts in a linear fashion is described by the detectors' *dynamic range.*

- be capable of integrating and storing the image in any desired timescale i.e. it should be able to both integrate for many thousands of seconds or, for applications where the input signal varies rapidly with time, a small fraction of a second.
- be 2 dimensional with as large an imaging area as possible, have a high *resolution*, i.e. be able to resolve closely spaced objects, and have good image *stability* and *reproducibility.*
- have a *simple operation*, be *reliable* and *robust.*

The input signal detected by astronomical detectors are *photons* of electromagnetic radiation. These detectors take many different forms depending not only upon the wavelength range over which they are observing (from γ-rays to radio waves), but upon the way in which photons of the same wavelength are detected. The detector output signal may therefore take many different forms; for example, the blackening of a photographic emulsion, the current from a photomultiplier or the charge packet contained in a CCD pixel.

1.1 History Of Optical Detectors

Detectors observing photons at or close to optical wavelengths (200nm to 900nm) have changed significantly since the development of the first photographic films. **Fig 1.1** is a diagram representing the types of optical detector that are used (to differing degrees) in astronomy today. It also demonstrates the method by which photon events are captured and recorded by these detectors.

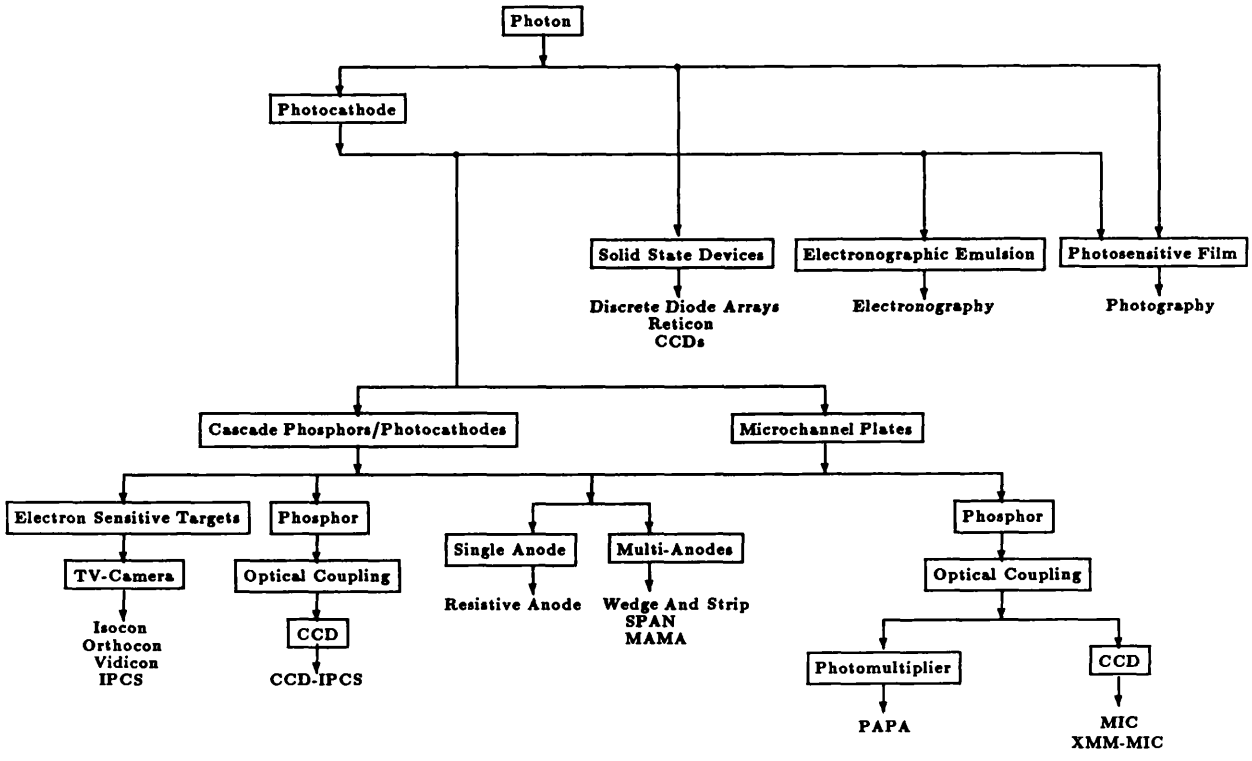

Fig 1.1. Optical photon detection methods used in astronomy

1.1.1 Photographic Film

Photographic film is the oldest image recording mechanism used in astronomy. It is still the only mechanism which can fully utilize the wide angle view of a Schmitt telescope which is why full sky surveys such as the Palomar Sky Survey are done with photographic plates. It is capable of storing the equivalent of 10^9 bits of information on one plate and having a resolution of 100 line pairs/mm [*Eccles and Tritton*] . However, photographic film does have several drawbacks:

- The maximum DQE of a (hypersensitized) photographic film is ~4% [*Mclean*] and each film has a slightly different wavelength response.
- Once a grain has been activated it becomes saturated and no further image information can be recorded by it.
- Its resolution depends upon the grain size. Small grains produce a higher resolution film with a better image contrast but require a larger photon flux to active them.
- Photographic image quality is dependent upon the way in which the film is developed.
- A microdensitometer is required to put the data into a digitized form. This is essential for software analysis of the image.

1.1.2 Electronography

Some of these drawbacks were overcome with the development of the electronographic camera. The process of *electronography* is one in which photons are firstly converted into electrons using a photoemissive material called a *photocathode*. Each electron is then accelerated towards a charge sensitive electronographic emulsion which stores a record of the photoelectron image. This method of photon detection has several advantages over using photographic film.

- Electronography has a higher quantum efficiency than photography due to the high sensitivity response of the photocathode. Once the photocathode has emitted a photoelectron, it is accelerated and easily detected by the emulsion.
- Electronography produces a more linear response at low light levels as single events can be recorded on sections of the electronographic film. Electronography is therefore a far better method for observing faint objects.
- Electronographic emulsions are fine grained with a large storage capacity. There is a very low instance of adjacency effects (where the exposure of one grain affects that of another), and the emulsion can give accurate representations of image structure over a large density range and high density gradients.
- The difference in grain sensitivity across the field is very low so that only variations in photocathode sensitivity are appreciable.

Despite some of these advantages over photography, electronographic devices have a smaller field of view and still need a microdensitometer in order to digitize the data.

1.1.3 TV-Type Readout Cameras

TV-type detectors produce an output voltage level which is a function of the incident photon flux intensity. Photons fall onto a photocathode, the photoelectrons from which are accelerated towards a target area (usually Antimony Sulphide) in which a large number of electron-hole pairs are formed leaving a positive charge pattern in the target (**Fig 1.2**).

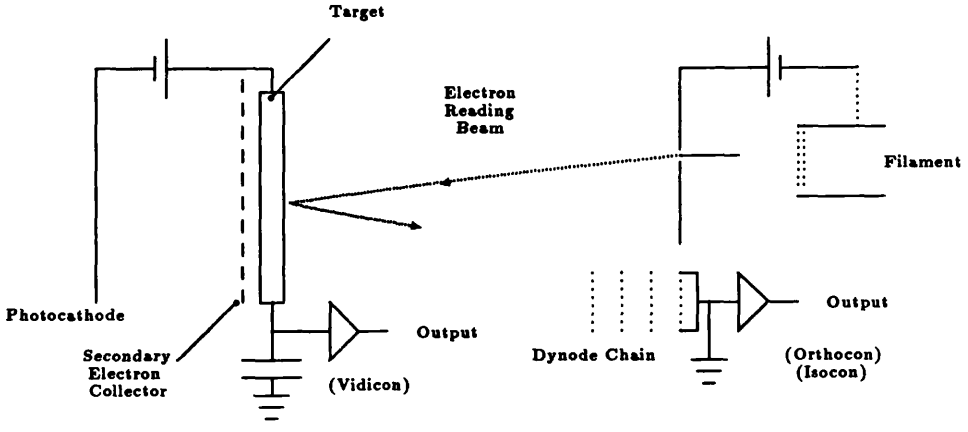

Fig 1.2. The principle components of a TV-type readout camera.

At the end of each integration an electron beam is raster scanned across the target. Some of this beam recombines with the holes created by the image signal and produces an instantaneous voltage change in the target. Some of the beam is scattered by the positive charge signal but most is reflected back towards the anode. The image signal is measured in one of three ways depending upon the type of detector used [*Walker*].

1. The Orthocon Camera: Only the reflected beam is collected and amplified by a dynode chain. The output charge is a measure of the inverse photon image intensity as the highest charge represents regions of the target in which there is no signal.

2. The Isocon Camera: Both the reflected and scattered portions of the beam are separately amplified by a dynode chain, the combined signal being a measure of the inverse photon image. The Isocon is a more sensitive detector than the Orthocon but is very bulky and some charge spreading can take place in the target during long integrations.

3. The Vidicon Camera: In the Vidicon camera the instantaneous voltage change in the target is measured as the beam is raster scanned across the target area. With a knowledge of the beam position and the voltage change associated with that region of the target, a measure of the photoelectron image across the target is made.

Like the photographic and electronographic recording devices, TV-type detectors also have problems associated with them. Only the most energetic of the beam electrons manage to

penetrate deep into the target and neutralize the small amount of positive charge produced in regions in which there has been a low photon flux. This may mean that the target has to be scanned ten or more times before all the signal is throughly discharged.

If the charge build up is too great then the potential across the target may decrease so much that the incident electron-hole pairs do not separate but recombine again. This produces a loss of linearity and can also decrease the detector resolution as areas of high positive charge pull the scanning electron beam towards it, distorting the final image.

Most of these problems have been overcome by replacing the Antimony Sulphide target with a Lead Oxide target. The type of camera which uses a lead oxide target is called a Plumbicon camera and is the readout detector in the *Boksenberg* IPCS (described in Section 1.2.1).

1.1.4 Solid State Devices

Solid state devices make use of the photoelectric effect where a sufficiently energetic photon can excite electrons in the valence band of a semi-conductor into the conduction band. The electron is stored locally to where it is excited in one picture element (*pixel*) of the detector array. The photon flux at any particular pixel is then represented by a proportionate amount of charge stored in that pixel. If the position of a pixel within the array is known, and the quantity of charge in that pixel measured, then a representation of the light intensity over the whole array can be made [*Beynon and Lamb*].

The most common type of solid state device used in modern optical astronomy is the *Charged Coupled Device* or CCD. This is a 2-dimensional detector made up of an array of pixels each of which can store free electrons produced by photon excitation. The basic design and theory behind the operation of a CCD is described in Chapter 2. They have several advantages over the TV-type detectors described above in that:

- Photons are converted into charge within the silicon lattice itself and so there is no need for a photocathode.
- There is no electron readout beam and so the detector is more compact and simple to operate.
- CCDs have intrinsic image stability as each pixel is fixed in the array.

- When cooled, CCDs produce very small amounts of *dark current* and saturate only after very long exposures to high light levels. Their linearity is thus maintained over a large range of light intensities.

Most CCDs used today have a relatively small size (up to 5cms×5cms) compared to most other types of optical detector and have cosmetic defects associated with them. They also have a readout noise of typically $5e^-$ rms when cooled [*McLean*] which means that in order to detect very faint light signals the CCD must integrate for large time periods in order to achieve the required signal to noise ratio.

CCDs also have other problems associated with their use. Because they produce high levels of thermally generated charge which would otherwise swamp the image signal, CCDs have to be cooled to temperatures of typically 130K. This involves placing the CCD within a cryostat or on a Peltier cooled mount which complicates its operation especially in a Space environment.

CCDs also suffer a loss of image quality if hit by cosmic rays. A cosmic ray striking the CCD during an integration can typically introduce $500e^-$ into the affected pixel element(s) and render the data in these pixels useless. During long integrations the number of cosmic ray hits is appreciable, especially when used at high altitude where at 5000m there are typically 25 cosmic ray hits/cm^2/1000secs [*Walker*].

1.1.5 Photon Counting Detectors

All CCDs and cameras mentioned previously can be run in what is called *analog mode* where the image signal is built up and stored on the detection surface (be that a photographic film, an Antomony Sulphide target area or in the silicon lattice of a CCD) and read out once at the end of an exposure. The output signal is formed from the accumulative effect of photons arriving over the whole integration period. Analog integration is distinctive from *photon counting* in that, with photon counting, each individual photon is detected as a separate event. Only after the presence of an event has been registered is it accumulated (usually in a computer memory array) with other events making up that image (or spectrum in the case of 1D detectors).

Astronomical CCDs have a very high quantum efficiency (typically peaking at 70-80% in the red) and are therefore very efficient in detecting photon events. But their readout noise of typically 5 e^- is equivalent to the signal produced by at least $\sim$ 7 photon events

per pixel element. So if faint objects are being observed, and the input signal rate is small compared to the CCD readout noise, large integration times are required to obtain the desired signal to noise ratio.

To reduce the effect of detector noise, photon counting detectors have an event amplification stage where photon events are (charge) amplified before being detected by a readout camera. Each amplified event has sufficient signal associated with it that the event signal greatly exceeds the cameras' readout noise and can therefore be easily detected. Imaging charge amplification devices have, in previous years, been provided by magnetically or electrostatically focussed intensifiers which employ a number of cascaded phosphor/photocathode elements. Most modern photon counting detectors today use proximity focussed intensifiers which employ microchannel plates to provide charge amplification.

The readout system can take one of two general forms. These are:

- a charge readout system which consists of one or more charge sensitive anodes. Each anode is connected to a charge amplifier and all the amplifiers are connected to some type of event detection electronics. Examples of this type of photon counting detector are the *Resistive Anode* [*Lampton et al*] which employs a single anode and the *MAMA* (Multi Anode Microchannel Array) [*Timothy et al*] and Delay Line Anode [*Siegmund*[2] *et al*] which employs wire like anodes on which events may be detected. In these cases the readout system detects the charge cloud associated with each event and produced by the intensifier.

- a photon sensitive readout system like a Plumbicon Camera, an array of photomultipliers or a CCD. These types of detector include the *IPCS* (Image Photon Counting System) [*Boksenburg*] which employs a Plumbicon Camera as its readout system, the *PAPA* (Precision Analog Photon Address) [*Papaliolios et al*] detector which employs an array of photomultipliers and *MIC* (Microchannel Plate Intensified CCD) [*Fordham et al*] which employs a CCD readout system. For this type of photon counting detector, the readout system detects not the charge cloud associated with each event, but a scintillation of light. The charge cloud is converted into light by means of a phosphor located at the rear of the intensifier.

All these types of photon counting detector are discussed in Chapter 8 where their per-

formance characteristics are compared against each other.

1.2 History Of The MIC Detector

This thesis is primarily concerned with the characterization of the latest developments in IPCS technology and it is appropriate here to give a more detailed description of the history of this development.

1.2.1 The Image Photon Counting System (IPCS)

The IPCS, which is shown schematically in **Fig 1.3**,

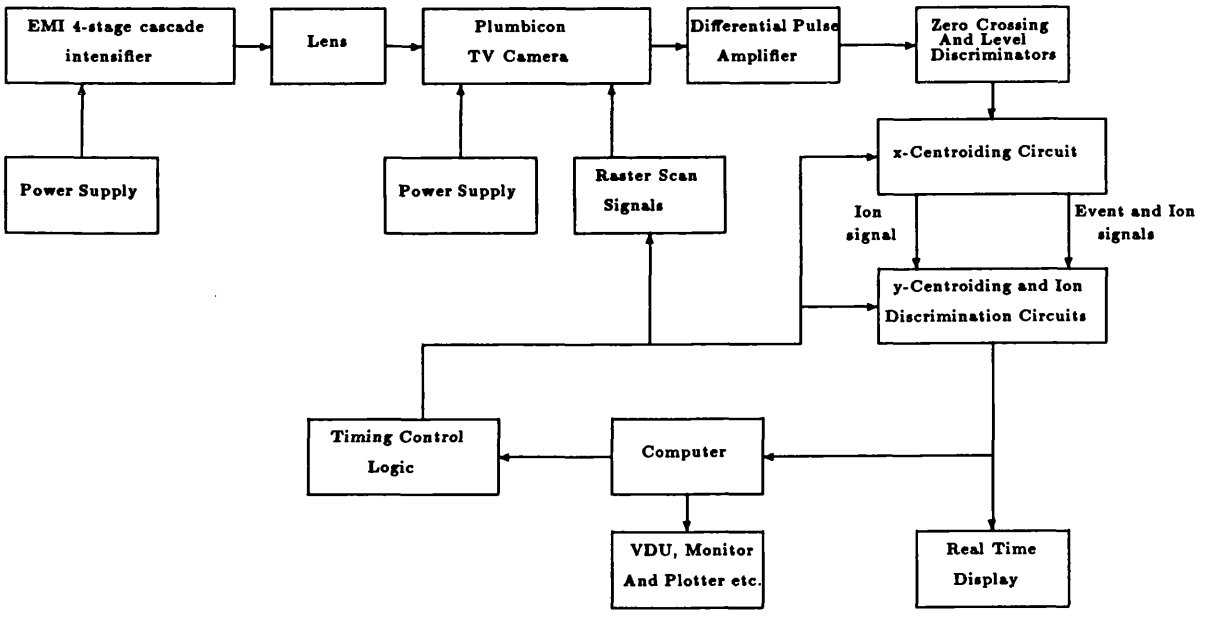

Fig 1.3. Block diagram of the IPCS

was conceived by *Boksenburg* and is made up of a detector head unit, consisting of a 4-stage cascade EMI intensifier lens coupled to a Plumbicon camera (shown in **Fig 1.4**), and the associated detector control and event processing electronics.

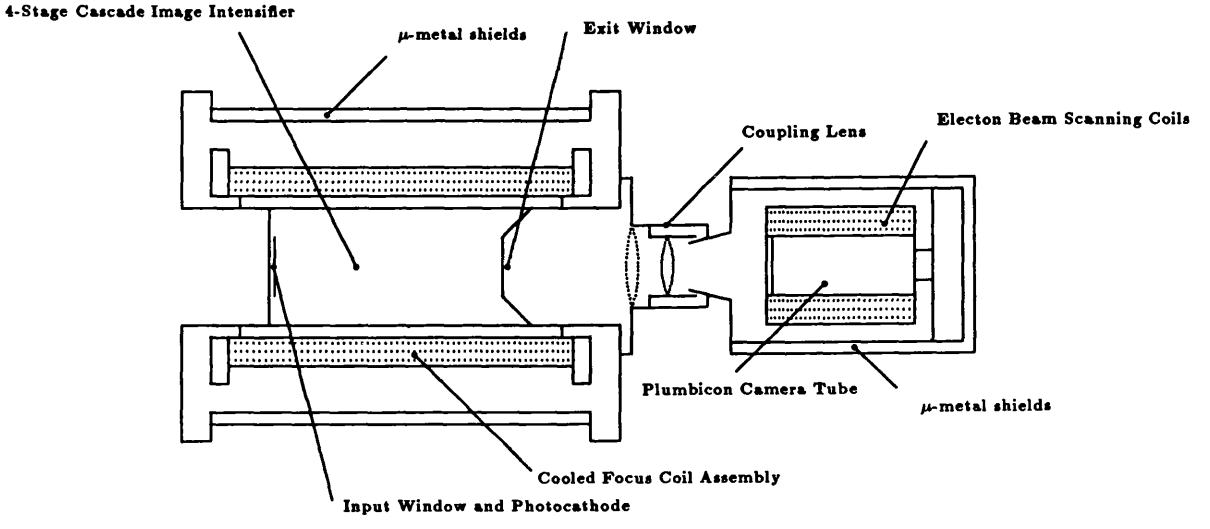

Fig 1.4. Sectional view through the IPCS detector head.

The intensifier consists of an input window which is highly transparent to incoming photons down to 300nm. A photocathode grown on the inside face of the input window is used to convert the incoming photons into photoelectrons. The photoelectrons are initially accelerated through the intensifier towards a thin mica membrane on whose near side is deposited a phosphor and on whose opposite side is deposited another photocathode. When the phosphor is hit by a photoelectron, a number of photons are emitted which strike the photocathode liberating further numbers of photoelectrons. This process is repeated through three other cascade stages whereupon a light scintillation of typically 10^8 photons emerges from the intensifier P11 output phosphor. The event position is maintained throughout by magnetically focusing each photoelectron as it passes through the intensifier. Magnetic focussing requires the use of a large, power consumptive solenoid which is placed around the intensifier body and cooled using circulating water. The intensifier is coupled to the Plumbicon camera by means of a fast lens having a magnification of 0.59 and a transmission efficiency of $\sim$ 1%.

The Plumbicon camera is a high performance vidicon camera whose lead oxide target has a spectral response which wavelength matches the peak emission from the P11 output phosphor. It has a very low *lag* which means it can be read out with one scan of the electron beam, and there is a very low degree of lateral charge spread through the target. Each event typically produces $7\times10^5 e^-$ in the target which is easily detected above the camera readout noise.

The advantages of employing an image intensifier in photon counting mode and sampling each event with a fast scanning Plumbicon camera are that:

- only the central position of each event is recorded. The IPCS has the facility to find the centre of an event produced by the image intensifier. By causing the event to spread over more than one scan line of the camera, an event may be *centroided*, whereby its centre is found from its distribution of event energy in each target pixel over which it spreads. This gives the detector a very high resolution capability.

- it enables a choice of pixel size to suit the application. The pixel size is set by the scan waveforms applied to the Plumbicon camera and can be varied. Thus, for example, in spectroscopy a 30μm pixel can be used in the spatial dimension if the seeing is good or an 80μm pixel used if the seeing is poor. This optimizes the signal to noise ratio.

- it can be used to measure rapid time varying effects. Depending upon the camera format the target can be scanned once every 30-100ms.

- data can be displayed in real time. An image can be seen to build up during an observation ensuring efficient use of telescope time. By watching the image as it builds up, the astronomer can tell at which point the required signal to noise ratio has been reached and thus when to stop the integration.

but the IPCS does have certain problems associated with it.

1. The IPCS is not perfectly stable i.e. there are small drifts in the pixel positions because of small drifts in the waveforms applied to the Plumbicon camera. Image 'flat fielding' is therefore made more difficult.

2. As a result, the IPCS used to suffer from the effects of granularity noise, a pixel to pixel sensitivity variation deriving from the granular nature of the first phosphor within the intensifier. In order to drastically reduce this effect the intensifier is 'dithered' [*Jorden and Fordham*] using a scan coil placed around the gap between the first cathode and phosphor in such a way that an image is stepped across many pixels in order to average through the granularity. The event position is then corrected for by using another scan coil at the rear of the intensifier.

3. It suffers from a characteristic S-distortion caused by distorted magnetic field lines within the intensifier.

4. In terms of system performance the most important restriction in using the IPCS is its low bright limit on dynamic range i.e. the count rate at which the detector has significant numbers of *coincidence losses*, (Chapter 4).

The performance characteristics of the IPCS which is currently used at the Isaac Newton Telescope (INT) and the Anglo Australian Telescope (AAT), are shown in **Table 1.1**

Detector Resolution	25μm in the blue (but is wavelength dependent)
DQE	14%
Point Source Dynamic Range	0.05 cnts/pix/sec on full format 2048×512 pixels 1-2 cnts/pix/sec on spectroscopic format 2048×32 pixels
Dark Count (S20)	30-50 cnts/cm^2/sec

Table 1.1 Performance characteristics of the Boksenburg IPCS

1.2.2 The CCD-IPCS

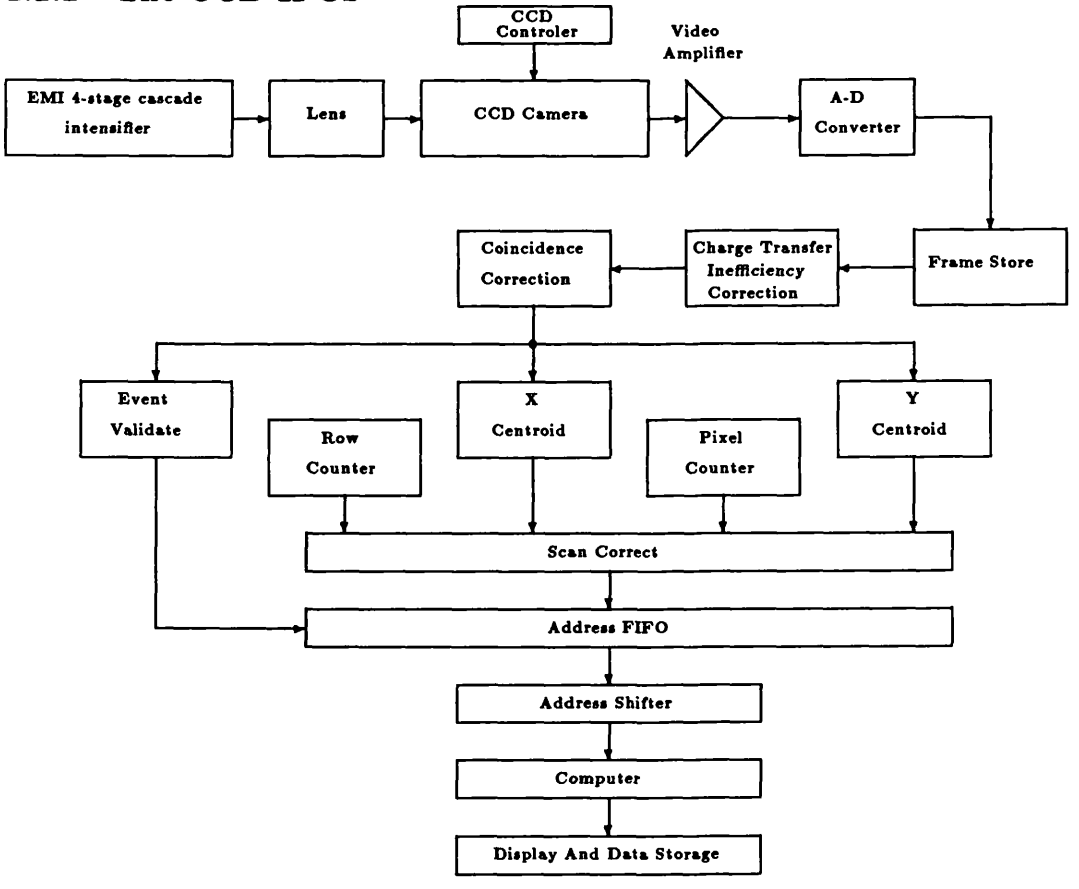

Fig 1.5. Block diagram of the CCD-IPCS

The CCD-IPCS [*Fordham* [2] *et al*] uses a CCD readout camera instead of a Plumbicon camera, **Fig 1.5**, and the same 4-stage cascade intensifier as that used with the IPCS.

The first CCD-IPCS employed an RCA CCD which had 320 ×256 active imaging pixels while the CCD-IPCS at the WHT has an EEV CCD with 384×288 pixels. The CCD is run in frame transfer mode and its operation is overseen by a CCD controller. This can allow partial readout of the CCD to take place, increasing the detectors *dynamic range* for reasons explained in Chapter 4. The CCD-IPCS is able to centroid events to $\frac{1}{2}$,$\frac{1}{4}$ or $\frac{1}{8}$ of a CCD pixel. By applying a centroiding algorithm to the event profile, the result of the algorithm is the channel (or sub-pixel) in which the event is centered.

The CCD-IPCS has a frame store in which each frame of data is stored before being processed. This enables the current CCD frame to be subtracted from the previous one (called *frame subtraction*). Not only does this allow the CCD bias to be subtracted from each frame of data but also ensures that any persistence of the P11 phosphor over two contiguous frames of the CCD does not result in any event being double counted.

Employing a CCD camera has several advantages over a Plumbicon camera:

1. The CCD can be run at faster frame rates, typically 2ms for spectroscopic formats and 15ms for the maximum format.

2. The CCD provides high image stability as each pixel is physically fixed to its neighbours.

3. A CCD is smaller, lighter and less power consumptive than a Plumbicon camera.

Because the CCD can be run at such fast frame rates the CCD-IPCS was expected to have a considerably larger bright limit of dynamic range than the IPCS. Although this was true to a degree the bright limit was only increased by a small amount, **Table 1.2.**

Detector Resolution	25μm in the blue (wavelength dependent)
DQE	14%
Point Source Dynamic Range	1 cnts/pix/sec on full format 3072×2304 pixels 7 cnts/pix/sec on spectroscopic format 3072×32 pixels
Dark Count (S20)	30-50 cnts/cm^2/sec

Table 1.2 Performance characteristics of the CCD-IPCS

There are thought to be two separate reasons for this:

1. the dynamic range of the CCD-IPCS is limited mainly by the 4-stage cascade intensifier and not the CCD. The long persistence time of each phosphor within the intensifier causes multiple events which are closely coincident in both arrival time and position and are therefore mistaken as a single event.

2. the method of *frame subtraction* also restricts the detectors bright limit of dynamic range. Any event which arrives in the same position as another event in the previous frame is not counted, as these two frames are subtracted from one another.

1.3 The Ground Based MIC Detector

The third generation IPCS uses an intensifier with a completely different design. This new type of intensifier has increased the detectors' dynamic range performance and made the detector suitable for use with both small ground based telescopes and Space telescopes.

After the development of the CCD-IPCS another type of intensifier using Micro-Channel Plates (MCPs) was jointly developed by Imperial College London, RGO and Instrument Technology Limited (ITL). This type of intensifier was used with the third generation IPCS called MIC (Micro-channel plate Intensified CCD). A schematic of the MIC detector is shown in **Fig 2.1** where the major difference between the CCD-IPCS and MIC is the intensifier design.

The MCP intensifier has several advantages over the 4-stage cascade EMI intensifiers.

1. It allows flexibility in the detectors scientific application, allowing the use of different types of window materials (Sapphire, Quartz and Magnesium Fluoride) and photocathodes (multi-alkali, bi-alkali or Gallium Arsenide). The choice of intensifier window and photocathode determines the wavelength range over which the detector is sensitive to light.

2. It employs proximity focussing instead of magnetic focussing and so negates the need for a solenoid and its associated water cooling components. It is therefore far less power consumptive than magnetically focussed intensifiers.

3. There is no granularity noise or S-distortion associated with the MCP intensifiers.

4. It employs a P20 output phosphor which is more appropriately wavelength matched to the peak QE of the CCD.

5. The MCP intensifier is far smaller and lighter in weight than the EMI intensifier, **Fig 1.6**. This reduces problems associated with telescope flexure which is especially important for small telescopes.

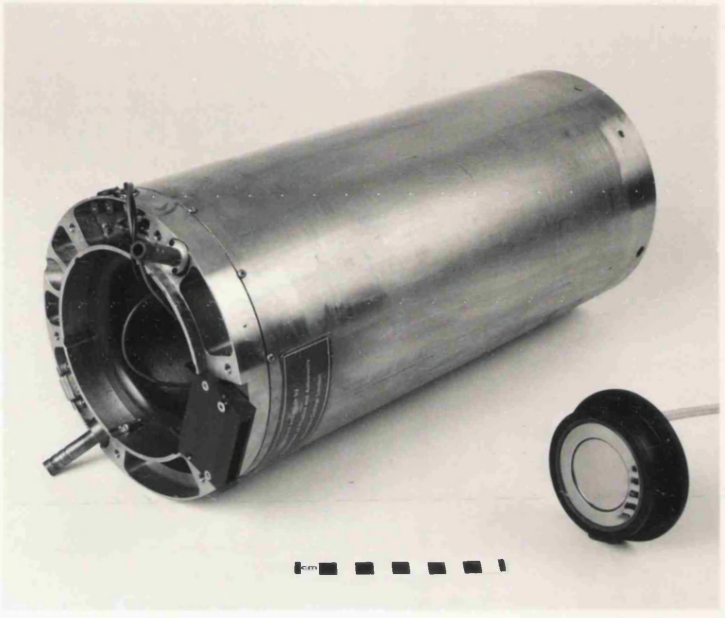

Fig 1.6. Comparative size of a MCP intensifier and a 4-stage cascade EMI intensifier

In addition, MCP intensifiers have a fibre optic output window which allows them to be coupled to other components using fibre coupling devices. The MCP intensifier is coupled to the CCD camera with a fibre optic taper instead of a fast lens, improving the efficiency with which light is transferred between them by a factor of 6.

The types of CCD used with the MIC detector are a Thomson7863A (possessing 384×288 imaging pixels) or an EEV P8602 (possessing 385×289 imaging pixels). Each event can be centroided to an accuracy of $\frac{1}{8}$ of a CCD pixel giving a maximum format of 3072×2304 pixels.

1.4 The Space Based MIC Detector

The ground based MIC detector is light in weight, compact and has a low power consumption making it ideal for use not only on large telescopes but on small telescopes as well. These qualities are also essential to Space based detectors where power consumption, detector volume and detector mass all have to be kept to a minimum. A natural evolu-

tion of the detector is to therefore develop a system which is suitable for use in a Space environment. A picture of the Space prototype version of the MIC detector (XMM-MIC) is shown in **Fig 1.7**.

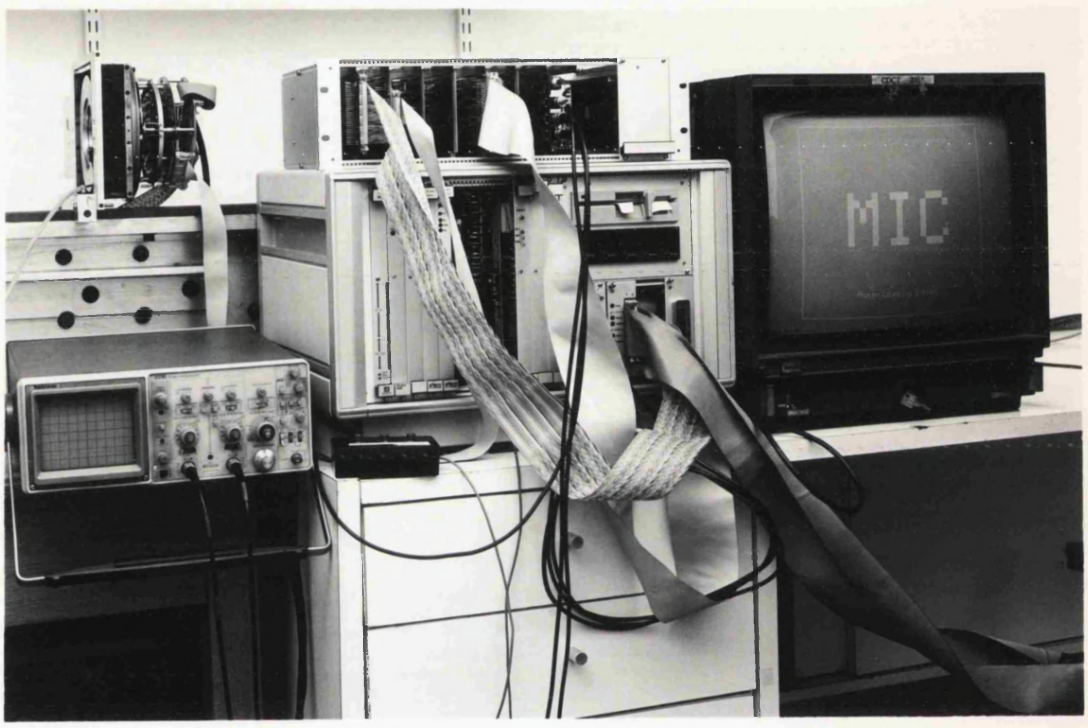

Fig 1.7. The Space Prototype MIC Detector (XMM-MIC)

Funding for the development of a prototype Space version of the MIC detector was provided from two sources:

1. The European Space Agency (ESA), with the intention of applying such a system in the focal plane of an Optical Monitor (OM) telescope that can produce images of stellar objects. By including the OM in a payload where the primary imaging telescopes operate at non-visible wavelengths e.g. X-ray, radio etc. simultaneous studies of target objects can be made over a very wide range of wavelengths in the electromagnetic spectrum.

2. The Science And Engineering Research Council (SERC), for the development of an Optical Monitor (OM) designed to ride 'piggy back' on an X-ray satellite called XMM (X-ray Multi Mirror telescope). The OM is intended to make simultaneous observations of X-ray objects in both the blue/UV (using a photon counting detector)

and the red/infra-red (using a peltier cooled CCD). The XMM mission is one of ESAs '*Horizon 2000*' projects due for launch in 1999.

In order to develop a Space qualifiable version of the ground based MIC detector several factors had to be taken into account:

- The physical size and mass of a Space based detector should be kept to a minimum. The origi nal intensifiers used a cold weld for vacuum sealing the tube. This has now been replaced by a hot, solder, seal. The development of the 'hot seal' intensifier tube has decreased its size and weight, and by re-designing sections of the event processing electronics the Space prototype system is nearly half the size of the ground based system. Most of the electronics may eventually be 'surface mounted' reducing the physical size taken up by each chip and the accommodation requirements even further.

- The detector should have a very low power consumption, most of which is consumed in the event processing electronics. The power consumption has been reduced by:

  1. Employing a 3-pixel centroiding algorithm instead of a 5-pixel centroiding algorithm (Chapter 2).
  2. Not using any charge transfer correction electronics used by the ground based system. With the development of CCDs with a high charge transfer efficiency the Space prototype detector does not require this correction.
  3. The use of low power CMOS electronic components.

     Additionally, for Space applications, particular circuits may be incorporated into low power Actel chips (programmable logic devices) to further reduce the power consumption of the electronics.

- The detector should have a long lifetime and be resistant to radiation damage. Extensive lifetime tests are to be carried out on the image intensifier as their lifetime properties are as yet unknown. Research into the effects of radiation damage on CCDs are being carried out by *Thomsons* and *EEV*, and on optical materials such as the intensifier input window and the fibre optics by UCL and SIRA.

- A Space based detector will have different performance requirements to that of a ground based detector.

The performance of a Space based detector is determined by the scientific requirements of the Space mission unlike for ground based applications where the detector must be flexible in terms of the applications to which it can be put. In the following chapters a detector (the XMM-MIC) designed to meet the requirements of the XMM-OM is described.

1.4.1 Scientific Objectives Of The XMM-OM

The XMM-OM is to provide observations in the UV/Optical and near infra red regions of the spectrum simultaneous with X-ray observations taken with the X-ray telescope, **Fig 1.8.** Obtaining data over such a broad region of the spectrum provides greater understanding of X-ray emitting objects such as active galaxies, X-ray binary stars and cataclysmic variable stars.

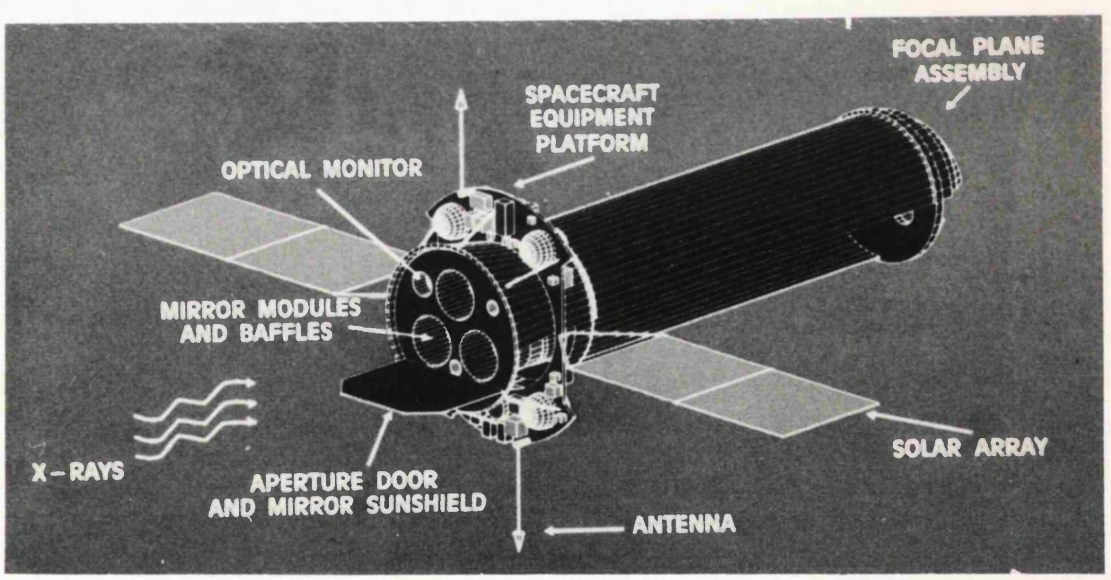

Fig 1.8. Schematic of the XMM Satellite

The Optical Monitor is expected to provide:

- Real time observations of both X-ray emitting and non X-ray emitting objects in the field of view.
- Measurements of optical variability (with a period of hours to years).
- High accuracy relative photometry of both bright and faint stars.

- A system by which the satellite can be tracked across the sky.

1.4.2 Performance Required By The XMM-OM Blue Detector

In order to achieve these goals a set of performance targets have been set for the XMM-OM photon counting detector. These, together with the expected background and stellar light intensities, are described in **Table 1.3.**

	White Light (150-650nm)	B-Band
Zodiacal Light Background (cnts/sec/arcsec^2)	0.2	0.04
Count Rate from B=15th mag star (cnts/sec)	200	60
3σ detection limit in 1000s (equiv. B mag.)	24.0	23
Maximum Point Source Count Rate (cnts/sec/object)	1000	
Detector Dark Count (cnts/sec/arcsec^2)	4×10^{-4}	
Brightest Star Observable (Mag)	13.2	12.0
Brightest Star Observable With Electronic Defocussing		~ 9
Magnitude At Which 10% Variation Detectable in 1000s	20.5	19.5
Spectral Range	150-650nm	
Detector Lifetime	10 years	

Table 1.3 Performance Required By The XMM-OM Photon Counting Detector

These performance targets require that XMM-MIC have the characteristics shown in **Table 1.4.**

Detector Resolution	<20μm
Image Intensifier Diameter	25mm
Active Detector Area	17.7mm x 17.7mm
Maximum Pixel Format	2048x2048
Pixel Size	8.8μm

Table 1.4 Required Characteristics The XMM-OM Photon Counting Detector

A count rate of ~0.05 cnts/sec from a 24th magnitude star defines the detectors faint limit. The bright limit is required to be 1000 cnts/sec allowing the detector to count linearly on a 15th magnitude star. Because the detectors' field of view is 16 arcmins^2 the expected zodiacal background light will typically be 0.042 cnts/pixel/sec. This is far

higher than the detector dark current of 3×10^{-5} cnts/pixel/sec so the detector will in most cases be sky background noise limited.

In addition, because XMM-MIC is required to have satellite tracking capabilities, a data acquisition windowing facility has been designed, **Fig 1.9.**

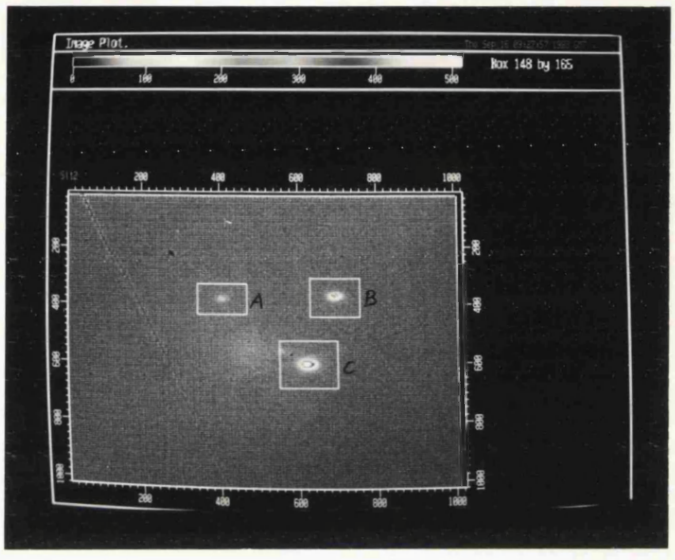

Fig 1.9. Example of the XMM-MIC windowing facility. Data is only acquired in windows A,B and C. Data in B and C might be used for tracking whilst data in window A would be used for scientific data acquisition

This enables data to be acquired from a number of guide stars in the field of view independently of regions from which scientific data is being acquired. Up to 16 windows can be placed around both guide stars and regions of scientific interest within the 2048×2048 maximum format. The guide star data can then be analysed separately from the rest. By analysing the guide star positions between successive measurements (made every 10-50 secs), tracking errors due to satellite drift can be corrected for during long integrations on scientific data.

Windowing the data has the added advantage of reducing the amount of memory required to store each image. If only half the pixels in the active imaging area are acquiring data then only half the memory space is required to store it. This facility is essential for XMM-MIC because memory limitations dictate that data from the full 2048×2048 pixel format cannot be stored at any one time. Windowing data can also reduce the time taken to read out each frame thus increasing the CCD frame rate. This has the effect of increasing the detector dynamic range.

Chapter 2

Description Of The MIC Detector

2.1 Introduction

The MIC detector consists of 4 main components, a microchannel plate intensifier, a fibre optic taper, a CCD and the associated control and data processing electronics. A picture of MIC is shown in **Fig 1.7** and drawn in schematic form below in **Fig 2.1.**

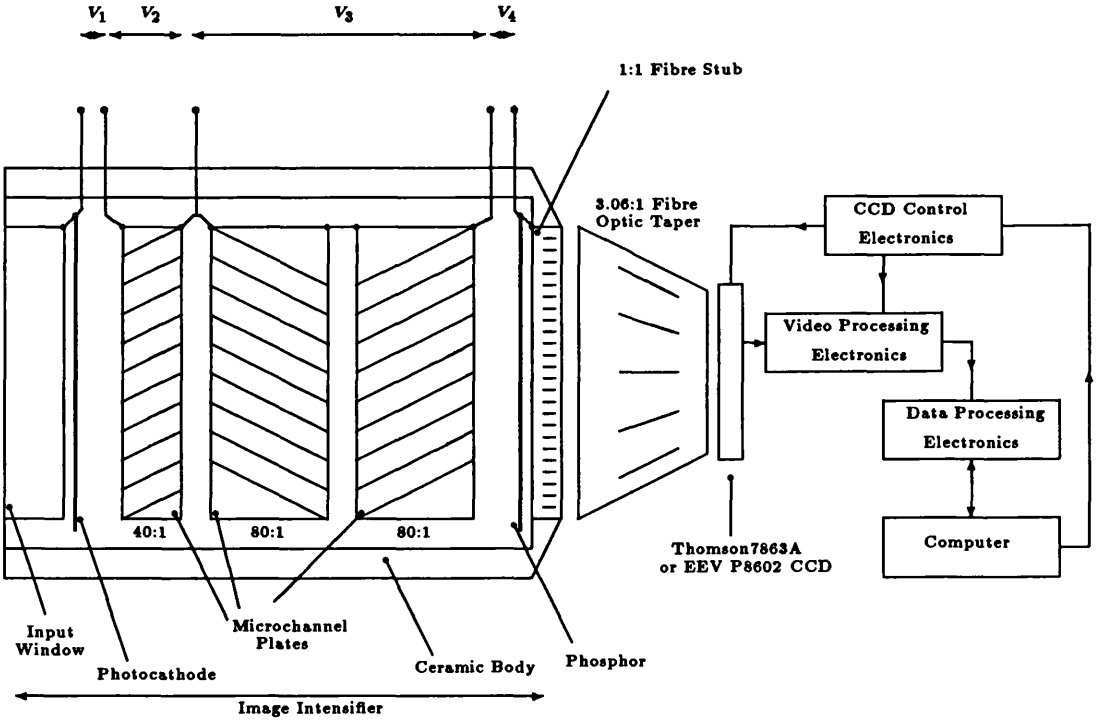

Fig 2.1. Schematic of the MIC photon counting detector

The intensifier, fibre taper, CCD and the CCD driver electronics are all housed together in the *detector head* which is the imaging section of the detector. The data processing electronics are remote from the detector head, but the two are connected by a link which carries the 8-bit video data and CCD control signals. An observer can communicate with and control the operation of the CCD camera and the processing electronics via a computer interface. The computer, which is described in Chapter 3, also provides the memory in which the image is integrated, an interface to external storage media, and the means with which to display data on a monitor.

2.2 The Detector Head Assembly

The detector head has a total length of 15cm and is 17cm in diameter and is shown in **Fig 2.2**.

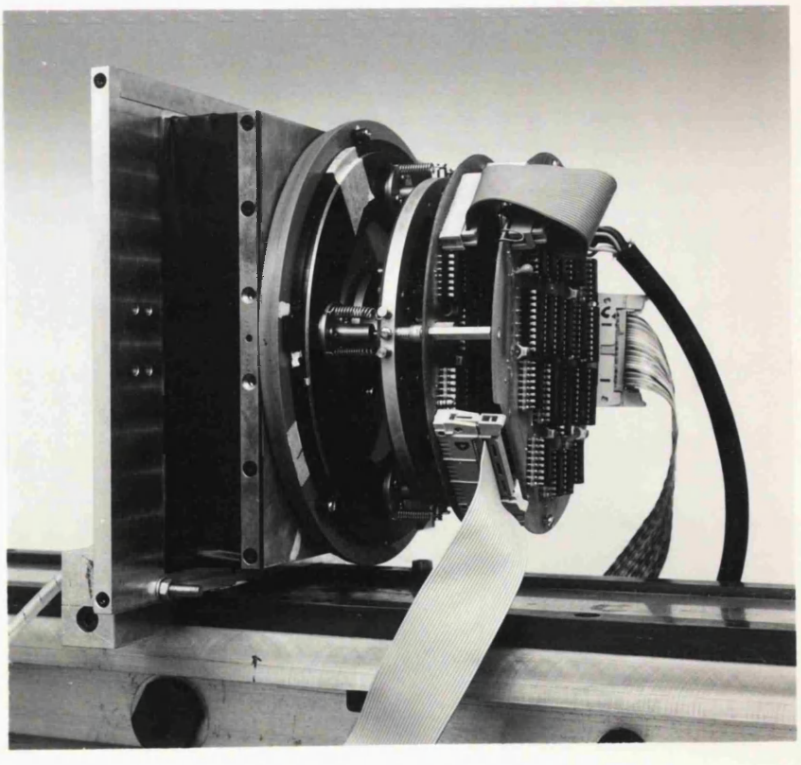

Fig 2.2. The Detector Head

The MCP intensifier produces high gain photon amplification, individual photons of light at the front end of the intensifier being amplified into visible light scintillations at the rear. Each scintillation is then captured by a fast scanning CCD, read out, processed and integrated in computer memory.

The intensifier is coupled to the CCD using a fibre optic taper. The fibre optic taper is coupled to the rear window of the intensifier using Gurr optical oil [1], which minimizes optical losses at the interface between the two surfaces. The taper is held in place by clamping it to the intensifier.

The CCD is mounted on a circular shaped PCB which contains the driver electronics. A fibre block is bonded to the surface of the CCD which enables it to be coupled to the fibre taper by simply making a physical contact between the two surfaces. The CCD is lowered onto the fibre taper using three micrometers on a kinematic mount, tension being provided by three springs. Care must be taken to ensure that the faces of the CCD fibre block and the fibre taper are parallel, in order that light spreading does not occur at the interface.

2.3 The Microchannel Plate Image Intensifier

An image intensifier can be likened to a multichannel photomultiplier, producing light amplification, whilst also maintaining its input spatial position. Individual photons of light are firstly converted into charge (a single photoelectron) with the use of a photoemissive material called a *photocathode*. The photoelectron is accelerated towards the first micro-channel plate, through which there are cylindrical shaped *pores* whose walls are semi-conducting. When the photoelectron strikes a pore wall it ejects more electrons from its surface. These are accelerated down the pore, striking the pore walls and ejecting even more electrons as they do so. A charge cloud of typically 5×10^4 electrons emerges from the rear MCP which is converted back into optical photons by means of a phosphor. This produces a small scintillation of light from the rear of the intensifier which is then captured by the CCD. The intensifier maintains the input position of an event by employing proximity focussing between the photocathode, MCPs and output phosphor, and by physically containing the charge cloud in the MCP pores.

The intensifier body is a ceramic cylinder through which electrodes penetrate to connect the photocathode, MCPs and phosphor to a constant current power supply. The intensifier is sealed at each end by a window. The front, input window, is made from a transparent material such as quartz or magnesium fluoride on which the photocathode is

[1] With a refractive index of 1.52, close to that of glass

deposited. This window is sealed in place using an Indium Tin solder having a melting point of only 130°. The solders' low melting point ensures that the photocathode is not damaged during the sealing process. The rear intensifier window consists of a 1:1 fibre optic stub on the inside of which the output phosphor is deposited. A vacuum is maintained within the intensifier so the seals bonding the windows to the intensifier body, are vacuum tight.

The process of detection and amplification is best explained by individually describing each of the intensifier components, as well as their function.

2.3.1 The Intensifier Input Window

The intensifier is sealed at the front end with a window through which photons pass in order to reach the photocathode. The functions of the input window are to:

1. vacuum seal one end of the intensifier.
2. allow as many photons of as broad a spectral range as possible to pass through it.
3. provide a smooth substrate on which a uniform, high QE photocathode can be grown.

Two types of window are currently being considered for use with XMM-MIC. These are *magnesium fluoride* (MgF_2) and *sapphire*. Both windows have a high transmission over the spectral range required by XMM-OMs' blue detector, but because of its more regular, defect free lattice structure, sapphire is thought [*Ref* [1]] to provide a better substrate on which photocathodes can be grown.

Of equal importance when choosing between the two types of window are their lifetime characteristics, where sapphire is thought in some cases to lose its good transmission properties once exposed to high doses of radiation (Chapter 7). Additionally sapphire windows have been found to phosphoresce if the sapphire lattice contains certain types of impurity [*Siegmund*[1] *et al*]. Impurities, such as ^{40}K, radioactively decay producing a spray of photon events within the window, considerably increasing the intensifier dark noise (Chapter 4).

The merits of employing either window are discussed in Chapters 4 and 7 where their effect on detector dynamic range and DQE are examined.

2.3.2 The Intensifier Photocathode

The MCP intensifier is a *charge* amplification device, with each photon of light at the input to the intensifier firstly being converted by the photocathode, to a photoelectron. The conversion of a light photon into a photoelectron, (**Fig 2.3**), is one example of the photoelectric effect, where if the photon energy E_p is greater than the photocathode work function ϕ_p, a photoelectron is liberated from the photocathode surface.

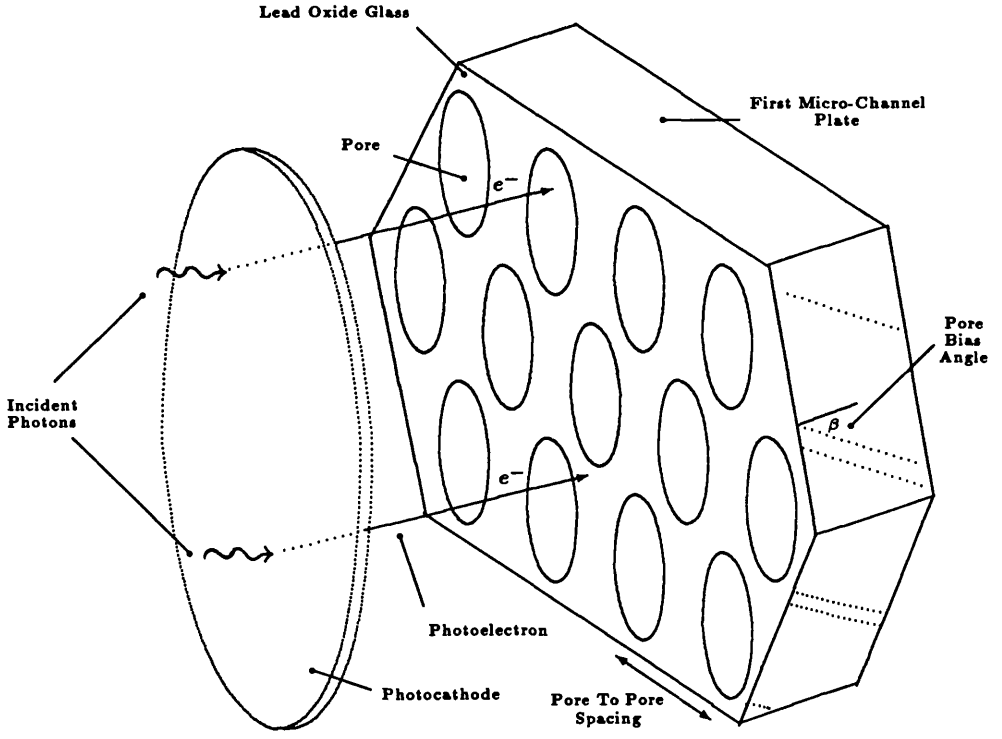

Fig 2.3. Small section of the photocathode and first micro-channel plate

The photocathode is grown on the inside of the input window and maintained at a potential of 0V. A potential V_1 is applied across the intensifier front gap so that any liberated photoelectrons are accelerated towards the first MCP. Because the photocathode is the first detection surface encountered by an event, it is required to have:

1. a broad spectral sensitivity which extends from the near infra-red through to the UV.

2. a high sensitivity in the blue/UV, the wavelength region for which MIC has primarily been designed.

3. a uniform QE response across the whole active imaging area.

There are several photocathodes which satisfy these first two conditions (discussed in Chapter 7) and the third condition is satisfied by the manufacturer having adequate control of the chemical deposition processes and maintaining a high degree of cleanliness during manufacture.

In addition, the rate at which events are liberated due to thermal excitation, should be kept to a minimum. These thermally generated photoelectrons contribute to what is known as the intensifier *dark current* which determines the faint limit of the detectors' dynamic range (Chapter 4). Because the photocathode isn't temperature controlled the dark current mainly depends upon the photocathodes red response.

The photocathode should also have a QE response which does not vary greatly over long time periods [*Beaver et al*] especially in the high radiation flux environment expected in space [*Fowler et al*].

2.3.3 Microchannel Plates

When a photoelectron is released from the photocathode it is accelerated towards the front microchannel plate (MCP), as shown in **Fig 2.3**. The function of each MCP is to provide charge amplification whilst still maintaining the spatial position of the event.

Physical Description

The MIC intensifier has circular shaped MCPs whose diameters are larger than the active imaging area of the detector and extend into the ceramic body of the intensifier. A MCP has a thickness of typically between 0.5mm and 1.5mm and is made of an insulating lead oxide glass. Through the glass are etched a series of cylindrical shaped *pores* (as shown in **Fig 2.3**), the walls of which are semi-conducting.

The face of each plate is covered with an inconel electrode which also extends into the body of the intensifier and which is either connected to another plate, or connected directly to the power supply (see **Fig 2.1** for the electrode structure of the 40mm intensifier).

Manufacture

MCPs are manufactured by a process similar to that of fibre optic bundles, where

- A number of glass rods are clad with a lead silicate.
- Both the rods and the cladding are then drawn to such a length, that each rod is of the required diameter, (the pore diameter) at which point, they are fused together in hexagonal bundles.
- The hexagonal bundles are packed together and fused, to form a glass plate, which is then cut to the required thickness (that of the MCP), ground and polished.
- The glass rods are then etched away to form pores through the glass plate, and then dilute HCl is used to leach lead oxide from the surface of the pore wall.
- The resulting silica rich, lead oxide layer is hydrogen fired, reducing the remaining lead oxide at the surface, to oxygen (which is liberated as a gas) and lead (which remains in situ).
- The presence of a thin layer of lead on top of the lead oxide glass, produces a semiconducting region which coats the inside of each MCP pore and has a characteristic secondary electron emission curve.
- A thin layer of either Nichrome or Inconel, is then vacuum deposited onto each face of the MCP, providing an electrical contact to the external power supply. By controlling the penetration depth to which the electrode enters the pore, the emerging charge cloud can be somewhat focused, by capturing those electrons with the highest transverse velocity components.

Scrubbing

During manufacture MCPs are fired in hydrogen, a percentage of which becomes embedded in the pore wall. If the hydrogen is not removed then high energy electrons can ionize the gas which is then accelerated back towards the front end of the intensifier and damages the photocathode. To reduce the amount of hydrogen embedded in the wall, each plate is electron *scrubbed* subsequent to its manufacture. High quality tubes are typically irradiated with an electron flux of $\sim 0.8\mu A cm^{-2}$ over a period of 300 hours [*Ref* [3]].

Detection Of The Photoelectron

Charge amplification takes place by firstly accelerating the photoelectron released from the photocathode towards the front MCP. The photoelectron will either enter a pore or strike the inconel electrode on the MCP front face. If it strikes the inconel electrode, the electron has a small probability of 'bouncing' into a surrounding pore (Chapter 5) or most usually becomes absorbed into it.

When the semi-conducting pore wall absorbs energy from an energetic photoelectron it can release a varying number of secondary electrons from its surface. The number of secondary electrons it emits is defined by the materials' Secondary electron Emission Coefficient (SEC or σ) at any given photoelectron energy [*Hill*]. The variation in the number of secondary electrons it emits for different photoelectron energies has been described by *Frazer* [2] *et al.* They calculated that the SEC for a semi-conducting pore wall material peaks at a value of ~ 3 for a photoelectron energy of 300eV. Therefore, in order to maximize the probability of a photoelectron liberating secondary electrons the intensifier front gap voltage is typically set close to 300V.

Charge Amplification Through A Pore

Secondary electrons are accelerated through the MCP by applying a potential across the plate. The electrons travel through a MCP pore until they eventually collide with another section of the pore wall. These electrons then liberate further numbers of electrons which are, in turn, accelerated along the pore. Each time an electron collides with a section of the pore wall increasing numbers of electrons are liberated and so charge amplification takes place along the pore length.

A secondary electron liberated close to the front of a microchannel plate will typically travel in a parabolic path through a pore and strike the pore wall a distance l from where it emerged. The amplification process will continue along the pore length (L) with $n=\frac{L}{l}$ collisions between electrons in the charge cloud and the pore wall.

If we assume that a potential V_p is applied across the MCP and the SEC (σ) of the pore wall material is α for an incident electron energy of V_s eV (i.e. $\sigma(V_s) = \alpha$) then in this simple model the MCP gain will be:

$$G = \alpha^n \tag{2.1}$$

where V_s is the average electron collision energy $\frac{V_p}{n}$.

Because l is a function of the pore diameter d, n is $\propto \frac{L}{d}$, the pore length to diameter ratio. The greater the $\frac{L}{d}$ ratio is for a particular MCP the greater the number of collisions there are between secondary electrons and the pore walls. Manufacturers define the length of a MCP by quoting the pore diameter and the MCP $\frac{L}{d}$ ratio which also gives an indication of the MCP gain.

The intensifier used with any photon counting detector is required to have a large enough gain such that the output event (be that a charge cloud in the case of charge sensitive readout detectors, or a light scintillation in the case of light sensitive readout detectors like MIC) be easily detected above the camera readout noise.

The signal to noise ratio of an event captured by the CCD is typically set to 60:1 by obtaining sufficient photon gain from the intensifier. Taking into account the quantum efficiency of the CCD (Chapter 7), optical losses in the fibre taper and the intensifier output phosphor electron to photon conversion factor, the intensifier charge gain is required to be $\sim 5 \times 10^4$. This is achieved by *stacking* MCPs in series and applying the appropriate potentials across each MCP in the stack.

Charge Saturation

Photon counters, like MIC, employ an energy threshold as part of the readout system above which events are assumed to be real, and below which events are assumed to be due to detector noise (Chapter 7). An event captured by the readout system must have a peak height above this threshold in order for it to be recorded. If the output event height distribution from the intensifier is very broad then a large proportion of real events will fall below the threshold and are not counted. This has the effect of decreasing the detectors' counting efficiency. So not only must the intensifier produce a large gain but it must also produce events with a narrow gain distribution.

For the intensifier to produce a narrow event gain distribution events are *charge saturated* in order that, at some critical charge density within a pore, the event gain ceases to increase. An event becomes charge saturated when the charge density in a pore becomes

so large that the SEC of the pore wall falls to a value of 1. This occurs when the energy required to excite an electron from the valence to the vacuum level of the semi-conducting glass approximates the energy transferred by the striking electron to the semi-conducting layer. In effect, the pore wall acquires a positive electron affinity raising the vacuum energy level.

By saturating the charge associated with each event the intensifier produces an event height distribution like that in **Fig 2.4.**

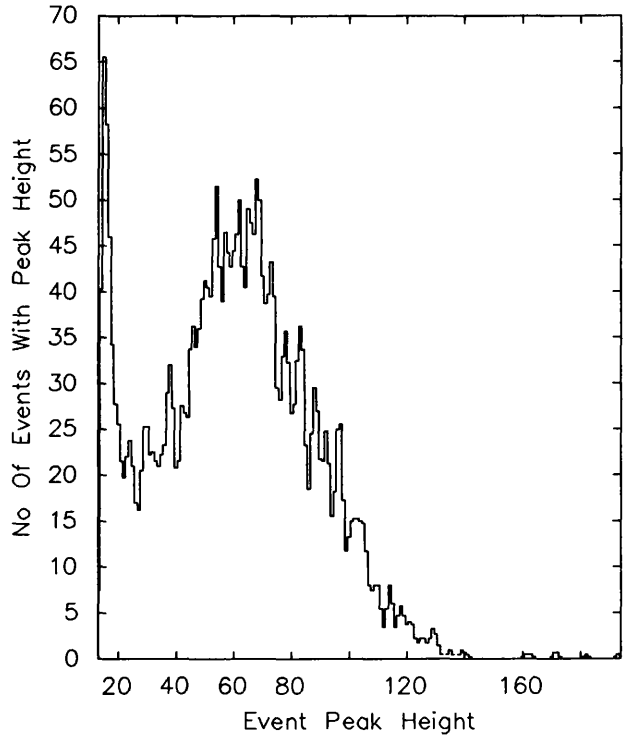

Fig 2.4. MCP intensifier event height distribution recorded with a photomultiplier tube

Arrangement Of MCP Pores

To maximise the number of photoelectrons which travel directly into a MCP pore, the 'dead space' between each pore is made as small as possible. The most efficient way of packing cylindrical shaped pores is in a hexagonal structure. The ratio of the area subtended by the pore openings to that of the total area of the MCP face, is defined as the Open Area Ratio or **OAR.** For example, hexagonally packed cylindrical pores whose diameters are 12.5μm and whose centre to centre spacings are 15μm, have an OAR of $\sim$ 63%. This means that $\sim$ 63% of photoelectrons incident on the front MCP travel directly

into a pore.

The axes along every pore is parallel and set at a *bias angle* of typically between 8° and 12° to the normal of the MCP face (shown as β in **Fig 2.3**). This ensures that:

1. electrons incident on a MCP strike the pore wall close to the front face of the MCP, thus increasing the charge gain.

2. positively charged ion events produced in subsequent MCPs within the stack are not accelerated back towards the photocathode.

Microchannel Plate Stack Configurations

By employing a stack of MCPs and allowing the event to spread into more than one pore the event can be charge saturated at a higher gain. The V-chevron stack configuration consists of two MCPs, the angle between both pores axes being twice their bias angle (**Fig 2.5**). In order to produce charge gains of typically 5×10^4, the first channel plate is used as a medium gain plate, while the second plate is used as a high gain plate. Because the front MCP is not a very low gain stage, most V-chevron intensifiers, have an ion barrier film [*Norton*[2] *et al*] made of SiO_2. This is required to prevent gas, originally trapped in the pore walls (and not removed by scrubbing) and ionized by higher energy electrons, being accelerated back to the photocathode. These films are typically 50μm thick and are placed across the input to the first MCP. Ion barrier films suppress the number of ions traveling back towards the photocathode but they also decrease the intensifier DQE by absorbing photoelectrons from the photocathode [*Niescmidt et al*]. Intensifiers employing an ion barrier film also suffer from an effect known as *halation* which is thought to be caused by two mechanisms [*Norton*[2] *et al*]:

1. Electrons having initially struck the inter-pore wall of the front channel plate, are subsequently scattered back off the ion barrier film and into neighbouring pores.

2. Photons which initially passed through the photocathode are reflected by the ion barrier film, back towards it.

The affect of halation is to cause, for example, bright emission lines in a spectrum to be surrounded by low level wings and to cause the infilling of absorption lines. As a result, halation reduces both the detector resolution and image contrast (Chapter 5). The more

recent 40mm and 25mm intensifiers do not have ion barrier films and as a result, halation has not been observed in data taken with either of these types of intensifier.

The MIC intensifier employs three MCPs in what is called a **Z-stack**. The three plates are placed in series, each separated by a distance of $\sim 50\mu$m. When the charge cloud reaches the end of the first MCP (as in **Fig 2.5**) it travels across the inter-plate gap and spreads out in a transverse direction as it does so.

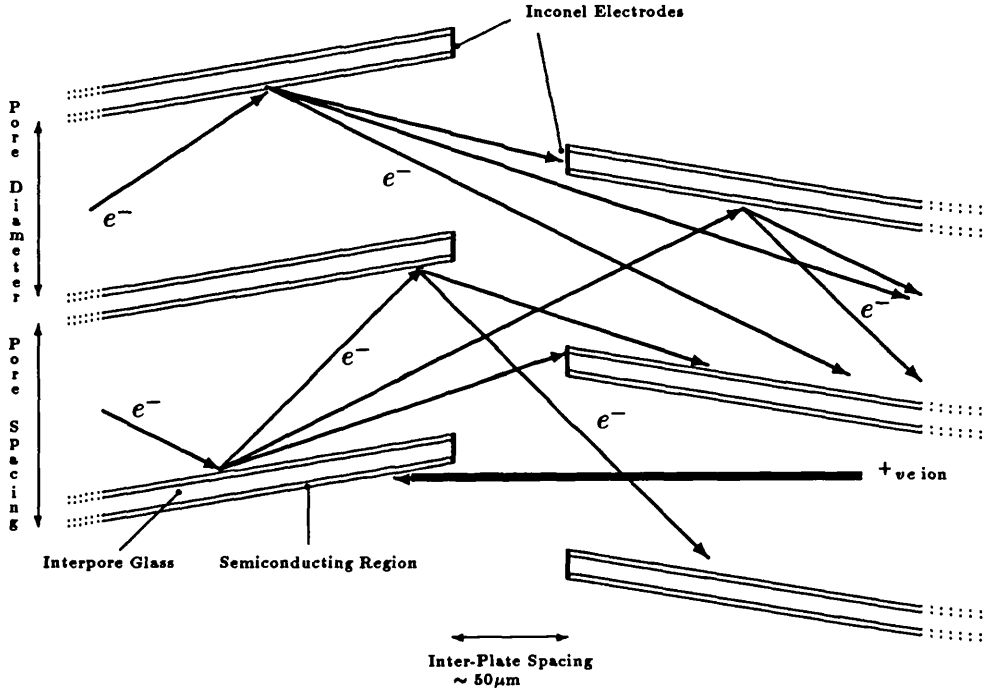

Fig 2.5. Interface between two MCPs of a V or Z-chevron intensifier

For the Z-stack, the first MCP is used as a *low* gain ion barrier (with an $\frac{L}{d}$ ratio of 40:1), protecting the photocathode from ions produced in the high gain second and third channel plates (which both have $\frac{L}{d}$ ratios of 80:1).

Because the front channel plate is used as a low gain stage the electron energy within the pores is small and because it is highly scrubbed very few ions are created in the front plate itself. Large numbers of hydrogen atoms are ionized in the second and third channel plates, where the electron densities and energies are much higher. The ions travel back towards the front end of the intensifier but become absorbed in the previous channel plate.

Another alternative to the V and Z chevron configurations is the *Curved straight* stack configuration [*Boutot et al*], **Fig 2.6**, which consists of two MCPs, the front plate having

pores with a curved axis and the second plate having pores with a bias angle of 0°.

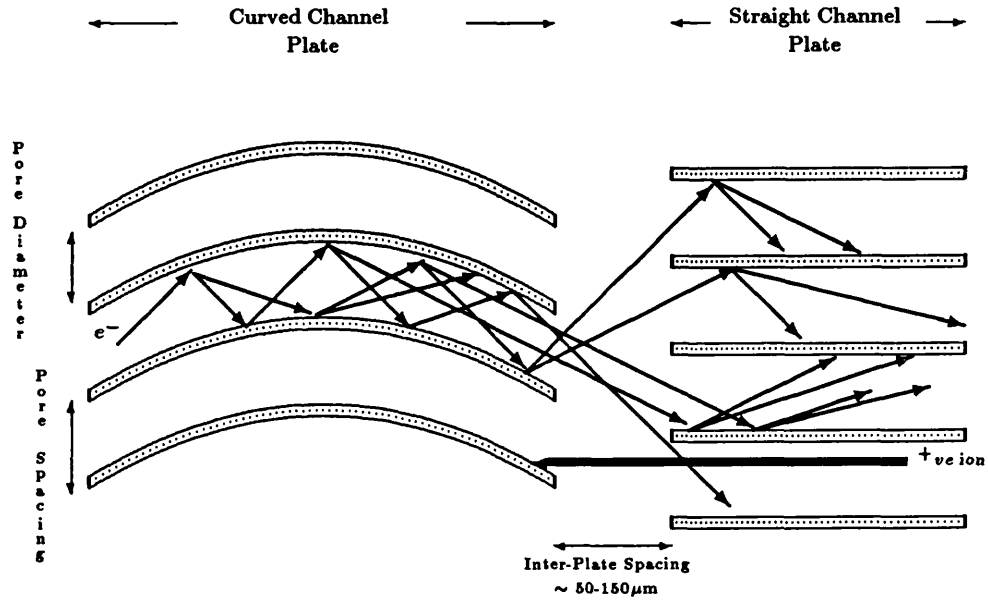

Fig 2.6. Schematic of the Curved-straight MCPs

In this configuration, the curved pores of the front plate, act as a medium gain ion barrier, while the second MCP produces the saturated event [*Timothy*[1]]. This type of stack is used infrequently due to the curved plate being difficult to manufacture and therefore costing a large amount.

The Event Size And Position

As an event travels through a MCP it is contained within the confines of a pore. If the intensifier employs a stack of MCPs, each of which is separated from the next, then charge spreading can take place between the plates. The degree to which charge spreading takes place depends upon the size of the inter-plate gap which is made sufficiently large to allow the charge cloud contained in a single pore of the first MCP to spread into typically three pores of the second channel plate [*Eberhart*[1]]. If, like in the Z-stack intensifier, there are three MCPs in the stack then the second inter-plate gap is made large enough such that an event contained within three pores of the second plate, spreads into typically seven pores in the third plate. Although the event is allowed to spread its centroid position is maintained throughout the MCP plates.

By allowing charge to spread between MCPs the event saturates at a higher gain than if no charge spreading took place. The charge density/pore at the front of the second MCP will be lower than the charge density/pore at the end of the first MCP because the event spreads into more pores of the second MCP.

Defects

Because of the highly successful technique of drawing glass fibres into bundles, MCPs have few defects associated with them. The hexagonal packing structure of the pores is highly regular (as may be seen from SEM photographs [*Wiza*]), as is the consistency of pore sizes. Most of the defects occur during the final processing stages when the intensifier components are put together and housed in the ceramic body. The most common problems are:

- **Switched On Channels:** If a grain of dust becomes trapped in one of the pores during processing then a similar effect occurs to that on the photocathode where a field emission point is created. Here, field emission is contained within a single pore and is called a *switched on channel.* Because each event associated with the switched on channel derives from a single pore, their output profiles are constant and are centroided into a single channel of the detector. If MCPs are processed under clean room conditions then usually no switched on channels occur.

- **Ion Feedback Events:** In order to decrease the probability of ion feedback occurring, the MCPs are *scrubbed* during their manufacture, whereby they are continuously bombarded by a high electron flux. A perfectly scrubbed plate is one where the electrons have dislodged all the gas particles present on, or close to, the surface of the MCP and its pores.

- **Signal Induced Background:** SIB is also associated with ion events which, when accelerated back towards the photocathode strike the previous MCP and release further numbers of electrons. These electrons produce low gain events whose spatial positions are typically between 15-45μm from that of the primary event but can be as far as 300μm away. **Fig 2.7b** shows an event with signal induced background. In order to visually image the signal induced background events, **Fig 2.7b** was taken with a 1:1 coupling between the intensifier and CCD.

Under normal circumstances (where a 3.08:1 fibre taper is used to couple the intensifier and CCD) SIB events cannot be distinguished from the primary event but superimpose themselves on top of the primary event and change its output profile in a random way. Primary events therefore tend not to be centroided correctly and there is a corresponding loss of resolution. The problem is made worse if the degree to which plates have been scrubbed varies across the intensifier. In some cases the outer regions of the plate are scrubbed to a lesser degree than the centre in which case SIB can be rife around the outer regions of the intensifier imaging area, and can cause gain variations across the tube.

Fig 2.7a shows another image of a single event using a 1:1 fibre coupling between the intensifier and CCD. This event has no SIB associated with it. The image was obtained using an image tube which was highly scrubbed and so did not suffer from SIB.

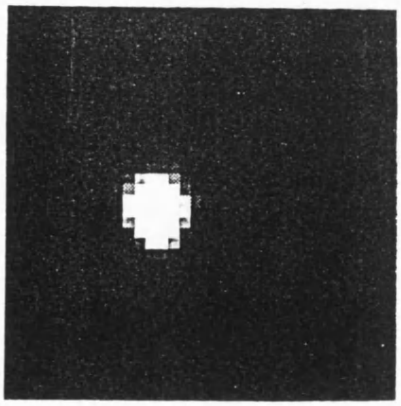

Fig 2.7a Single event profile without signal induced background.

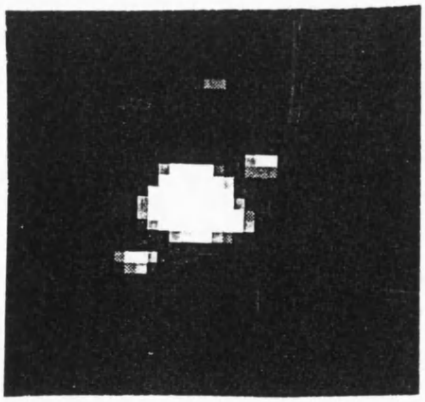

Fig 2.7b Single event profile with signal induced background.

2.3.4 The Output Phosphor

A charge cloud emerging from the rear MCP is proximity focused across the intensifier back gap onto the output phosphor. As it travels across the gap the cloud tends to

spread out due to both the transverse velocity components of individual electrons and the electrostatic repulsion between them. The potential across this back gap dictates the average event size and is set such that the average event FWHM becomes $\sim 100\mu$m at the phosphor. An event of this width is subsequently centroided with the highest accuracy (Chapter 5) hence optimizing the detector resolution.

The purpose of the phosphor is to convert the charge cloud into photons of light which are then imaged onto the CCD camera. In order to do this most effectively, the phosphor is required to:

- Emit light with a wavelength close to the wavelength at which the CCD has its peak QE response.
- To have a high electron-photon conversion factor in order to produce the necessary photon gain whilst keeping the required charge gain to a minimum.
- To have a uniform electron-photon conversion factor to ensure that there is a low gain variation across the intensifier.
- To have a fast decay time (one that is small compared to a CCD frame period), to ensure that an event does not appear in two successive CCD frames. The typical transit time of an electron cloud through an MCP is $\sim$1ns while the transit time spread is 500ps [*Wiza*], so the phosphor decay characteristics govern the time over which an event is captured by the CCD camera.

The P20 phosphor satisfies the first of these criteria, emitting light at a wavelength of 560 nm, very close to the CCDs QE peak. It also satisfies the second criteria by having an electron to photon conversion factor of typically 50eV = 1 photon. In order to obtain an output event whose size is $\sim$ 100μm in diameter the intensifier back gap voltage is typically 5kV. Individual electrons in the charge cloud bombard the phosphor with an energy of typically 5keV producing $\sim$ 100 photons at the phosphor.

The only potential problem associated with the P20 phosphor is its long decay time components which are thought (under certain circumstances), to cause a single event to be captured in two successive frame of the CCD. Only the P46 and P47 phosphors emit light at a similar wavelength to the P20, and have fast enough decay constants (5 times faster than the P20 [*Jaanimagi et al*]) to produce no double counting of events, but they

have electron to photon conversion factors only 500eV = 1 photon. If these phosphors were used with the MIC detector then the intensifier would have to be run with ~10 times the charge gain. This would not only decrease the detector dynamic range performance (Chapter 4) but also the intensifier lifetime.

The effect of having long phosphor decay components is described more thoroughly in Chapter 4, where their effect on the detectors' dynamic range discussed.

2.4 The Fibre Optic Taper

The intensifier output phosphor is imaged by the CCD camera which captures each event. Previous generations of the detector, like the CCD-IPCS, have used a fast relay lens to couple the intensifier to the camera. The CCD-IPCS employs an EMI intensifier whose rear window is made of glass and as a result the light from each event is emitted into a solid angle of 2π steradians. The lens is used to focus the light associated with each event onto the CCD but because the lens has a mass of $\sim$ 3Kg, a transmission efficiency of only 1%, as well as producing image distortions, it is far from ideal.

Instead of a glass window, MCP intensifiers are sealed at the rear with a 1:1 fibre optic stub, which collimates light from the phosphor and allows the use of a fibre optic device to couple the intensifier to the CCD camera. Because of the large size difference between the intensifiers and the typically 9×7mm sized CCD the fibre optic coupler is tapered. The fibre taper acts as a light guide, transmitting light by means of internal reflections through a glass core which is surrounded by a cladding of lower refractive index. The advantages of coupling with a fibre optic taper over that of a lens are:

1. The transmission efficiency of the fibre taper is $\sim$ 6 times higher than that of a lens (see Chapter 7).

2. The distortions associated with a fibre taper are lower than those of a lens (see Chapter 6).

3. A fibre taper is physically less bulky (weighing typically 120g instead of 3Kg), easier to mount and less prone to mechanical shock.

Fig 2.8 shows the relative sizes of both the fast relay lens used with the CCD-IPCS, and the 3.08:1 fibre optic taper used with the MIC detector.

Fig 2.8. The MIC fibre taper and the CCD-IPCS coupling lens

2.5 The CCD

The CCD is an imaging detector made up of individual picture elements called **pixels**. Photons of light striking the CCD are converted into charge which is then stored under the nearest pixel. The quantity of charge produced is directly proportional to the photon flux. The charge distribution over the whole CCD is thus a measure of the incident photon flux distribution, and by measuring the charge under each pixel element an image of the illuminating scene may be built up.

2.5.1 Imaging CCDs

There are two ways in which CCDs are operated for use in astronomy. The first is when the image is integrated on the CCD itself. In this case, all the pixels are used for imaging and the CCD is read out once, at the end of the integration. Because integration times can be as long as 30 minutes or more, the CCD must be cooled in order to reduce the amount of thermally generated electron noise which would otherwise swamp the image signal. CCDs run in this mode are cooled to typically < 130 K, at which point thermally generated electrons are produced at very low rates (< 30 electrons/pixel/hour)[*McLean*].

2.5.2 Fast Scan CCDs

The MIC detector and similar CCD readout photon counters [*Carter*[1] *et al*] use a CCD which is operated in a different mode. Here the CCD is run in fast scan mode where, instead of reading the charge out once at the end of an integration, it is read out at frame rates of between 1ms and 50ms (one *frame period*) depending upon the CCD pixel format and the number of pixels used for data acquisition. The image is not integrated on the CCD itself, but externally, for instance, in computer memory. In photon counting applications the level of thermally generated charge/pixel ($\sim$ 4000 electrons/pixel/sec at 300K) is small compared to that from a captured event and may be subtracted using *black level clamping*, thus negating the need for cooling.

For CCDs run in this mode only half the pixels are used for imaging, those in the *imaging area*, while the other half, those in the *storage area*, are used for temporary charge storage and are therefore covered with an aluminium coating to shield them from light. After accumulating events for one frame period, the charge stored in each pixel of the imaging area is transferred to the corresponding pixel within the storage area. The time taken to transfer the imaging area into the storage area is called the *frame transfer period*. At the end of a frame transfer period the next frame period begins and events are once again integrated on the image area. At the same time, the charge captured in the previous frame period, and now in the storage area, is transferred into the readout register one row at a time in order that it may be sampled.

2.5.3 Interline Transfer CCDs

There are two different ways in which the layout of the image and storage areas can be constructed. One of these, in which columns of image and storage areas lay side by side, is called an **Interline Transfer CCD, Fig 2.9**. In this type of CCD, charge from the image area is transferred just one pixel into the adjacent storage column at the end of a frame period. During the next frame period, the charge in each pixel of the storage area is measured, by transferring it into the readout register one row at a time, and then reading from the readout register one pixel at a time. Because the transfer from image to storage area is just a single pixel, the frame transfer time is very small (typically 0.1μs), but it means that alternate columns of the image area are insensitive to light, lowering the quantum efficiency of each pixel.

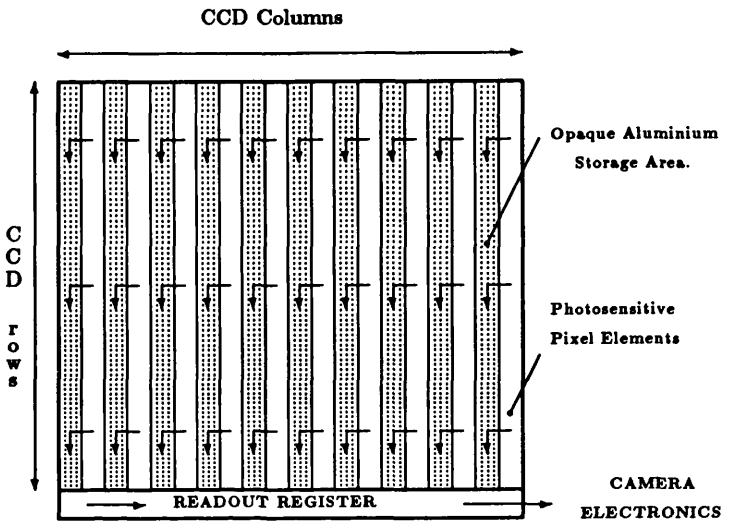

Fig 2.9. Layout of an interline transfer CCD

2.5.4 Frame Transfer CCDs

The other type of CCD layout is one in which the image and storage areas are at opposite ends of the CCD, **Fig 2.10.** This type of CCD is called a **Frame Transfer CCD.** The charge accumulated in the image area is transferred from one end of the CCD to the other.

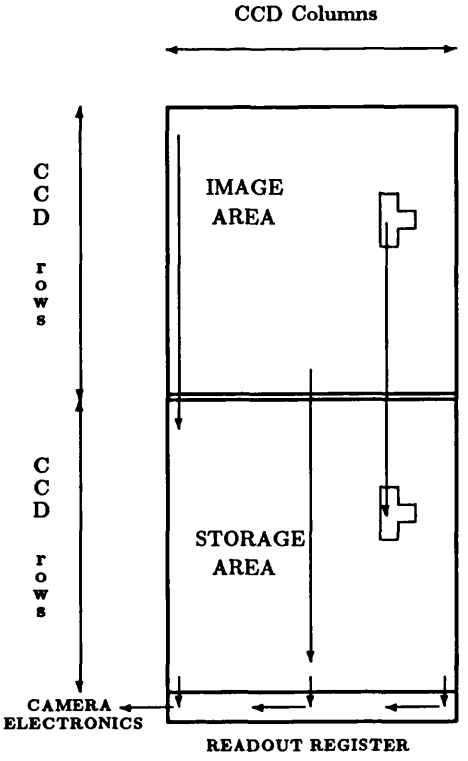

Fig 2.10. Layout of a frame transfer CCD

2.5.5 Comparison Between Interline And Frame Transfer CCDs

Advantages Of Interline Transfer CCDs

Interline and frame transfer CCDs with a similar number of CCD pixels use different numbers of pixels for imaging. Because half the pixels of a frame transfer CCD are completely insensitive to light an interline transfer CCD has twice the number of active imaging pixels. Interline transfer CCDs have frame transfer periods (of typically $1\mu s$) which are very much smaller than those of frame transfer CCDs (typically 100-200μs). A small transfer period thus reduces the probability of any event arriving whilst the image area is being transferred to the storage area and hence reduces the number of events which become smeared during a frame period.

Advantages Of Frame Transfer CCDs

Because a fibre optic taper is used to couple the intensifier to the CCD the active imaging area of the detector is not limited by the size of the CCD (provided that the taper ratio is not too large). A CCD imaging area of typically 7mm×7mm, for example, can be used to image an area of 21mm×21mm if a 3:1 fibre optic taper is coupled to it. Therefore, for MIC, the imaging area of the CCD is not important when comparing interline and frame transfer CCDs in this application.

Although frame transfer CCDs do have frame transfer periods which are far higher than interline transfer CCDs we now believe that this has little detrimental effect on its DQE performance. Events captured during a frame transfer period are smeared across the imaging area and are not detected in that frame. However, because the intensifier output phosphor has long term decay components which emit light during the next frame period, the event can still be detected in the next contiguous frame of data. This means that so long as the frame transfer period is small compared to the time taken for all the intensifier phosphor components to decay to a low level, its effect on CCD DQE is relatively small (Chapter 4).

For photon counting applications the most significant difference between an interline transfer CCD and a frame transfer CCD is that their pixels have different QEs. All the pixels of an interline transfer CCD are half covered over with aluminium making them insensitive to light. This means that an interline transfer CCD would capture half as much

energy from an event as a frame transfer CCD. To compensate for this, the intensifier would have to have twice the event gain which would be detrimental to the detectors dynamic range. This is the reason why the MIC detector uses a frame transfer CCD instead of an interline transfer CCD.

2.5.6 CCD Operation

Charge Storage

Most CCDs made today are **Buried Channel** CCDs (BCCDs), meaning that charge is stored in the silicon bulk, buried in a narrow channel within the lattice. This greatly enhances its charge transfer performance. Silicon has a band gap energy ,E_g, of 1.12eV at 295 K [*McLean*] which means that photons with a wavelength less than λ_{max}, where $\lambda_{max} = \frac{h.c}{E_g}$, can promote an electron from the valence to the conduction band. For silicon at 295 K the value of λ_{max} is $\sim$ 1100nm, although in practice this is not a sharp cut-off wavelength as defects and impurities in the silicon alter the energy levels within the lattice.

When an electron is promoted to the conduction band of a BCCD it is attracted towards the buried channel region where the potential energy of an electron becomes a minimum. The channel is created in a layer of n-type semiconductor which is sandwiched between a layer of p-type semiconductor and an electrode having a positive potential. The electrode is insulated from the n-type material by a thin layer of silicon oxide. Photons of light (with a wavelength $\leq \lambda_{max}$) incident on the CCD create an electron-hole pair in the silicon. The opposing $^{+}$ve potentials of the electrode and the p-type semiconductor are a maximum in the buried channel and so the electron migrates towards it. The electron is confined to the buried channel whilst the electrode maintains its positive potential. The electrons stored under an electrode cannot (during the integrating period) travel freely through the silicon. The charge is trapped on two sides by *channel stops* which form a potential barrier against any movement of charge, and on the other two sides by a potential barrier created by the potential applied to other electrodes within the same pixel (**Fig 2.11**).

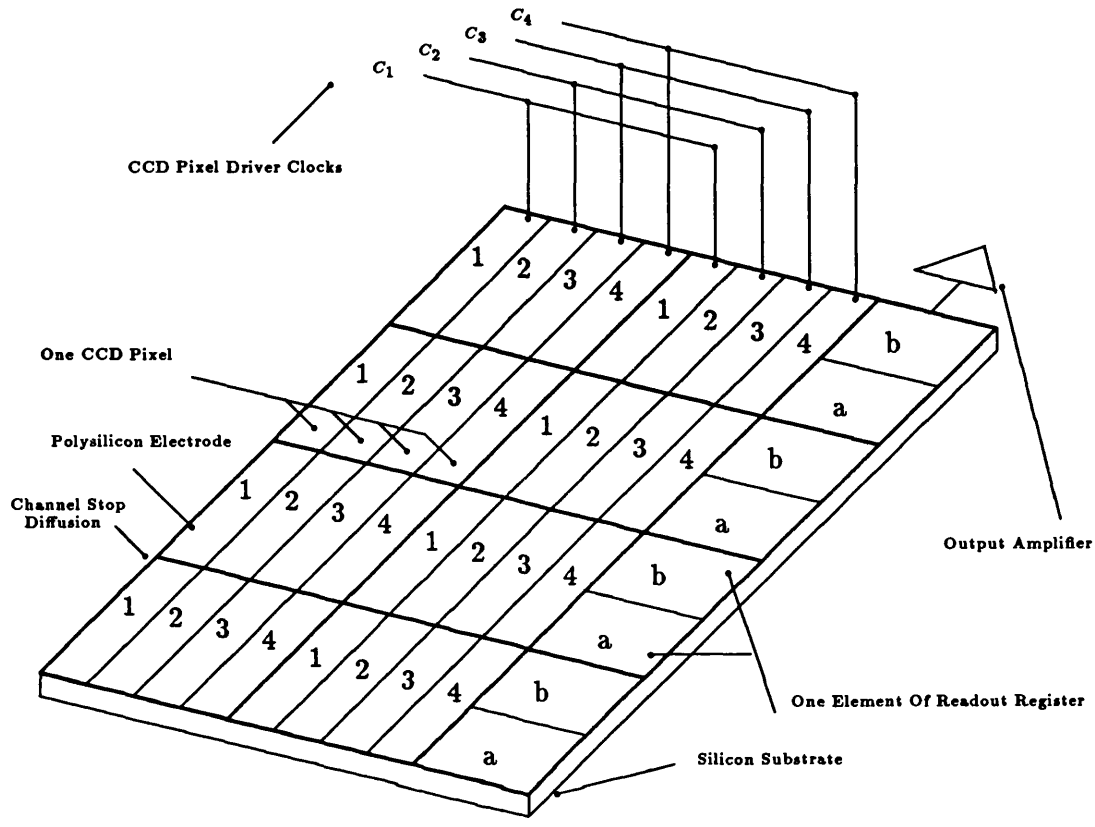

Fig 2.11. Electrode structure at the storage area and readout register boundary

Charge Transfer

In order to transfer charge from one pixel to the next a potential energy difference has to be created in the direction of charge transfer. This is done by changing the potential difference between both successive electrodes of the same pixel and neighbouring electrodes in adjoining pixels. The CCD shown in **Fig 2.12** has four electrodes associated with each pixel element.

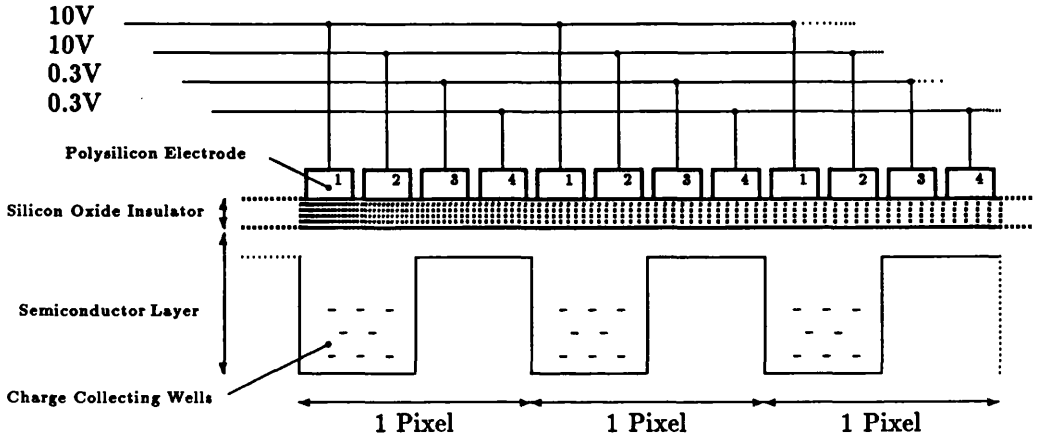

Fig 2.12a. Charge accumulating under three pixels of the CCD

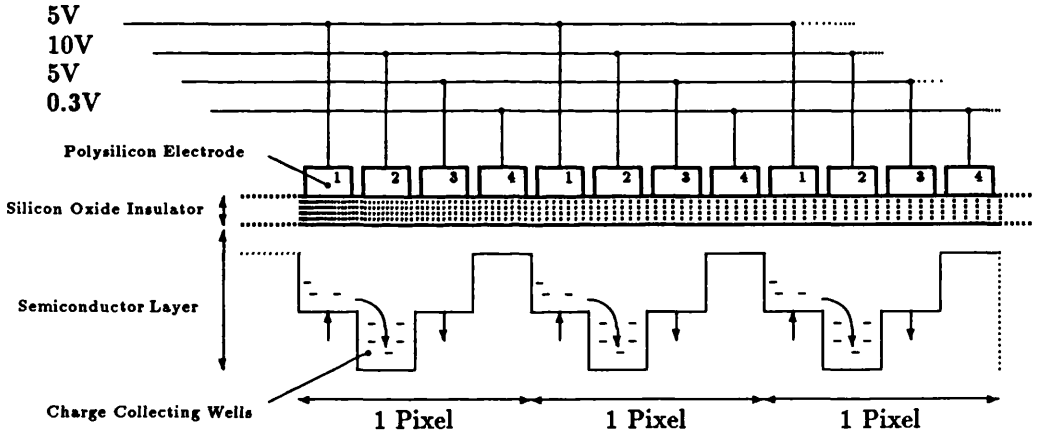

Fig 2.12b. Intermediate transfer of charge between electrodes

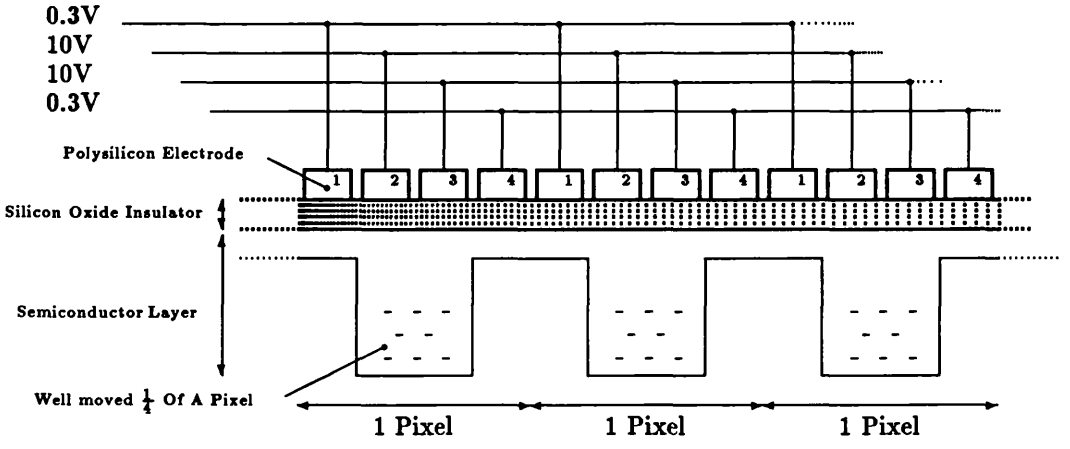

Fig 2.12c. Distribution of charge after being transferred $\frac{1}{4}$ of a pixel

During a frame period two of the four electrodes associated with a CCD pixel have a large positive potential and so free electrons in the vicinity of these electrodes become trapped under them. At the end of the frame period the charge is passed from one pixel to the next by, in this case, decreasing the potential on electrodes 1 and 2 and increasing the potential on electrodes 3 and 4 (**Fig 2.12b**).

Each of the four electrodes are connected to a separate clock voltage. To ensure a smooth transfer of charge the voltage at which two successive electrodes cross over during charge transfer is half way between the minimum and maximum electrode potentials.

Charge Sampling

At the end of each frame period all the charge captured in the image area is transferred to the storage area. During the next frame period;

- Each pixel in the storage area is moved down by one row, the first row moving into the readout register.
- The readout register is clocked horizontally pixel by pixel, the charge in each pixel being sampled by the charge sensing amplifier.
- Each pixel of data in the storage area is moved down by another row, and the whole process repeated until the whole storage area has been read.

When sampled, the accumulated charge (Q) in each pixel causes an instantaneous voltage change (V) of $V = Q/C$ on the signal output, where C is the capacitance of the input to the output amplifier of the CCD.

2.5.7 CCD Type Selection For MIC

The only two major companies from which the group could purchase CCDs for the XMM-MIC detector were Thomson and EEV. The CCD is required to:

- be a frame transfer CCD.
- have a very high (> 0.999997) charge transfer efficiency.
- have at least 256×256 CCD pixels in order to give an event centroided format of 2048×2048 pixels.

- be radiation hard.
- be easy to operate i.e. have a simple electrode structure.

The Thomson7863A CCD

The CCD currently used with XMM-MIC is a Thomson7863A. It has 576 pixel rows and 384 pixel columns, and a 1:1 fibre optic output window which can be coupled to the fibre optic taper. It is run in frame transfer mode and so 288 rows of pixels are covered with aluminium to form the storage area, leaving a further 288 rows to form the image area. Each pixel is $23\mu m \times 23\mu m$, giving a total imaging area of 6.624mm by 8.823mm. The clocks used for vertical transfer of charge (between rows), are run at 2 MHz so the time taken to transfer a whole frame of data (the frame transfer period) is $140\mu s$, while the clocks used for horizontal transfer of charge (in the readout register), run at 10 MHz. The CCD has a peak QE of $\sim$ 25% at 700nm, which is governed primarily by photon absorption in the polysilicon electrodes [*McLean*].

The Thomson 7863A CCD was initially used with XMM-MIC because of its simple (4-phase vertical and a 2-phase horizontal) clock structure which reduced the complexity and power consumption of the CCD driver electronics. Additionally, the Thomson 7863A CCD was believed to be radiation hard.

The EEV P8602 CCD

Another CCD which may, in future, be used in place of the Thomson CCD is the EEV P8602 CCD. This has 578 pixel rows and 385 pixel columns of which only half the rows are used for imaging. It has a pixel size of $22\mu m \times 22\mu m$ providing an imaging area of 6.35mm by 8.5mm. The EEV CCD is expected to have the same frame transfer and readout times as the Thomson CCD but has a 3-phase vertical, 3-phase horizontal clock structure. The two types of CCD also have similar QE responses.

The main reason for changing the Thomson CCD for an EEV CCD is their difference in radiation hardness. The EEV P8602 CCD is now thought to be significantly more radiation hard [*Ref* [2]] than the Thomson7863A CCD making it of more use for Space applications.

2.6 CCD Camera Electronics

The camera electronics are responsible for both the control of the CCD camera and the conversion of raw video data from the CCD into a digital output form. **Fig 2.13** is a block diagram of the individual components making up the camera electronics.

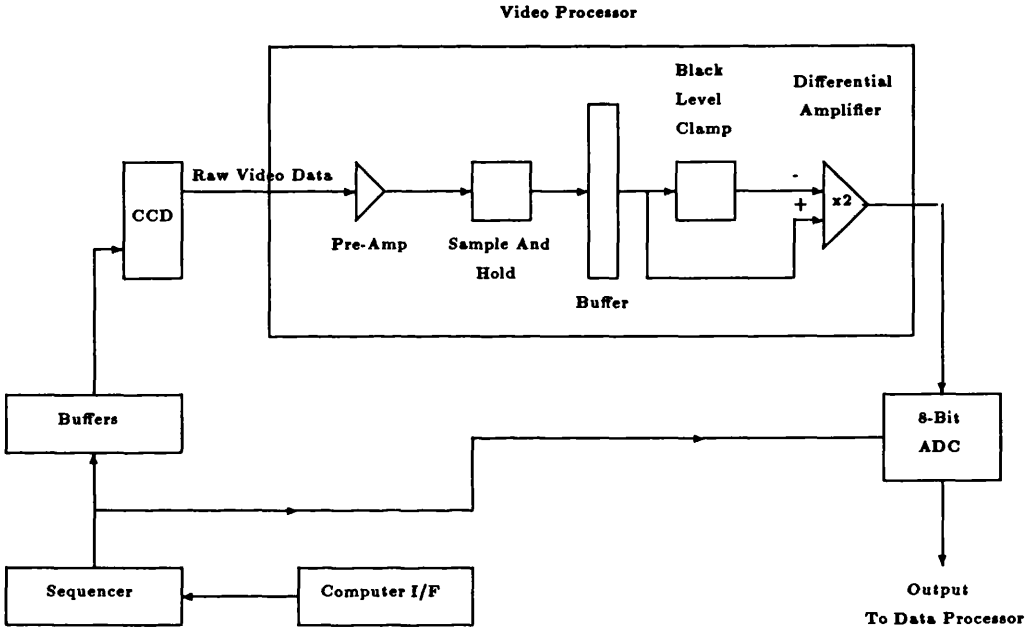

Fig 2.13. Block diagram of the CCD camera and video processing electronics

The CCD is controlled by a sequencer, which contains two master clock generators and the control counters.

1. The Horizontal Clock Generator has a frequency of 20MHz, from which the 10MHz horizontal clock is derived. The horizontal clock is the baseline system clock.

2. The Vertical Clock Generator has a frequency of 16MHz, from which the 2MHz vertical clock is derived. This clock drives the vertical transfer of data independently in the image and storage sections of the CCD.

3. The Control Clock Counters These counters are used to control the readout of the CCD and the generation of control signals such as *line sync* and *frame sync.*

The vertical clock which drives the storage section of the CCD and the horizontal clock which drives the readout register are synchronized to ensure that when data is loaded into

the readout register, it is immediately processed. The sequencing is controlled by a 'bit-map' loaded into a *lookup table* by the computer. The bit-map defines those pixels which are to be used for data acquisition and those which are to be dumped. Those rows of data, which are not used for data acquisition, are dumped in the readout register, one on top of the other. The readout register is then read out and the data disguarded. If the CCD is only partially sampled in this way, the storage area can be read at a much faster rate thus decreasing the frame period. The consequence of partial scanning on the detector dynamic range is discussed in Chapter 4.

The raw video signal from the CCD is firstly passed through an amplifier, after which it is sampled and held. The DC bias measured by sampling data in the last seven pixels in each row (overscan pixels which are not exposed to light). This bias signal is buffered on one input of a differential amplifier, and then subtracted from data in each pixel of the next row. An 8-bit 'flash' analog to digital converter (ADC) then converts the analog signal to an 8-bit digital output which is sent to the data processing electronics.

2.7 The Intensifier Power Supply

A typical 25mm intensifier used with XMM-MIC has working voltages of:

- V_1 from the photocathode to first channel plate 300V
- V_2 across first channel plate 1.2kV
- V_3 across the second and third channel plate 2.4kV
- V_4 from the third channel plate to the phosphor 4.5kV

These voltages are at present provided by a single 30kV Wallis power supply and individually tapped off using a divider chain. A large potential is placed across the divider chain which consists of four pairs of resistors in series with one another. Each resistor pair is made up of a fixed resistor and a variable resistor which are also in series. The potentials $V_{1..4}$ are tapped from each of the four resister pairs. Each individual potential is changed by altering the value of the variable resister in the associated resister pair.

2.8 Data Processing Electronics

The data in each pixel is analysed in order to recognise and position any events captured in the CCD frame. If an event is recognised the data processing electronics, **Fig 2.14**,

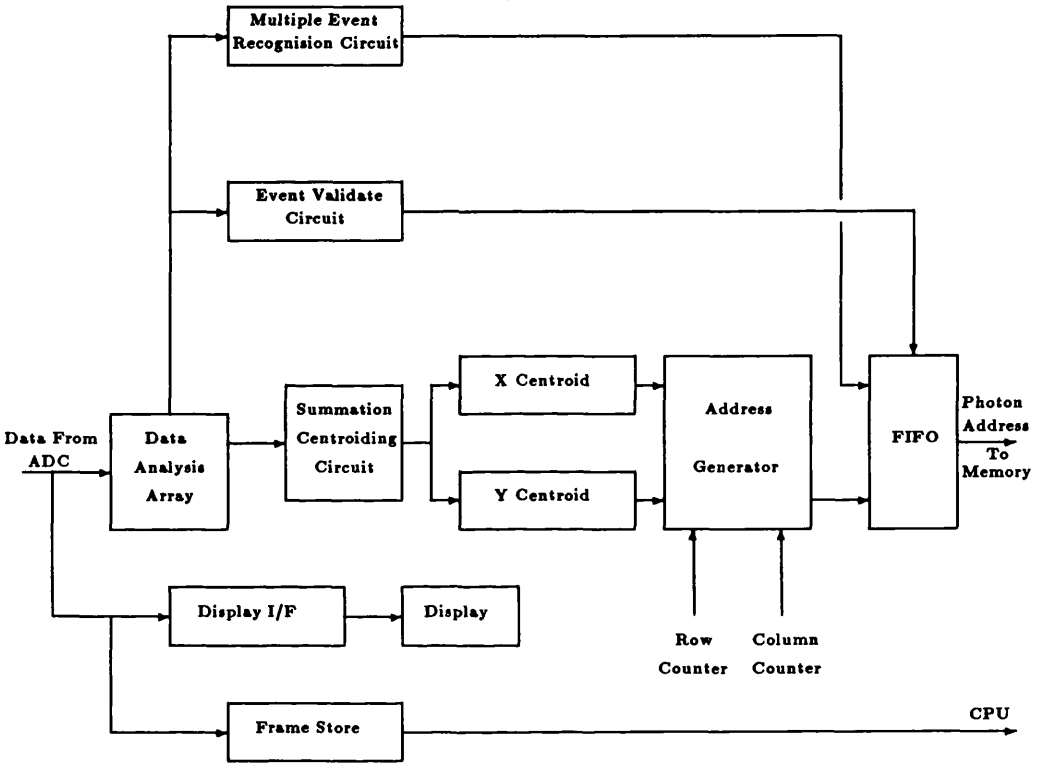

Fig 2.14. Block diagram of the data processing electronics

calculates the event position and transmits its address to the computer for storage. An event is identified by detecting a peak in the data, i.e. one pixel containing more data than those surrounding it. In order to test for this condition, the data is systematically passed through what is called the *Data Analysis Array* (DAA), where a small array of pixels (neighbouring pixels on the CCD) can be analysed.

The ground based MIC system differs from that of XMM-MIC in the size of the DAA, analysing data in a 5 x 5 array of pixels instead of a 3 x 3 array used by XMM-MIC. In the next sections I shall describe how data from the larger, 5 x 5 DAA is analysed, and then state how any analysis differs from that when using a 3 x 3 DAA.

2.8.1 The Data Analysis Array

The DAA consists of five sequential shift registers, whose lengths are equal to the number of horizontal pixels in the CCD (384 for the Thomson CCD), and which are connected in series the first being the CCD readout register itself. The last five elements of each register can be accessed and used in the detection of events. Thus, from **Fig 2.15**, it can be seen that the data in row D is exactly one CCD row delayed from that in E and row C delayed one row from that in D and two from that in E etc.

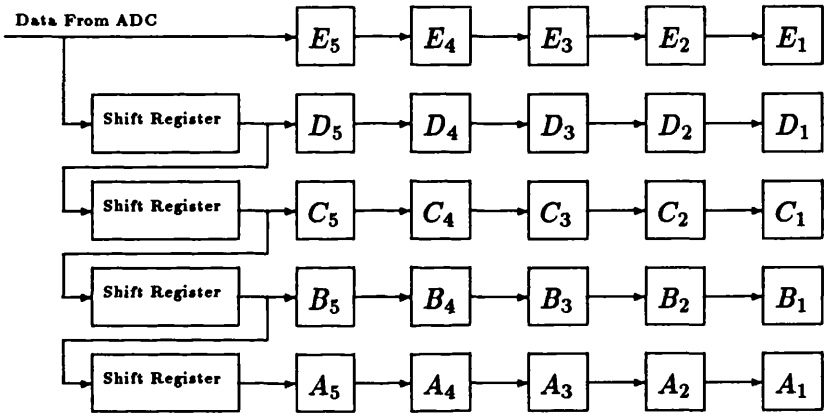

Fig 2.15. Block diagram of the 5-pixel data analysis array

Thus the registers always contain data from five contiguous rows of the CCD which are passed through the grid of 5 × 5 pixels. By reading successive rows into the registers pixel by pixel, every event in the frame passes through the centre of this array and the 25 array elements are used to determine the presence, position and energy of the event. XMM-MIC only has three shift registers, and only the last three elements of each one is used for event analysis, as in **Fig 2.16**.

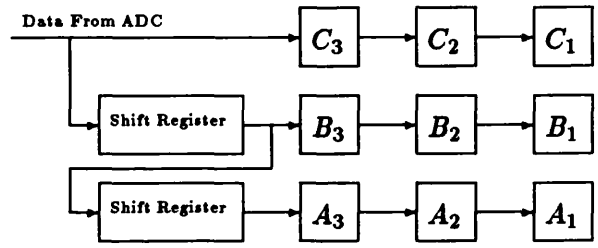

Fig 2.16. Block diagram of the 3-pixel data analysis array

2.8.2 Event Validate Circuit

This circuit is used to determine whether a valid event is central within the DAA. An event is identified when the elements of the DAA meet certain criteria. These are tested for using a number of comparators, each of which samples two elements of the array at any one time. Let us consider the case of **Fig 2.15**, where the DAA is a 5 × 5 element array. The presence of a valid event is found by determining:

1. Is An Event Central Within The DAA ? For this to occur the event must be central in both the x and y directions. This is determined by comparing the data in the central row and column of the DAA with data in the rows and columns surrounding it. For example, to determine whether the event is central in y, C' must be greater than both B' and D' where:

   $B'=B_1+ B_2+ B_3 + B_4 + B_5$
   $C'=C_1+ C_2+ C_3 + C_4 + C_5$
   $D'=D_1+ D_2+ D_3 + D_4 + D_5$

   Similarly, to determine whether the event is central in x, the same condition holds this time where:

$B'=A_2+ B_2+ C_2 + D_2 + E_2$

$C'=A_3+ B_3+ C_3 + D_3 + E_3$

$D'=A_4+ B_4+ C_4 + D_4 + E_4$

If the condition is true in both cases then the event is judged to be central within the DAA. If however, C' is equal to B', for example, we need to know whether the event is centered in B' or C'. In this case A' and E' are then compared. If $E' < A'$ the event is central within the DAA. If however, C' is equal to D' then A' and E' are compared again. This time if $E' < A'$ the event is not central within the DAA.

A similar method is used to determine whether an event is central within the DAA of XMM-MIC. Because, in this case, the DAA is only 3×3 pixels, **Fig 2.16**, an event is judged to be centered in y within the DAA if $B' > A'$ and $B' \geq C'$ where:

$A'=A_1+ A_2+ A_3$

$B'=B_1+ B_2+ B_3$

$C'=C_1+ C_2+ C_3$

Similarly, to determine whether the event is central in x, the same condition holds this time where:

$A'=A_1+ B_1+ C_1$

$B'=A_2+ B_2+ C_2$

$C'=A_3+ B_3+ C_3$

If B' is equal to C' it cannot be judged whether the event is centered in B' or C'. In this case the centroid position is, by default, biassed towards the left hand pixel.

2. Is The Event Real ? Two criteria are used in order to determine whether the event is real or not. Firstly, the event peak must be greater than the *lower event detection threshold.* This threshold is nominally set at $\sim$ 30 ADU (analog to digital units) and

discriminates against low energy noise events. [2]

Secondly, to ensure that the event is not a noise spike, the four pixels directly adjoining the central (peak data) pixel must contain non-zero data. This discriminates against defects such as a hot pixels and switched on channels which would produce a large amount of charge in a single pixel unlike real events.

If the event is both central within the array, and judged to be real, the event validate flag is set.

2.8.3 The Event Centroiding Circuit

The event validate electronics determine whether a real event is central within the DAA. If this were the only information gleaned from the DAA then the event centre could only be determined to an accuracy of 1 CCD pixel. In order to increase the resolution of the CCD camera, the distribution of data values around the central peak pixel is used to estimate the event centre to a higher accuracy. This gives an estimate of where the event centre is within the central pixel.

The ground based version of MIC has the facility to centroid an event to 1, $\frac{1}{2}$,$\frac{1}{4}$ or $\frac{1}{8}$ of a pixel, while XMM-MIC only employs centroiding to $\frac{1}{4}$ or $\frac{1}{8}$ of a pixel. The centroiding electronics centroids an event by using an algorithm in order to find its 'centre of gravity', weighting the data in pixels surrounding the event peak. The solution to the algorithm is the position of the event centroid from the centre of the peak pixel. The technique of event centroiding is best illustrated by considering just one dimension at a time. **Fig 2.17** shows a typical event profile, centered in C_3.

[2] It is assumed that the intensifier is set up in such a way, that the threshold lies in the valley of the event height distribution.

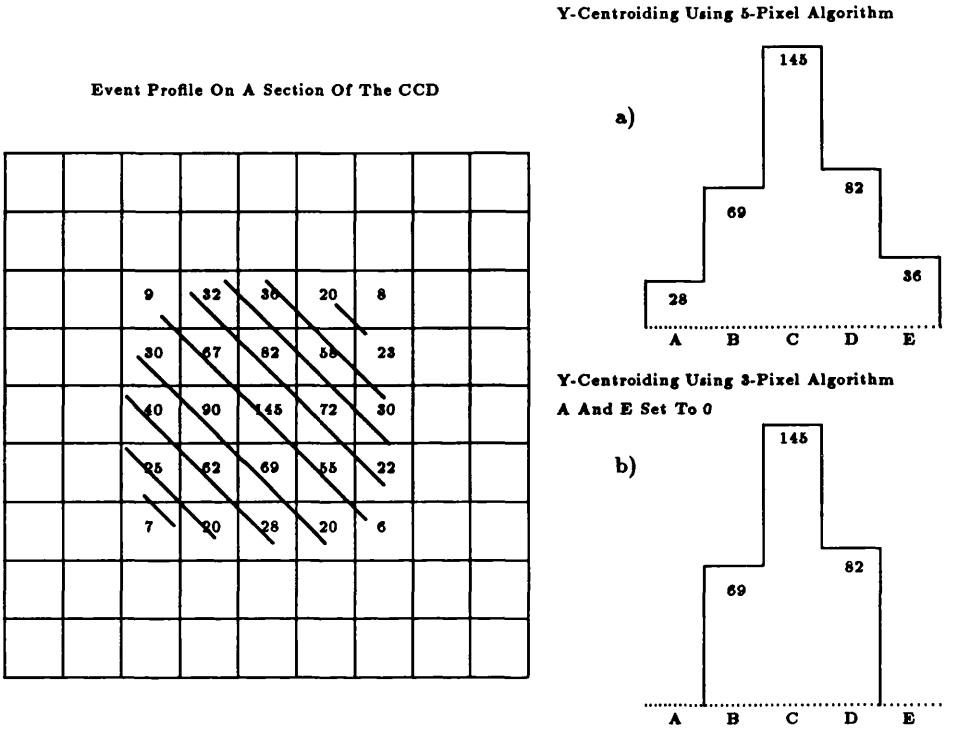

Fig 2.17. Centroiding an event on a section of the CCD

Its centre of gravity is determined, in the ground based system, by applying the 5-pixel centroiding algorithm where, if C has the highest data, the answer is in the range -0.5 to 0.5 if the event profile is symmetrical;

$$\text{Centre Of Gravity} = \frac{2E + D - B - 2A}{A + B + C + D + E} = \frac{M}{N} \tag{2.2}$$

The numerator and denominator of this equation are calculated discretely and are used to define a 16-bit address within a computer loaded *lookup table*, **Fig 2.18.** An identical circuit is used for x centroiding.

The numerator (**M**) and denominator (**N**) are used to define an address within the centroid lookup table, where **M** defines the upper 8 bits of the address and **N** defines the lower 8 bits of the address. For any given combination of **M** and **N**, and hence any location within the lookup table, there is stored a 3-bit number defining the channel in which the associated event centroid is located. Further details on loading the lookup tables can be found in Section 3.3.4.

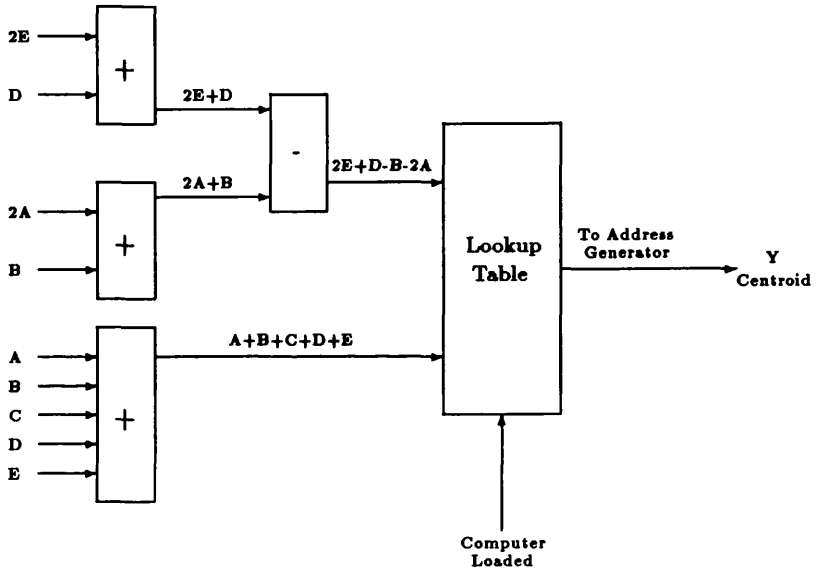

Fig 2.18. The Y-centroiding circuit for a 5-pixel centroiding algorithm

XMM-MIC cannot employ a 5-pixel centroiding algorithm because the DAA is only 3×3 CCD pixels in size. Instead it uses a 3-pixel derivative:

$$\text{Centre Of Gravity} = \frac{C - A}{A + B + C} \tag{2.3}$$

Once again, the numerator and denominator are calculated discretely and are used to define an address within a centroiding lookup table. The ground based system has the option of using a 3-pixel algorithm by simply setting the values of A and E in **Equ 2.2** and **Fig 2.18** to zero.

Within the past couple of years two enhancements have been made to the centroiding electronics, one in each of the two systems. They are:

1. The Coincidence Correction Circuit is an option for the ground based MIC detector. Consider the case in **Fig 2.19a** where two events have landed so close together on the CCD that their event profiles overlap.

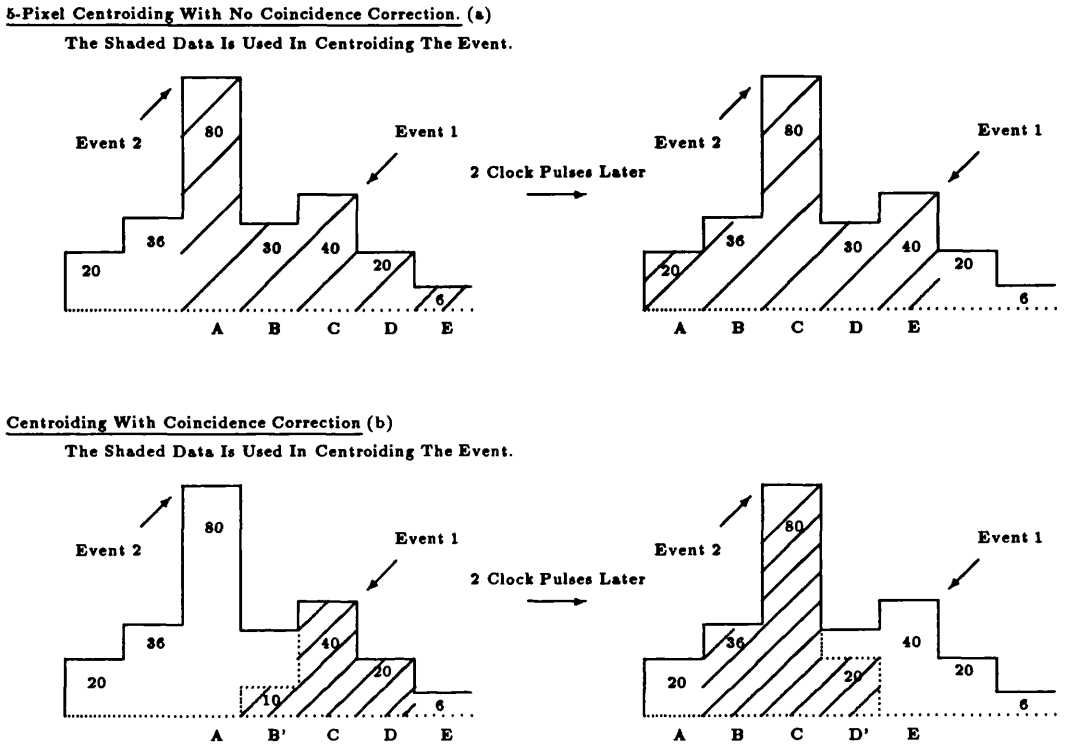

Fig 2.19. Centroiding using the coincidence correction circuit

Initially, event 1 is centred in the DAA but two clock cycles later event 2 becomes centred in the DAA. If either the 3 or 5 pixel algorithms are used to centroid these events without the use of the coincidence correction circuit, the calculated x centroid value of both would be inaccurate. The coincidence correction circuit tests for overlapping event profiles by determining whether;

i) $C > D$ and $E > D$ or

ii) $C > B$ and $A > B$

When event 1 is centred in the DAA, case ii) is true. Here we need to determine what the value of the data in B would have been if event 2 were not present. This is estimated by calculating the ratio of data in C and A, and modifying the data in B accordingly. If A is twice that of C (as it is in this case) then we assume that the value of B due solely to event 1 is $\frac{1}{3}B$, with $\frac{2}{3}$ the data in B belonging to event 2. More generally, if case ii) applies then the value of B used to centroid event 1 is ;

$$B' = \frac{C}{A+C} \times C_3$$

After two clock cycles when event 2 is centred in the DAA, case **i)** is true. The same method is used to find the value of D due to event 2 only. This time the value of D is modified by calculating D' where;

$$D' = \frac{C}{C+E} \times D$$

The event is then centroided using a 3-pixel algorithm (setting the values of A and E to zero), using the modified value of either B or D depending upon whether case **i)** or **ii)** applies, **Fig 2.19b**. So for case **i)** the event is centroided by applying the 3 pixel centroiding algorithm;

$$\text{Centre Of Gravity} = \frac{D' - B}{B + C + D'} \tag{2.4}$$

and for case **ii)**

$$\text{Centre Of Gravity} = \frac{D - B'}{B' + C + D} \tag{2.5}$$

This method of centroiding gives a better estimate of each event centre, increasing the centroiding resolution of the CCD camera.

The coincidence correction circuit is only useful when the probability of two or more event profiles overlapping is high. A theoretical evaluation of its performance has been made and is described in Chapter 5.

2. The Summation Centroiding Circuit is an option for the XMM-MIC detector. Consider the case where an event is centroided in x, using the 3-pixel centroiding algorithm. Instead of simply using elements A_2,B_2 and C_2 in **Fig 2.16** to centroid the event, this circuit uses the algorithm;

$$\text{Centre Of Gravity} = \frac{C' - A'}{A' + B' + C'} \tag{2.6}$$

where

A'=A_3+ B_3+ C_3

B'=A_2+ B_2+ C_2

$C'=A_1+ B_1+ C_1$

Similarly when centroiding in y **Equ 2.6** still applies but this time

$A'=A_1+ A_2+ A_3$

$B'=B_1+ B_2+ B_3$

$C'=C_1+ C_2+ C_3$

The algorithm uses all nine elements of the DAA and thus all the information available to the centroiding electronics in calculating where the event centroid lies.

2.8.4 The Multiple Event Recognition Circuit

The profiles of two or more events landing directly on top of one another in the same CCD frame will completely overlap, producing a single event peak. If the multiple event recognition circuit is not enabled then only one event would be detected as there is only one data peak associated with the multiple events. Because events from the intensifier have a narrow energy distribution an upper energy threshold can be set where event(s) having an energy greater than this threshold are treated as two events. The multiple event recognition circuit is used to identify these multiple events by summing the energy in the whole DAA when an event peak is detected at the centre. If the energy is above the predefined threshold value (determined from the event energy distribution for single events), then the data acquisition memory is incremented by two counts instead of one count. By applying this threshold, a percentage of event profiles are recognized as being due to multiple events and the detectors' dynamic range is increased as a result.

Although the presence of a second coincident event is detected, the profile is centroided as if it were a single event (Chapter 5). A description of how the multiple event threshold is set, and what the corresponding increase in dynamic range performance is, are given in Chapter 4.

2.8.5 The XMM-MIC Address Generator

After both the x and the y centroids have been generated they, together with the pixel counter, are sent to the address generator. The pixel counter counts from 1 up to the total number of data acquisition pixels. It is incremented each time a data acquisition pixel is analysed by the processing electronics and thus records the current data acquisition pixel being analysed, (Chapter 3). The address generator combines these three pieces of

positional information, the pixel counter, the y centroid, and the x centroid, into a single address of the form

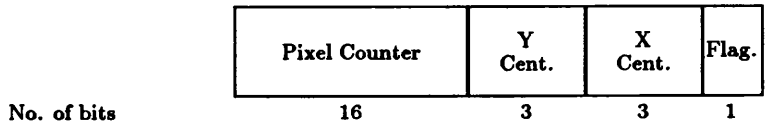

Fig 2.20. Form of an event address sent to the computer

where the pixel counter takes up 16 bits of the address and the x and y centroids take up 3 bits each. The last address bit is used as a flag, which is set when the detected event peak height is above the multiple counting threshold. The address is then latched to the FIFO before finally being sent to the computer.

2.8.6 The FIFO

The number and position of events arriving in any one CCD frame is random so that the rate at which an event address is sent to the FIFO is also random. The FIFO acts as a buffer between the processing electronics and the computer, synchronizing the rate at which event addresses leave the FIFO to the access time of the computer memory. An event address is only sent to the FIFO if the event validate flag is set, and only placed on the address lines when the computer has processed the previous event. Each FIFO is 256 locations deep. If the rate at which events arrive is greater than the rate at which the computer processes the events, then the FIFO will start to fill up and eventually a loss of data results.

2.8.7 The Frame Store

The frame store is a memory array of 128Kbytes (for the ground based system) and 64Kbytes (for XMM-MIC). It is used as a test facility by performing the following two functions:

1. Individual frames of CCD data can be loaded into the frame store and the events in those frames transferred to the computer for analysis. As a result, event energy, height and width distributions can be built up. These aid in the set up of the intensifier and ensure that the event detection threshold is set at the correct position.

2. Pseudo frames of data can be loaded into the frame store and subsequently passed to the processing electronics. The centroiding electronics can be tested by taking an integration on the test pattern and finding in which memory addresses each pseudo event is placed. By comparing the real centroided positions (known from the test pattern) with the incremented memory addresses, the performance of the processing electronics can be evaluated. The frame store is therefore also a valuable diagnostic tool in finding faults in the centroiding electronics.

Chapter 3

MIC Control System

3.1 Introduction

A VMEbus computer acts as an interface between the user and the MIC detector, controlling its operation and carrying out several important tasks which include

1. Controlling both the CCD camera and the processing electronics.
2. Providing a memory array for data acquisition.
3. Performing image processing and display functions.
4. Providing an interface with data storage media, e.g. floppy disks and magnetic tape.
5. Performing diagnostic testing of the data processing electronics.

A schematic of the computer layout is shown in **Fig 3.1**

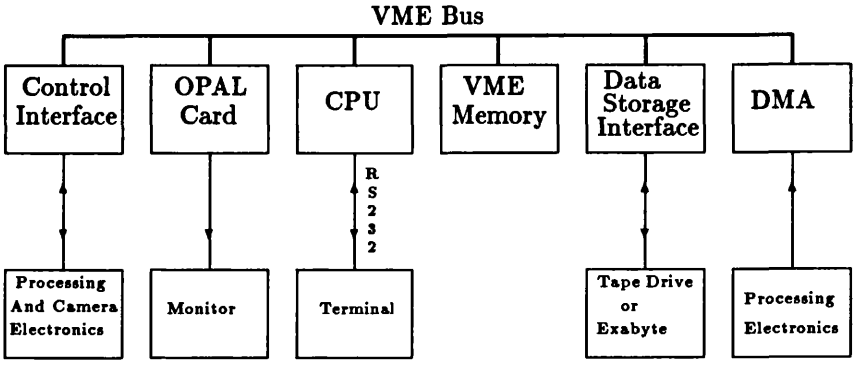

Fig 3.1. Layout of the MIC computer system

The user operates the detector by typing a series of commands from the computer keyboard. These commands execute software routines most of which are written in C but some of which are written in assembler (i.e those requiring fast execution). Each software routine performs a task associated with the detectors' operation or control and because the detector is only in its prototype stage of development a foreknowledge of each command and the task it performs is required.

The following sections describe the computer system presently used with the prototype XMM-MIC detector. This is very similar to that used with the ground based MIC detector.

3.2 Description Of The Computer System

The operations carried out by the computer are split between different component boards each of which has a specific function. These *cards* are housed together and interconnected via a VME bus. The user communicates with the computer from a terminal which is connected to the computer via an RS232 data link. The following section describes the function of each card.

3.2.1 Function Of The Control Interface Card

The control interface card is used to communicate with both the data processing electronics and the CCD camera, allowing the user to, for example:

- Set both the camera and data acquisition formats.
- Start and stop an integration.
- Set the multiple event threshold.

It is also connected to a *button box* which can be used to stop or pause an integration as well as allowing the user to gain access to the computer whilst an integration it taking place.

Link To The Data Processing Electronics

The link between the processing electronics and the control interface card consists of an 8 bit command bus, which defines the hardware destination address to be accessed, and a 16 bit bi-directional data bus. The data bus carries either data to the processing electronics

during write operations, or data from the processing electronics during read operations. Both the command and data busses have designated VME bus addresses associated with them.

Address	Function
0	Start an Integration (no data associated)
1	Stop an Integration (no data associated)
3	Defines the 10 bit double event threshold
4	Defines the 4 bit data to be loaded into the X centroid LUT
5	Defines the 16 bit address in the X Centroid LUT to be loaded
6	Defines the 4 bit data to be loaded into the Y centroid LUT
7	Defines a 16 bit address in the Y Centroid LUT to be loaded
8	Selects The Frame Stores' Mode Of Operation Data = 0 Default, Normal operation Data = 1 Set Frame Store for computer access Data = 2 Test Mode, data in Frame store replaces real data passing through processing electronics
9	Defines the Frame Store memory address to be loaded
10	Defines the 8 bit data loaded into the selected frame store memory location
11	Sets The Data Acquisition Mode Data (2 bits)= 0 Window Mode Data = 1 Full format - high resolution mode Data = 2 Low resolution mode
12	Enables/Disables The Multiple Event Recognition Circuit Data =0 Enables multiple event recognition Data =1 Disables multiple event recognition
14	Data sent to the MIC detector head
15	Defines to what use data in OC 14 is put Data=0 Takes 8 bit data in OC 14 as the 8 LSBs of the Bitmap LUT address Data=1 Takes 8 bit data in OC 14 as the 8 MSBs of the Bitmap LUT address Data=2 Takes 4 bit data in OC 14 as the data to be written into the LUT address Data=3 Enables writing to LUT. If the data associated with OC 14 =0, Enable writing If the data associated with OC 14 =1, Disable writing Data=4 Resets the Camera to a default status. If the data associated with OC 14 =0, Reset camera If the data associated with OC 14 =1, Disable reset

Table 3.1. Command functions for the data processing and camera electronics

Data is sent to the processing electronics by firstly placing it on the data bus using a subroutine called **WD** (*Write Data*). By executing 'WD y' the value y is placed on the data bus. Secondly, the hardware destination address is placed on the command bus. A subroutine called **OC** (*Output Command*) has been written to carry out this procedure. It takes the form 'OC x' where x is the hardware destination address. A list of all the OCs' are given in **Table 3.1.**

One example in which data is sent to the processing electronics occurs when the double counting threshold is redefined. To change the double counting threshold, the new threshold is placed on the data bus by executing 'WD y' where y is the new threshold value, and then executing 'OC 3' to define its hardware destination address. Not all OCs' have data associated with them, like 'OC 1' which simply stops an integration.

In XMM-MIC only frame store data can be read from the processing electronics. It is read from the data bus using the subroutine **RD** (the *Read* command).

Link To The CCD Camera

The link from the computer to the CCD camera consists of an 8 bit write only data bus and a 3 bit address bus, defining to which location within the camera data is sent. So, for example, to reset the camera the user inputs **WD 0 ; OC 14** to define the camera default status, and then **WD 4 ; OC 15** to send the new status data to the CCD camera.

Most of the data sent to the CCD camera is associated with loading the bitmap lookup table which defines those CCD pixels used for data acquisition. The bitmap lookup table has 256^2 memory locations (64K$\times$ 4 bits) associated with it, because the maximum CCD format used with XMM-MIC is 256^2. So in order to write to the whole range of lookup table addresses, the address has to be sent in two halves, the 8 least significant address bits (LSBs) first, followed by the 8 most significant address bits (MSBs). To load a value x into the bitmap lookup table location whose LSBs are a and MSBs are b, the following procedure has to be carried out;

WD 0 ; OC 14

WD 3 ; OC 15 to enable writing to the bitmap lookup table.

WD a **; OC 14**

WD 0 ; OC 15 to define the 8 LSBs of the lookup table address.

WD b **; OC 14**

WD 1 ; OC 15 to define the 8 MSBs of the lookup table address.

WD x ; OC 14

WD 2 ; OC 15 to send x to this location in the bitmap lookup table.

3.2.2 The OPAL Graphics Card

The OPAL graphics card provides a suite of graphics functions which can be called from within a C program, and are used in all the image display routines. The OPAL has 8 colour planes (which give rise to a 256 colour palette), and a display buffer of 512Kbytes. It is directly connected to a colour monitor via four coaxial cables (carrying the Red,Green,Blue and Sync signals) whose display resolution is 768H by 577V pixels.

3.2.3 The CPU Card

The computer has a 68020 CPU which runs at 16MHz. The CPU card also contains a SCSI interface for the two disk drives, a real time clock, and an RS232 interface port.

It also has an 8Kbyte block of memory called the *Global table* which, when the user logs onto the system, is loaded from the Winchester hard disk with the default value of each global variable e.g. the default multiple event threshold and the default run number. Each global variable has a status register associated with it. The status register contains a pointer to a memory location within the global table and in this memory location is stored the value of a particular global variable. By using a global table which can be read from and written to by different software routines:

- a piece of software knows the present status of the detector and can decide whether or not it is appropriate for the remainder of the program to execute. For example, if the user tries to change the centroiding resolution while an integration is in progress, the request will be rejected.

- a piece of software can change, for example, the display mode and hence change the image display register. Thus any software run subsequent to this change is aware of it.

3.2.4 The VME Memory

Unlike direct CCD imaging where an image is built up on the CCD itself, photon counting detectors integrate an image in computer memory. The VME memory is divided between the data acquisition memory, in which the image is integrated, and a display buffer, in which the image is stored in a form used by the display routines. The total size of the VME memory is 16 Mbytes. The size of the data acquisition section of the memory is dependent upon the camera format and the centroiding resolution but is limited to a maximum of 12Mbytes. Each pixel address is 16 bits deep and so the total number of available pixels is 6×10^6.

As is explained below, the VME memory is split between the data acquisition memory and the display buffer because the way in which data is stored in the data acquisition memory is incompatible with that required by the graphics display routines. In order to display an image it must first be unscrambled into a form required by the graphics routines, and placed in the display buffer. Small images (usually up to 1024×1024 pixels) can both be acquired into the acquisition memory and unscrambled into the display buffer without any memory constraints. In this case the whole image can be updated on the monitor all at once. After starting an integration the unscrambling routine is run as a background task by executing **UNSCRAMBLE**.

Because of the present VME memory constraints an image as large as 2048×2048 cannot be both integrated in the acquisition memory and unscrambled into the display buffer at the same time. Instead 2048×2048 memory locations are used for data acquisition and the image is unscrambled one quarter at a time. In this case, the display buffer would consist of 1024×1024 memory locations and data can be unscrambled and displayed using the command **MOSAIC** which updates the display one quarter of the image at a time.

Unscrambling Data

Consider the diagram in **Fig 3.2** showing the position of three software defined data acquisition windows in the CCD image area. In this example, windows **1** and **3** each contain nine CCD pixels while Window **2** contains fifteen CCD pixels. After transferring this data into the storage area of the CCD, each pixel contained within the windows is read out in the order with which they are numbered i.e the bottom left CCD pixel of Window **1** is the first CCD pixel contained within any window, to be read out. A pixel

counter c keeps track of which pixel is being read out and so if, for example, an event is centred in the middle of Window **3**, the pixel counter c will equal eleven when the event is centred in the DAA of the processing electronics.

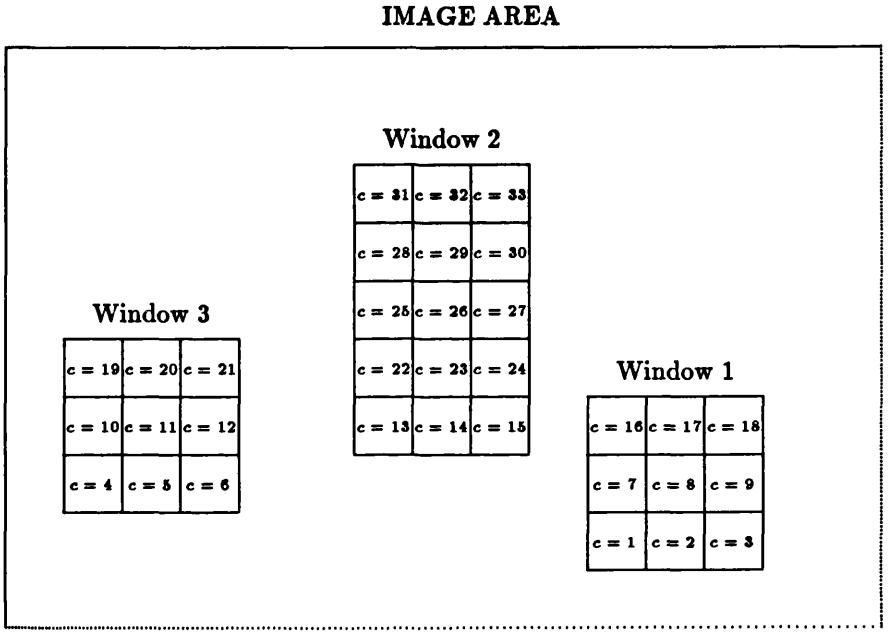

Fig 3.2 Order in which pixels within data acquisition windows are read out.

Each event detected by the data processing electronics is sent to the computer in the form of an event address which represents its centroided position on the CCD. The address takes the form of that in **Fig 3.3**:

	Pixel Counter	Y Cent.	X Cent.	Flag.
No. of bits	16	3	3	1

Fig 3.3 Form of the event address sent to the computer

After testing the double event flag and right shifting by one bit to remove the flag from the address information, the DMA card (as will be explained in Section 3.2.6) adds a bias address to the event address, reads the data stored in that VME memory location and increments it by one (or two if the double counting flag is set). It is then written back to the same memory location from which it was read. As a result, if for example, events were centroided to $\frac{1}{8}$ of a CCD pixel, all the data associated with events centroided in a single CCD pixel (having a pixel counter value of c=x) will be mapped into 64 contiguous

memory locations of the VME memory. The data associated with events centroided in the next CCD pixel (having a pixel counter value of c=x + 1) are then assigned to the next 64 contiguous memory addresses etc.

For this reason, the order in which events are stored in VME memory is incompatible with the display routines which instead require the data making up any one row of the display be stored in contiguous locations of the VME memory i.e. the display routines require that each event be stored according to the addressing system shown in **Fig 3.4**:

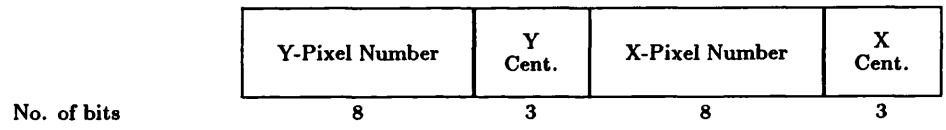

Fig 3.4 Form of the event address after unscrambling

The conversion from one form of addressing system to the other cannot be done in hardware because of constraints placed on the detectors' power consumption imposed by the XMM-OM project. Instead, because data is displayed in real time, a software unscrambling routine is run as a background task, updating and decoding data stored in a scrambled form into data stored in an unscrambled form which can then be accessed in the correct order by the display routines.

3.2.5 The Data Storage Interface Card

This card as its name suggests is the interface card to the Cipher tape drive and the Exabyte tape drive. Either of these units can be used for permanent storage of data.

3.2.6 The Direct Memory Access (DMA) Card

The DMA card is used to gain fast access to the data acquisition memory in order to store events as fast as possible during an integration. When an event address is sent from the processing electronics to the DMA, the DMA carries out a read-modify-write on the location within VME memory associated with that event. It does this by firstly taking control of the VMEbus, allowing it to have access to the VME memory. It then adds the VME memory base address, defining the start of the data acquisition array, to the event address and reads from the location in VME memory associated with the detected event. The data is incremented by one count unless the double counting flag is set in which case it

is incremented by two counts. It is then written back to the same VME memory location from which it was read and the VMEbus released.

3.3 Setting Up For An Observation Run

This section is intended to describe how to set up the detector for an observation run, as well as describing those tests that must be carried out to ensure the best performance from the detector.

The user controls the detector by entering a series of commands at the keyboard, each command being the name of a computer program which carries out a specific function. In order for the user to type the correct sequence of commands he must first be familiar with the order in which each function should be carried out.

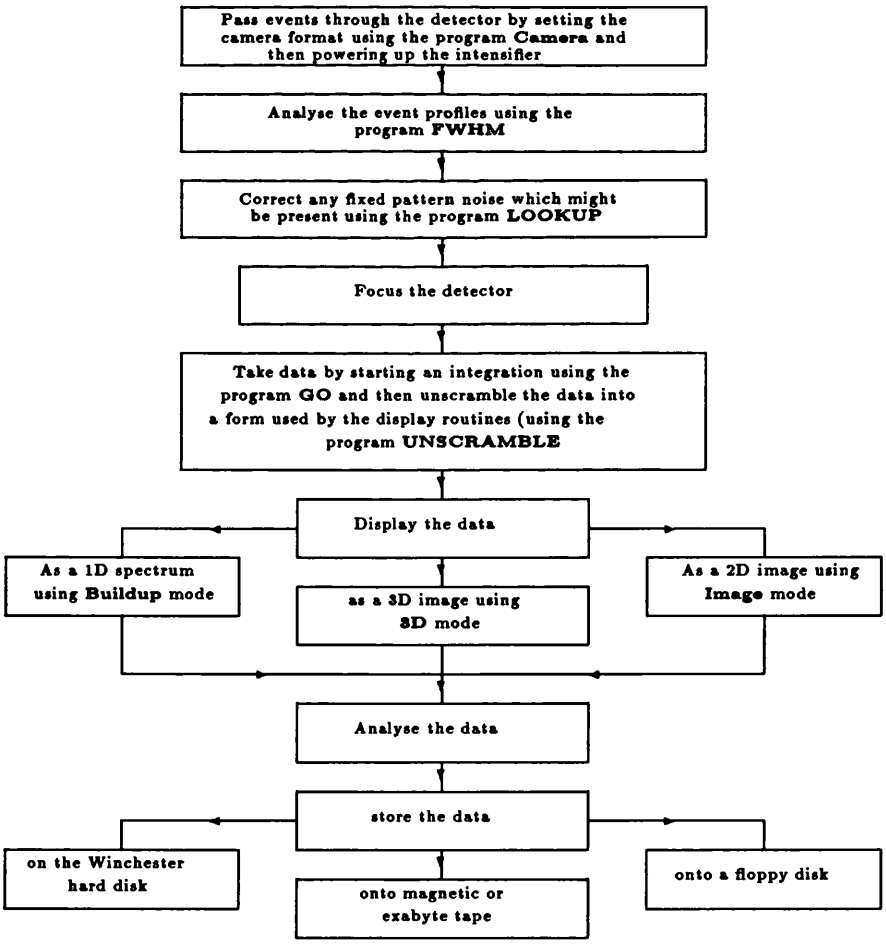

Fig 3.5. A typical sequence of events which occur whilst using the detector

Fig 3.5 shows a typical sequence of events which might take place whilst using the detector. Some of these functions may not need to be carried out, for instance if the

detector is already setup for use, but the diagram gives an idea of the order in which each procedure should take place. Some of the procedures have words which are highlighted and these represent just one of the many commands associated with that procedure.

The following sections describe each of these procedures in more detail giving a list of all the other commands used in the control of the detector.

3.3.1 Logging Onto The Computer

After switching on the power supply to the processing electronics, the CCD camera and the real time display, the computer can be turned on. Once it has booted up, the user can log into the computer by firstly executing **Ctrl D** and logging in as **XMM**. This gives the user access to all the system command routines.

3.3.2 Setting Up The MCP Intensifier

The first procedure to carry out is powering up the MCP intensifier and passing real events through the detector. Initially the CCD camera format has to be set in order to observe events on the real time display. This is done by executing **CAMERA** whereby the computer prompts the user for:

- The first and the total number of pixel rows for the first data acquisition window. When setting up the detector, the number of rows should be set to the maximum of 256.

- The first and last pixel column of the first data acquisition window. Once again, when setting up the detector, the number of columns should also be set to the maximum of 256.

- Whether there are any more windows to be defined. The user should reply *NO* as only one window of the maximum format is required at this stage. Further windows are only defined when using the multiple window facility.

- Whether the image stack should be cleared before making an image slot for this new window. If more than one image is stored in the data acquisition memory at one time they are said to be stacked in memory. Before another image can be stored an image slot must first be created. The image slot defines the first memory location used to

store the image and the number of memory locations required to accommodate the image.

The user should reply *YES* to this question in order to make room for data contained within the new window.

This sets the camera format to full size so that the maximum 256 x 256 CCD pixels are used for data acquisition. The real time display now shows a display representing the data acquisition area. As yet no events will be seen (when they are present, events appear as small scintillations of light within the data acquisition area). After ensuring that the voltage control dial on the main intensifier power supply is set to zero, both this and the divider box can be turned on. By a series of adjustments to both the main power supply and the divider box, the intensifier voltages $V_{2..4}$ are steadily increased until they are at their optimum values (see **Table 3.2**). The intensifier front gap voltage (V_1) should be kept at zero during this time.

Intensifier	V_1 (V)	V_2 (V)	V_3 (V)	V_4 (V)
MCP3I Chevron (40mm tube)	200	1300		4750
Hot Seal Z-Stack	300	964	2930	4660
MCP2910723 (25mm tube)	200	870	2840	4550
DEP (25mm tube) No.1	200	900	3100	4700
DEP (25mm tube) No.2	200	900	3040	4700
DEP (25mm tube) No.3	200	820	2850	4550

Table 3.2 Optimum operating voltages for six MIC intensifiers

The optimum intensifier voltages vary from intensifier to intensifier because of the variability in channel plate characteristics and are initially found by changing each voltage one by one until a tight pulse height distribution is obtained. The valley of the distribution should lie at 30ADU and the mean event height is typically 60ADU (see Chapter 7).

Once these voltages have been set, the detector is illuminated with a very faint (typically 500 counts/sec) flat field light source. The front gap voltage V_1 is increased very slowly, watching the real time display all the time. If the real time display shows a saturated image, representing too high a light level, the front gap voltage should be quickly decreased to zero and the illumination intensity reduced.

3.3.3 Analysing The Event Characteristics

Now that MIC is detecting events, their height and width distributions can be analysed to respectively ensure that the detector counting efficiency and centroiding resolution are optimized. This is done using the following procedures:

1. Obtaining a CCD bias frame to subtract from frames containing real events. This is done by firstly turning the intensifier front gap voltage to zero (so that no events are amplified by the intensifier) and executing **SNAP**. The program SNAP, grabs a single frame of CCD data from the frame store. The data is then placed on the memory stack by executing **PUSH**. This bias frame is subsequently subtracted from frames containing real data, during the event analysis.

2. Returning the voltage across the intensifier front gap to its normal operating value and taking an integration of the intensifier dark noise. This is carried out in order that when events are analysed later on, only events from a defect free area of the intensifier and CCD are used, thus ensuring that the event height and width distributions are not contaminated by noise events. Defects such as *switched on channels* within the intensifier and *hot pixels* on the CCD (see Chapter 7) produce events which have no relation to the image and do not have the same height and width distributions as real events.

   The procedure is carried out by firstly setting the integration time by executing **TIME** and then specifying the integration time required ($\sim$ 300 secs). An integration is started by executing **GO**. To display the integrating image **UNSCRAMBLE** is executed and the display size defined by using firstly **ROWS** and typing in the first data acquisition row to be displayed (in this case 1) and then the last data acquisition row to be displayed (in this case 256). Secondly the number of displayed data acquisition columns is defined by executing **START** and the start column (in this case 1) and then typing **LENGTH** and the number of data acquisition columns to be displayed (in this case 256). The data is displayed as an image by executing **RAINBOW** to obtain a colour display, **IMAGE** to define the display mode, and finally **SHOW** to display the image on the monitor.

3. Once the integration has stopped, the detector is illuminated with the same intensity faint flat field as was used previously. The event height width and energy distribu-

tions can then be analysed by running the event analysis program **FWHM**. This program prompts the user for an area within the data acquisition area in which events are to be analysed. By examining the dark noise image the user should select the start and end CCD row/column (whose size is typically 50 × 50 pixels) of an area free from the defects mentioned above. The program then asks if there is a SNAP frame on the stack (which there now should be) and how many events are to be analysed (typically 3000). FWHM then starts to analyse events captured in a series of SNAP frames taken from the frame store. Once the total number of events have been analysed each event distribution can be written to a file which are then stored on the hard disk.

4. Once saved, each distribution can be displayed on the monitor by executing **PLUP**, a program which is used to display 1D data. The program firstly prompts the user for the filename of the 1D data and the minimum and maximum ordinate values. Two data sets can be displayed simultaneously (each in a different colour to avoid confusion) if they need to be compared. If any of the distributions show a marked difference from that expected the appropriate intensifier voltage can be changed, and the whole procedure repeated.

3.3.4 Correcting For Fixed Pattern Noise

Fixed pattern noise comes about because of small centroiding errors resulting from the mismatch between event profiles and the centroiding algorithm (Chapter 6). As a result, depending upon the severity of this mismatch, a certain fraction of the events are centroided into the wrong subpixels in such a way that patterning with a period of 1 CCD pixel is superimposed onto the true image (**Fig 3.6a**).

Each event is centroided by firstly determining the event profile's 'centre of gravity' using the 3-pixel centroiding algorithm

$$\text{Centre Of Gravity} = \frac{A - C}{A + B + C} \tag{3.1}$$

where **B** is the peak data value associated with that event. The algorithm outputs answers in the range of -0.5 to 0.5. In order to place the event into one of eight channels (subpixels) this range of answers is initially subdivided into eight channels using boundary values which are separated by 0.125 CCD pixels. For example, an event would be placed

into *Channel 1* if the result of the centroiding algorithm lay between -0.5 and -0.375 or would be placed in *Channel 2* if the result of the centroiding algorithm lay between -0.375 and -0.25.

If the centroiding algorithm were to accurately centroid each event from a flat field, equal numbers of events would be centroided into each subpixel and the output image would appear 'flat' (**Fig 3.6d**). However, fixed pattern noise typically causes unequal numbers of events to be centroided into each subpixel if the subpixels have equally spaced boundary values.

The centroid position in x and y of each event is defined in what are called the *centroid lookup tables* (Chapter 2). The position of a subpixel can be redefined in software by changing the data stored in these centroid lookup tables. By changing the subpixel boundary positions (i.e. by redefining the centroid positions of events), the effect of fixed pattern noise can be minimized. A subpixel in which events are preferentially centroided can be made smaller by reducing the range of answers given by the centroiding algorithm, which apply to that subpixel. Similarly, a subpixel in which few events are centroided can be made larger by increasing the range of answers (from the centroiding algorithm) which apply to it.

Finding by how much to change the position of each subpixel boundary is an iterative process and involves firstly sampling a flat field image and analysing the count distribution in each subpixel. From a knowledge of this and the subpixel boundaries, the boundary positions can be changed in order that the next time a flat field is sampled a more equal number of events are centroided into each subpixel (**Fig 3.6b**). A new flat field image is then resampled and the subpixel boundaries are changed until eventually (after several iterations) the ideal subpixel boundaries have been defined in the centroid lookup tables.

The fixed pattern noise can be corrected for by carrying out the following procedures;

1. Selecting a centroiding resolution of $\frac{1}{8}$ of a CCD pixel so that data in each of the eight subpixels is available. The centroiding resolution is set by executing **FORMAT** and entering the number of subpixels/pixel required. This number is limited to 4 and 8 for XMM and so in this case the user should type **FORMAT 8**.

2. Run the program **LOOKUP** which is used to analyse the count distribution in each subpixel and calculate the subpixel boundaries which are most likely to minimise the level of fixed pattern noise. A menu appears which asks the user whether the

subpixel boundaries should be equally spaced (**E**), reloaded from the last time they were saved (**R**), individually entered by the user (**O**), or calculated from the subpixel count distribution of a flat field image (**C**). The user has to firstly load the centroid lookup tables with equally spaced subpixel boundaries in both x and y to provide the initial starting boundary positions. The user types **E** at the menu prompt and then x to specify in which direction the subpixel boundaries should be equally spaced. **LOOKUP** is run again and at the menu prompt the user retypes **E** and follows this by typing y to load the centroid lookup tables with equally spaced subpixel boundaries in y.

3. Carrying out an integration on a faint flat field image (to avoid a high proportion of coincident events), using a small section of the CCD. An integration is started, and continued until each subpixel has, on average, 10-20 counts in it. By co-adding rows or columns a cross section through this image will typically look like **Fig 3.6a**.

4. If, after imaging the flat field illumination, each subpixel does not contain an approximately equal number of events then the program **LOOKUP** is rerun in order to calculate a new set of subpixel boundary values. The user types **C** at the menu prompt and then enters an area of the CCD over which the subpixel count distribution is to be calculated. This area should be free of the types of defect mentioned in Section 3.3.3 and have a size of typically 20×20 CCD pixels. The computer proceeds to sum the number of counts in each subpixel of a CCD pixel using Modulo 8 addition (e.g summing counts in the first subpixel (in x) of every CCD pixel within the specified area). By summing the counts in each subpixel over an area of the CCD, the subpixel count distribution has good count statistics with which to calculate new subpixel sizes. The program calculates the mean number of summed counts/subpixel and then for each subpixel it estimates the change in boundary position required in order to minimize the degree of fixed pattern noise. For example, after analysing the count distribution in **Fig 3.6a**, the data shown in **Table 3.3** might be presented.

Channel	Counts	Old Boundary Values	Suggested New Boundary Values
0	7600	-0.5	-0.5
1	7750	-0.375	-0.389
2	7785	-0.25	-0.282
3	7694	-0.125	-0.175
4	7350	0.00	-0.067
5	1064	0.125	0.047
6	7410	0.25	0.277
7	7640	0.375	0.386
		0.5	0.5
		Mean Count/Channel= 6786	

Table 3.3 Example of output from the program LOOKUP

It does this from a knowledge of the deviation of each summed subpixel count from the mean and the present size of each subpixel. One of the two following algorithms are used to calculate each new subpixel size.

$$\text{New Subpixel Size} = \text{Old Subpixel Size} + 1/8\frac{\text{(Mean-SubpixelCounts)}}{\text{Mean}} \tag{3.2}$$

$$\text{New Subpixel Size} = \frac{\text{Old Subpixel Size/Counts In Subpixel}}{\sum(\text{Old Subpixel Size/Counts In Subpixel})} \tag{3.3}$$

where the *Mean* refers to the mean number of summed counts per subpixel over the area specified, and the *Subpixel Counts* are the number of summed counts in the subpixel whose size is being changed. From experience, it is found that for certain 'chronic' fixed patterns i.e. with one subpixel either having most, or almost none of the counts, that the second algorithm is more able to correct the fixed pattern than the first algorithm. The software recognises when one of the subpixel counts is > 2 SD's from the mean subpixel count, and accordingly suggests the second algorithm to calculate the new pixel boundary positions. The user can change the algorithm if required, and once calculated, the old and new subpixel sizes are printed out. If the user agrees to use the newly calculated subpixel sizes, the centroiding lookup table is updated and the subpixel boundary values saved in the global table.

5. Carrying out another integration of a 'flat field' image using the newly calculated subpixel sizes. The program **LOOKUP** is re-run, and new subpixel sizes calculated once more.

The whole process of taking an integration and recalculating each subpixel size should be continued until the level of fixed pattern noise is unnoticable above that of the photon noise i.e. the RMS subpixel count deviation is $\simeq \sqrt{\text{Mean Subpixel Count}}$.

Fig 3.6a shows the typical level of fixed pattern noise for subpixels having equal boundary values and **Figs 3.6b,c** and **d** show the typical level of fixed pattern noise after applying three successive iterations of the correction algorithm.

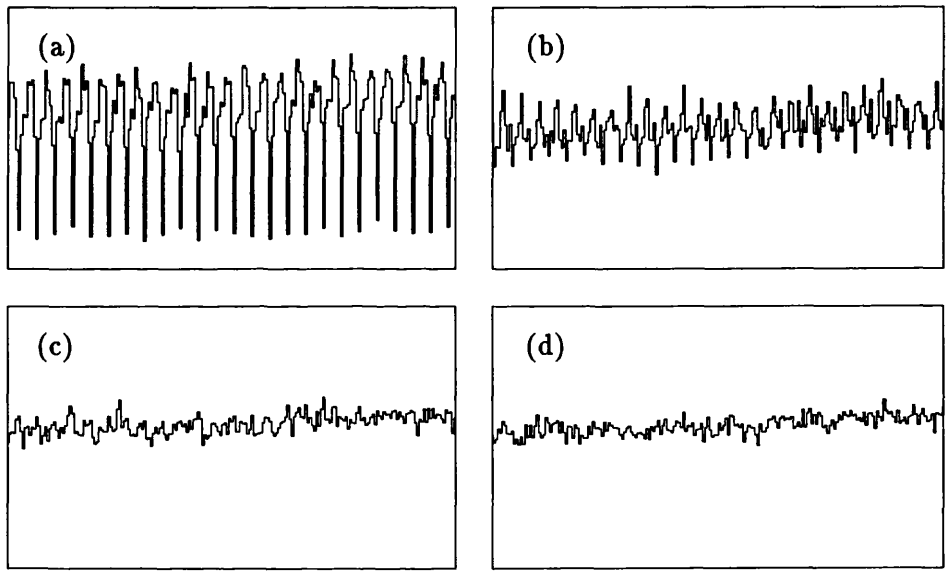

Fig 3.6. Level of fixed pattern noise for three successive iterations of the correction algorithm

After the fixed pattern correction has been carried out, the centroiding algorithm and centroid lookup table combine to correctly centroid each event so long as the event profile remains constant. The correction is only valid for events whose profiles closely match those with which the correction was carried out. If the event profile changes for any reason, the fixed pattern correction no longer applies and fixed pattern noise is re-introduced.

3.3.5 Focussing The Detector

To visually measure the changes in an image profile introduced by moving the focus position, and hence, decide the best focus position, histograms of slices (or cross sections) through the image profile need to be displayed. The *buildup* display mode allows the user

to select areas of an image from which individual rows or columns can be co-added to produce a cross section.

In practice the detector is focused by maintaining a centroiding resolution of $\frac{1}{8}$ of a CCD pixel and imaging a point source illumination (or in spectroscopic applications, arc lines). The focus position is then found by one of two methods, depending upon the imaging optics placed in front of the detector. These are:

- At major telescopes such as the the AAT and the WHT the focus on spectrographs can typically be found by using a Hartmann test. **Fig 3.7.**

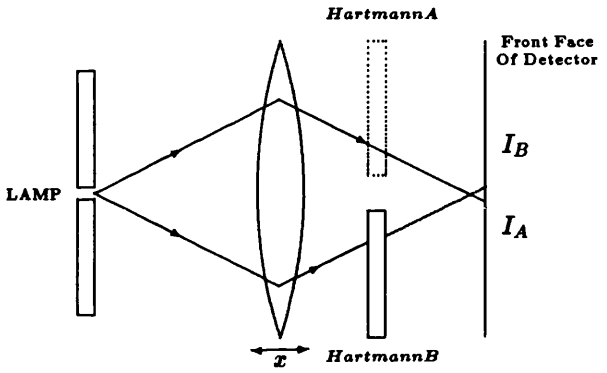

Fig 3.7. Obtaining focus using the Hartmann test

The method consists of taking two images of the point source illumination, one with Hartman A blocking off half the image and another with Hartman B blocking the other half of the image. If the image is focused, then the position of images I_A and I_B coincide with one another. If the two images do not coincide the focus position is easily found by observing the separation of I_A and I_B for changes in x. The focus position is changed by moving (in x) the telescope collimator, but if focus cannot be obtained anywhere in the collimator range, either the detector has to be moved closer to the collimator (by redesigning the detector mount) or stood off from the telescope using shims.

To display image cross sections side by side, the user must first change the display to *buildup mode* by executing **RESET**. This allows cross sections through an image to be displayed. If the user wishes to produce a cross section parallel to the x axis then the user types **BUILD** and then the build up number where up to 8 buildups can be defined. The program **BUILD** prompts for the start row and the number of

rows to be summed into a 1D cross section. This *buildup* definition is then saved, and can be recalled at a later date by typing **LOAD** and the associated buildup number.

Similarly, if the user wishes to produce a cross section parallel to the y-axis the user types **YBUILD** to define how many columns are summed together to make the 1D cross section. The program **YBUILD** prompts for the start column and the number of columns to be summed. The *ybuildup* can be recalled at a later date by executing **LOAD** as before.

Once a buildup is selected it is displayed by executing **SHOW**. The range over which a buildup can be displayed is altered by either typing **ROWS** (and the row start and end values) when displaying a ybuildup, or **START** and **LENGTH**, when displaying a buildup. Up to six (y)buildups may be displayed on the monitor at any one time (see the section on buildup commands).

Images I_A and I_B are displayed on top of one another by firstly taking an integration using one Hartmann and then executing *SAVE* to fix the image on the screen. An image is then taken with the other Hartmann and this becomes superimposed on top of the previous image. Several such cross sections can be saved on the screen at any one time.

- In the laboratory or on instruments that do not contain Hartmann shutters, a simpler but just as effective way of finding the focus position exists. This method also involves taking a cross section through the a point source image, but this time measuring its full width at half maximum (FWHM). Focus occurs when the image FWHM is a minimum and so in the laboratory (where in our case the source of illumination is provided by a Baum projector), the projector position from the front face of the detector is moved until the image FWHM is a minimum. This is only found by moving the image through the focus position and observing an increase in FWHM either side of the focus position.

3.4 Taking Observations With The MIC Detector

An observing program may involve the observation of very different types of object having vastly different sizes, wavelength coverage and intensity. The following procedures should

be carried out in order to observe each of these objects most efficiently;

1. If the object or background illumination is expected to be bright, either neutral density (ND) filters or narrow transmission band filters should be placed in front of the detector. Before exposing MIC to light of an unknown intensity the intensifier front gap voltage V_1 should be turned down to 0V. When exposed, V_1 is increased slowly whilst watching the real time display.

2. Set the initial data acquisition format to its maximum size i.e. 256 pixel rows by 256 pixel columns.

3. Select the appropriate centroiding resolution using the program **FORMAT**. A high centroiding resolution is required for closely spaced objects (like closely spaced stars or in the case of spectroscopy, closely spaced spectral lines). It is also required in order to adequately sample a single star profile, for example, or a single arc line.

4. If the double counting threshold (Chapter 4) needs changing then type **THRESHOLD** followed by the double counting threshold. If the user enters a value of -1 then the double counting circuit is disabled. The threshold is preloaded with its optimum value and so it should only be redefined if testing the system.

5. Move the image onto a defect free or 'flat' part of the detector (usually the centre).

6. Place a data acquisition window around the object(s) in the field of view. Minimizing the data acquisition area not only helps to decrease the amount of memory required to store the image but also increases the detectors' dynamic range performance by decreasing the CCD frame time (Chapter 4). Prior to placing a window a short integration of the field using the maximum data acquisition format must be taken and then displayed on the monitor. Up to 16 data acquisition windows can then be defined by calling the program **BOX**, which places a box cursor on the image display and allows the user to define subsets of the image for future integrations. The cursor can be moved around the image and its size changed.

7. Integrate on the image (by executing **GO**) until the desired signal to noise ratio (Chapter 7) is obtained. The image can be displayed whilst being integrated by executing **UNSCRAMBLE** to initiate the data unscrambling routine, and then

choosing the display mode, which is described in more detail below. Whilst an observation is taking place, a *button box* may be used in order to gain access to the computer keyboard. This could be used for one of several reasons;

- **Stopping An Integration**; The integration can be stopped prematurely by pressing the **STOP** button. The duration over which the observation took place, is displayed on the screen and the data collected within this time is held in computer memory. An integration can also be stopped from the command line by executing **ABORT**.
- **Holding An Integration**; The integration can be paused by pressing the **HOLD** button. The data remains in memory, and the observation is restarted by executing **CONTINUE**, whereby the newly accumulating data is added to that stored in memory. This feature is helpful, for example, when cloud affects an observing run. The integration can be held, and restarted as soon as the cloud disappears.
- **Changing The Display**; By pressing the **CHANGE DISPLAY** button, the computer prompt will appear on the screen. This allows the user to change the display whilst the integration continues as a background task. The continually updated image is returned to by executing **SHOW**.

8. If the detector is being used to directly observe astronomical objects, use the sky background to obtain a flat field image using the same camera format, data acquisition windows and centroiding resolution. This ensures that all objects are 'flat fielded' with sky background imaged over exactly the same area of the detector.

The detector status can be displayed on the VDU at any time by firstly obtaining the computer prompt and then executing **LIST**. The program displays information about the detector status obtained from variables stored in the global table e.g.

- The size and position of each data acquisition window.
- The current and previous integration times.
- The observers name, the current run number and the data destination.
- The current display status.

3.4.1 Displaying Data

There are three different ways in which data can be displayed on the monitor. In **IMAGE** mode, data is displayed as a 2-dimensional array of pixels, where the data associated with each pixel is represented by a colour. The colour is related to the data value by a colour bar placed across the top of the screen, whose colour scale is defined within the colour lookup table. Up to four images can be displayed on the monitor at any one time. The number of displayed pixel rows and columns are placed around each image together with a label representing its associated window number.

In **BUILDUP** mode, cross sections through the 2-dimensional image can be displayed as a 1-dimensional histogram. Up to six buildups can be displayed on the monitor at any one time and each one has a set of axes, these being the channel number and the number of counts in that channel.

In **3D** mode small areas of an image can be displayed in a 3-dimensional format. Half the monitor is used to display the 2-dimensional representation of the image while the other half is used to display the same area of data but in 3-dimensions.

Many of the most simple commands associated with the image display have been mentioned above, but there are many more display features that enable the user to view and interpret his data. All the commands as well as their function are listed for each of the three display modes.

1. Image Mode

    - **IMAGE**. Used to set the display to image mode.
    - **DISPLAY**. Allows the user to display up to 4 images on the monitor at any one time.
    - **MOSAIC**. Used to unscramble and display images larger than 1024 × 1024 pixels. The display is updated one quarter at a time.
    - **ROWS**. Defines the first and last row to be displayed.
    - **START**. Defines the first column to be displayed
    - **LENGTH**. Defines the number of columns to be displayed.
    - **SCALE**. Rescales the colour lookup table.
    - **AXES**. Draws axes on display

- **IM_AVERAGE.** If the data is scrunched (due to the acquisition format being larger than the display resolution), then only the average data value from the scrunched pixels is displayed.
- **IM_SUM.** If the data is scrunched, then the sum of all the data values from the scrunched pixels is displayed.
- **IM_MAX.** If the data is scrunched, then only the maximum data value from all the scrunched pixels is displayed.
- **GREY.** Changes the display lookup up table to a grey scale.
- **RAINBOW.** Changes the display lookup table to a colour scale.
- **SQUARE.** Optimizes the image size on the monitor to maintain the aspect ratio.
- **PICK.** Displays a cross hair cursor whose row, column and data value are displayed. A separate colour plane is used for the cursor.
- **REDRAW.** Redraws the image with a different colour lookup table in order to clear the colour plane used for cursors. If REDRAW is typed again then the image is redrawn using all the colour planes.
- **2COMPARE.** Displays the top two images on the image stack.
- **CLEAR.** Clears the display as well as any overlay cursors.
- **ASPECTRUM.** Creates a box cursor which can be used to create automatic buildups or define an area in which a statistical analysis of data within the box can be carried out.
- **SHOW.** Displays an image on the monitor using the display parameters defined above.

Fig 3.8 shows how data is displayed in Image Mode.

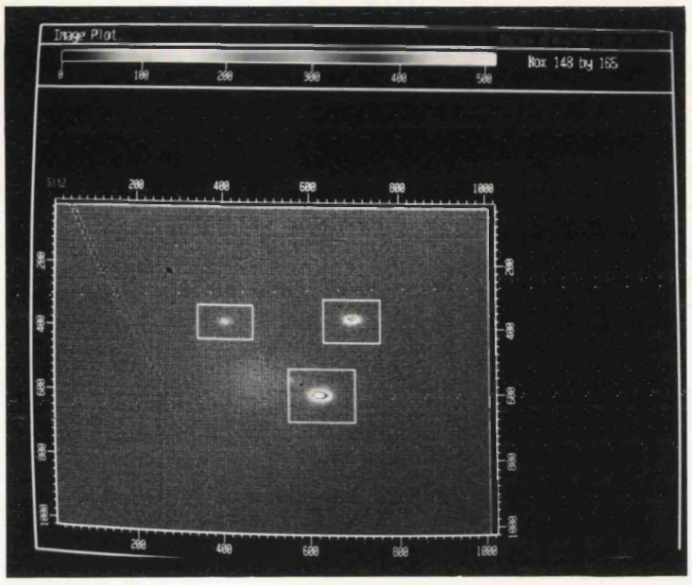

Fig 3.8. Data displayed in image mode

2. Buildup Mode

- **RESET**. Used to set the display to buildup mode.
- **BUILDUP** *n*. Used to define a buildup along the x (column) axis. The start row and the number of rows to be co-added have then to be entered. *n* is the buildup number.
- **YBUILDUP** *n*. Used to define a buildup along the y (row) axis. The start column and the number of columns to be co-added have then to be entered. *n* is the buildup number.
- **TOTALS**. Shows the total number of counts displayed in the buildup.
- **ROWS**. Defines the first and last row displayed using a *ybuildup*.
- **START**. Defines the first column displayed when displaying a *buildup*.
- **LENGTH**. Defines the number of columns displayed when displaying a *buildup*.
- **SCALE**. Sets the maximum data value for the display of any buildup.
- **BIAS**. Sets the minimum data value for the display of any buildup.
- **BLOCK**. Smooths through data defined in a buildup.
- **HISTOGRAM**. Buildup data is displayed in the form of a histogram.

- **LINES**. Data is displayed by connecting each data point with a straight line.
- **DELAY**. Sets the delay time between updating the display when an integration is in progress.
- **PICK**. Displays a cross hair cursor whose channel number and data value is displayed.
- **SAVE** n. Saves data in the last displayed buildup on the monitor. n defines the colour plane in which the data is saved. Data from a previous exposure but defined by the same buildup can be displayed on the screen in parallel with the current data set. This allows comparison of one exposure with another. This feature is mostly used when focussing the detector.
- **UP** a, b, c, d. Allows up to four buildups (where a, b, c and d are the buildup numbers) to be displayed across the upper half of the display.
- **LO** a, b, c, d. Allows up to four buildups to be displayed across the lower half of the display.
- **SHOW**. Displays buildups on the monitor using the display parameters defined above.

Fig 3.9 shows how data is displayed in Buildup Mode.

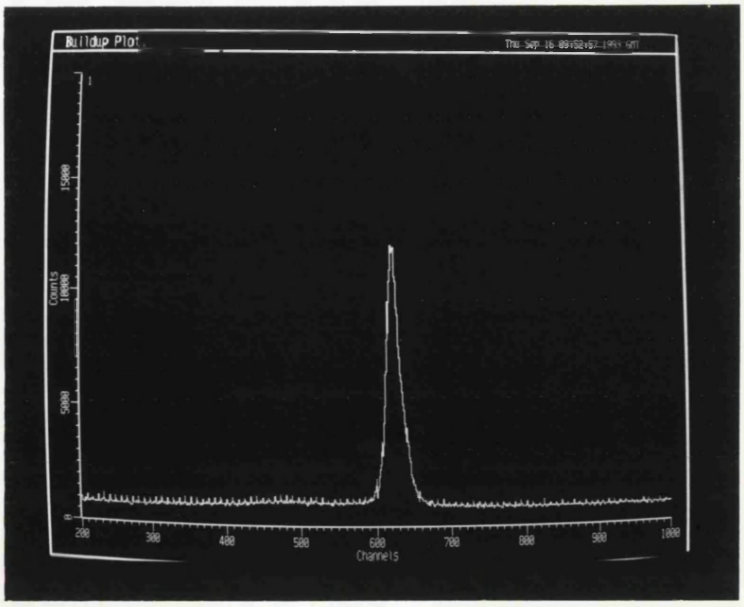

Fig 3.9. Data displayed in buildup mode

3. 3d Mode

- **3d**. The program 3D is a 3-Dimensional plotting program, which allows the user to display a small section of an image in 3D form. It is useful mostly for examining single or multiple event profiles captured in a SNAP frame, or a point source image profile. The image must be one which is already on the data stack in an unscrambled form. The user selects the image area to be displayed (up to 25×25 pixels), which is then drawn in 2D form, on the right hand side of the screen, and in 3D form on the left hand side of the screen. The data can be viewed in one of four viewing modes, each having a different orientation about the Z-axis.

Fig 3.10 shows how data is displayed in 3D Mode.

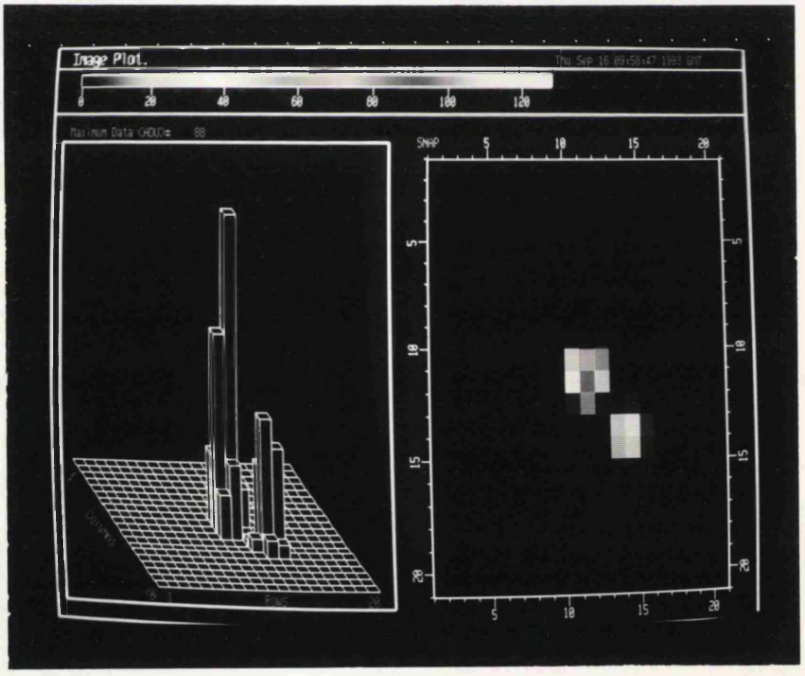

Fig 3.10. Data displayed in 3D mode

3.4.2 Analysing The Data

Although the online data processing is limited (as most of the data is analysed using STARLINK software), the following facilities do exist:

- **ADD**. Adds two images of the same size together.
- **SUB**. Subtracts one image from another of the same size.

- **DIV.** Divides one image by another.
- **MULT.** Multiplies one image by another.
- **CADD.** Adds a constant value to all data in an image.
- **CMULT.** Multiplies all image data by a constant.
- **XFWHM.** Analyses spectroscopic data stored in a 1D data file, by finding each line FWHM and its centroid position.
- **IFILL.** Floods an image with a single value. This is used to either clear all the data within an image slot, or to test whether the computer can write to the VME memory correctly.
- **STATS.** Produces a statistical analysis on data confined to an area of the image specified by the user. The program **STATS** produces the total count in the area, the mean count/pixel, the maximum count in any one pixel, the lowest count in any one pixel, and the standard count deviation.
- **PUSH.** Push an image onto the stack.
- **POP.** Pop an image from the stack.
- **SWAP.** Exchange the top two stack images.

3.4.3 Data Storage

The VME memory is volatile so in order to permanently store data it can be saved using one of four possible storage mediums. The usual procedure for analysing data is to store it on magnetic tape in FITS format, and transfer it onto the university VAX computer. Once on the VAX, data is analysed using STARLINK software which provides comprehensive and easy to use software packages which are used by a wide section of the astronomical community.

1. The Winchester Hard Disk. Permanent on board data storage is provided by an 8Mbyte Winchester hard disk. This is usually only used for storing software, but is sometimes used to store small images and 1D spectra. Data can be stored and recalled from disk using the following commands:

- **WINCHESTER.** Data destination is the Winchester hard disk.
- **RCL.** Recalls an image from a disk file.
- **BSTORE.** Saves data in a buildup onto disk.
- **STORE.** Stores a section of an image to the current data destination.

2. Floppy Disk. This is used mainly for system backups and for storing 1D spectra. Data can be stored and recalled from floppy disk using the following commands:

   - **FLOPPY.** Data destination is floppy disk. The floppy disk drive should first be mounted by logging into the computer as *ROOT* and then typing **MOUNT fd0 /x**. This mounts the floppy drive (fd0), which acts as if it were the directory **/x**. The program **FLOPPY** defines this 'directory' as the data destination source. Files can be taken off the floppy disk by copying them from **/x** to the Winchester hard disk. To finish, the floppy drive should be unmounted by typing **UMOUNT fd0** from the root directory.

3. Magnetic Tape. Most of the data presently taken with MIC is stored on 6250 cpi magnetic tape. The tape drive is a Cipher (11020) which is bulky and difficult to transport. Data can be stored and recalled from magnetic tape using a selection of the following commands:

   - **TAPE.** Data destination is magnetic tape once an integration has finished.
   - **TINIT.** Initialize a tape in order to write to it for the first time.
   - **MOUNT.** Mount a partially full tape.
   - **DISMOUNT.** Rewind a tape and reset the tape controller.
   - **FIND** n. Finds and loads an image whose tape run number is n
   - **TPOSITION** n. Position the tape at the file whose tape file number is n.
   - **FITSLIST.** Lists all the tape file headers on tape.
   - **FITSLOAD** n. Loads a FITS format file whose tape file number is n, from tape into memory.
   - **FITSSAVE.** Saves an area of memory as the next FITS file on tape. The user specifies the VME memory location in which the first data value of that image is stored, and then the dimensions of the image area required.

- **FITSIN** n. Recalls a file whose tape file number is n from tape to a disk file.
- **FITSOUT**. Store a disk file to tape. The tape file number will be one greater than the last file saved on that tape.
- **NULL**. Data is not automatically saved (after an integration).
- **DSTORE**. Saves a limited area of an image onto tape. The area is either the image area displayed on the monitor, or the area can be defined independently by the user.
- **TSTORE**. Saves data in a buildup onto tape.
- **TNUMBER**. Changes the label given to the tape currently mounted. The label is represented by a number.
- **NEXTR**. Change the current run number.
- **OBSERVER**. Sets the observers initials.

4. Exabyte Tape. Although the Exabyte drive has not yet been fully tested, it is expected to provide a more compact medium for data storage. The drive itself is extremely light and easily portable. Data can be stored and recalled from Exabyte tape using the following commands;

   - **EXABYTE**. Data destination is the EXAbyte tape once an integration has finished.
   - **EXIN**. Reads the next file on EXAbyte tape.
   - **EXOUT**. Saves an image onto EXAbyte tape.
   - **EXREWIND**. Rewinds the EXAbyte tape.

3.5 System Testing

In order to ensure the detector is operating correctly, some built-in test facilities have been developed for the system. The most valuable of these is the *frame store*. The frame store is a memory array, having the same dimensions as the maximum number of CCD pixels used for data acquisition (i.e. 256^2), and can be used in one of two ways, depending upon the mode of operation;

1. **FRAME GRABBER**: The frame store acts as a frame grabber, acquiring a frame of data from the CCD camera and storing it in the frame store memory. This data can then be transferred to the computer via the control interface. A single frame of data from the CCD camera is called a *snap* frame (Section 3.3.3), and may be manipulated like any other image, by pushing it onto the image stack. A CCD frame is examined (using the program **FWHM**) in order to determine:

   - the shape of the event profile.
   - whether the intensifier is producing the optimum photon gain, i.e. the lower counting threshold is lying in the valley of the event height distribution (Chapter 7).
   - whether SIB events are likely to be present (as the event width distribution would become broader).
   - whether the CCD has been lowered onto the fibre taper correctly (as the event width distribution would vary across the CCD).

   It can also be used to examine two contiguous frames of data by executing **2SNAP**. This allows the frame store to capture two contiguous frames of data with a CCD format of 128×256 pixels instead of the normal single frame format of 256×256 pixels. **2SNAP** then reads the data into the computer as two separate images placing them into different slots within the image stack. These two images can then be displayed side by side by executing **2COMPARE**. **2SNAP** is used to examine the extent to which events arriving in one frame of the CCD, produce secondary (or phosphor decay) events in the next contiguous frame. As will be described in Chapter 4 the energy associated with an event can (in some circumstances) be deposited over two CCD frames and so the program **FWHM** (which can use 2SNAP to obtain contiguous CCD frames) helps to quantify this effect.

2. **TEST MODE**: In test mode, the frame store memory is loaded directly by the computer. The program **FRAME** is used to check the operation of the frame store. It includes a facility used to clear the frame store or check for any non-zero data.

   The program **XNSG** writes a frame of pseudo data into the frame store. The pseudo data consists of one or more 'events', gaussian in shape, and whose position within

the frame can be specified by the user. After writing the data, an integration may be taken using the frame store, instead of the CCD camera, as the data source. During the integration, the frame store data is processed, and counts accumulated in the data acquisition memory. If the incremented memory locations are different from those calculated (knowing the centroid position of the event profiles in advance), the user then knows that there is something wrong with the processing electronics.

After using either of these modes, the system can be returned to normal operation by placing it in **NORMAL MODE**. This is given as an option at the end of each of these programs.

The centroiding electronics may also be tested by centroiding an image in software instead of hardware, and comparing the image profiles produced by both methods. The program **CENTROID** takes a series of snap frames from the CCD camera, and events are then centroided using software. A choice between several centroiding algorithms can be made (either 3 or 5 pixel algorithms) and their effect seen in the resulting software centroided image.

Chapter 4

Detector Dynamic Range

4.1 Introduction

Before carrying out astronomical observations with a photon counting detector knowledge of the detectors' response to different light intensities must first be established. This enables the astronomer to judge whether the detector is suitable for measuring the intensity of astronomical objects they want to observe.

Ideally, the detector output is expected to be directly proportional to the detector input. In addition, this *linear* relation between detector input and detector output is expected to hold over all light intensities e.g:

1. there being no counts detected if there is no input signal.

2. the output signal being equal to the (input signal × detector DQE) at the highest light levels.

In reality no detector can achieve these ideals and this linear relation does not hold over all light intensities. A graph showing the typical response of a photon counting detector to a varying light signal is shown in **Fig 4.1**.

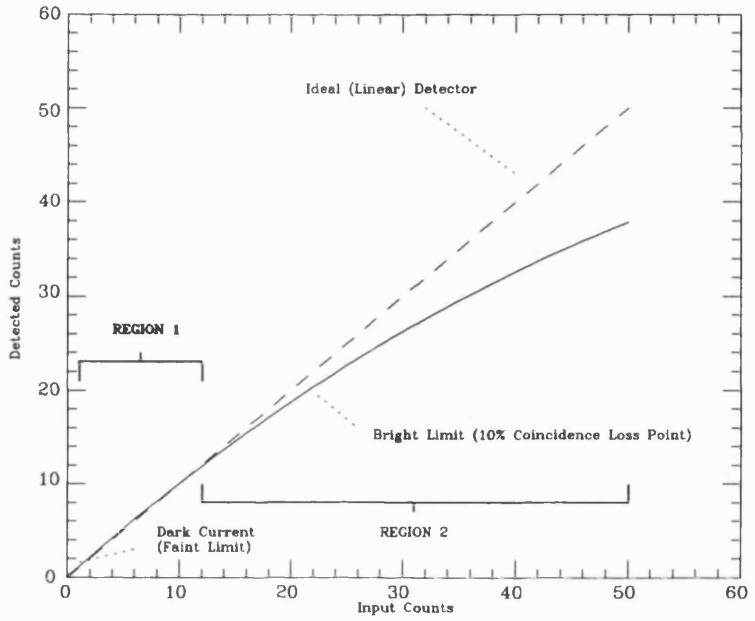

Fig 4.1: A typical dynamic range curve from a photon counting detector.

There are two distinct regions to this graph:

- **Region 1:** In this region the detector is close to counting linearly, the input count rate being nearly directly proportional to the output count rate. Even at very small count rates there will be *some* degree of coincidence taking place and so it cannot be said that *no* coincidences occur in *region 1*, only that the level of coincidence loss is negligible. When there are no incident photons, the detector gives a non-zero reading, due to a small number of events generated internally within the detector, the *dark current.* In most intensifiers dark current is derived mainly from the photocathode with a small contribution from the intensifier input window and microchannel plates.

- **Region 2:** In this region the detector no longer counts linearly. This is due to coincidence losses within the detector. Coincidence losses take place when two or more events become indistinguishable from one another and are only detected as a single event.

In order to derive the input light intensity from the output count rate of a detector without the use of calibration curves like that in **Fig 4.1** the observer needs to know the intensity range over which the detector counts linearly. In the case of photon counting detectors this range of intensities, called the **Dynamic Range**, is quoted in terms of:

1. a *Faint Limit* which specifies the detected count rate equivalent to when no input signal is present i.e. this is equal to the detector dark current.

2. a *Bright Limit* which normally specifies the input count rate at which 10% of the events become undetected due to coincidence losses within the detector (which will be referred to from now on as the 10% coincident point).

4.2 The Faint Limit Of Dynamic Range

The faint limit of dynamic range is governed by the detector dark current which, in the case of MIC, derives from three components of the image intensifier.

4.2.1 The Intensifier Photocathode

A photocathode produces dark current due to the thermal excitation of electrons from its surface. Once released, these electrons are detected in the same way as photoelectrons released by photoexcitation and hence contribute to the output signal in exactly the same way as real events. The rate at which photocathode dark current is produced depends upon both:

- the chemical composition of the photocathode. Photocathodes having a small band gap energy between their conduction band and their vacuum level (like the S20 photocathode) tend to have a high red response. Consequently, these photocathodes will have a small thermionic work function and so tend to produce high levels of dark current at room temperature. Photocathodes having a low red response (such as the bi-alkali photocathode) produce correspondingly lower levels of dark current.

- the photocathode temperature. The rate at which photocathode thermionic emission changes with temperature is determined by the Boltzmann factor $exp(\frac{-E_g}{kT})$ where E_g is the band gap energy between the Fermi Level and the vacuum level, k is the Boltzmann constant and T is the photocathode temperature. At room temperature an S20 photocathode typically produces twice the dark current if the temperature is increased by 5K.

The typical dark current of an S20 photocathode is between 30-50 counts cm^{-2} sec^{-1} at 300K. The dark current can vary between photocathodes of the same type due to differences in their manufacture, so the dark current associated with individual photocathodes is found by making direct measurements. A typical bi-alkali photocathode has a dark current of 4-6 counts cm^{-2} sec^{-1} at 300K [Ref^3], some 8 times lower than the S20.

Once launched, XMM-MIC is expected to operate in a stabilized temperature environment of 293±5K. In this temperature range an S20 photocathode would be expected to have a dark current of 10-50 counts cm^{-2} $secs^{-1}$. In the same temperature range a bi-alkali photocathode would be expected to have a dark current of 1-6 counts cm^{-2} sec^{-1}. The white light background count (from zodiacal light, moonlight etc) is expected to be $\sim$ 6×10^4 counts cm^{-2} sec^{-1} whilst observing with XMM, totally swamping the background photocathode dark current contribution. With narrow band filters the sky background will still dominate which means that the choice of XMM-MIC photocathode is not determined by the S20 or bi-alkali dark current contributions.

4.2.2 Intensifier Input Window

Certain materials used as intensifier input windows can contribute to the intensifier dark current. For example, upon powering an ITL 25mm intensifier (Ref No 2910723) which had a sapphire input window, large instantaneous groups of events were found to be present. There was no visible increase in the rate at which these groups of events were occurring with incident photon illumination, which suggested that the problem was not caused by ion feedback. The only other mechanism which could produce these events are scintillations in the input window. In order to determine the nature of these light scintillations, a simple analysis was carried out by the author.

The average number of photons produced in a localized group of events was estimated by taking a series of one second integrations and summing the photons detected. If no scintillations occurred during the integration then the data was used to estimate the average background count produced by photocathode dark current and stray light. A total of 60 groups of events were recorded, some of which were not localized but scattered across the whole detector area, producing a severe increase in the number of detected photons. However, most groups were contained within a small section of the image. There were 4 delocalized event groups out of the 60 sampled and they produced an average of 4500 counts each.

A histogram of the number of detected events per group (with background subtracted) is shown in **Fig 4.2** for all the localized groups.

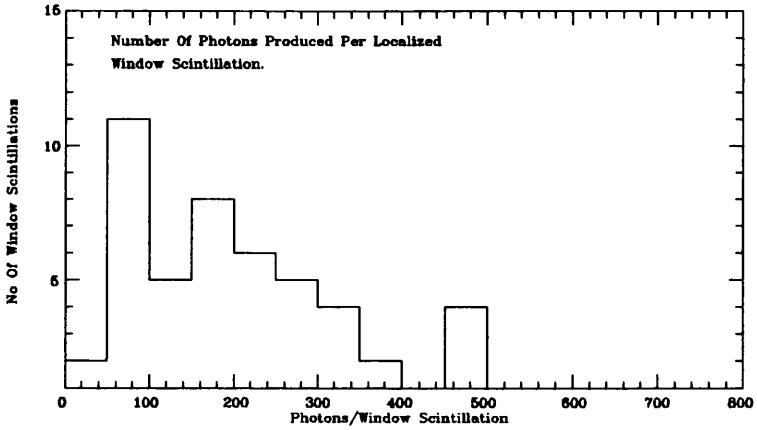

Fig 4.2 The distribution of events produced per group

These results gave the average background count as 2160 counts sec^{-1} over the whole CCD (256×256 pixels) whilst the average number of events in each group was 220.

Secondly, twelve 100 second integrations were taken so that the total contribution from stray light, dark noise and window scintillations were detected. The average number of events detected was 3530 sec^{-1}. When the background counts were subtracted from this, the average number of events detected due to window scintillation was found to be 370 sec^{-1}.

These figures indicate that the average rate at which groups of events occur is

$$\text{Event Rate} = \frac{370}{(\frac{4}{60} \times 4500 + \frac{56}{60} \times 220)} = 0.7 sec^{-1} \tag{4.1}$$

which, if the detector DQE is assumed to be 25%, produce

$$370 \times \frac{100}{25} = 1480 \text{ photons } sec^{-1} \text{ within the input window.} \tag{4.2}$$

Possible Sources Of Window Scintillation

There are two possible causes of scintillation in the sapphire window. One of these is cosmic rays which occur at a rate of < 0.016 events cm^{-2} sec^{-1} at sea level [*Siegmund et al*]. This indicates that the rate at which cosmic ray events would hit a 25mm window would not be greater than:

$$\text{Cosmic Ray Event Rate} = (\frac{2.5}{2})^2 \pi \times 0.016 = 0.079 \text{events } sec^{-1} \tag{4.3}$$

compared to the estimated 0.7 events sec^{-1} observed in the window. Cosmic rays would then produce scintillations in the input window by *phosphorescence.* [1]

The additional contribution to the event rate can be explained by the radioactive β decay of ^{40}K present as an impurity in sapphire and causing florescence in the window.

^{40}K naturally occurs in potassium at a level of 0.0118% [*Siegmund et al*]. When ^{40}K decays, 89% of the decay events are due to the emission of β radiation [*Siegmund et al*]. By knowing the mass of the window and the activity rate of β decay in ^{40}K we can obtain a rough estimate of the percentage potassium concentration in the window and hence its impurity.

$$\text{Event rate due to } \beta \text{ decay} = \frac{89}{100} \times (0.7 - 0.079) = 0.55 \text{sec}^{-1} \tag{4.4}$$

If the ^{40}K specific activity rate for β decay is 0.23 disintegrations sec^{-1} μ g^{-1} [*Siegmund et al*] then

$$\text{Mass of } ^{40}K \text{ in the window} = 2.4 \times 10^{-6} \text{grams} \tag{4.5}$$

so the mass of potassium in the window is 2.0×10^{-2} grams.
The mass of the sapphire window was estimated as 15g from calculating the window volume and assuming a sapphire density of 4 g cm^{-3} [*Hodgman*]. Therefore an estimate of the potassium concentration in the sapphire window is 0.13% by mass.

Fluorescence in sapphire windows is a well known effect [*Viemann et al*[1,2]]. The only ways in which to decrease the scintillation rate are to purify the sapphire window further, to make the window thinner and to decrease its active imaging area.

Unless very pure sapphire is used, observations utilizing narrow band filters become impractical as the dark current contribution induced by fluorescence and phosphorescence in a sapphire window swamps the image signal. Magnesium Fluoride windows suffer little from either florescence or phosphorescence [*Pellicori et al*] and so a magnesium fluoride window is preferred to a sapphire window. The transmission properties of the two windows are discussed in Chapter 7.

4.2.3 Intensifier Microchannel Plates

There is another source of dark current, initiated in the channel plates of the intensifier and having a different event height distribution to that of normal events. It is derived from

[1] The contribution of phosphorescence to the detectors' dark current is expected to increase once XMM-MIC is in a Space environment due to the corresponding increase in cosmic ray events.

the thermal excitation of electrons within the MCP. The events are accelerated through the remaining MCPs in the stack and can contribute to the events detected by the readout system. Because the MCP lead glass has a high work function the rate at which these events are detected is minute compared to the photocathode dark current.

4.2.4 The CCD Camera

Although the CCD camera produces thermal dark current in every CCD pixel this does not contribute to the output count rate. The DC level of CCD dark noise is subtracted from the event signal by using a black level clamp (Chapter 2), any residual being far lower than the detectors' event recognition threshold (Chapter 7). This threshold also ensures that the electronic noise contribution is also zero.

4.3 The Bright Limit Of Dynamic Range

The *Bright limit* of dynamic range is governed by *Coincidence Losses*, which occur when a photon event arrives in coincident proximity (both spatially and temporally) with another event. Photon counting detectors generally have low bright limits compared to CCDs for example, because they detect the presence of individual events instead of integrating on the chip itself. A low *bright limit* of dynamic range can potentially restrict the applications to which the detector can be put, and so it is important to understand how coincidence losses come about.

4.3.1 Coincidence Losses In The MCP Intensifier

Pore Paralysis

Photon counting requires that the intensifier produce events whose signal is well above the cameras' readout noise [2] and that each event be charge saturated (Chapter 2).

At these high electron gains, charge stripped from the pore wall during charge amplification leaves the pore wall depleted of charge. *Eberhart*[1] calculated that most of the charge replenished from the constant current supply is not done so along the pore (axially), but from the surrounding plate structure (laterally). This means that events do not only

[2] typically the MIC CCD collects 9×10^4 photons/event whilst charge readout detectors collect typically 10^7 electrons/event.

deplete a single pore of charge but also the surrounding pores. *Edgar et al* employing an intensifier charge gain of 10^7 has observed gain depression at distances as high as 1.5mm (100 pore spacings) from an intense point source illumination, although at lower gains this distance is known to decrease dramatically. Thus, pore paralysis is more of a problem for charge readout detectors than for MIC which operates at a typical charge gain of 1×10^5.

Charge depleted from a pore is not replenished instantaneously [*Eberhart* [1]]. Instead, the depleted pores take a certain time (dependent upon the CR time constant of the plates), known as the intensifier *dead time*, to replenish their charge during which the pores are *paralysed* [*Sharma et al*] i.e. unable to charge saturate another event.

Affect Of Pore Paralysis On Dynamic Range

If an event arrives within the dead time of a previous event and travels through pores which are paralysed by the previous event the second event will suffer a degree of gain depression. Depending upon the spatial separation of the two events the second event may emerge from the intensifier with sufficiently small gain that it falls below the readout cameras' event detection threshold. In this case the second event is not detected but is lost due to coincidence within the intensifier.

Intensifier Dead Time Characteristics

The dead time of a MCP depends upon the mechanisms involved in replenishing the pore with charge. Attempts made to model the intensifier dead time [*Sharma et al*][*Gatti et al*] from the intensifiers' gain characteristics have mostly been based around a model first proposed by *Eberhart* [3]. Eberhart carried out experiments with different MCP stacks, and found that the saturated gain from Z-stack MCPs was some 50 times that obtained when the same stack was used in linear (low gain, d.c.) operation. He concluded that there must be a strong lateral capacitance (coupling paralysed and quiescent pores) between pores, some 50 times greater than the axial capacitance, across the pore length. This explains why an event can not only paralyse the pores down which it travels but also the neighbouring pores surrounding it.

From these findings *Eberhart* [3] devised a commonly used model of the MCP pore structure in which the pore is described by a series of 'dynodes' which act independently of the MCP voltage, and which have a spacing equal to the average distance traveled by

an electron between collisions with the pore wall (**Fig 4.3**).

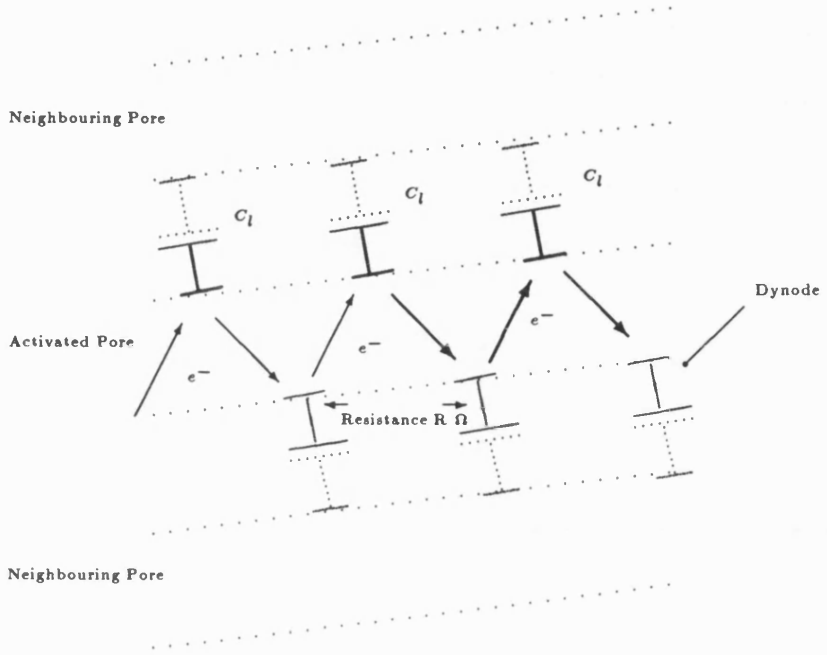

Fig 4.3: Dynode model of the MCP pore

The dynode model can be treated as having a dead time dependent mostly on the lateral RC time constant,τ, and as being paralysable (remaining depleted so long as spatially coincident events continue to arrive at times less than the dynode dead time).

The existence of lateral capacitance between pores is further reinforced by experiments [*Pearson et al*][*Garcia*] which show that the maximum count rate/pore at which a MCP can count linearly decreases with increased illumination area. *Pearson et al* state that the dependence of event gain on image size is determined by the ratio of quiescent (unactivated) to paralysed (activated) pores. At low count rates (where the arrival time between events is large compared to the intensifier dead time) the event gain is independent of image size, whereas at high count rates (where there are few quiescent pores) the event gain is highly dependent on image size.

Such models have predicted the MCP dead time as being between 0.1ms and 100ms

depending upon the intensifier gain and the channel plate resistance. There is as yet, no completely satisfactory model for the recharge characteristics of an MCP. As further data becomes available, such models as those described above, can be refined in order to describe more accurately the complex behaviour of MCP operation.

4.3.2 Coincidence Losses In The CCD Camera

The bright limit of dynamic range is also dependent on coincidence losses which take place within the CCD camera. Events from the intensifier are captured by the CCD and deposit their energy over an array of typically 3×3 CCD pixels. The processing electronics detect events by examining the data in a 3×3 pixel array which, as a frame of data is being read out, is centered on each pixel within an active imaging window (Section 2.8.1). An event is identified if a pixel contains data which is above the event detection threshold and which is greater than data in directly adjoining pixels.

Two events which are captured by the same CCD frame and which are separated by a distance greater than the event FWHM will be detected as separate events, centroided and then the appropriate data acquisition memory locations incremented by one count (Chapter 2). **Fig 4.4** shows the typical intensifier output phosphor intensity after excitation by two charge clouds separated by more than an event FWHM, and the corresponding binned CCD pixel data which might be read by the event detection electronics.

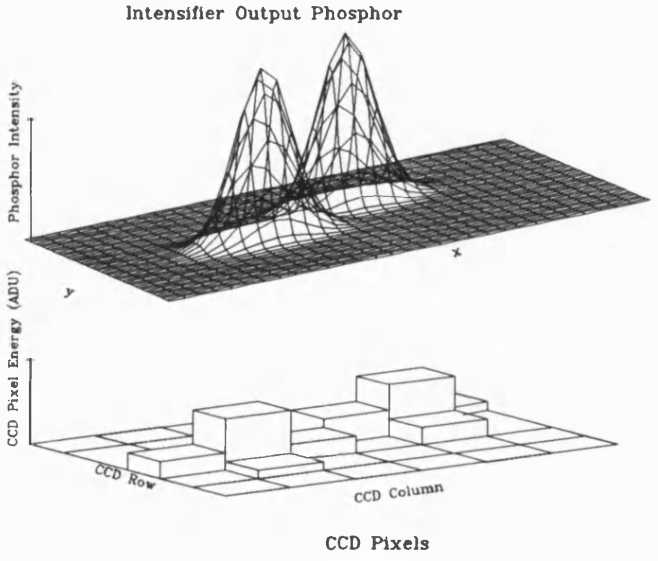

Fig 4.4. Intensifier output phosphor and CCD pixel energy distributions for two single events.

If however, the two events are captured by the same CCD frame and are separated by less than an event FWHM, only a single peak will occur in the CCD data. The detector is unable to sense the presence of both events, and will centroid the profile as if only one event were present, incrementing a single data acquisition memory location by one count (unless the multiple recognition threshold is enabled). These events are said to be coincident with one another, resulting in an event being undetected.

Fig 4.5 shows a typical intensifier output phosphor intensity after excitation by two charge clouds separated by less than an event FWHM, and the corresponding binned CCD pixel data which might be read by the event detection electronics.

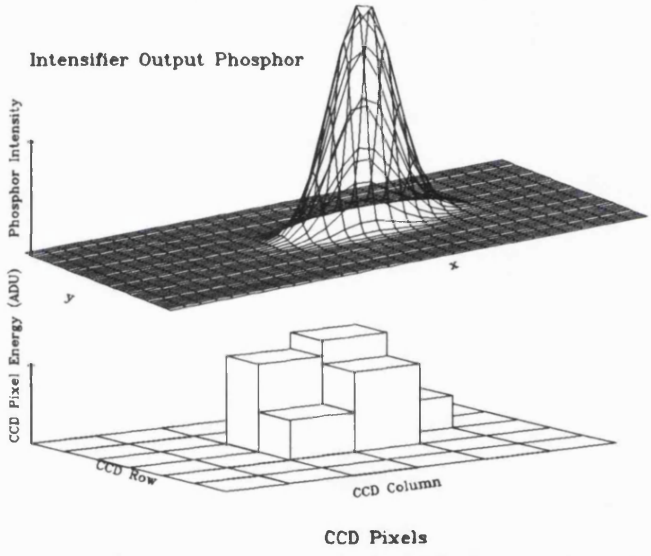

Fig 4.5. Intensifier output phosphor and CCD pixel energy distributions for two coincident events.

Coincidence losses occurring on the CCD camera cause the detector to count in a non-linear manner. At high count rates the event profiles of more than two events can overlap in such a way that only one event peak is detected. This causes an even greater loss of events with a corresponding loss of linearity.

4.3.3 Factors Affecting Event Coincidence Within The CCD Camera

In order for a coincidence loss to occur on the CCD camera events have to be both coincident in time (i.e. be captured by the same CCD frame) and spatially coincident i.e. be separated by no more than one event FWHM. There are many factors which affect the probability with which coincidences take place on the CCD camera, these being:

The Input Image

If the input image projects onto a small proportion of the detector (eg a pinhole or star), then coincidences will primarily be due to direct spatial coincidence - i.e. events lying directly on top of each other as in **Fig 4.6a**. For dispersed images or flat fields however, coincidences will mainly be associated with events in close proximity to each other but not totally overlapping, as shown in **Fig 4.6b.**

(a) Directly Coincident Events

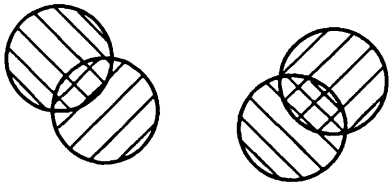

(b) Events In Close Proximity

Fig 4.6. An illustration of how spatial coincidences occur in point sources and flat fields

Thus for a particular *count rate per pixel*, the coincidence losses in a dispersed image will be higher than those for a point source as an event in one pixel of an extended image will be spatially coincident with events centered in surrounding pixels. Hence, the maximum number of events/pixel/sec to which MIC can count linearly will be far less for an extended source than for a point source.

For an *image of constant intensity* the rate at which coincidence losses take place also depends upon the image size. This becomes a problem when undertaking star photometry in variable seeing conditions, where the stars' point spread function changes and so therefore do the number of coincidence losses. If seeing conditions are very good all events associated with a point source object will be spatially coincident as most will fall directly on top of each other. However, if the seeing is poor then the image of a point source object can be spread over many pixels. In this case the number of coincidences are low because

not all the events will be spatially coincident to each other.

The Event Width

The probability of two events being spatially coincident within the same CCD frame is dependent upon the event FWHM. The smaller the event FWHM the closer two events have to be in order to be spatially coincident (but is ultimately limited by the CCD pixel size). However, events should be the optimum width required by the centroiding electronics (typically 1.3 CCD pixels FWHM).

There is a trade off between resolution and dynamic range when determining the optimum event width. If the width is too small then the dynamic range will increase, but each event will be undersampled by the centroiding electronics and a loss of resolution will occur. If the event width is too broad then the event profile will be well sampled but coincidence losses will increase. As stated in Chapter 2, the event width is somewhat fixed by the size of the intensifiers' inter-plate gaps but can be modified slightly by changing the back gap voltage.

The CCD Frame Time

All photon counting detectors have an upper limit of dynamic range governed by their inability to process events at high count rates. In the case of MIC it is limited by the CCD frame rate which can vary between 1ms and 12ms depending upon the CCD pixel format. The greater the frame rate, the lower the probability of two coincident events occurring in the same frame. The CCD frame rate is governed by the time taken to read out a frame of data, with which two components are associated:

1. **The CCD Clock Speeds**

   - The time taken to transfer data from the CCDs image to storage area is governed by the vertical clock speed (V_c) , which runs at 3MHz.
   - The time taken to read out each row of the readout register is governed by the horizontal clock speed (H_c), which runs at 10MHz.

   The clock speeds are ultimately limited by the internal capacitance of the CCD. If they are run too fast a reduction in the charge transfer efficiency occurs.

2. **The number of CCD rows required for data acquisition.** In order to increase the CCD frame rate the MIC detector is able to read out a subsection or subsections of the imaging area reducing the number of CCD rows required to be read out (see below). If, for example, the detector is being used for spectroscopic observations then the spectroscopic image typically projects itself onto a few rows of the CCD. In this case only those few rows of the CCD need to be read out. Reading out sections of the imaging area in this way reduces the readout time of a CCD frame and hence increases the CCD frame rate.

Subsections of the image area can be read out by defining what are called *data acquisition windows* where only rows within these windows are read out. In order to explain how the frame time is related to the size and positions of the data acquisition windows an example is shown in **Fig 4.7** where three windows have been defined.

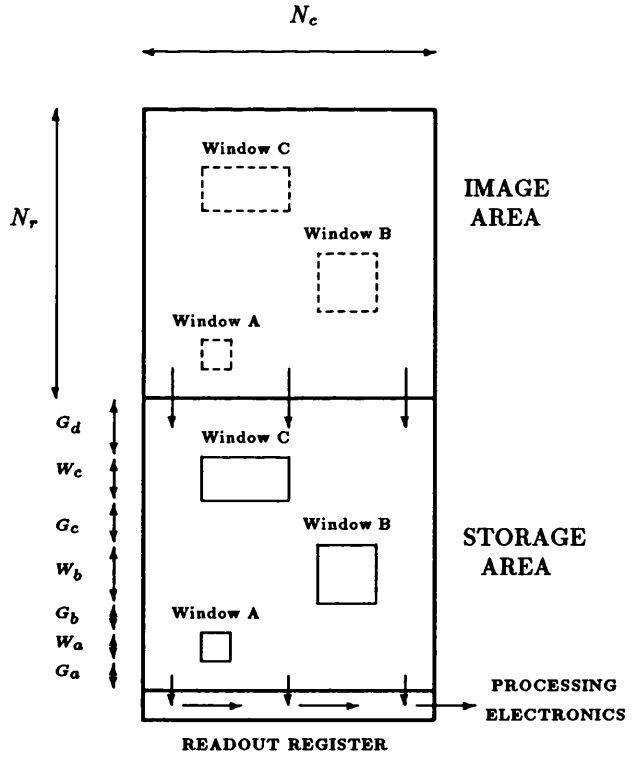

Fig 4.7: Three data acquisition windows read from the CCD.

In order to read the data in each data acquisition window the whole image area is firstly transferred to the storage area. This takes a time ($V_c \times N_R$) μs where V_c is the vertical clock speed (in μs) and N_R is the total number of CCD rows.

Secondly, the storage area is clocked downwards by G_a rows which are dumped on top of each other in the readout register, taking $(V_c \times G_a)$ μs. These rows contain unwanted data and so are read out together and discarded. This takes $(H_c \times N_c)$ μs, where H_c is the horizontal clock speed (in μs) and N_c is the number of CCD columns.

Rows W_a are then clocked into the readout register and read out one row at a time. These rows contain the data within *Window A*. This takes $(W_a \times V_c) + (H_c \times N_c)$ μs.

The process of reading out data from within acquisition windows and the unwanted data surrounding them continues until each row of the storage area has been read out. The time taken to read out a whole CCD frame is then;

$$\text{Frame Time} = 2N_R V_c + N_c H_c(\sum_{i=1}^{d} W_i + g)\mu s \tag{4.6}$$

where g is the number of vertical gaps between windows (in this case 4, $G_{a..d}$) and d is the number of data acquisition windows, (in this case 3) [3]

If the whole image area is used for data acquisition then Equation 4.6 simplifies to

$$\text{Frame Time} = 2N_R V_c + N_c H_c N_R \tag{4.7}$$

giving a frame time of 11.25ms for a CCD image size of 288 rows and 384 columns, for the clock speeds stated above. Alternatively if one 32 row window is used for data acquisition, the frame time will be 1.5ms. A frame time 8 times shorter can therefore be achieved by decreasing the CCD format from 288 to 32 rows. Results shown in Section 4.6 show how the dynamic range increases as a consequence.

Benefits from increasing dynamic range in this way occur if only selected rows of the CCD are required for data acquisition. This would not be the case if an extended object were being imaged. However, for spectroscopic applications on point sources, the dispersion axis of the spectrograph can be aligned perpendicular to the frame transfer direction, requiring only $\sim$ 16 rows for data acquisition.

[3] The data acquisition window is made two rows and two columns larger than the area containing image data. The window is made larger in order to obtain data required by the processing electronics in order to centroid events close to the edge of the window.

4.4 Dynamic Range Simulations

The dynamic range of MIC depends upon each of the detector characteristics mentioned above. If any of these characteristics were to change then its dynamic range response would also change. For example:

- If the number, size or position of data acquisition windows were to change it is likely that the CCD frame time would also change. This would alter the rate at which coincidence losses would occur and hence change the bright limit of dynamic range.
- If the intensifier were to suffer from long term gain depression over the operational lifetime of the detector then its gain characteristics would change. This might affect the intensifier dead time which would alter the bright limit of dynamic range.

In order to help explain not just how coincidence losses occur within the intensifier and the CCD but also predict which characteristics of the detector are most critical in determining the rate of coincidence loss, the author has attempted to model the dynamic range response of MIC. By modeling the dynamic range response of MIC the affects of changes in, for example, the intensifier dead time and the CCD frame time can be quantified and also used to predict the detectors dynamic range response for each set of detector characteristics.

4.5 Initial Dynamic Range Simulations

The initial dynamic range simulations firstly involved randomly firing 'photons' at a simulated MCP intensifier. Each photon was given a position and time tag, and the intensifier was given both a *dead area* and a *dead time* which could be varied as required. Two photons where assumed to be coincident within the intensifier if one event arrived within both the dead time and dead area of a previous event. If one or more events were coincident within the intensifier only the first of the coincident group of events were passed to the next stage of the simulation, the CCD. If an event was not coincident with any other event it too was passed to the next stage of the simulation.

Events were assumed coincident on the CCD if they they were captured within the same CCD frame and if they arrived within one FWHM of each other. Each event was placed in a particular CCD frame, this being dependent upon the frame speed and the value of the events time tag. Each event was also given a width (taken from a real event

width distribution), which was used to determine whether two events were close enough on the CCD to be spatially coincident. If one or more events were coincident on the CCD only one of the coincident group of events was recorded. If an event was not coincident with any other event it was also recorded.

A simulated dynamic range curve can be built up by firing different numbers of 'photons' at a given area of the detector. The number of events input to the detector is then plotted against the number of recorded (output) events in order to build up the dynamic range curve. An estimate of the input count rate at which 10% coincidence occurred could then be made.

4.5.1 The Intensifier Dead Radius

In order for the intensifier to suffer a coincidence loss the affect of gain depression on an event must be so severe that its event height falls below the event detection threshold of the CCD camera. Events produced by the MIC intensifier have, on average, a height of 60 ADU whilst the event detection threshold is set at typically 30 ADU. This means that the average event typically needs to suffer at least 50% gain depression before it falls below the event detection threshold. This suggests that the dead radius of the intensifier may be small because of the large gain depression required for a coincident event to be lost.

Experiments carried out by *Edgar et al* have shown the effects of gain depression to extend beyond 1000μm for intensifiers whose charge gains are typically 10^7. No known work had been carried out on the spatial extent to which gain depression occurs at charge gains of 10^5 and so experiments were carried out at UCL by the author and other members of the group in order to quantify this affect.

These experiments involved the use of pairs of pinholes whose distance from each other were varied. The aim of the experiment was to determine at what separation gain depression caused by events from one pinhole affected the number of coincidence losses occurring in the other pinhole. This was carried out by firstly illuminating both pinholes with the same light intensity and measuring the count rate from each. One of the pinholes was then covered up and the count rate from the other pinhole measured. If the affect of spatial gain depression was significant at this pinhole separation differences in the two count rates would then be noticed. These experiments were carried out for a number of

pinhole separations and for very high and low illumination intensities.

No change in the count rate from either pinhole was detected no matter what the pinhole separation or the illumination intensity. However, pinhole separations of less than 450μm could not be measured because below this separation the event profiles from each pinhole started to overlap on the CCD but this experiment gives an upper limit of 450μm for the dead radius associated with the MIC intensifier.

If there is no observable gain depression for distances greater than 450μm the distance for which 50% gain depression will take place is most likely to be far smaller than 450μm. If we consider that charge saturation takes place at the end of the last channel plate where the event is typically spread over seven pores [*Eberhart*]^{1}, then events separated by two event widths will substantially overlap. A best estimate for the intensifier dead radius is therefore the event FWHM within the intensifier, this being 3 pore spacings. This is the dead radius used in the simulations, so if any two events are separated by less than 45μm (the pore spacing being 15μm) they are simulated as being spatially coincident within the intensifier.

4.5.2 The Intensifier Dead Time

The intensifier dead time is a variable which can be entered by the user. Each dynamic range simulation has been carried out for at least three values of the intensifier dead time to observe how the detectors' dynamic range is dependent upon it.

The dead time of the MIC intensifier has been estimated from tests carried out at Imperial College. In these tests a point source dynamic range curve was obtained for the MIC intensifier (running at its normal operating voltages) and a photomultiplier tube (PMT). The PMT has very fast dead time (typically 1μs) so any coincidence losses which occur during these tests are associated solely with the intensifier and not the PMT. The intensifier dead time was estimated from the point source dynamic range curve, **Fig 4.8.**

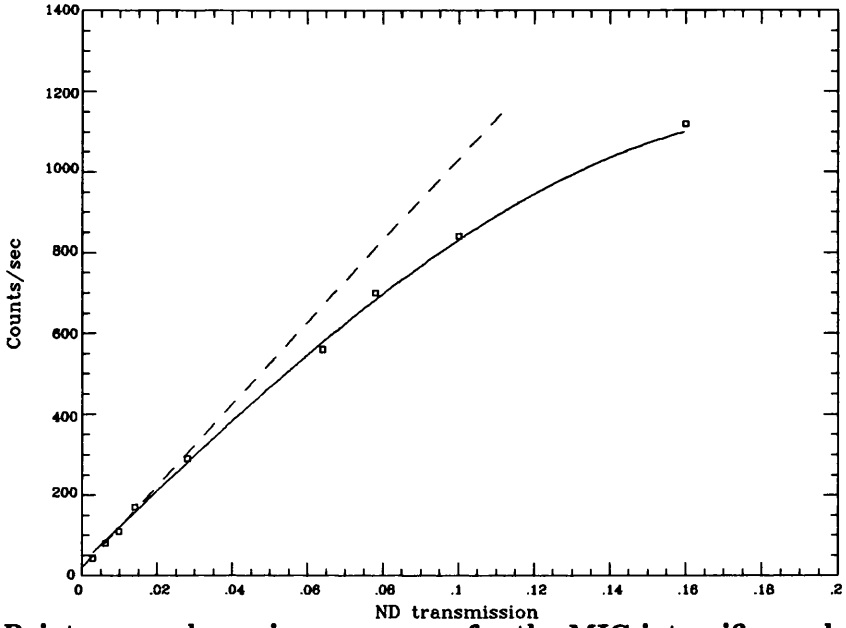

Fig 4.8. Point source dynamic range curve for the MIC intensifier and a PMT

10% coincidence was found to occur at a count rate of $\sim$ 700Hz. From this, and taking into account the random arrival rate of the events, an intensifier dead time can be deduced. This was found to correspond to $\sim$ 0.1ms.

4.5.3 The CCD Frame Time

The user is also able to enter the frame time of the CCD. This is calculated from a knowledge of the data acquisition format. In these simulations two data acquisition formats are used, 256x256 CCD pixels (with an associated frame time of 10ms) and 256x32 CCD pixels (with an associated frame time of 1.5ms). Each event is allocated a CCD frame by matching the events' time tag to a CCD frame. For example, if the frame time is 1.5ms then there are typically 670 CCD frames/sec. An event arriving within the first $1.5\text{x}10^{-3}$ seconds is placed in the first CCD frame, and an event arriving between $3\text{x}10^{-3}$ and $4.5\text{x}10^{-3}$ seconds is placed in the third CCD frame, etc.

4.5.4 The Event Width

The MIC detector is able to sample events from individual CCD frames and determine their FWHM (Chapter 3). With the intensifier running at its normal operating voltages an event width distribution for single events was taken. This distribution was translated into a form which could be used in the simulation. The simulated events were given a width

distribution which matched those of real events. The average event width was typically 30μm at the CCD.

4.5.5 Results Of Point Source Dynamic Range Simulations

Fig 4.9a shows three simulated point source dynamic range curves.

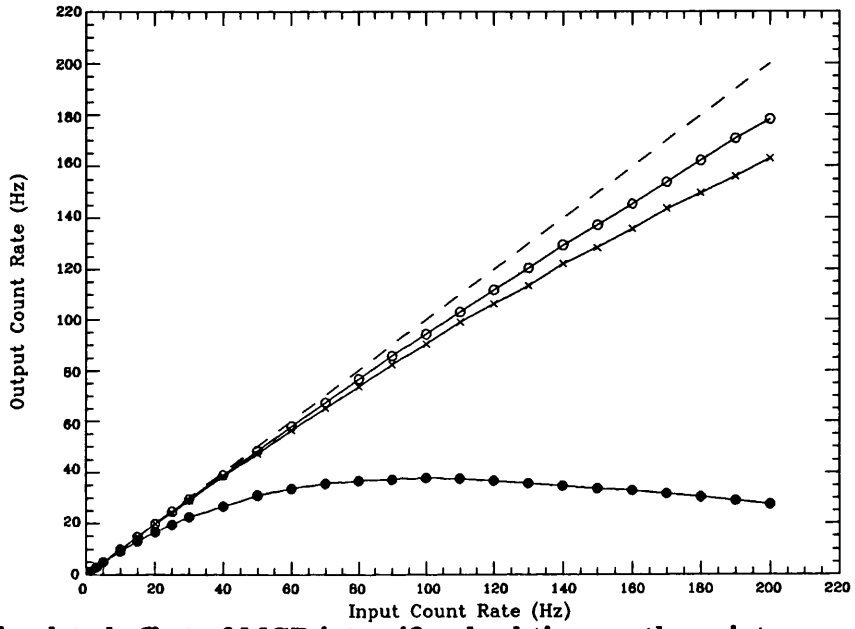

Fig 4.9a. Simulated affect of MCP intensifier dead time on the point source dynamic range response of the MIC detector. Intensifier dead times 0.1ms (Curve 1 (o)), 1ms (Curve 2 (×)) and 10ms (Curve 3 (•)).

The curves represent the dynamic range response of the MIC detector when:

- The radius of the intensifier dead area is 45μm i.e. three pore spacings. Because the intensifier dead radius is larger than the FWHM of a point source illumination every event is assumed to be spatially coincident with each other.
- The CCD frame time is 1.5ms (using the spectroscopic format).

Fig 4.9a shows the affect of a changing intensifier dead time on the dynamic range response of the MIC detector. Because curves **1** and **2** are associated with a detector whose intensifier dead time is smaller than the CCD frame time, these two curves are very similar. For an intensifier dead time of 0.1ms the input count rate at which 10% coincidence occurs is at 180Hz, and for a dead time of 1ms it occurs at 100Hz. Most of the coincidence losses will take place on the CCD because the probability of two events arriving

within the same CCD frame is higher than an event arriving within the (intensifier) dead time of a previous event.

Curve **3** is associated with an intensifier dead time of 10ms which is some seven times greater than the CCD frame time. In this case most of the coincidence losses take place within the intensifier and 10% coincidence occurs at a count rate of 11Hz.

This set of simulations indicate that the dynamic range is highly dependent upon the intensifier dead time especially if the dead time is large compared to the CCD frame time. Because the MIC intensifier has an estimated dead time of 0.1ms these simulations predict that MIC has a point source dynamic range whose bright limit is 180Hz assuming the spectroscopic format is employed.

Fig 4.9b shows the affect of a change in CCD frame time on the dynamic range response of the MIC detector. The curves represent frame times of 1.5ms (o) and 10ms (×), with the following characteristics applied:

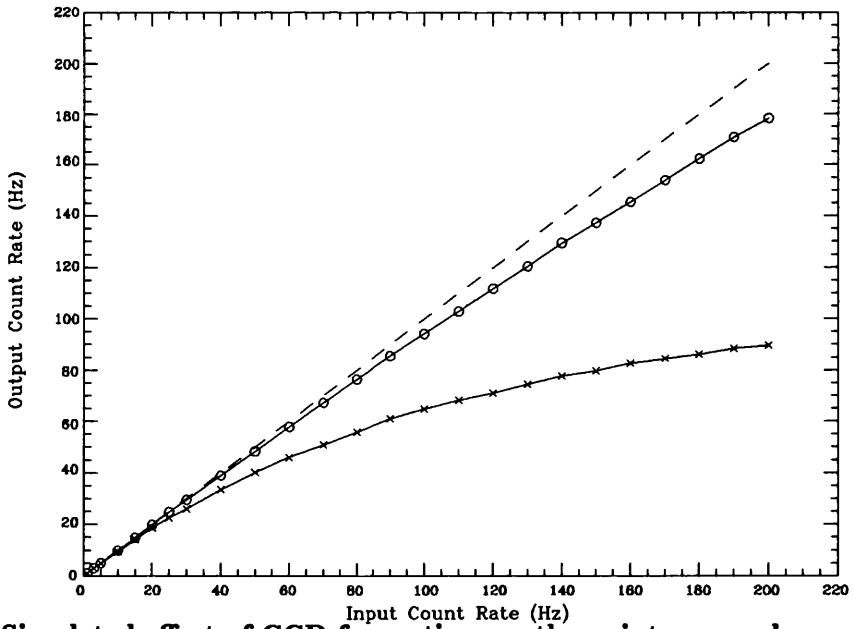

Fig 4.9b. Simulated affect of CCD frame time on the point source dynamic range response of the MIC detector

- The radius of the intensifier dead area is 45μm i.e. three pore spacings.
- The intensifier dead time is 0.1ms.

Curve **1** in **Fig 4.9b** is the same curve as curve **1** in **Fig 4.9a** and represents the case where the MIC detector has a CCD frame time of 1.5ms. In this case 10% coincidence is

estimated to occur at an input count rate of 180Hz.

Curve **2** represents the case where MIC has a CCD frame time of 10ms which corresponds to imaging with the full CCD format (256×256 CCD pixels). In this case 10% coincidence is estimated to occur at a count rate of only 25Hz, some seven times smaller than when employing a spectroscopic format.

There are three points that can be made about the results of these point source dynamic range simulations:

- For small intensifier dead times the 10% coincidence point is nearly inversely proportional to the CCD frame time.
- For intensifier dead times which are large compared to the CCD frame time a small change in the CCD frame rate will hardly affect the 10% coincident point. This is due to most of the events being lost within the intensifier.
- If coincidences within the intensifier and the CCD camera are treated separately then for an intensifier dead time which is equal to the CCD frame time, the 10% coincident point will be more sensitive to changes in the intensifier dead time. Events paralyse neighbouring pores of the intensifier for an entire dead time after they arrive. Events captured by the CCD are only coincident with other events captured within the same frame independent of its arrival time with respect to the start of a frame period.

4.5.6 Results Of Flat Field Dynamic Range Simulations

Fig 4.10a shows three simulated flat field dynamic range curves.

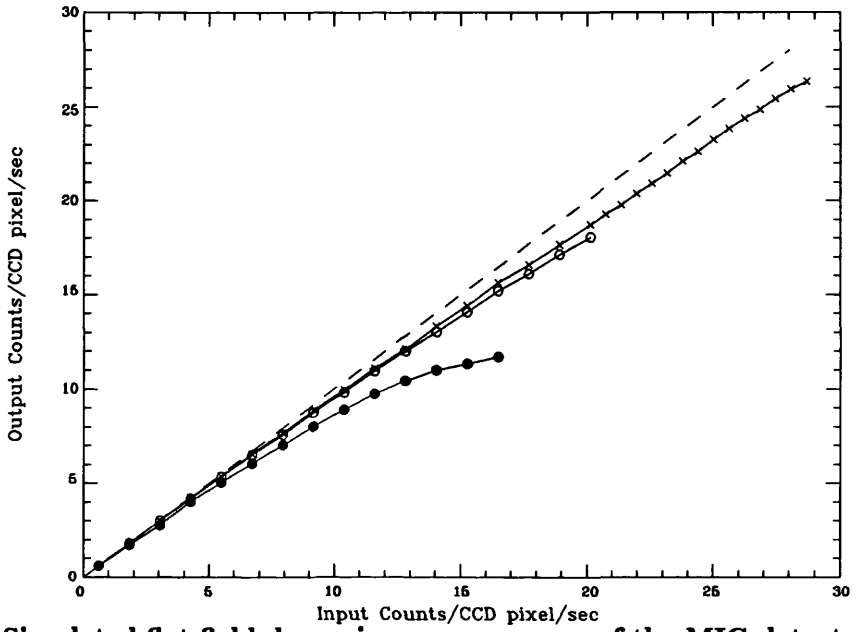

Fig 4.10a. Simulated flat field dynamic range response of the MIC detector using a spectroscopic CCD format. Intensifier dead times 0.1ms (Curve 1 (o)), 1ms (Curve 2 (×)) and 10ms (Curve 3 (•)).

These curves represent the dynamic range response of the MIC detector when:

- The radius of the intensifier dead area is 45μm i.e. three pore spacings.
- The CCD frame time is 1.5ms.

For curve **3**, the MCP dead time is large compared to the CCD frame time and so 10% coincidence occurs at only $\sim$ 6.5 counts/CCD pixel/sec. This is far lower than the count rate at which 10% coincidence takes place for a point source image (11Hz) for the same intensifier dead time and CCD frame time. This is because a high degree of spatial coincidence is taking place.

Up to count rates of $\sim$ 10 counts/CCD pixel/sec curves **1** and **2** follow each other very closely but as the count rate increases, curve **2** deviates from linearity at a slower rate. At these high count rates most of the coincidence losses are occurring on the CCD. This is because the rate at which spatial coincidence losses take place on the CCD is greater than that within the intensifier. Because the intensifier dead radius is 45μm and the event FWHM on the CCD is 30μm (which is equivalent to 100μm at the intensifier) coincidences occur on the CCD at a higher rate than within the intensifier even if the intensifier dead time is the same as the CCD frame time.

For an intensifier dead time of 1ms many events are lost in the intensifier meaning that fewer events are captured by the CCD. So the rate at which coincidence losses occur in the detector as a whole, decreases. In this case 10% coincidence occurs at 29 counts/CCD pixel/sec.

An intensifier dead time of 0.1ms is so small that few events are lost within the intensifier. Many more events are therefore captured by the CCD on which very high levels of spatial coincidences are taking place. Because fewer events are lost in the intensifier more events are lost in the detector as a whole. In this case 10% coincidence occurs at a count rate of 20 counts/CCD pixel/sec. This effect only occurs because the CCD frame time is comparable to the intensifier dead time. If the CCD frame time could be decreased to 0.1ms for example, curve 1 would show greater linearity at high count rates.

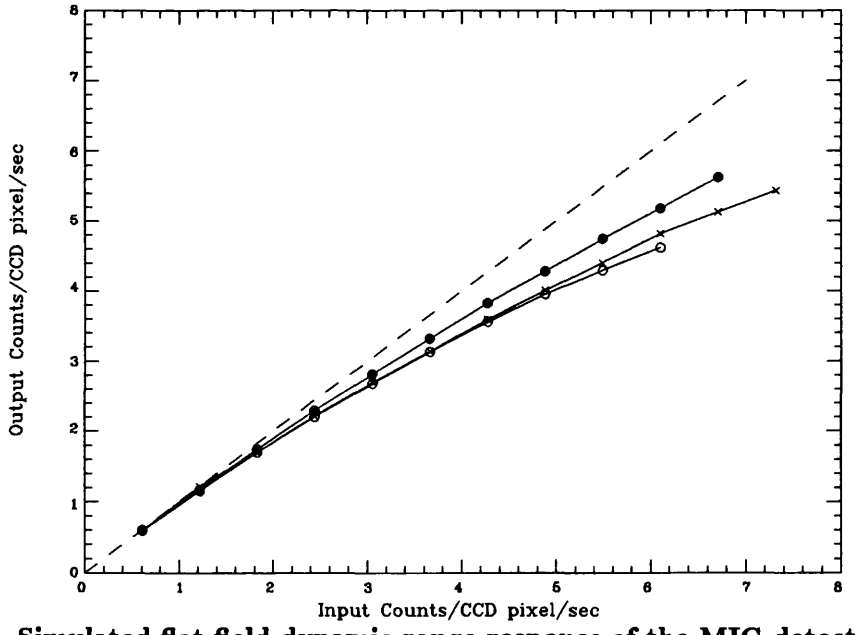

Fig 4.10b. Simulated flat field dynamic range response of the MIC detector using the maximum (256×256) CCD pixel format. Intensifier dead times 0.1ms (Curve 1 (o)), 1ms (Curve 2 (×)) and 10ms (Curve 3 (•)).

Fig 4.10b shows three simulated flat field dynamic range curves for a 10ms frame time and an intensifier dead radius of 45μm i.e. three pore spacings.

Here, the affect of CCD frame time on flat field dynamic range is even more clearly seen. The frame time is so high that the rate at which spatial coincidences occur on the CCD is far greater than that within the intensifier. In this case, for an intensifier dead time of 10ms, 10% coincidence occurs at $\sim$ 4 counts/CCD pixel/sec whilst for an intensifier

dead time of 0.1ms and 1ms, 10% coincidence occurs at 2.5 counts/CCD pixel/sec and 2.6 counts/CCD pixel/sec respectively.

There are three main points that can be made about the results of these flat field dynamic range simulations:

- The rate at which spatial coincidences occur between neighbouring events in a flat field image is greater than the rate at which temporal coincidences occur between overlying events in a point source image. For this reason, 10% coincidence occurs at a lower count rate/CCD pixel in an extended image than in a point source image.
- The FWHM of an event at the CCD is far greater than the dead radius of the intensifier. Because most events are lost due to spatial coincidence most coincidences take place on the CCD if the intensifier dead time and CCD frame time are similar.
- Because most spatial coincidences take place on the CCD, the CCD frame time and the event FWHM are the most critical factors affecting the flat field dynamic range of MIC.

4.6 Measuring The Dynamic Range Of The MIC Detector

The dynamic range of the MIC detector has been measured in the laboratory by the author. This was done by measuring the intensity of different point source and flat field illuminations with the MIC detector. In order to carry out these tests use was made of an optical bench, a Baum slide projector and several ND (Neutral Density) filters.

4.6.1 Measuring The Point Source Dynamic Range Of MIC

Experimental Setup

The Baum slide projector incorporated a tungsten lamp whose intensity could be varied using an external power supply, and ND filters which could be slotted into one of the two available slide holders. A 25μm pinhole was made up into a slide which could fit into the second slideholder.

An image of the pinhole was projected from the front of the projector onto the front of the MIC detector. The projector used a 4.35:1 demagnifying lens in order to project the pinhole onto as small an area of the detector as possible. By changing the combination of

ND filters placed in front of the pinhole, the illumination intensity could be changed and the number of photons/sec detected by MIC, measured for each intensity level.

The intensity of the tungsten lamp was kept constant throughout the experiment. Its intensity was set at such a level that if a low value ND filter was placed in front of the pinhole, the pinhole intensity was such that the MIC detector would totally saturate. This ensured that the dynamic range could be measured up to the saturation point.

Carrying Out The Experiment

Whilst setting up the MIC detector and allowing the intensifier power supply to stabilize the tungsten bulb was also turned on and allowed to stabilize. The lamp stability was measured by taking several integrations of the pinhole over a period of typically 30 minutes ensuring the intensity did not change over this time period. Once the CCD format had been set a small area around the pinhole was selected in which only the counts in that area were summed. This area was kept constant throughout the experiment and included the whole point source image.

By covering up the pinhole completely a measure of the detector dark count was taken over that area. Once the lamp was stable a series of integrations were taken with different ND filters. The exposure for each integration was set to ensure adequate integrated signal.

4.6.2 Measuring The Flat Field Dynamic Range Of The MIC Detector

The method by which MICs' flat field dynamic range was measured was exactly the same as that described above except that the pinhole was removed from the projector. This time the counts in an area of typically 100×100 pixels were summed for each combination of ND filters placed in the projector.

4.6.3 Dynamic Range Results

Fig 4.11 shows the point source dynamic response of the MIC detector for two different CCD formats, 256×256 CCD pixels (represented by symbol (o)) and 256×32 CCD pixels (represented by symbol (△)).

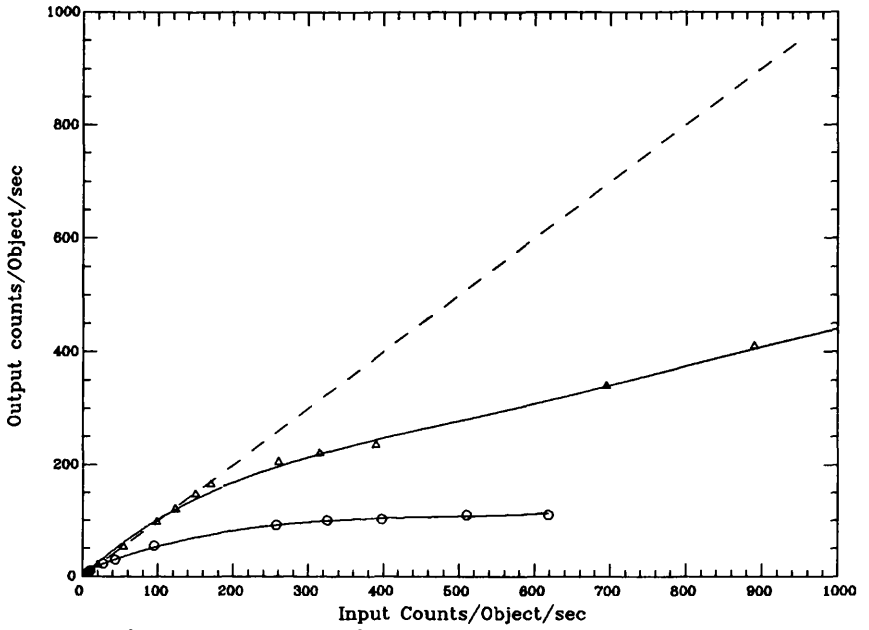

Fig 4.11. Point source dynamic range response of the MIC detector

The dynamic range response of the detector for the two CCD formats is very different as predicted from the simulations. For the full CCD format, 10% coincidence occurs at a count rate of 25 counts/object/sec whilst for the spectroscopic CCD format (256x32 CCD pixels) 10% coincidence occurs at the far higher rate of 200 counts/object/sec. This is very close to that predicted by the initial simulations. The simulations predicted that for a maximum CCD format, 10% coincidence would take place at a count rate of 25 counts/object/sec and that for the spectroscopic format it would take place at 180 counts/object/sec.

Fig 4.12 shows the flat field dynamic response of the MIC detector for both the full and spectroscopic CCD formats, represented by the same symbols as before.

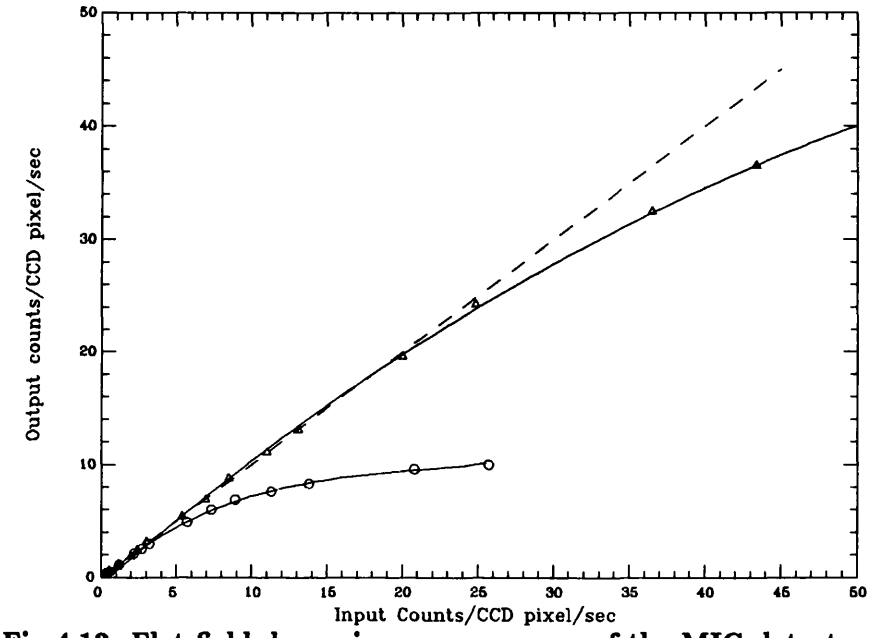

Fig 4.12. Flat field dynamic range response of the MIC detector

Once again, the dynamic range response is very different for the two CCD formats. This time, 10% coincidence takes place at 5 counts/CCD pixel/sec for the full CCD format and at 35 counts/CCD pixel/sec for the spectroscopic format. Both these values are far lower than the corresponding point source dynamic range values for the same CCD format. This was also predicted by the simulations but this time the simulations were less able to predict the count 10% coincidence point. These initial simulations predicted that using the full CCD format, 10% coincidence would occur at 3 counts/CCD pixel/sec and using the spectroscopic format, 10% coincidence would occur at 20 counts/CCD pixel/sec.

4.7 The Second Dynamic Range Simulations

There are two characteristics of the detector that the initial dynamic range models did not take into account when simulating MICs' dynamic range curves. These are the change in the CCD cameras' DQE for different data acquisition formats, and the way in which the CCD samples the P20 output phosphor.

4.7.1 Incorporating The CCD Camera DQE Into The Dynamic Range Simulations

Any event captured during the transfer of a frame of CCD data from the image area to the storage area is smeared over several CCD pixels in the direction of frame transfer. The data in each of these pixels is typically so small that the event is not detected above the event detection threshold. The time taken for the CCD to transfer a frame of data from the image to the storage area is known as the *frame transfer time* during which any event that is captured by the CCD will not be recorded in that frame.

The frame transfer time is a constant time period which is independent of the data acquisition format. It is a product of the CCDs vertical clock speed and the number of rows comprising the CCD. The XMM-MIC detector has a frame transfer period of 96μs which for a data acquisition format of 256x256 CCD pixels makes up only 1% of the total frame time. However, if a CCD format of 256x32 CCD pixels is used then the frame transfer time makes up 6.5% of the total frame time which as a result, could decrease the DQE of the CCD camera. This second, more sophisticated model takes this effect into account.

4.7.2 The Effect Of Phosphor Decay On Detector Dynamic Range

During routine testing of the XMM-MIC detector a strong positional correlation was found between events in one CCD frame and much lower energy events in the following CCD frame. Many contiguous pairs of CCD frames were analysed in order to determine the extent to which a low energy event was located in exactly the same position as an event in the previous frame. After finding that at least 10% of events had a low energy secondary event associated with it in the next frame, it was decided to find the cause of this phenomena.

The fact that the energy associated with an event was sometimes spread over two contiguous CCD frames implies some form of storage mechanism being involved. There are only two mechanisms that could possibly cause this affect:

1. The CCD. Some charge could, in principle, be left behind in each CCD pixel after a readout. However, this can be discounted as a huge charge transfer inefficiency must be associated and would be immediately noticeable in the profiles and amplitude of

the events of the video data. This is not seen.

2. The output phosphor of the image intensifier. The phosphor must be causing the additional counting as no other known mechanism remains. The phosphor is a P20 and the decay time has been measured as 2μs to 10% implying that there should not be a problem. The hypothesis here, though, is that there is a low level, long time period, tail to each event as it appears on the output phosphor. This tail, when integrated over a frame period could then accumulate enough charge in the associated CCD pixel(s) of the next frame to create a false event. If this false event were then large enough to lie above the photon counting threshold a form of double counting could take place.

In order to quantify the degree to which double counting was taking place an experiment was carried out in order to measure the intensifiers' phosphor decay curve.

The Intensifiers Phosphor decay Curve Characteristics

The detector was set up so that a LED was flashed once every two frames. In the flash frame, frame **A**, photon events were recorded in the form of accumulated charge on the CCD. In the next frame, frame **B**, in which there were no photon events, smaller amounts of charge were seen to have accumulated in the same place as photon events in frame **A**; these residual 'events' were caused by the energy emitted by the longer secondary decay components of the phosphor. The two frames were analysed to find correlations between residuals in **B** and photon events in **A**. Having found a correlation the computer used a 3 $\times$ 3 array of pixels around the photon event and calculated the energy in frame **B** as a percentage of the energy in both frames. An average was found for two hundred correlations.

The energy of the residual depends upon the time of arrival, t, of the photon event with respect to the end of frame **A**. Photon events were simultaneous with the LED flash and so by altering the time of the flash, which was known, it was possible to obtain a graph of percentage residual energy, E, versus t.

In order to deduce the decay constants and relative intensities of the secondary components it is necessary to consider the area under the decay curves, which are assumed to be exponentials. This assumption is valid since many phosphor decay curves are well

modelled by exponentials or their sum [*Smith*[2] *et al*]. Let τ_i be the decay constant of the i^{th} component and let k_i be its intensity at $t = 0$. If there are n components the energy emitted by the phosphor in frame A is then

$$E_a = \sum_{i=1}^{n} \int_0^t k_i e^{-\frac{t}{\tau_i}} \, dt \tag{4.8}$$

After the end of frame **A** there is a frame transfer period, t_t, during which the entire frame is transferred to the storage area. Any photon events arriving in this period will not be counted and nor will their residuals contribute to the mean residual energy since they will not be correlated. Frame **B** begins at the end of t_t and ends one frame period, t_f, after the end of frame **A**. The relationship between t, t_t and t_f is shown schematically in **Fig 4.13.**

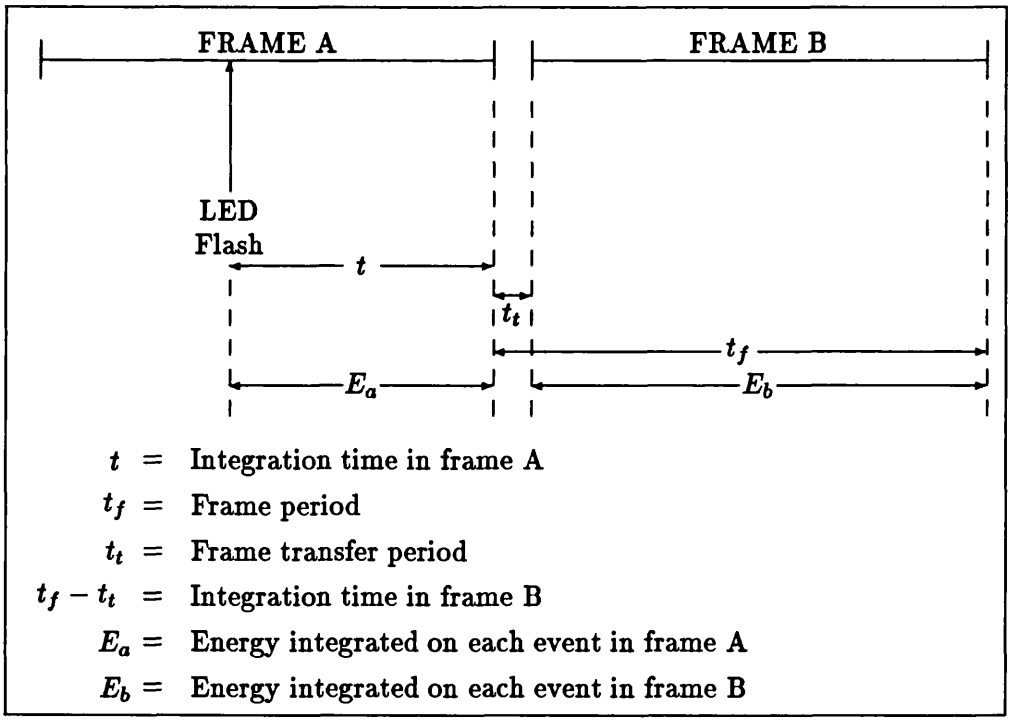

Figure 4.13 The relationship between t, t_t and t_f and between E_a and E_b.

Frame transfer is always sufficiently long that the $2\mu s$ main component completely decays before the start of frame **B**. The energy emitted by the phosphor in frames **A** and **B** can then be written

$$E_a = \sum_{i=1}^{n} \int_0^t k_i e^{-\frac{t}{\tau_i}} \, dt \tag{4.9}$$

$$E_b = \sum_{i=2}^{n} \int_{t+t_i}^{t+t_f} k_i e^{-\frac{t}{\tau_i}} \, dt \tag{4.10}$$

From these equations *Bellis* [*Fordham*[3] *et al*] was able to fit the data with exponential decay curves which could describe the phosphors secondary decay components. A best fit to the data, which is shown in **Fig 4.14**, was derived using three decay components. The long term decay components, curves 2 and 3, are characterized by their magnitude and time constants, τ_i and k_i where τ_2=340μs, k_1/k_2=570; τ_3=7300μs and k_1/k_3=23000.

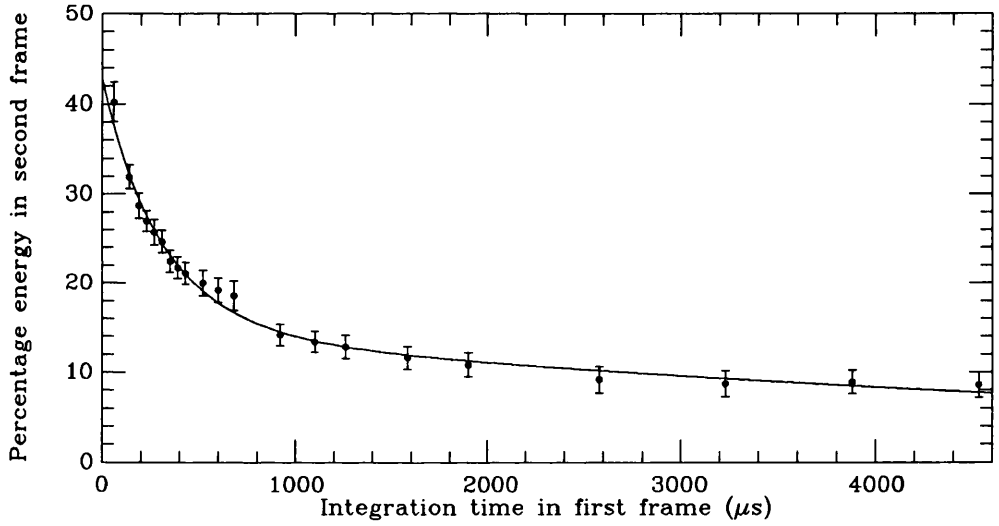

Figure 4.14 Smooth curve fitted to real data using three exponential components: τ_1=0.8686μs; τ_2=340μs, k_1/k_2=570; τ_3=7300μs, k_1/k_3=23000. Error bars extend σ above and below each point.

Although the decay time of the P20 phosphor has been measured as 2μs to 10% the two long term components decay at a much slower rate. When the energy associated with these long term components is integrated over a frame period it is large enough to create the residual events seen previously.

How Residual Events Can Affect The Detectors Dynamic Range

The amount of residual energy that an event deposits in a CCD frame (in this case, Frame B) is dependent upon the total event energy (E_A+E_B) and the time at which it arrived

within the first frame (frame A). The greater the total event energy and the closer the event arrives to the end of the first frame, the more energy is deposited in the second frame (Frame B).

The way in which energy can be deposited in the next frame can take one of three forms;

- **By a single event**; An event arriving close to the start of a CCD frame period will deposit almost all of its energy in that frame (**Fig 4.15a**). The phosphor intensity will have decayed to such a low level by the time the next frame period starts, that virtually no light will be captured in the next frame. If an event arrives towards the end of a frame period (as in **Fig 4.15b**), then the phosphor will still be emitting some light at the start of the next frame period, and this will be captured in the next frame (Frame B). This energy, E_B will only be a small fraction of the total light emitted by the event, so although energy is captured in the second frame, it is unlikely to produce an event above the event detection threshold.

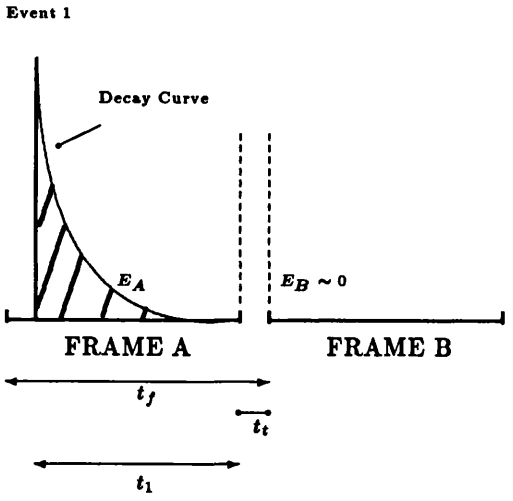

Fig 4.15a Single event arriving at the beginning of a frame period.

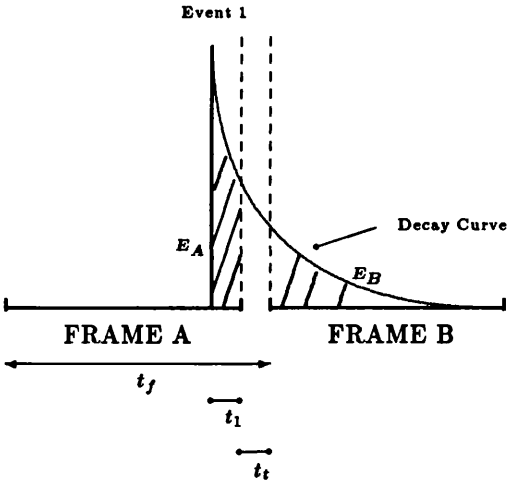

Fig 4.15b Single event arriving at the end of a frame period.

- **By two or more coincident events**; If two or more events are spatially coincident and arrive in the same frame period, the intensity of light from the phosphor will approximate to the sum of that from each individual event. If both events arrive close to the beginning of a frame, then the phosphor will not be emitting much light at the start of the next frame (**Fig 4.15c**). In this case, energy captured in the second

frame is unlikely to produce an event above the detection threshold. However, if both events arrive towards the end of a frame period (as in **Fig 4.15d**), then the phosphor will be emitting a much greater amount of light at the beginning of the second frame, and will be captured by it. The energy E_B could be large enough to be above the detection threshold and thus be counted as an event. This causes an increase in detector linearity because two events are counted when two (coincident and otherwise indistinguishable) events are captured.

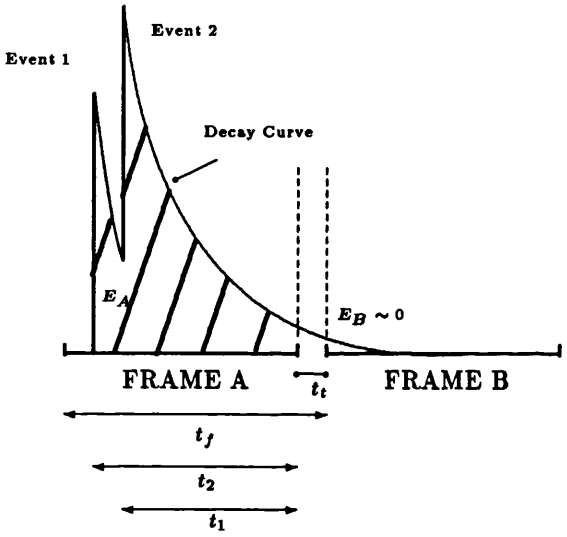

Fig 4.15c Two events arriving close to the beginning of a frame period.

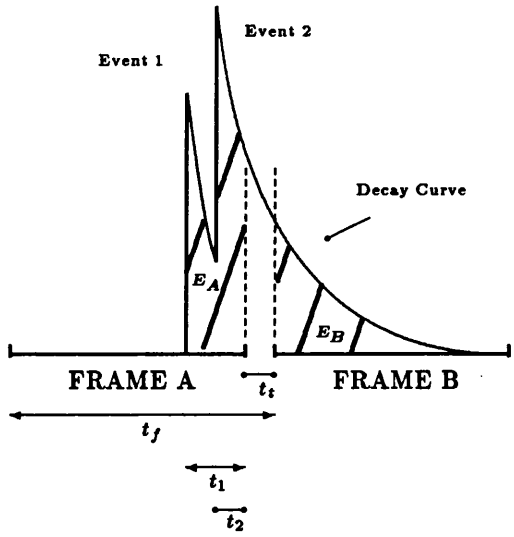

Fig 4.15d Two events arriving close to the end of a frame period.

- **By an event arriving in the frame transfer period**; If an event arrives whilst the image is being transferred to the storage area, it will not be detected in the first frame. A proportion of the energy will be captured by the CCD as the image is being transferred from the image area to the storage area but this will be smeared along a CCD column. Once the second frame period begins, all remaining energy will be captured as an image. Because the event has arrived so close to the beginning of the second frame, a large fraction of the energy will be deposited in the second frame, and from the LED tests, it was shown that most events are actually detected.

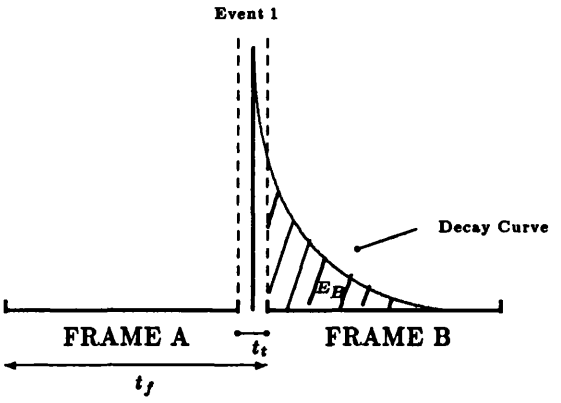

Fig 4.15e Single event arriving in the frame transfer period.

By having slow phosphor decay components, the bright limit of dynamic range is increased by detecting an otherwise coincident event (or an event arriving in the frame transfer period) by capturing a large proportion of its energy in the next frame. The easiest way in which to judge its effect on dynamic range is to incorporate it into the dynamic range computer simulations.

Different Intensifier Output Phosphors

It is possible to change the output phosphor from a P20 to a P46 or P47, which have decay components which are 5 times faster. These two phosphors have electron to photon gains some 10 times smaller than a P20 and so the intensifier would have to compensate by producing a higher electron gain. This would have the effect of decreasing the dynamic range because pore paralysis would occur at lower count rates.

4.7.3 Dynamic Range Simulations With The Phosphor Decay Incorporated

In order to incorporate the effect of phosphor decay into the dynamic range simulations many changes had to be made. No change was made to the way in which coincident events within the intensifier were recorded, only to the way in which the CCD captured events. The models simulate the effects of phosphor decay by carrying out the following steps:

1. Calculating the time at which each event is first captured by the CCD.
2. From the exponential decay curves derived above, the event energy deposited in Frame A is found assuming a value of 1 for k_1, **Fig 4.14.**

3. The event is assigned a height from the real pulse height distribution.

4. The energy associated with an event of this height is calculated assuming the event to have a gaussian distribution.

5. The real value of k_1 is then derived by scaling the phosphor decay energy calculated in 2) to that calculated in 4).

6. The event energy deposited in Frame B is then calculated by integrating the phosphor decay components between the start and end of Frame B.

7. Once the energy associated with the residual event has been calculated, its event height is found (once more assuming the event to have a gaussian distribution).

8. If the residual event has a height which is above the event detection threshold then the event is counted in Frame B.

The simulations also allows for the case in which there are coincident events within a CCD frame. If two events are coincident with each other on the CCD then the phosphor decay components associated with each coincident event are co-added taking into account the time at which each event arrived with respect to the start of Frame A.

4.7.4 Results For The Second Dynamic Range Simulations

Both point source and flat field simulations have been carried out with this second, more sophisticated dynamic range model.

Fig 4.16 shows the real and simulated point source dynamic range response of the MIC detector using a format of 256×32 CCD pixels.

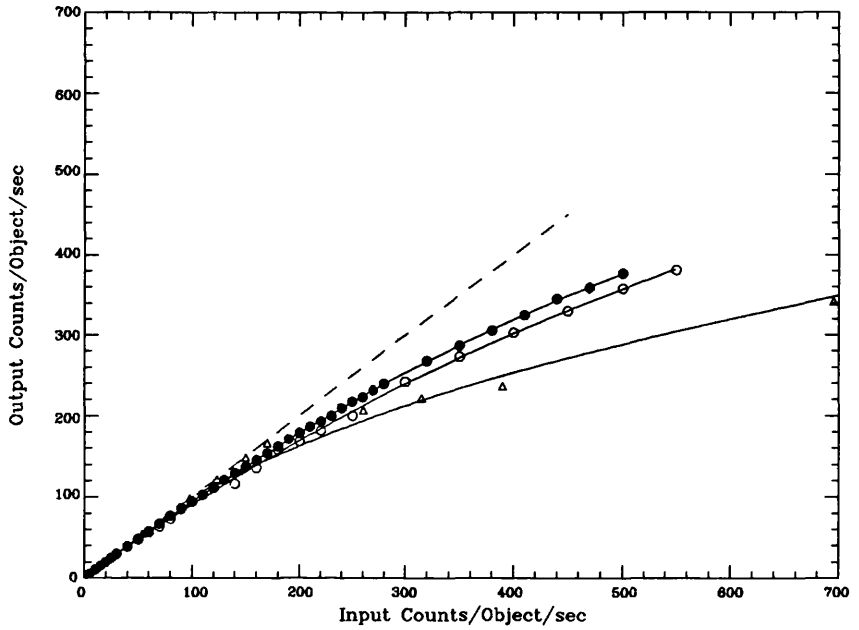

Fig 4.16. Simulated and real point source dynamic range response of the MIC detector. Format 256×32 CCD pixels. Real MIC data (△), first model data (•), second model data (o)

The second model is better able than the simple model to follow the real MIC data at high count rates. The second model predicts 10% coincidence to take place at 175 counts/object/sec very close to the actual value of 200 counts/object/sec. Because the CCD format is small the frame transfer period takes up a large percentage of the frame time. An appreciable number of events are therefore likely to arrive at the start of a frame transfer period and are thus less likely to be counted in the next frame period. So, in this case a decrease in the CCD cameras' DQE slightly outweighs the effect of double counting due to phosphor decay.

Fig 4.17 shows the real and simulated point source dynamic range response of the MIC detector using a format of 256×256 CCD pixels. The same symbols apply to this data.

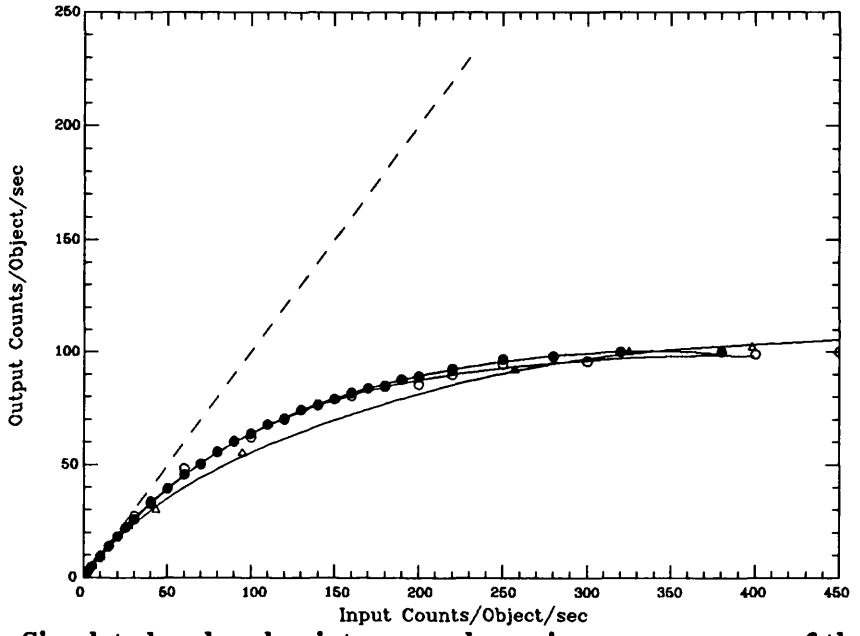

Fig 4.17. Simulated and real point source dynamic range response of the MIC detector. Format 256x256 CCD pixels

In this case the first and second models follow each other very closely, but the second model follows the real data slightly better at count rates above 200Hz. Both models predict 10% coincidence to take place at 25 counts/object/sec, the same as that obtained with the MIC detector.

Because the CCD format is larger in this instance, the frame transfer period only takes up a small fraction of the frame period and so few events are captured in the frame transfer period. Also, because the frame period is longer (10ms) the effect of phosphor decay will be minimal because the probability of events arriving very close to the end of a frame period is reduced. This means that double counting is less likely to take place.

Fig 4.18 shows the real and simulated flat field dynamic range response of the MIC detector using a format of 256x32 CCD pixels.

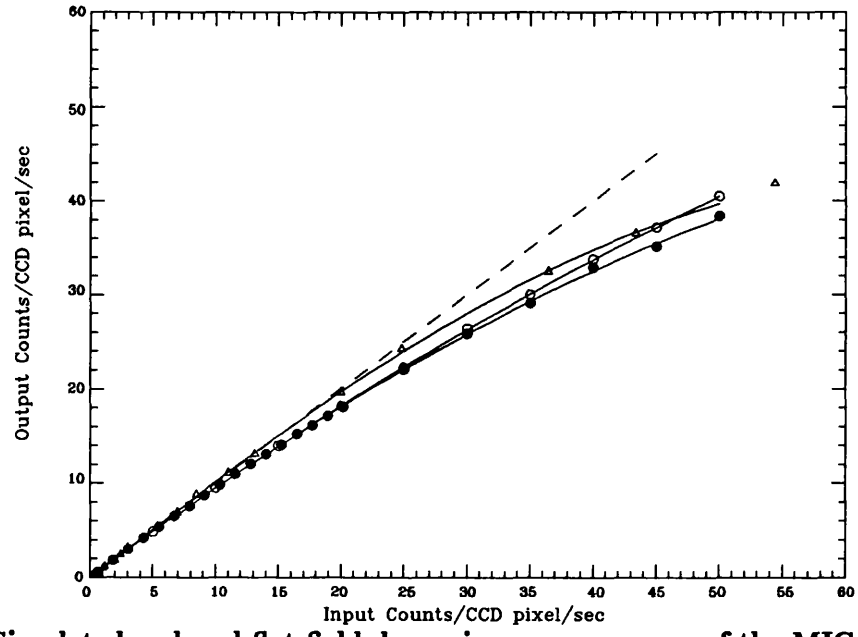

Fig 4.18. Simulated and real flat field dynamic range response of the MIC detector. Format 256×32 CCD pixels

For this flat field simulation the second model predicts a lower rate of coincidence over that predicted by the simple model. The second model predicts 10% coincidence to take place at 24 counts/CCD pixel/sec compared to 20 counts/CCD pixel/sec which is still well below the 35 counts/CCD pixel/sec obtained using MIC.

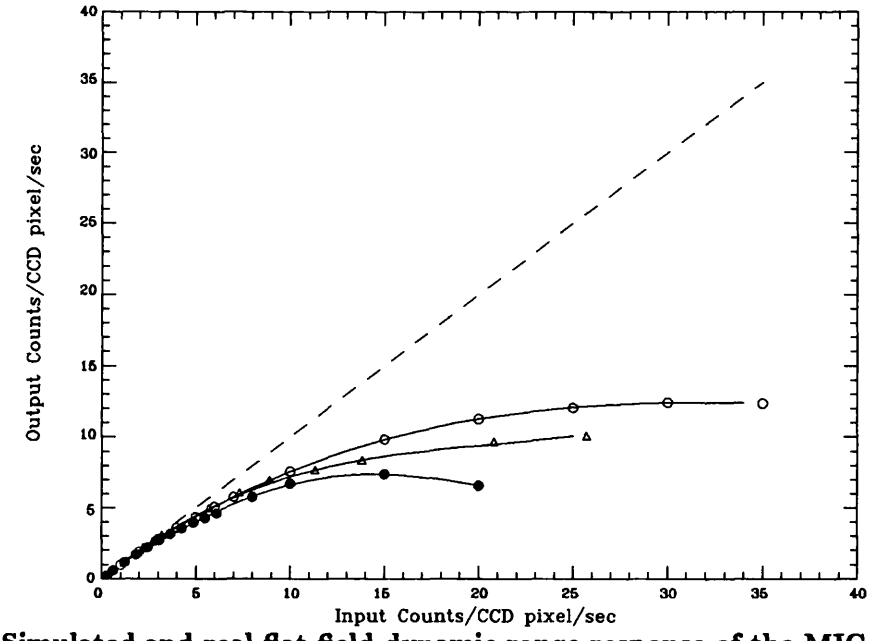

Fig 4.19. Simulated and real flat field dynamic range response of the MIC detector. Format 256×256 CCD pixels

This is also true, but to a lesser extent, for a camera format of 256×256 CCD pixels, **Fig 4.19**. In this case the second model predicts the 10% coincidence point as 4 counts/CCD pixel/sec which is still slightly smaller than the 5 counts/CCD pixel/sec obtained using MIC. Both the flat field results suggest that one of the simulation parameters governing the rate at which *spatial* coincidence takes place, maybe slightly too high.

4.7.5 Best Fitting Detector Parameters

The point source simulations in which no spatial coincidences are taking place, tend to indicate that the value used for the MCP dead time maybe too low. Increasing the intensifier dead time would not affect the rate of coincidence too much at low count rates (around the rate at which 10% coincidence takes place) but would do so at much higher count rates, bringing the simulation results closer to that observed with MIC.

The dynamic range simulations were repeated for different MCP dead times in order to best model the point source dynamic range curve. The simulations were found to match the real MIC data closest for a MCP dead time of 1ms. The results of these simulations (represented by symbol (o)) are shown in **Figs 4.20** and **4.21** for CCD frame times of 10ms and 1.5ms respectively.

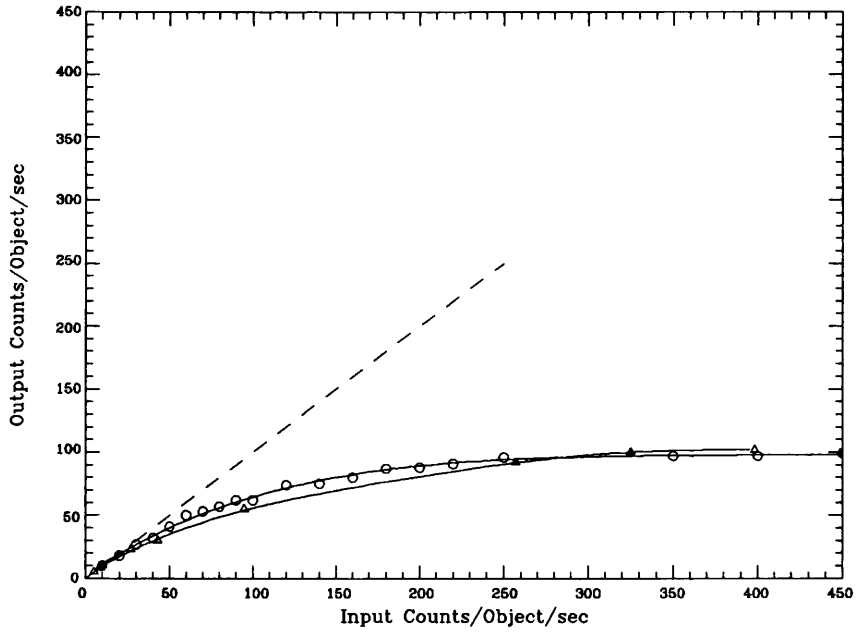

Fig 4.20. Simulating MICs point source dynamic range using a MCP dead time of 1ms. Format 256×256 CCD pixels.

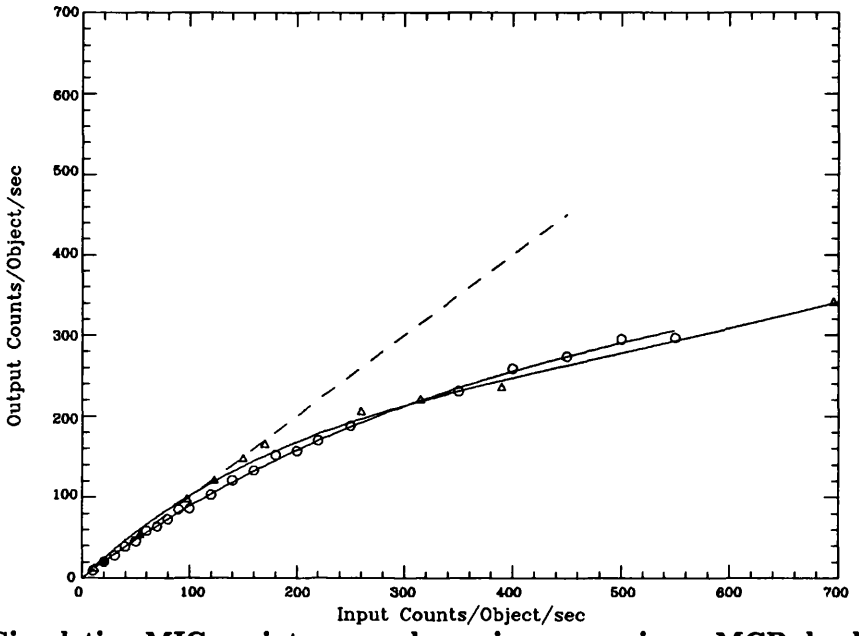

Fig 4.21. Simulating MICs point source dynamic range using a MCP dead time of 1ms. Format 256×32 CCD pixels.

Both these simulated curves follow the real data closely up to very high count rates where a high percentage of coincidences are taking place. Models which simulated the dynamic range curves using a MCP dead time of 0.1ms did not follow the real data so closely at high count rates which suggests that the real MCP dead time is closer to 1ms than the value of 0.1ms suggested by results carried out with the photomultiplier. This could be explained by the difference in which the photomultiplier and the CCD camera capture each event. Because the event sampling time of the photomultiplier is so small the effects of long phosphor decay components may cause it to over count the number of detected events. The CCD camera on the other hand has a relatively long sampling time (a frame period) during which most of the energy associated with each event is captured (except in the cases mentioned above where double counting is expected to occur).

More simulations were also carried out in order to more closely fit the flat field dynamic range curves. These simulations used a MCP dead time of 1ms but varied the MCP dead radius and the event width until the best fit to both curves was made. The best fit was found to occur if the MCP dead radius was kept at 45μm (three pore spacings) but the event width was increased by 7μm (0.1 CCD pixels). **Figs 4.22** and **4.23** show these curves (represented by symbol (•)) next to the real MIC data, for frame times of 10ms

and 1.5ms respectively.

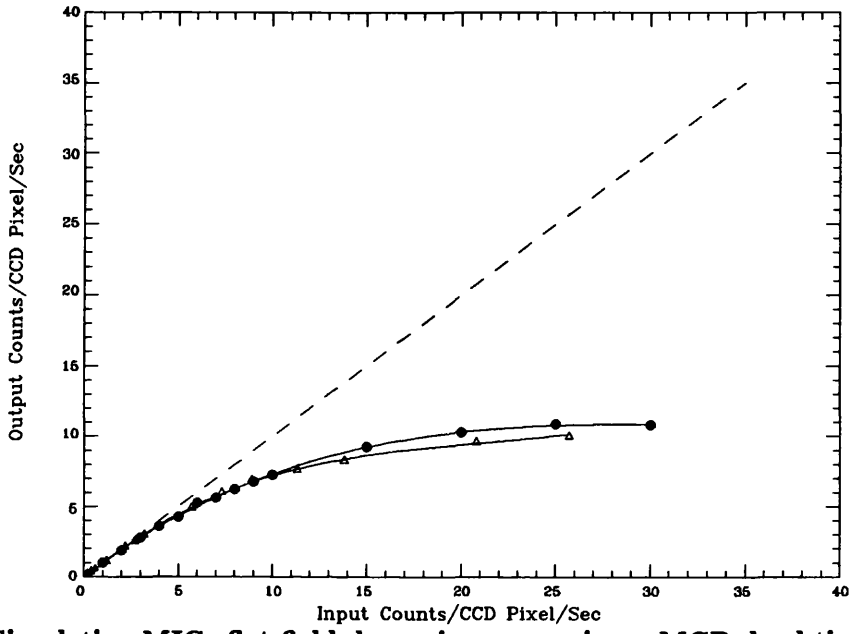

Fig 4.22. Simulating MICs flat field dynamic range using a MCP dead time of 1ms and an event width of 1.4 CCD pixels. Format 256×256 CCD pixels

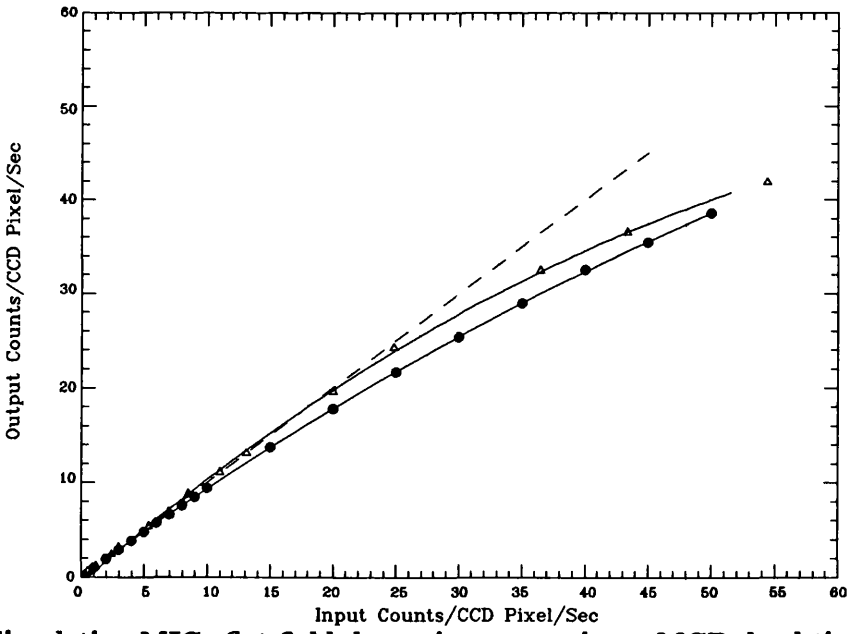

Fig 4.23. Simulating MICs flat field dynamic range using a MCP dead time of 1ms and an event width of 1.4 CCD pixels. Format 256×32 CCD pixels.

An increase in both the MCP dead time parameter (from 0.1ms to 1ms) and the event width parameter (from an average of 1.3 CCD pixels to 1.4 CCD pixels FWHM) is far better able to describe the flat field dynamic range response of MIC than the simulations

carried out previously. The simulated dynamic range curves have the same shape as the real dynamic range curves and follow them at most count rates, to better than 10%.

The reason why the measured event FWHM (taken from an event width distribution) and that used to most accurately simulate the dynamic range curves were different, can be easily explained. The program which generates the event width distribution has small errors associated with it simply because of the difficulty in sampling an event width so close to 1 CCD pixel. The real event width could be closer to 1.4 CCD pixels (100μm) instead of 1.3 CCD pixels (90μm) obtained from a width distribution simply because the event is sampled with insufficient accuracy.

4.7.6 Summary Of The Dynamic Range Simulation Results

The second (decay) model was more successful than the first in predicting MICs' dynamic range curves especially for flat field illuminations. When the MCP dead time parameter was changed to 1ms and the event width parameter changed to 1.4 CCD pixels the second model simulated the dynamic range of MIC closely over a very broad range of count rates.

Table 4.1 lists the 10% coincidence point for both point source and flat field data as predicted by both models.

Data Type	Point Source Dynamic Range (Counts/Object/Sec)		Flat Field Dynamic Range (Counts/CCD Pixel/Sec)	
	Frame Time 10ms	Frame Time 1.5ms	Frame Time 10ms	Frame Time 1.5ms
Real Data	25	200	5	35
First Model	25	180	2.5	20
Second Model (Initial Parameters)	25	175	4	24
Second Model (Best Fit Parameters)	27	115	5	20

Table 4.1. MICs' simulated and real dynamic range characteristics

The second model, using the 'initial detector parameters', in most cases predicts the 10% coincidence point more accurately than the second model using the 'best fit' parameters. However, it only does so over a limited range of count rates. Using the best fit parameters the dynamic range response can be predicted much more accurately over a wider range of count rates. Because XMM-MIC is expected to observe objects whose brightness may be much greater than its upper limit of dynamic range the 'best fit' model is more useful in describing the response of XMM-MIC when imaging these objects.

4.7.7 Improvements To The Dynamic Range Models

The largest errors in predicting MICs' dynamic range occur when the CCD frame time is small, otherwise the errors are very small. This strongly suggests that the simulations are able to accurately model the affect of coincidences taking place on the CCD but less able to model the affect of coincidences taking place within the intensifier.

At present, no data (that is known to the author) has been published which describes the intensifier gain characteristics for different spatial and temporal count distributions, especially for intensifier charge gains close to those used with the MIC intensifier. This data would enable a more accurate assessment of the way in which coincidences take place within the MIC intensifier. This could then be utilized by the simulations in order to more accurately predict the dynamic range characteristics of MIC especially for small CCD frame times.

4.8 The Multiple Counting Threshold

The dynamic range of the MIC detector can be increased by employing a multiple counting threshold (MCT). The MCT is an energy threshold used to distinguish between single and multiple (coincident) events captured by the CCD camera. When an event peak is detected at the centre of the DAA (Chapter 2) the total of all data within the DAA is summed and compared with the MCT. If the total energy within the DAA is greater than the MCT a multiple counting flag is sent to the address generator. When the multiple counting flag is set the data acquisition memory location corresponding to the event centroid position is incremented by two counts instead of just one.

4.9 Setting The Multiple Counting Threshold

The MCT is used to detect the presence of coincident events on the CCD and thereby increase the detectors linearity by treating them as two events instead of one. If the MCT is set too low an energy then single events could be counted as multiple events, falsely increasing the apparent count rate. If the MCT is set at too high then only a small percentage of coincidences are recognized.

The MCT value has been found by carrying out several dynamic range tests, some with the MCT disabled and others with the MCT enabled. **Fig 4.24** shows the results of

flat field dynamic range tests for several different values of the MCT.

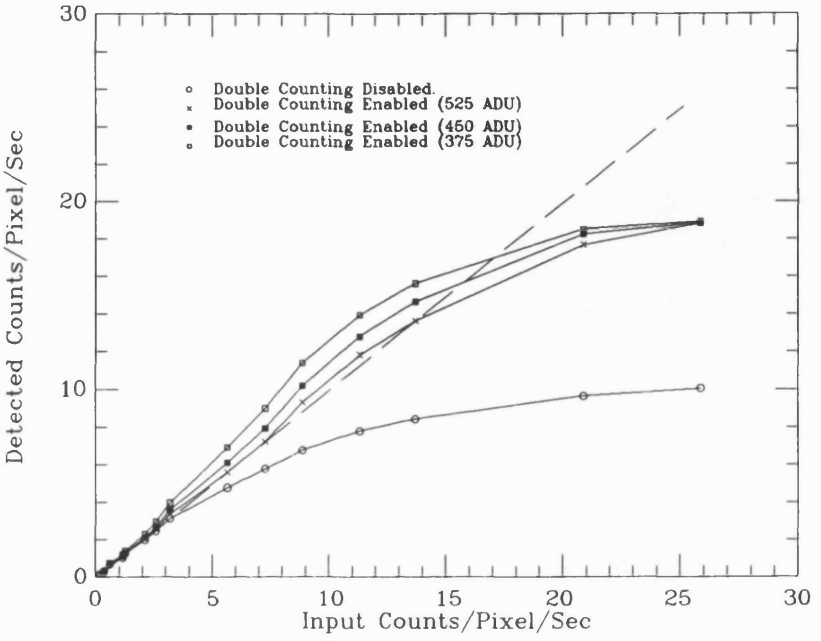

Fig 4.24. Flat field dynamic range curves for several values of the multiple counting threshold. Format 256×256 CCD pixels

Except at high count rates, the detector overcounts in all the cases where the MCT is enabled. This is due to the threshold being set at too low an energy. The degree of over counting is greatest for a threshold of 375 ADU. In this case, many single events are being counted as multiple events. For a threshold of 525 ADU few single events are mistaken for multiple events and the amount of over counting is greatly reduced.

A MCT greater than 525 ADU say, 550 ADU would produce virtually no over counting but simply increase the detectors flat field dynamic range. Extrapolating from the graph, 10% coincidence is expected to take place at $\sim$ 15 counts/CCD pixel/sec which corresponds to 10^6 counts over the full detector area. This would be significantly larger than the 10% coincidence point of 5 counts/CCD pixel/sec, (3×10^5 counts over the whole area), obtained when the threshold is disabled.

Events which *partially* overlap on the CCD can still be resolved (being individually counted) whilst also contributing to the total energy associated with another event within the DAA. In this case a degree of double counting takes place, events:

1. being counted once because it has a data peak associated with it.

2. being counted again because its energy together with other events around it, push the total energy within the DAA above the double counting threshold.

However, if the threshold is set correctly, the double counting is offset by coincidence losses introduced by events arriving directly on top of each other. Because a threshold of 550 ADU is close to three times the average event energy, coincidences between groups of two events will not be detected. The degree to which over counting takes place is offset by coincidence losses until a high percentage of events start to completely overlap. In this case each CCD frame becomes saturated with events, leading to a fall over in event detection.

These dynamic range tests were repeated for a point source illumination this time for a single MCT of 550 ADU. **Fig 4.25** shows the point source dynamic range response of the detector for a CCD frame time of 10ms,

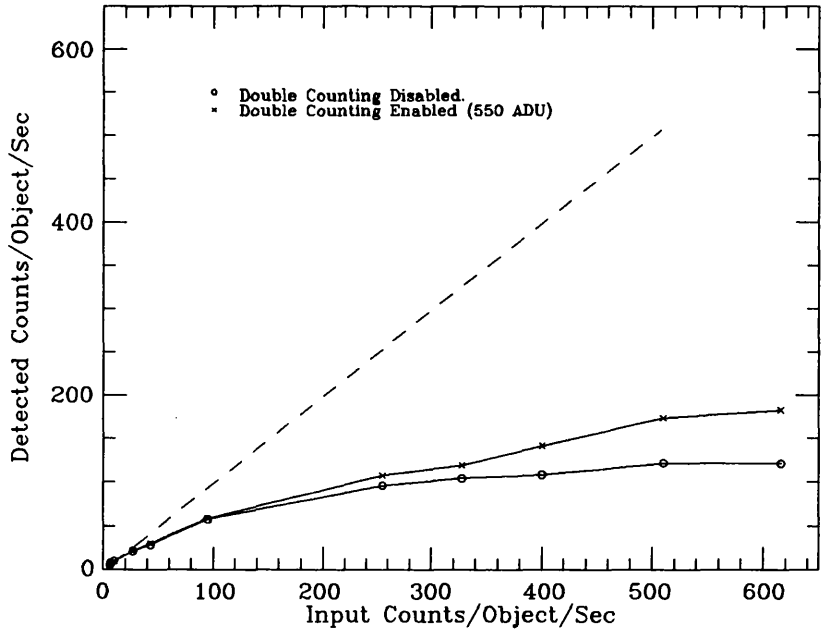

Fig 4.25. Improvement in point source dynamic range for a multiple counting threshold of 550 ADU. Format 256×256 CCD pixels

whilst **Fig 4.26** shows the results for a CCD frame time of 1.5ms.

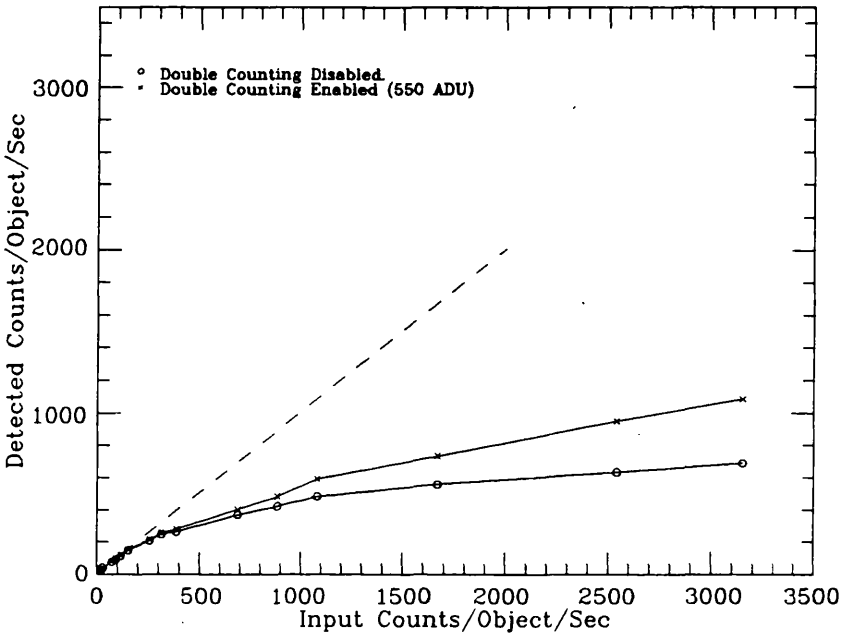

Fig 4.26. Improvement in point source dynamic range for a multiple counting threshold of 550 ADU. Format 256×32 CCD pixels

Fig 4.26 shows that the detector linearity can be increased by up to 25% for an input count rate of 1000Hz (the brightest point source count rate expected for XMM). This increases the count rate to which point source dynamic range curves can be used to extrapolate the input count rate from that detected by MIC.

The detector does not double count at low count rates because the threshold is almost three times the average event energy of 200 ADU. This is why the multiple counting threshold does not have much effect on the detectors' linearity until the number of coincidences between three or more events becomes significant (3-4 times the count rate at which 10% coincidence normally takes place).

As a result of these tests the multiple counting threshold is, by default, set at a value of 600 ADU. This threshold is large enough to make sure that no overcounting takes place at low count rates. If the intensifier gain characteristics change for any reason then the threshold value must be recalibrated.

4.10 Dynamic Range Testing Of The MIC Detector Under Astronomical Conditions

The MIC detector has undergone astronomical field trials at the University of London Observatory (ULO). The aim of these trials was primarily to evaluate the detectors' dynamic range behaviour under astronomical conditions and to do so in a way which would closely mimic the background conditions expected in the XMM-OM Space environment. The high pressure sodium street lamps around the observatory were able to provide enough scattered light to simulate the high levels of background illumination expected in Space. The 24in Radcliffe telescope used for these trials had a plate scale of 30 arcsec/mm i.e. 1 arcsec/33μm, which, if the seeing is good, would project a star image onto typically 60μm of the detector. This was as close to 20μm (the star size expected to project onto XMM-MIC once in Space) that could be obtained.

4.10.1 Method Of Obtaining A Dynamic Range Curve For MIC

The aim of these trials was to produce a point source dynamic range curve for the MIC detector. Each point on the curve was obtained by imaging groups of both faint and bright stars in the same field, whose relative intensities were already known. The intensity of a bright star within a group was compared to the intensity of a faint star (on which MIC was assumed to be counting linearly) and the relative intensity compared to the known ratio. Any difference between the two figures was assumed to be due to coincidence losses within the MIC detector. By plotting what the count rate of the bright star should have been (the input count rate) against that measured with the MIC detector (the output count rate) a dynamic range curve could be built up.

In some cases the same pair of stars were used to produce several points on the dynamic range curve by varying the ND filters placed in front of the detector.

4.10.2 Calibration Of The Detector

In order to make accurate photometric observations of different star fields both the wavelength response of the telescope and the variation in intensifier DQE over the imaging area must be known. These were not known at the time of observing and so the MIC data could not be compared with previously published photometric data on the chosen

star fields.

Variations in the telescopes' wavelength response were negated by observing stars through a narrow band colour filter which was centered on the Na D line to maximise the throughput of background light. This negated the effects of frequency dependent sensitivity variations across the telescope but required us to obtain accurate relative photometry of each star field through the same colour filter. This data was acquired with a direct CCD camera (on the 24in Allen telescope at ULO), the CCD dynamic range response being linear if CCD saturation is not experienced.

4.10.3 The Observing Program

The star fields used in these tests were chosen for the following reasons:

1. They contained two or more stars of different intensity, one star being faint enough to lie on the linear region of MICs' dynamic range curve.

2. They either contained very closely or very widely spaced stars to see what effect channel plate gain depression had on dynamic range.

The fields ranged from well separated double stars, equivalent to single isolated stars, to close binaries and multiple star fields where the affect of gain depression might have been apparent. **Table 4.2** shows the detectors' observing log and **Fig 4.27** shows four of these star fields imaged with the MIC detector.

object	other	type	Mv approx	Separations	ND	time secs	format square
NGC1912	M38	Cluster	stars $\leq$ 8		0.9	2000	2048
HR1895	θ Ori	Group	5.1,7.9,6.7,6.4...	in 120″	1.5	1000	2048
					1.5	1000	1024
NGC2169		Cluster	6.9,7.0,8.6,7.5...	in 8′	0.9	2100	2048
HR2298	ϵ Mon	Triple	4.4,6.7,12.2	13″,93″	2.0	772	1024
					2.0	2000	1024
HR2456	15 Mon	Group	4.7,9.0,8.3,7.6...		2.0	2000	2048
					2.0	2000	1024
HR3395		Double	6.0,7.2	10.3″	2.0	1000	1024
HR3427		Quad'	6.4,6.6,9.2,8.8	150″,135″(2)	0.9	2000	2048
					0.9	600	1024
					1.5	1000	1024
HR3428		Quad'	6.4,7.7,9.4,10.4	63″,83″,21″	0.9	2000	1024
HR3429	ϵ Cnc	Double	6.3,7.4	135″	0.9	600	1024
					2.0	817	1024
HR3474	ι Cnc	Double	4.0,6.6	30″	2.6	2000	1024
					0.9	2000	1024
HR3759	τ Hya	Double	4.6,7.6	66″	2.0	1000	1024
HR3811		Triple	6.7,8.2,8.3	25″,118″	0.9	1500	1024
HR4203	42 Lmi	Double	5.2,8.0	198″	2.0	1000	1024
HR4363		Double	6.5,8.2	12.7″	0.9	1015	1024
					1.5	2000	1024
HR4408	81 Leo	Double	5.6,9.2	56″	1.5	1000	1024
HR4414	83 Leo	Triple	6.5,7.6,9.9	28.5″,90″	0.9	1000	1024
					2.0	1000	1024
HR4761	7 Cvn	Double	5.2,8.0	198″	0.9	500	1024
					1.5	700	1024
					2.0	2000	1024
HR4914	α Cvn	Double	2.9,5.6	19.4″	3.0	1900	1024

Table 4.2. Observing log for the XMM-MIC detector

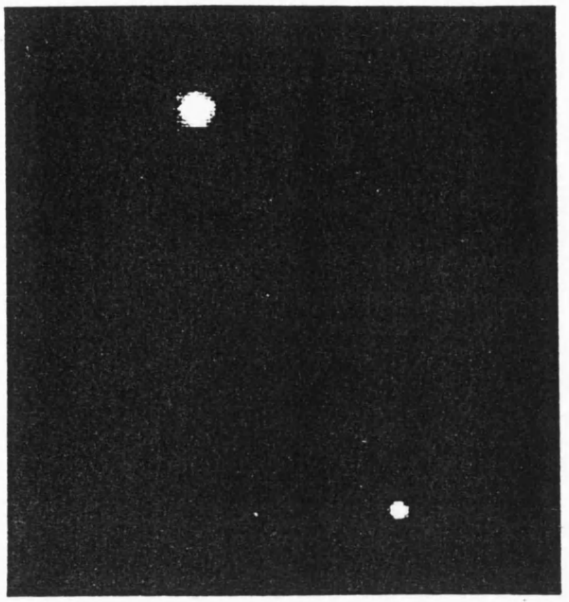

HR4761
Star Separation 198"

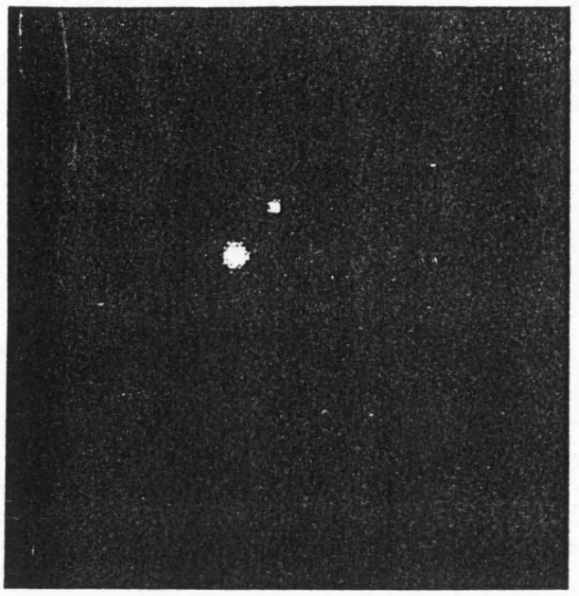

HR3474
Star Separation 30"

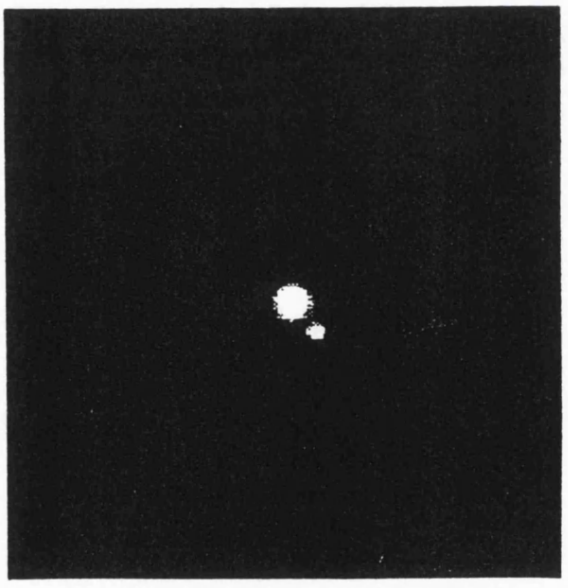

HR4914
Star Separation 19.4"

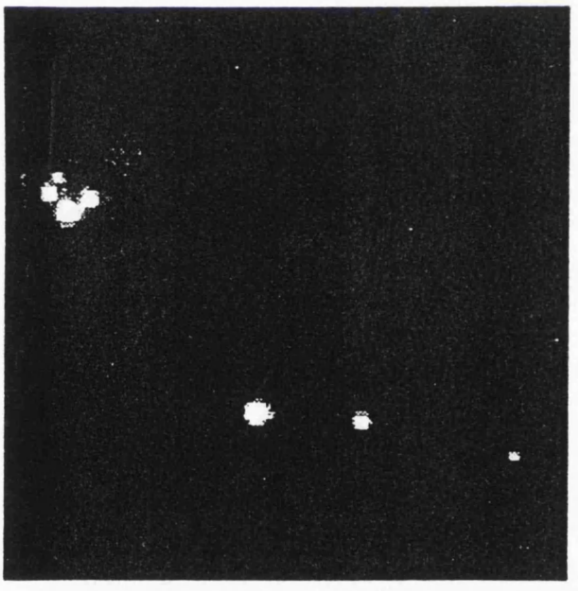

HR1895
Star Group including "The Trapezium"

Fig 4.27 Examples of star fields acquired with the MIC detector during observing trials

All the scientific observing was carried out with a detector format of 2048 x 2048 pixels and hardware windowing was then employed to select an area of 1024 x 1024 pixels for data acquisition. The observing was carried out with a pixel size of $\sim 9\mu$m and the Coincidence Recognition circuit operational (with the MCT set at 600 ADU).

The seeing during the observing trials was on average 4 arcsecs giving an image size of $\sim 120\mu$m FWHM. The background conditions were variable, being primarily dependent upon the neutral density filter used but also upon the variation in sky background intensity. The range of background count rates typically varied between 80K c/s (ND 0.9) and 5K c/s (ND 2).

4.10.4 Data Analysis

All of the MIC and CCD data were analyzed by the author on the STARLINK computer system at UCL. For the CCD data, the CCD bias (acquired as a separate integration during the observing) was initially subtracted from the each data set.

Ideally, the CCD and MIC data then needed to be calibrated to remove any instrumental artifacts and compensate for any variations in RQE across the detector area. This would normally be achieved by dividing by a uniform 'flat field'. Separately acquired flat fields using, for example, a tungsten lamp cannot be used in this application as they do not produce the uniform intensity distribution that is essential for removing quantum efficiency variations across the detector. Thus, standardly, the flat field is derived from a number of image fields where it is assumed that the sky background is uniform, the basic principle being to filter out the star images from a single field and replace these by a normalized sky background from other fields. Unfortunately, for the MIC data, we were unable to carry out this procedure due to the method of data acquisition used. For each star field, a 1024 x 1024 window was positioned in the 2048 x 2048 maximum format of the detector to maximise the number of stars in a single integration. By moving this window between integrations on different fields, different areas of the photocathode were exposed thus disabling the possibility of obtaining a uniform sky background flat field. Both the MIC and CCD data were therefore analyzed as follows :

1. the average sky background in close proximity to each star deduced

2. this was then subtracted from the associated star image to produce sky subtracted

star images

3. the total flux in the star images deduced

4. the ratio (star count):(faintest star count) for each field derived

This procedure has a number of problems associated:

1. it assumes that the RQE of the photocathode is a constant over MICs' imaging area

2. it does not allow for any localized instrumental artifacts

These increased the errors associated with each data point but this analysis was the best that could be achieved.

In principle, for each star field, the ratio of star magnitudes for MIC should be identical to those obtained with the CCD. Any change in the ratio can be attributed to MIC coincidence loss on the brighter star, it being assumed that the faintest star in each field is in the linear region of the MIC dynamic range curve.

The most important fields in the observing programme are those containing just double stars as they provide star ratios that cannot be contaminated by other stars that are present. The separations on these double star fields range from 198" (HR4761 and HR4203) to 10.3" (HR3395). 198" is equivalent to 6.5mm at the detector a distance at which no channel plate gain depression is expected and thus from the ratio of the star magnitudes in the fields of HR4761 and HR4203 a point source dynamic curve can be drawn, HR4761 being observed through 3 different neutral density (ND) filters to provide four uncontaminated points on the curve.

A plot of the results is shown in **Fig 4.28** where the Calculated Input Count Rate is derived from the CCD data and the Detected Count Rate derived from the MIC data. The dashed line is that associated with a linear detector. The vertical error bar on each star is that associated with the MIC data and the horizontal error bar is the product of the CCD and MIC error bars, this resulting from star intensity ratios, not absolute magnitudes, being known. The stars with large error bars associated are those where their are large error bars on the faintest star in each field due to the total count level (i.e. signal to noise) not being high enough. For clarity not all of the stars on the curve are identified.

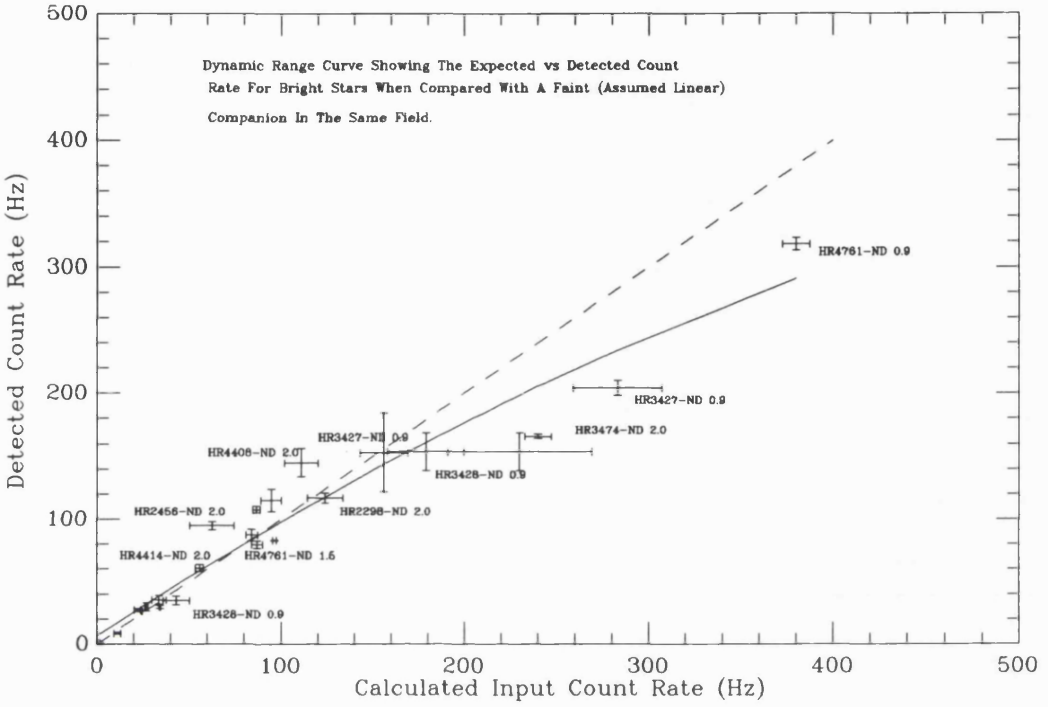

Fig 4.28. Point source dynamic range curve for the MIC detector derived from astronomical observations

A second degree polynomial was fitted to the data in **Fig 4.28**. The results show that the 10% coincidence loss point is at 170 c/object/s which is far greater than the 25 c/object/s obtained in the laboratory trials. This can be explained by the object size being ~130μm FWHM (an average of 4" of arc). This leads to a lower number of coincidence losses at high count rates because not all the events are spatially coincident. As the seeing conditions were a variable during the observations, and the observations were taken over a total of three partially clear nights, it is expected that a number of the objects do not fit the curve within their error bars. There are two points to be noted from this graph:

1. the affect of the background count rate does not seem to greatly affect the dynamic range curve of the star images. For example it could be expected that the count rate associated with HR4761 at ND 0.9, where the background was 40K c/s over the detector, is affected more than that at ND 1.5 but this appears not to be the case.

2. their appears to be no great affect from channel plate gain depression. On HR 2298,

for example, where two bright stars (M_v 4.4 and 6.7) are within 13" of each other there appears to be no dramatic loss of data from the brighter star. This confirms the dynamic range tests carried out using variable spaced pinholes.

4.11 Summary

The dynamic range of the MIC detector is limited at the faint limit mainly by the intensifier photocathode dark current which for a S20 photocathode is typically 50 counts/cm^2/sec at 300K. This is very small compared to the estimated 6×10^4 counts/cm^2/sec background count expected when observing with XMM-OM.

The MIC intensifier is run at a relatively low charge gain of typically 1×10^5. Because the gain is so low the intensifier has been shown to have a very small dead time associated with it ($\sim$ 1ms) and the area over which each event depletes charge is typically 45μm. As a result, the dynamic range of the MIC detector is limited by the CCD camera and not the intensifier. The detectors' dynamic range can be increased by reducing the time taken to read out each CCD frame. This is done by only reading out selected regions of the CCD. For example, the maximum CCD format for XMM-MIC is 256×256 CCD pixels which is read out in 10ms. If only 256×32 CCD pixels are read out then the frame time is reduced to only 1.5ms.

The detectors' dynamic range is, in some circumstances, improved by the way in which the CCD camera samples energy from the P20 output phosphor. Events captured in one frame can also be captured in the next contiguous frame but usually, only in cases where an event would otherwise be lost. The effect of these secondary phosphor decay events is therefore not to produce double counting but to merely count events that would otherwise be lost due to coincidence or because they arrived during the frame transfer time of a frame period.

The detectors' linearity can also be increased by employing a multiple counting threshold above which events are counted as two events instead of one. The threshold has been set at 600 ADU, high enough to ensure that single events are not double counted but low enough to ensure that most coincidences between two or more events are counted as multiple events. Its effect is best seen when applied to extended sources where the implementation of a multiple counting threshold can double the detectors' dynamic range.

The astronomical trials which took place at the ULO have shown that MIC is capable of achieving the dynamic range results which have been obtained in the laboratory. They have also shown that the detectors' dynamic range is unaffected by a high background count (at least up to 4×10^4 counts/sec over the whole detector) and that the effects of gain depression cannot be detected down to distances as small as 400μm.

Chapter 5

Detector Resolution

5.1 Introduction

Unlike single channel photomultiplication devices, MIC is an imaging detector, designed to capture and reproduce an image scene. Photon counters, like other types of imaging detector, have limitations on the quality to which an image can be reproduced. One of these limitations is its resolution.

In practice, two objects are said to be resolved if, after being imaged, they are both individually discernable at the detector output. The detector resolution is a measure of the minimum angular or spatial separation above which objects incident on the detector are resolved by it. Astronomers are concerned with the ability of an imaging system (usually a telescope and a detector) to be able to resolve objects with a given angular separation, as the separation of celestial objects is quoted in terms of angle. However, because different telescopes can have different *plate scales*, quoting the detector resolution in terms of angular separation is somewhat ambiguous. The detector resolution is therefore quoted in terms of spatial resolution which can be translated into angular resolution for any given plate scale.

The field of view of the OM telescope is 16 minutes of arc, which is projected onto the active imaging area of the MIC detector ($17.67^{\times 17.67}$ mm). Thus, for the blue detector, the OM has a plate scale of $\frac{16}{17.67}$ =0.905 arc minutes/mm. One of the scientific requirements of the blue detector is that it have a resolution of 1 second of arc, and so MIC is expected to have a resolution of 20μm or better. In order to determine what governs the resolution of the MIC detector an understanding of how those components of the detector which

affect the event position must be sought.

As an event passes through MIC, its spatial position is determined by three characteristics of the detector. These are:

- The primary electron spread across the front gap of the image intensifier (a)
- The front channel plate pore spacing (b)
- The electronic centroiding resolution (c)

The detector resolution then approximates to a pythagorian convolution of these three components [*Eberhart*[2]], where:

$$\text{Detector Resolution} = \sqrt{a^2 + b^2 + c^2} \tag{5.1}$$

This equation assumes that the affect of each component on a point source image is to produce a smooth gaussian output distribution whose standard deviation is the resolution of that detector component. If we convolve these three gaussians, with standard deviations a,b and c, then the standard deviation of the resulting gaussian and hence their combined resolution, is $\sqrt{a^2 + b^2 + c^2}$ [*Hect et al*]. In order to theoretically predict the resolution of MIC, the resolution of each of these three components must be known.

5.2 Front Gap Resolution

A voltage applied across the intensifier front gap accelerates photoelectrons from the photocathode to the front channel plate. Each photoelectron either enters a pore or is absorbed into the inconel electrode placed between the pores. The photoelectron velocity vector has two components, one perpendicular to the face of the channel plate (normal velocity component) and one parallel to it (transverse velocity component). The equation governing the transverse distance traveled by the photoelectron can be derived from first principles, where the photoelectron transverse velocity is given by

$$v_t = \sqrt{\frac{2\epsilon}{m_e}} \tag{5.2}$$

where ϵ is the transverse escape energy of the photoelectron from the photocathode and m_e is the electron mass.

Assuming that the initial (normal component) of photoelectron velocity is negligible compared to its final velocity, the time taken for the electron to reach the front channel plate will be

$$t = \sqrt{\frac{2L^2 m_e}{Ve^-}} \tag{5.3}$$

where L is the front gap distance, V is the voltage applied across the gap and e^- is the electronic charge. Multiplying *Equs 5.2* and *5.3* we derive the transverse distance moved by the photoelectron whilst traveling across the front gap as

$$D_t = 2L\sqrt{\frac{\epsilon}{V}} \tag{5.4}$$

where the transverse electron energy ϵ is now quoted in terms of electron volts.

The value of ϵ is not a constant, but has a Maxwellian distribution [*Csorba*] about the value ϵ due to the variable energy transfer between photon and photoelectron. A point source image will thus have a point spread function at the front channel plate. The point spread function has been calculated by *Csorba*, adding a correction term to *Equ 5.4*, which gives

$$\text{Front Gap Resolution} = 3.3L\sqrt{\frac{\epsilon}{V}} \tag{5.5}$$

The value of ϵ depends upon the photon wavelength, the longer the wavelength the less energy is transferred to the photoelectron. The value of ϵ for blue light is $\sim$ 0.3V, for red light $\sim$ 0.05V, and the average for white light $\sim$ 0.14V [*Eberhart*[2]]. The front gap resolution is therefore wavelength dependent, being higher for radiation of longer wavelengths (typically 2.5 times higher for red light than blue). Using this equation, the front gap resolution of an image tube possessing a front gap of 200μm across which 300V is applied, and using white light, is $\sim$ 14μm.

5.3 The Front Channel Plate Pore Spacing

The accuracy to which the position of an event can be measured once it has passed through the intensifier MCPs is determined by the front MCP pore to pore spacing. Photoelectrons entering the front channel plate pore produce events at the output phosphor whose size is dependent upon, for example, the separation between each MCP and the distance from the rear MCP to the phosphor. However, once centroided, the events have inherent centroid positions which are one pore spacing apart. So the only positional information that can

be obtained from sampling events produced at the rear of the intensifier is knowing into which of the front MCP pores the photoelectron passed. Therefore the resolution of the MCPs is the pore to pore spacing.

5.4 The Centroiding Resolution

Event centroiding, as described in Chapter 2, is a method by which the position of an event centre is estimated to a greater accuracy than a sampling element (in this case a CCD pixel), by finding the event centre from an examination of the event distribution in surrounding elements. By doing this an event readout system is capable of having formats much greater than the number of sampling elements. The XMM-MIC uses a 384×288 pixel CCD of which only a maximum of 256×256 pixels are used for data acquisition. This means that without event centroiding the accuracy to which an event from the intensifier can be determined is one CCD pixel. A 23μm CCD pixel subtends to 70μm at the intensifier (assuming a 3.06:1 fibre taper coupling between the intensifier and CCD), so if subpixel centroiding is not employed the accuracy to which an event position can be found is 70μm. If event centroiding is employed, and the event is centroided to $\frac{1}{8}$ of a CCD pixel, the event position can be determined to within $\frac{70}{8}\mu$m=8.8μm at the intensifier, and the detector format increases to 2048×2048 pixel elements. [1].

The 'centre of gravity' centroiding algorithm (Chapter 2) is only an accurate method of finding the centre of an event if the event profile (as presented to the centroiding electronics) is derived from a symmetrical event. In order for this to occur, an event incident on the CCD must be symmetrical and no distortion of the event should occur once it has been captured. However, a number of distortion mechanisms lead to errors in centroiding each event resulting in a subsequent loss of resolution.

5.5 Causes Of Event Distortion

5.5.1 Distortions Due To The Intensifier

The MIC detector employs MCPs whose pore axes are at a bias angle of ~8° to the normal of the output phosphor. This means that events emerging from the rear MCP

[1] These elements into which a CCD pixel is split will from now on be referred to as *subpixels* or *channels*

with symmetrical gaussian profiles form events at the output phosphor which have an asymmetrical light intensity profile similar to that shown in **Fig 5.1.**

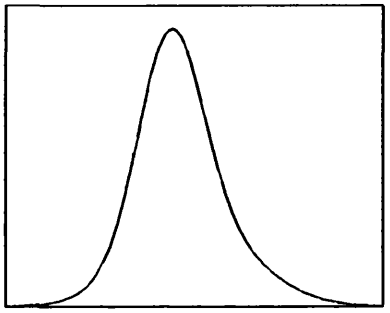

Fig 5.1. Cross section through a typical event profile

This can be improved by employing an intensifier whose rear MCP has a 0° bias angle, this being available from a number of manufacturers, and is being considered for XMM-MIC.

If the intensifier has been poorly scrubbed then the intensifier can introduce another type of event distortion called *signal induced background* (SIB). This manifests itself as small energy, secondary events, surrounding the primary event and randomly changing its event profile (Section 5.9.4).

5.5.2 Distortions Due To The Fibre Taper

The event profile can also become distorted when it passes through the fibre taper which couples the intensifier to the CCD. Fibre optic coupling devices do not suffer from distortions such as the aberrations associated with a lens [*Worswick et al* + Wynne]. This means that there is no event width or distortion dependency on radial position from the centre of the fibre taper. On the other hand, there is the potential for what are called *shear distortions* occurring on a very local (3-6μm) level. These occur if adjacent fibres are misaligned with respect to one another, so that the mapping of an event profile from the intensifier to the CCD is imperfect. The number of shear distortions associated with fibre tapers is believed to be small [*Bellis*].

Another form of event distortion is introduced if the fibre taper is incorrectly lowered onto the CCD. If the two contact surfaces (the fibre taper and the CCDs fibre block) are not parallel, event profile asymmetry is introduced. This is not expected to be a problem

for XMM-MIC, as the intention is to bond the taper directly onto the CCD.

5.5.3 Distortions Due To The CCD

Once an event has been captured by the CCD its' profile can be distorted in one of several ways before being passed to the centroiding electronics.

- Charge Transfer Inefficiency - If the frame transfer inefficiency is large enough (i.e. signal smearing is equivalent to a few ADUs) then it can cause the distortion of event profiles in the direction of frame transfer. Because both the Thomson and EEV CCDs have transfer efficiencies of > 0.99997 this affect is negligible in MIC.

- Hot Pixels - If, for some reason, the CCD becomes damaged (e.g. by energetic particles), defects in the silicon lattice can create 'hot pixels' in which valence electrons are rapidly excited into the conduction band. This causes any signal in the same column of the CCD but farther away from the storage area (in the direction of frame transfer) than the 'hot' pixel, to become superimposed on top of charge from the continuously replenished 'hot' pixel, saturating the ADC.

- QE Variations - Event profiles can also become distorted due to QE variations between CCD pixels. When this occurs the events' centroid position is bias away from the low QE pixel resulting in the pixel having fewer counts than those surrounding it, **Fig 6.14**. This effect can be minimized by simply rejecting CCDs with significant numbers of defective pixels, during the selection procedure. Their effect on the final image is small because these defects can be corrected for during data reduction.

- The CCD Readout Noise - which is $\sim 300\ e^-$ rms. In order to minimize the effect of readout noise, the ADC is set such that 1 ADU is between 200 and 600 e^- depending upon the intensifier gain. This means that for events having an event peak height of typically between 60-80 ADU, the affect of readout noise is minimal.

- The DC Bias - as discussed in Chapter 2. The DC bias provides a pedestal upon which the event data sits, and has the effect of biasing the event centroid towards the centre of a CCD pixel. This can be shown by considering **Figs 5.2a** and **5.2b** in which **Fig 5.2a** shows an event profile with no DC bias, and **Fig 5.2b** shows the same event profile superimposed on a DC bias of 20 ADU. The results of the

centroiding algorithms for each case are different, the profile in **5.2b** being centroided closer to the centre of pixel B.

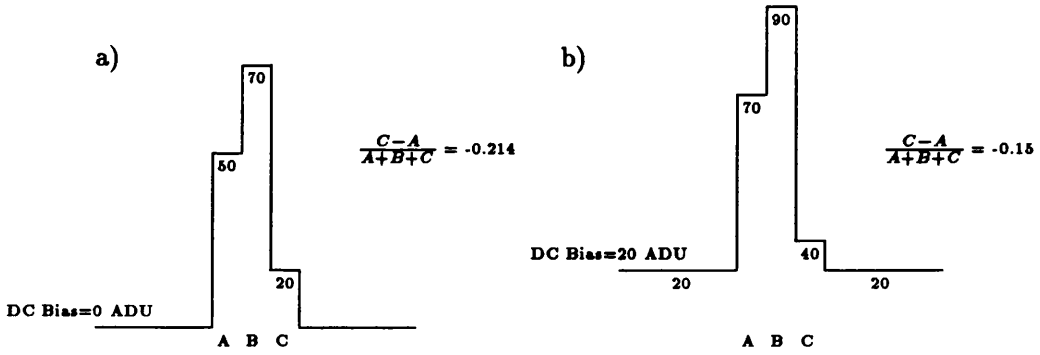

Fig 5.2. Affect of signal bias on event centroiding

To reduce the effect of DC bias *frame subtraction* can be employed whereby the previous frame of data is subtracted from the current frame of data. However, the associated circuit is power consumptive and leads to an increase in coincidence losses. XMM-MIC minimizes the effect of DC bias by employing a *black level clamp*, (described in Chapter 2) whereby the last seven CCD pixels of the previous row (which are covered over with aluminium) are sampled, and the average signal subtracted from the data in the current CCD row.

5.6 Centroiding Errors Introduced By Event Sampling

If a symmetrical event profile is undersampled, it can appear distorted. The way in which events are sampled is by binning the integrated event energy into CCD pixels and then using data in a fixed number of pixels around the data peak to centroid the event (this number of pixels is dictated by the size of the DAA and the centroiding algorithm). Ideally, the most accurate way of doing this is to bin an event into a large number of pixels so that the event profile is well sampled (i.e. integrated into bins whose size is small compared to the event size). In practice this cannot be done because, as explained in Chapter 5 because there is a trade off between resolution and dynamic range, which restricts the optimum event size with respect to the size of a CCD pixel.

An event is incorrectly sampled:

1. if the event width is so large that the number of pixels sampled by the centroiding algorithm represents only a small portion of the event profile, or

2. if the event width is so small that the number of pixels sampled by the centroiding algorithm is large compared to the range over which the event extends.

In both cases information about the event energy distribution is lost and the event profile presented to the centroiding electronics is unrepresentative of the true event shape.

Computer simulations used to model the effect of event sampling on centroiding resolution have been carried out by *Dick et al* and *Fordham and Hook*. They show that when sampling the data in a 5×5 array of pixels around the event data peak, the optimum event FWHM is 1.5-1.75 CCD pixels in order for correct centroiding to occur. If sampling the data in a 3×3 array of pixels around the event data peak, the optimum event width is 1.4-1.5 CCD pixels. As a result of this work the intensifiers used with the XMM-MIC have a back gap which produces events with a FWHM of typically 100μm, projecting down to 33μm (1.4 pixels) at the CCD if a 3.08:1 fibre taper is employed.

Events also become incorrectly centroided if the peak height is < 20ADU [*Dick et al*]. This sets a lower energy limit below which events cannot be processed without decreasing the centroiding resolution. A lower counting threshold of 20 ADU typically coincides with the valley of the saturated pulse height distribution from the MCP intensifier if the MCP voltages are correctly set (Chapter 7). Setting the lower counting threshold to around 20ADU not only ensures that most of the processed events are derived from real photon events at the input to the intensifier, but that all processed events are centroided accurately.

5.7 Distortions Due To Event Coincidence

In terms of their effect on detector resolution, two events are said to be coincident if they arrive so close together in the same CCD frame that their profiles overlap. There are three different degrees to which events can overlap, each one presenting a different problem to the event centroiding electronics in terms of centering each event (i.e. centroiding each event into the subpixel which it would normally be placed if the other event were not present). In case (i), **Fig 5.3**, the events are far enough apart that there is a gap of one or perhaps two pixels between the two data peaks. In case (ii), the events are closer together, giving rise to a broad flat 'top hat' profile, in which there is no single data peak. Finally in case (iii), the two events lie on top of each other and only one data peak is

present for both events.

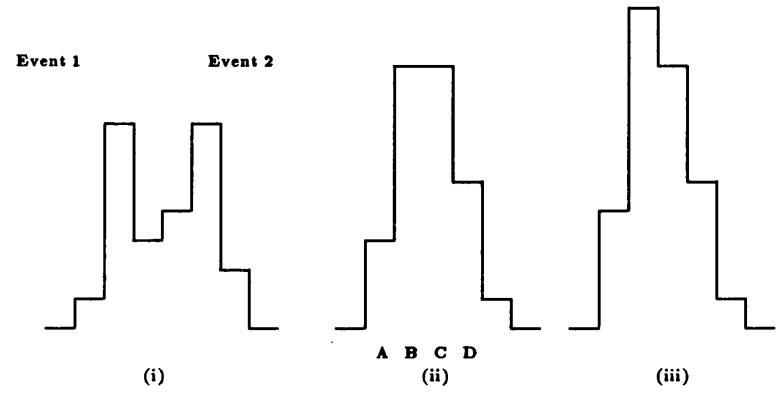

Fig 5.3. Cross section through coincident event profiles

For case (i) the ground based MIC detector, which samples a 5×5 array of pixels around the data peak, can utilize the coincidence correction circuit described in Chapter 2, to improve the centroiding of each event. The XMM-MIC detector uses a 3-pixel algorithm resulting in coincidence information not being available, and would incorrectly centroid both events, tending to bias Event 1 towards the right, and Event 2 towards the left.

For case (ii) the ground based MIC detector centroids the profile as if it were due to a single event, taking the central pixel as either B or C depending upon the data in A and D. The XMM-MIC as previously described in Chapter 2, treats this case by assuming that the event centre is in the left hand pixel (by default) and uses the normal 3-pixel algorithm to centroid the event.

In case (iii) there is no way in which the detector can differentiate between the profile being due to one or multiple events except by energy thresholding (Chapter 4). The event is centroided as if it were caused by a single event, both events being centroided in the same subpixel. [2]

Case (i) illustrates that for events typically having a FWHM of 100μm and covering a 5×5 pixel array on the CCD, the minimum distance that two events can be separated, without changing the profile of the other (as seen by the centroiding electronics) is

1. using the 5-pixel algorithm, 5× CCD pixels, which for a pixel size of 23μm is 115μm.

2. using the 3-pixel algorithm, 4× CCD pixels, which for a pixel size of 23μm is 92μm.

[2]The subpixel may be incremented by two counts if the multiple event recognition is active and the data peak is above the multiple event threshold

It therefore follows that if there is a high probability of two events arriving in the same frame and being separated by a distance of less than 115μm, event coincidence will significantly affect the centroiding resolution.

5.7.1 Simulating The Effect Of Event Coincidence On Centroiding Resolution

In order to show the extent to which event coincidence affects centroiding resolution, the author has carried out a series of computer resolution simulations. These simulations model the response of the centroiding electronics by showing how it would centroid two events which are initially separated by 5 CCD pixels and then brought together in steps of 0.1 CCD pixels. The computer program simulates two asymmetrical gaussian profiles (the shown in **Fig 5.1**) with a given separation (one remaining stationary while the other is moved 0.1 pixels closer each time) and places them into CCD pixel bins. The energy in each CCD pixel is integrated and the resulting event profiles passed to a software version of the appropriate centroiding algorithm. The program calculates the distance from the true event centre to the centre of the subpixel bin into which each event is centroided. The results are presented by showing the centroiding error (in subpixels) against the true event separation.

Three sets of simulations were carried out. They each show the effect of

- the type of centroiding algorithm (3 or 5 pixel) used,
- the subpixel size and event width,
- the coincidence correction circuit

on the centroiding resolution. Simulations were firstly carried out for events having a FWHM of 1.2 CCD pixels, being centroided to $\frac{1}{4}$ of a pixel. Both events were assumed to have the same total energy which was 100 ADU (each). The two events were then bought closer together in steps of 0.1 CCD pixels. Comparisons were made between events which were centroided

- with a 5-pixel centroiding algorithm **Fig 5.4**
- with a 3-pixel centroiding algorithm **Fig 5.5**

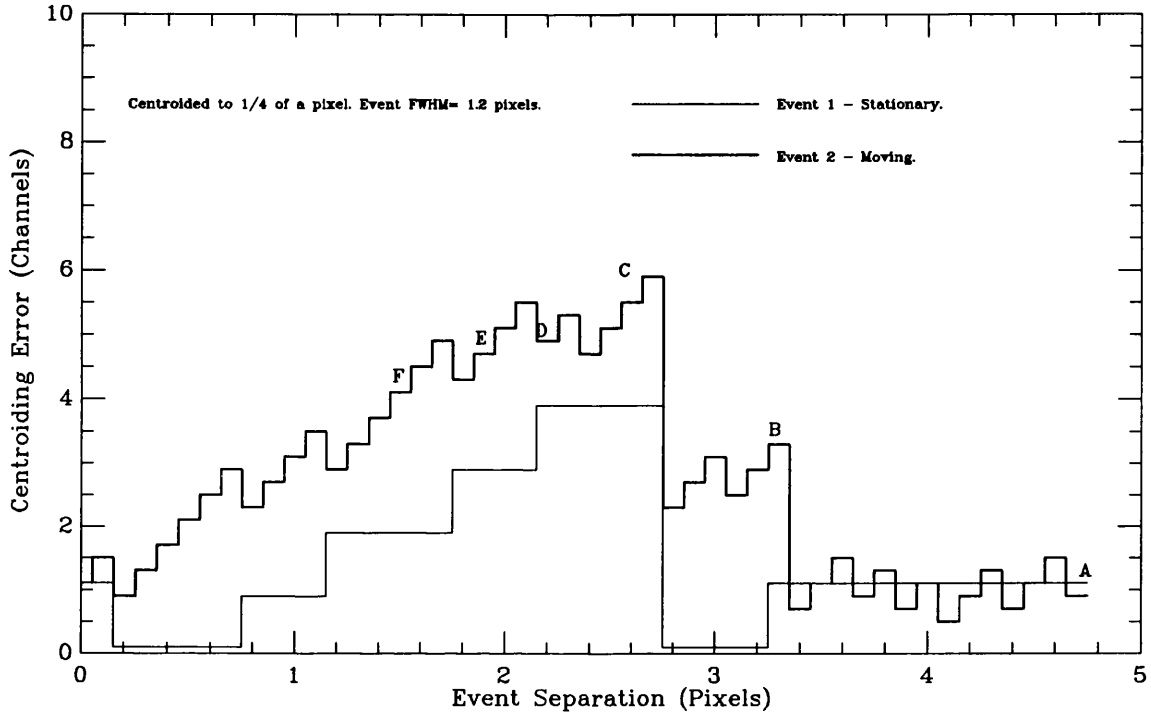

Fig 5.4. Centroiding errors when using a 5-pixel centroiding algorithm

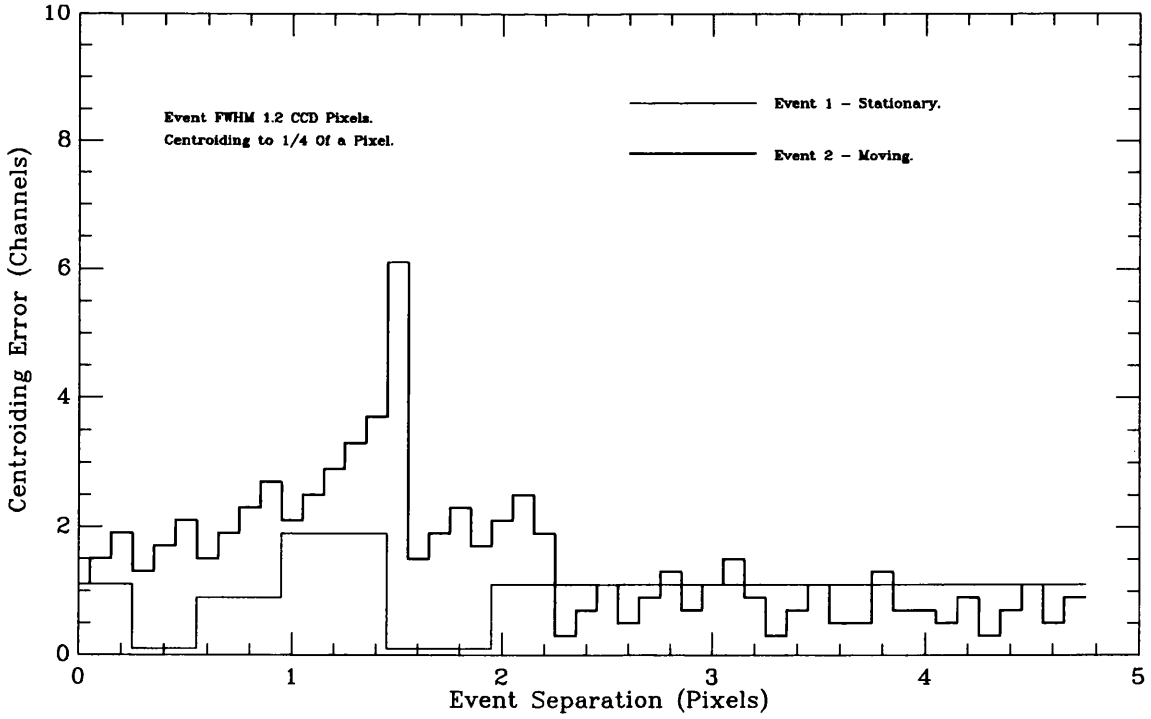

Fig 5.5. Centroiding errors when using a 3-pixel centroiding algorithm

The results of this set of simulations show firstly that the separation at which two events start to affect the centroid position of the other is larger when using the 5-pixel algorithm instead of the 3-pixel algorithm. At separations above 3.3 CCD pixels (for the 5-pixel algorithm) and 2.2 pixels (for the 3-pixel algorithm) the presence of a second event does not affect the subpixel into which the first event is centroided, provided the centroiding resolution is $\leq \frac{1}{4}$ of a CCD pixel. If the centroiding resolution is increased then the event separation at which the profile of one event starts to change the subpixel into which the other event is placed, increases.

Secondly, because the events are asymmetrical, even when they do not overlap (in the region between A and B in **Fig 5.4**) the centroiding error is occasionally greater than $\frac{1}{4}$ of a CCD pixel. This is due to the way in which the energy associated with an event profile is binned into CCD pixels. The centroiding error for both the 3-pixel and the 5-pixel algorithms are very similar in this region of the graph.

Between regions B and F in **Fig 5.4**, where the event profiles are partially but not fully overlapping, the 3-pixel algorithm centroids to a greater accuracy than the 5-pixel algorithm. This is because for partially overlapping events the 5-pixel algorithm samples a high proportion of the data from the other event. The 3-pixel algorithm only samples one pixel either side of the data peak and these pixels contain less of the data associated with the other event. This is why for overlapping events the 3-pixel algorithm is more accurate than the 5-pixel algorithm although when centroiding single events to a high accuracy the 5-pixel algorithm is better.

As the event separation decreases between the region marked F and the point at which events completely overlap the centroiding error associated with both events starts to decrease. At the point when they completely overlap the centroiding accuracy is very close to if not better than 1 subpixel. This is because where one event profile lands directly on top of another, the combined event profile is similar to that of a single event and so these simulations suggest that a narrow point source image would be centroided to a high accuracy.

In conclusion, although the 5-pixel algorithm centroids single events to a higher accuracy than the 3-pixel algorithm, the 3-pixel algorithm is sufficient for centroiding events to $\frac{1}{8}$ of a pixel. If there are a high number of coincidence events the 3-pixel algorithm centroids to a much higher accuracy than the 5-pixel algorithm because the algorithm

samples fewer pixels containing contaminating data from the second event. At the point where the two events completely overlap, the theoretical centroiding error approaches 1 subpixel.

Simulations were then carried out using only a 5-pixel centroiding algorithm and comparisons made between the following cases;

- Events having a FWHM of 1.2 CCD pixels, centroided to $\frac{1}{4}$ of a CCD pixel, **Fig 5.4.**
- Events having a FWHM of 1.4 CCD pixels, centroided to $\frac{1}{2}$ of a CCD pixel, **Fig 5.6.**

These simulations were carried out in an identical fashion to the first set and were intended to observe the affect of event width and subpixel size on the centroiding resolution.

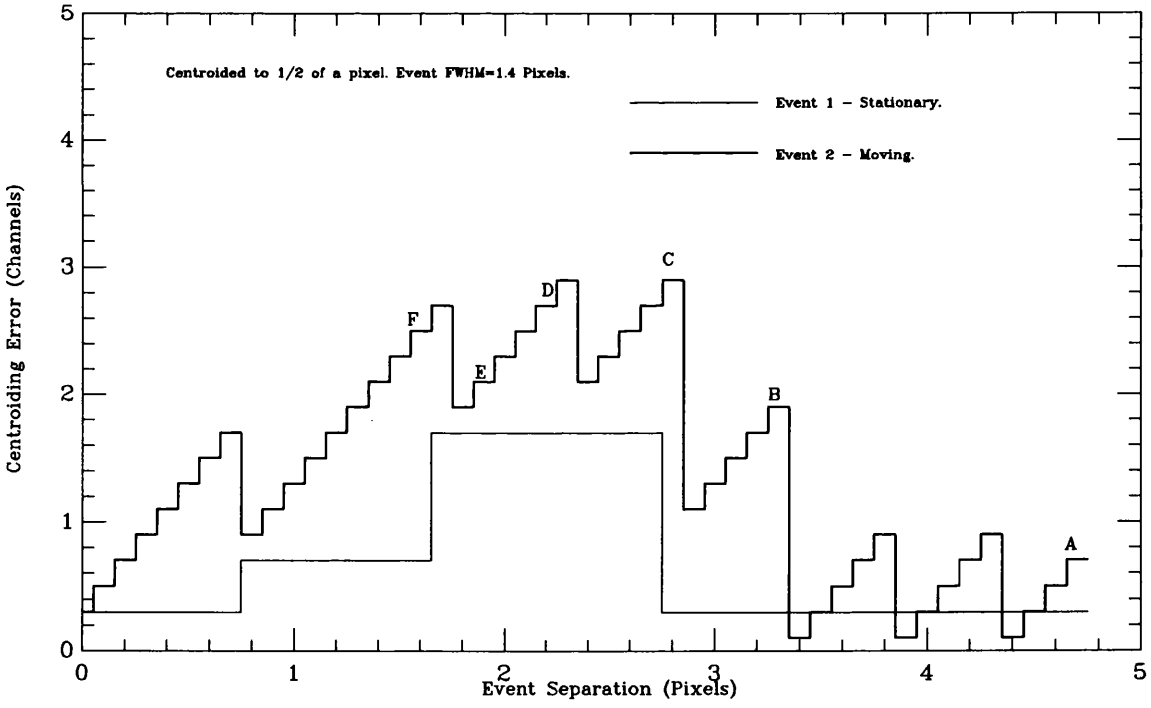

Fig 5.6. Centroiding errors associated with events having a 1.4 CCD pixel FWHM

The results of this second set of simulations show that there is very little difference between centroiding events with a FWHM of 1.4 CCD pixels, and centroiding events with a FWHM of 1.2 CCD pixels. From the simulations carried out by *Dick et al* the ideal event width to which the 5-pixel algorithm is best suited, lies in the region of 1.5-1.75 CCD pixels and so it is expected that events with a FWHM of 1.4 CCD pixels would be

more accurately centroided. This however, only applies to isolated events and so if we only examine the region between A and B then the events with a FWHM of 1.4 CCD pixels were centroided only slightly more accurately than those events whose FWHM were 1.2 CCD pixels.

The most obvious thing to notice about the results of this simulation is that when centroiding single events to an accuracy of $\frac{1}{4}$ a CCD pixel the centroiding error is sometimes > 1 subpixel, but when centroiding to $\frac{1}{2}$ a CCD pixel, the centroiding error for single events never increases above 1 subpixel. This is merely due to the inherent variation in subpixel sampling size. Varying the event width between 1.2 and 1.4 CCD pixels does not change this fact.

In these simulations, where there are no other event distortions apart from the inherent event asymmetry, any fixed pattern noise is due simply to the event asymmetry itself. They suggest that when centroiding to only $\frac{1}{2}$ a CCD pixel, no fixed pattern noise is present. However, in practice a small degree of fixed pattern noise does appear when centroiding to $\frac{1}{2}$ a pixel showing that it is the combined effect of all the event distortions, not just its inherent asymmetry, that affects the real level of fixed pattern noise.

Simulations were then carried out in a similar way as **Figs 5.4** and **5.6** but this time with the coincidence correction circuit (Chapter 2) was enabled.

- **Fig 5.7** shows events having a FWHM of 1.2 CCD pixels, centroided to $\frac{1}{4}$ of a CCD pixel.
- **Fig 5.8** shows events having a FWHM of 1.4 CCD pixels, centroided to $\frac{1}{2}$ of a CCD pixel.

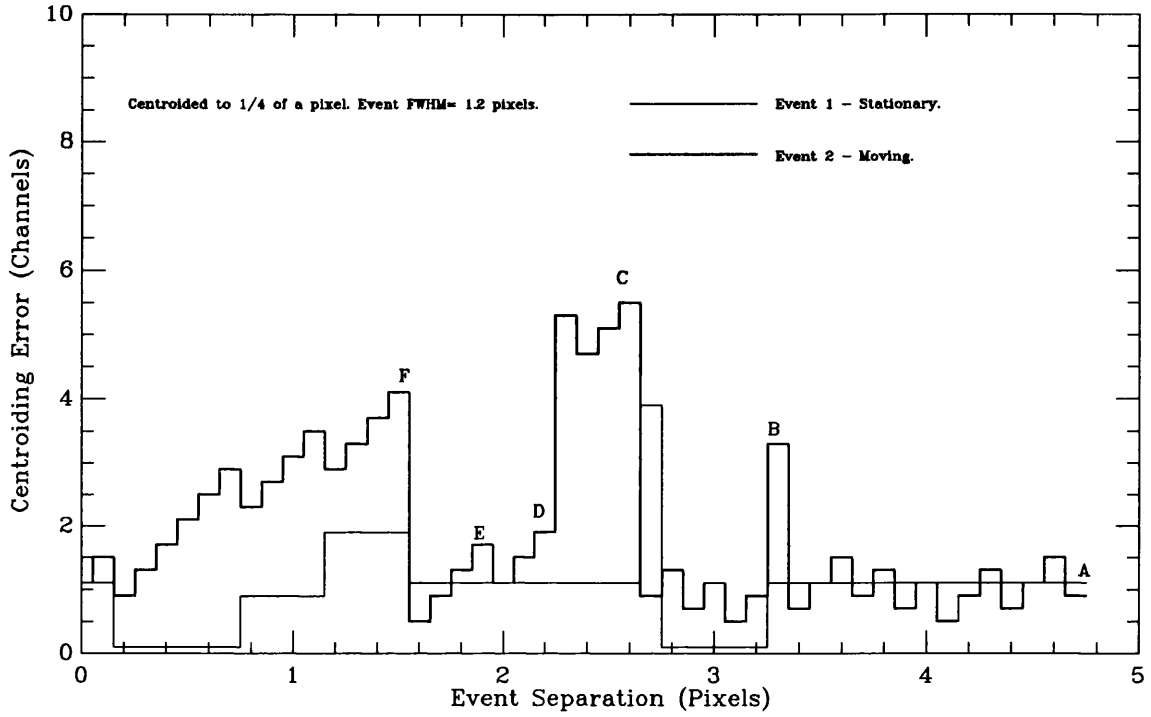

Fig 5.7. Affect of the coincidence correction circuit on centroiding resolution

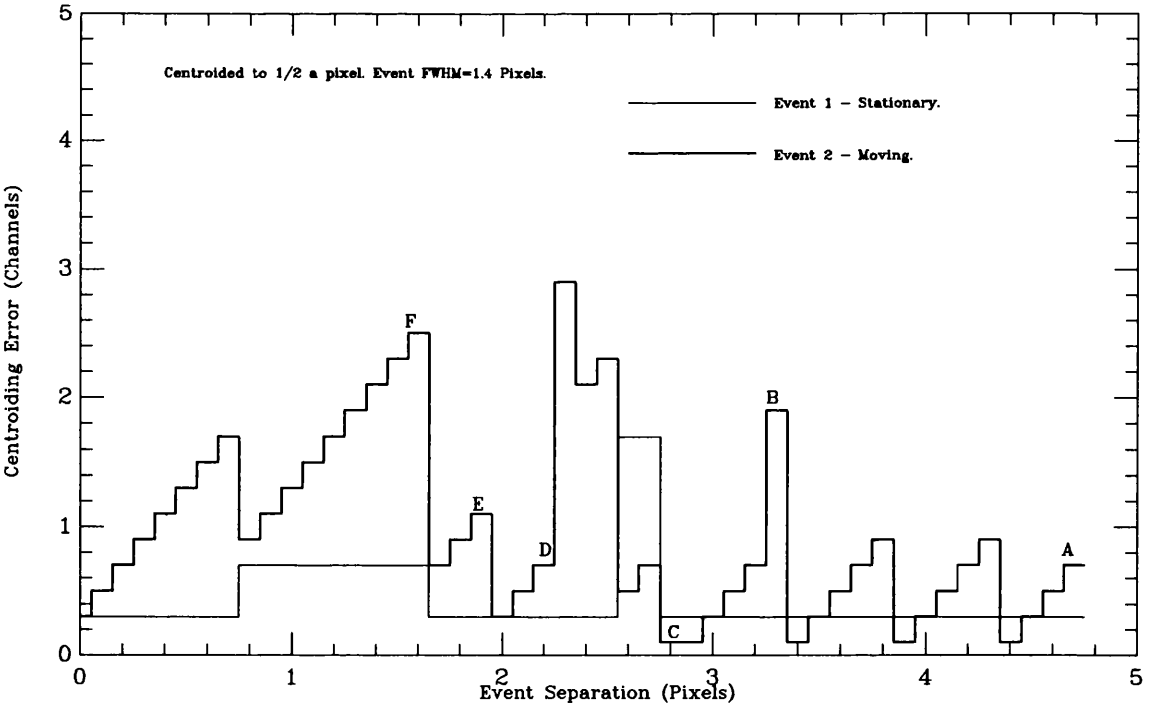

Fig 5.8. Affect of the coincidence correction circuit on centroiding resolution

The differences between **Figs 5.4** and **5.7** and those between **Figs 5.6** and **5.8** are best described by looking at different regions of the plot, where moving from **A** to **F** the second event is getting closer to the first.

1. In the region between **A** and **B** both graphs are very similar because there is no overlap between the two event profiles. The Coincidence Correction circuit is not used at these event separations as the events are not overlapping.

2. Point **B** is an anomalous condition, where due to the asymmetrical nature of the event profile the binned centre of gravity of Event 2 is not even in the same subpixel as the event peak. This leads to large centroiding errors.

3. From **B** to **C** only Event 2 is centroided using the Coincidence Correction, no correction being associated with Event 1. This situation arises when there are 2 pixels between the event peaks.

4. From **C** to **D** a similar situation to **B** arises where the centre of gravity of Event 2 is not in the same subpixel as the event peak, leading to relatively large errors except where the Coincidence Correction is applied.

5. From **D** to **F** Coincidence Correction is applied to both events with consequent improvement in resolution.

6. From point **F** onwards the two events completely overlap and hence the conditions for Coincidence Correction are not fulfilled.

These simulations show that the Coincidence Correction circuit is of great importance for optimum resolution where there is a high likelihood of resolved coincidences occurring. Such situations could, for example, occur when observing extended sources or point sources which are very close together. For both sets of simulations it can be seen that where Coincidence Correction is applied (primarily between **B** and **C** and between **D** and **F**) there is a large improvement in centroiding accuracy, typically greater than 2 subpixels.

5.8 Input Image FWHM

Not only is the output image size dependent upon the detector resolution, but also on the input image FWHM. For large images (ones whose FWHM are >> the centre to centre MCP pore spacing), the output image size is proportional to the input image size. In practical ground based astronomy a stars' FWHM is limited by the seeing, provided that the telescope optics are correctly focused onto the detector front end. This is not so for observations taken from a Space platform where a star is seen by the telescope as a point source. The stars' FWHM should then be equal to the convolution of the detector resolution with a delta function. In practice however, tracking errors, telescope optical aberrations and light scattered in the intensifier input window, contribute to a spread in the image size. The FWHM of a star imaged with the XMM-OM is expected to be 10-20 μm at the detector front end, with additional image distortion associated with rolling and tracking errors. This size is small compared to the front channel plate pore spacing of the present 25 and 40mm diameter image tubes and so if the same channel plates are used in the XMM-OM mission, the overall resolution is expected to be detector limited.

In order to experimentally determine the detector resolution, the input image FWHM has to be small compared to the intensifier pore spacing in order that the spread in event position be due simply to components of the detector. The smallest input image size obtained in the laboratory is 5μm FWHM, ideal for resolution testing.

5.9 Measurement Of Detector Resolution

5.9.1 Point Source Laboratory Data

An experiment was carried out in the laboratory in order to estimate the detector resolution from the FWHM of a narrow point source image. The experiment involved imaging a point source (green light) illumination for different positions of the point source with respect to the intensifier. The point source which had a FWHM of 5.7μm at the intensifier, was moved sideways across its face in small steps between successive integrations. The experiment was carried out at very low count rates so that coincidence losses were not responsible for any small changes in the profile. **Fig 5.9** shows a cross section through the image at each of these positions.

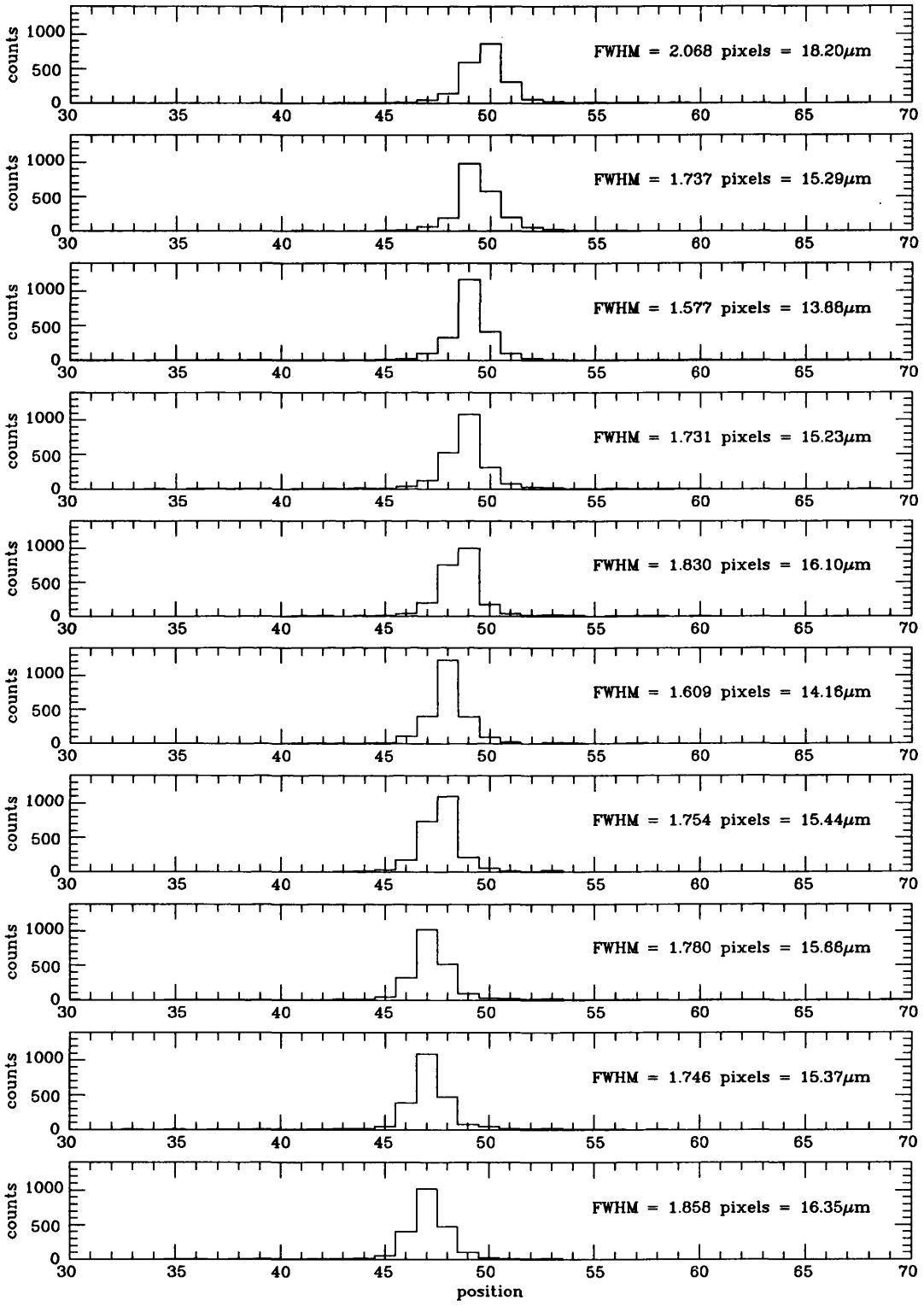

Fig 5.9. The effect of channel plate pore structure on detector resolution

As the input image was moved small distances across the detector fluctuations in the detector resolution produced output images whose FWHM varied between 13.9μm and

23μm. The variation in detector resolution with image position is due to the input image sampling the front channel plate pore structure. In the case where the best resolution is observed nearly all the photoelectrons from the input image travel down a single front channel plate pore.

In the case where the worst resolution is observed (**Fig 5.10**), the input image is centred on the inter-pore gap between three pores and hence photoelectrons have an almost equal probability of traveling down either one of the three. This is likely to give rise to an output image possessing a 'top hat' profile, with approximately equal numbers of events being centroided into three neighbouring channels.

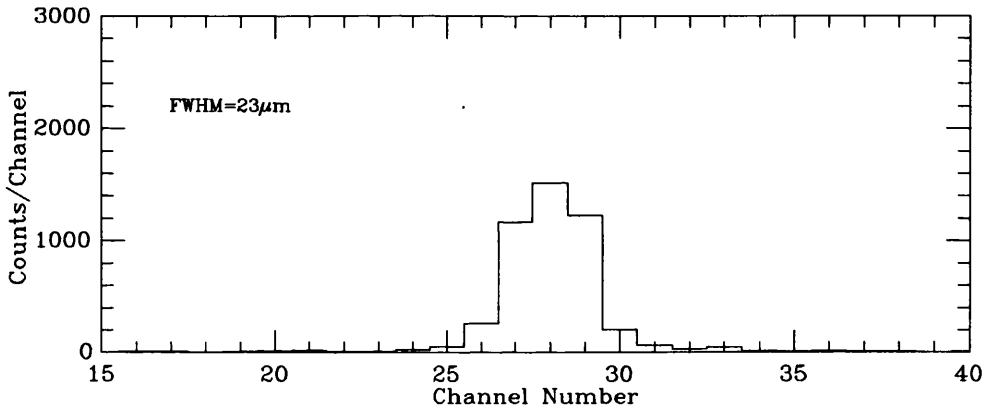

Fig 5.10. Output profile of an input image that spans three front channel plate pores

The variation in image FWHM is seen most clearly if the centroiding accuracy is higher than the resolution of the intensifier. If the centroiding resolution is increased further, the pores become even better sampled and are eventually resolved. This has been done by *Carter* [1] using a similar system to MIC.

5.9.2 Point Source Astronomical Data

The first field trials undertaken by the MIC detector were carried out at the AAT. Because of poor weather conditions very little astronomical observing was carried out. However, the detector resolution was tested by observing CuAr arc lines using the 82cm RGO spectrograph. The detector was firstly focused and then the dispersion axis aligned with a CCD pixel row in order that, should the spectra be binned perpendicular to the dispersion axis, it would not affect the spectral line widths. Images of the arc lines were taken using

a centroiding accuracy of $\frac{1}{8}$ of a pixel in the dispersion direction. One such spectrum is shown in **Fig 5.11** and a list of all the line FWHM for lines whose peaks are above 1000 counts are given in **Table 5.2.**

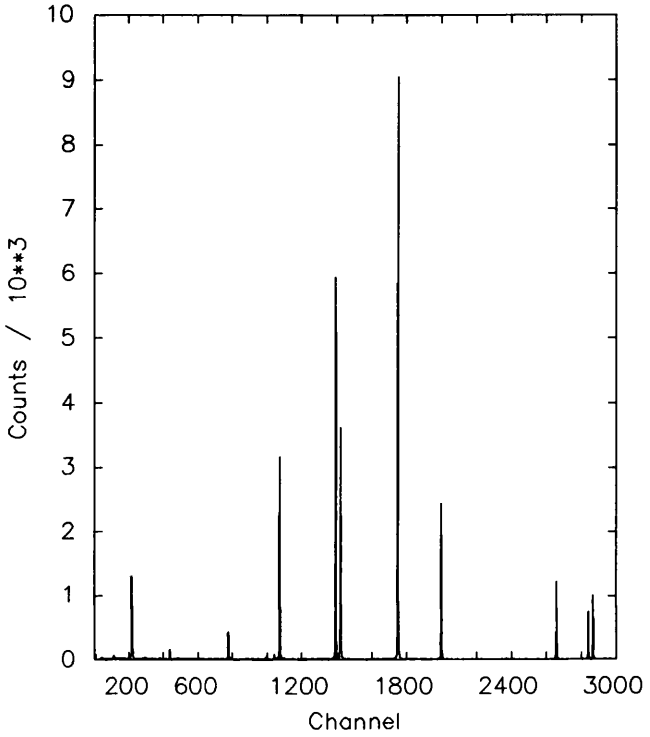

Fig 5.11. Image of a CuAr arc taken with the MIC detector

Line Number	Centroid Position (Subpixels)	Line Peak Intensity (Counts/subpixel/sec)	Line FWHM (μm)	Measured Detector Resolution (μm)
1	218.6	0.22	33.1	32.9
2	1073.5	0.55	16.5	16.2
3	1394.3	0.99	21.5	21.3
4	1423.4	0.60	22.8	22.6
5	1751.6	1.46	20.2	20.0
6	2000.3	0.38	27.6	27.4
7	2657.7	0.17	18.0	17.7

Table 5.1 Arc line FWHM

The average FWHM of arc lines listed in **Table 5.1** is 22.8μm which is a measure of the combined spectrograph and detector resolutions. By deconvolving the intrinsic arc line FWHM produced by the spectrograph and that produced by the detector, a measure of

the detector resolution can be made. The intrinsic spectrographic line FWHM at the input to the 82cm camera over this wavelength range is $\sim$ 3μm and so the average measured detector resolution is 22.7μm and the best measured resolution is 16.2μm.

In these tests the MIC detector used a 40mm intensifier having a front gap of 200μm across which 300V was applied. The intensifier front channel plate pore to pore spacing was 15μm and because the spectral lines were observed in the near infrared, the value of ϵ (*Equ 5.4*) was $\sim$ 0.04. The theoretical resolution of the MIC detector in this particular case is therefore 17.3μm assuming a detector centroiding resolution of 4.2μm.

The measured resolution of MIC taken from an average of seven arc line FWHM is some 5 μm worse than that predicted by *Equ 5.1*. This could be due to;

- The detector not being perfectly in focus across the whole of the detector.
- Errors in the value for ϵ (*Equ 5.4*) which is very dependent upon the composition of each individual photocathode.
- Arc lines not being centred on the front channel plate inter-pore gaps, different events associated with the same arc line traveling down more than one pore (as explained above).

Most of the arc line FWHM are close to that predicted by theory but a couple of lines have FWHM much greater than predicted and one has a FWHM smaller than that predicted. These observations can be explained from the results of the previous experiment where the detector resolution was found to be a function of object position with respect to the front channel plate pores.

5.9.3 The Affect Of Coincident Events On Resolution

The Affect Of Completely Overlapping Events On Resolution

Results of the simulations presented in Section 5.7.1 where the affect of event coincidence on resolution is given, predict that coincidences between very narrowly separated objects (i.e. nearly lying on top of each other) do not reduce the detector resolution. It therefore follows that changes in the count rate (and hence the number of coincidences) of a *single* point source object should not change its output FWHM i.e. should not reduce the detector resolution.

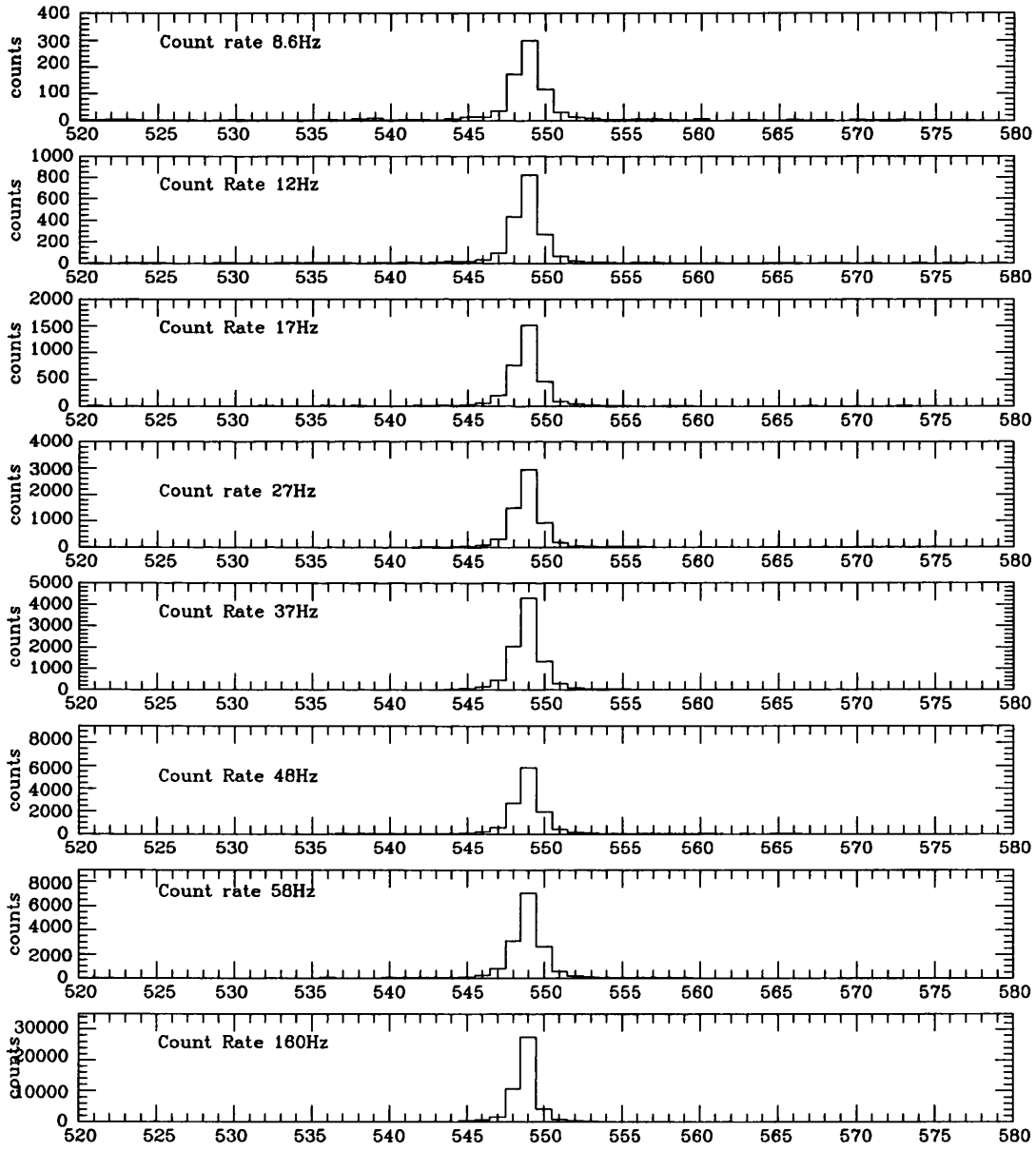

Fig 5.12. Profile of a 6μm point source image at different illumination intensities

An experiment was carried out in order to examine the way in which the profile of a point source image changed as its illumination intensity increased. As the image brightness

increases, so does the number of coincident events, all of which lie directly on top of each other. **Fig 5.12** shows the profile of a 6μm point source whose intensity is given in each of the 8 diagrams.

The CCD frame time was 12ms during the experiment and each event was centroided to $\frac{1}{8}$ of a CCD pixel. Examination of each of the 8 profiles shows that there is little difference between each of them even though the count rate has increased by a factor of 20. The results confirm that coincident events arriving directly on top of one another do not create a combined profile very different from that of a single event, otherwise the point source image profile would change dramatically as the count rate increased.

The Affect Of Partially Overlapping Events On Resolution

The simulations presented in Section 5.7.1 also predict that for events which only partially overlap, coincidences between them can contribute to a loss of detector resolution. In order to confirm this another experiment was carried out in the laboratory. Two pinholes separated by 90μm (at the intensifier) were illuminated with various light intensities using ND filters. Images of the pinholes were taken with XMM-MIC in order to observe any variation in the pinhole profiles as the light intensity through each was increased. Events were centroided to $\frac{1}{8}$ of a CCD pixel and then plots made of the count distribution. Although, for very low illumination intensities, very long integrations were taken to obtain good count statistics, each diagram represents data taken during the equivalent of a 100 second integration. Diagrams **A,B,C** and **D** in **Fig 5.13** show contour maps of the pinhole profiles for peak intensities of $\sim$ 15,13,4 and 3 counts/pinhole/second.

Fig 5.13A shows that there is a significant distortion in the profile of each pinhole at high count rates, when compared to **Fig 5.13D** taken with a low count rate. As the number of coincidences increases, a 'bridge' forms between the two objects and their profiles become elongated along the axis which joins them. When coincidences between events in different pinholes become more likely (with increasing count rate), the bridge makes up a higher percentage of the total number of counts from both pinholes.

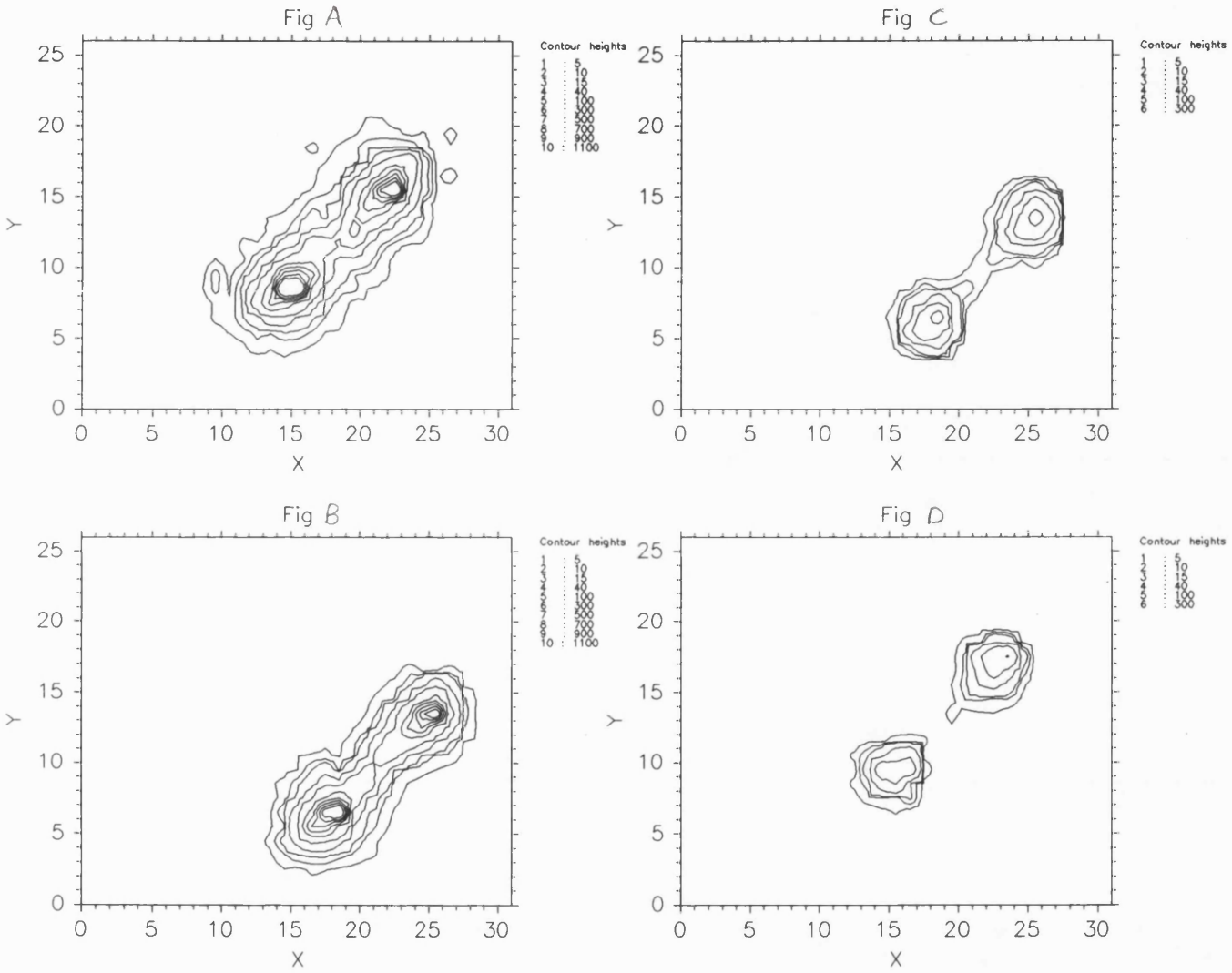

Fig 5.13. The count distribution for two pinholes, each set having a different illumination intensity

The bridge between pinholes in **Fig 5.13B** has a height of very close to 100 counts (as indicated by the contour representing 100 counts, crossing over in the centre of the bridge). This is close to 9% of the peak height of each pinhole which in the case of **Fig 5.13B** is $\sim$ 1100 counts.

This level of bridging ties up well with the predicted number of coincidence events that should be taking place. The two pinholes between them contribute 2 x 13 = 26 counts/second of which ~9% of these are spatially coincident with each other (and hence form the bridge). The dynamic range curve in **Fig 4.11** shows that for a CCD frame time of 12ms (the same as used in these pinhole experiments) 10% coincidence takes place at 25 counts/sec which is just higher but very close to the level of coincidence seen in the pinhole experiment. The reason why the bridge height is lower than that predicted by the dynamic range curves is that not all coincidences will take place between events in different pinholes. Some will take place between events associated with the same pinhole.

This 'bridging' effect does not cause much of a problem for objects of similar intensity because the signal in each object is still high compared to that in the 'bridge'. However, for two objects of vastly different intensities where most of the events in the low intensity object are coincident with those from the high intensity object, the centroiding resolution associated with the low intensity object markedly decreases.

5.9.4 The Affect Of SIB On Resolution

The presence of SIB was found in a 25mm MCP intensifier during an attempt to measure the centroiding resolution of the MIC detector. The experiment consisted of projecting a demagnified 25μm pinhole onto the intensifier and measuring the SD of the resulting pinhole image whilst applying several different voltages across the intensifier front gap. At the time of the experiment the size of the intensifier front gap was not known, but was calculated from the results. The experiment was based around an extension of *Equ 5.1* which predicts the width of the intensifier output profile to be;

$$\text{SD Of The Output Profile} = \sqrt{a^2 + b^2 + c^2 + d^2} \tag{5.6}$$

where

- **a** is the intensifier front gap resolution $3.3.L.\sqrt{\frac{\epsilon}{V}}$ and where ϵ is assumed to be 0.1 as a near monochromatic green pinhole illumination was used.
- **b** is the front channel plate pore spacing.
- **c** is the electronic centroiding resolution.
- **d**, is the SD of the pinholes' input profile.

Because, in *Equ 5.6*, **b**,**c** and **d** are constants, together with **L** and ϵ in *Equ 5.5*, we can rewrite *Equ 5.6* as;

$$\text{SD of Output Profile} = \sqrt{K + \frac{k}{V}} \tag{5.7}$$

where $k=3.3^2.L^2.\epsilon$

and $K=a^2+c^2+d^2$

The pinhole image FWHM was found for different intensifier front gap voltages, and K and L found by changing their values until a least squared fit to the data was obtained. **Fig 5.14** shows a plot of the output profile SD (in CCD pixels), against the intensifier front gap voltage (V).

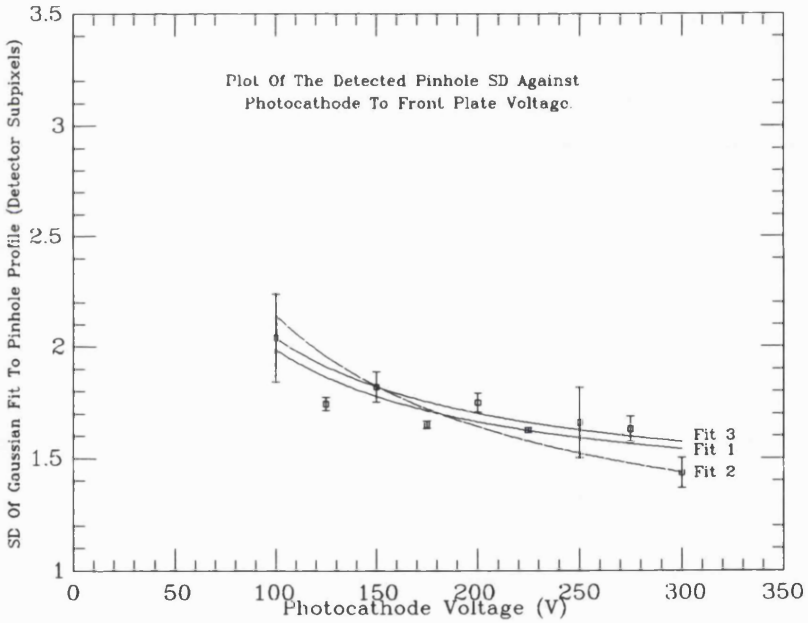

Fig 5.14. Change in the image profile SD for different intensifier front gap voltages

Three least squared fits were made to the experimental data, one of which was forced to pass directly through the first point on the graph and one which was forced to pass through the last point on the graph (to get an estimate of the fitting error), and finally a least squared fit to all the data. The results of each of these fits are shown in **Table 5.2** together with the values of **K** and **L** used in fitting the experimental data.

Line Fit	Calculated Front Gap Distance (μ)	Value Of K (μ^2)	Best Estimate Of Centroiding Resolution (μ)
1	310	$6.86*10^{-10}$	23.1
2	380	$3.72*10^{-10}$	14.9
3 (Best Fit)	300	$6.55*10^{-10}$	22.5

Table 5.2. Three estimates of the electronic centroiding resolution

An estimate of the centroiding resolution was then made from knowing the value of the input image SD **d**= ($\frac{25}{4.4 \times 2.35}\mu$m) and the pore spacing, **b** = (12μm).

The results of this experiment showed that so long as the front gap voltage was kept close to 300V (its normal operating potential), the centroiding resolution was by far the largest contribution to the overall detector resolution. The detector resolution was previously thought to be limited by the front MCP pore spacing while the centroiding resolution was thought to be closer to a value of 5μm. These experimental results appeared to show this assumption to be untrue for this 25mm intensifier, the centroiding resolution being closer to 22μm.

In the course of trying to explain why the centroiding resolution was so high, event profiles from the intensifier output phosphor were examined using a 1:1 fibre coupling the CCD and intensifier. Snap frames of the events showed the presence of low energy, secondary events clustering around that of the central main event. These were SIB events caused by the insufficient scrubbing of the MCPs during the manufacturing process. The effect of SIB events is to randomly change the primary event width so that the centroiding algorithm does not fit the event profile which is placed into the wrong subpixel, greatly decreasing the centroiding resolution. The experiment shows how the presence of SIB adversely affects the centroiding resolution and why intensifiers with SIB should not be used for high resolution observations. Results from a similar experiment, carried out with a 40mm intensifier tube having no SIB, show that the true centroiding resolution is $\sim$ 4.2μm.

5.10 Summary

The results of these experiments lead us into asking, how we should define the resolution of MIC ? If it is done in terms of image FWHM then the resolution varies depending upon

the image position with respect to the front channel plate pores. Instead, the resolution must be defined in terms of the minimum separation two images require in order for them to be resolved on the output. In the worst case (**Fig 5.10**) where the input image spans three pores, the two images have to be four channels apart in order to resolve them. As each channel is 8.8μm in width their minimum separation must be 35.2μm apart. This means that for this detector configuration, the resolution is $\frac{35.2}{2} = 17.6\mu$m.

If, for reasons mentioned in Chapter 6, future versions of the MIC detector employ similar types of intensifier but whose MCP pores have, for example, diameters of 6μm and spacings of 7.5μm, the detector resolution will increase. If we now calculate the theoretical resolution of this intensifier, using *Equ 5.4* but making the channel plate pore resolution 7.5μm instead of 15μm, the intensifier resolution is predicted to be 14.2μm for green light. The intensifier front gap resolution will then be by far the most dominant factor in determining the overall intensifier resolution and as a result, the degree to which the intensifier resolution will change with image position will decrease. Therefore it follows that the average point source FWHM will be 14.8μm or 1.7 channels if the centroiding resolution is 4.2μm, where individual line widths will not vary much from this figure. Two events could then be resolved if they are three channels apart resulting in an overall detector resolution of $\sim$ 15μm.

The detector resolution can decrease if, for some reason, the event profile is distorted. Event distortions can take place for one of many reasons, because of; a non-zero rear channel plate bias angle; the presence of SIB; fibre taper distortions; CCD charge transfer inefficiencies; the presence of 'hot' CCD pixels, CCD readout noise, DC bias on the CCD and finally QE variations between CCD pixels. Potentially the most common type of event distortion occurs due to event coincidence especially for events whose profiles only partially overlap as this alters the shape of each profile the most, making it very asymmetrical. If events are totally overlapping the effect of coincidence is much less, so coincidences between events deriving from the same point source do not affect the image profile.

The resolution simulations showed that for events which almost completely overlap, the combined profile of both events is similar to that of each individual event which is why the centroiding error is very low. This suggests that a high point source illumination can be centroided to a high accuracy despite there being a high proportion of coincident events because any events that are coincident lie directly on top of one another.

Chapter 6

Image Quality

6.1 Introduction

There are a number of artifacts associated with the MIC detector which contribute towards a reduction in image quality. These include fixed pattern noise, aliasing, photocathode defects, fibre taper distortions and defects associated with the CCD camera. Of these, all except fixed pattern noise, are reproducable and can be removed by flat fielding. However, fixed pattern noise is data rate dependent, as shown in Section 6.2.

6.2 Fixed Pattern Noise

A description of how a mismatch between the event profile and the centroid algorithm produces fixed pattern noise is given in Chapter 3. If fixed pattern noise is not corrected for, it can produce serious degradation in the image quality by superimposing a count modulation (whose period is 1 CCD pixel) on top of the image. One way of reducing the degree of fixed pattern noise in an image is to divide it by an image of a flat field illumination which also suffers from the same degree of fixed pattern noise.

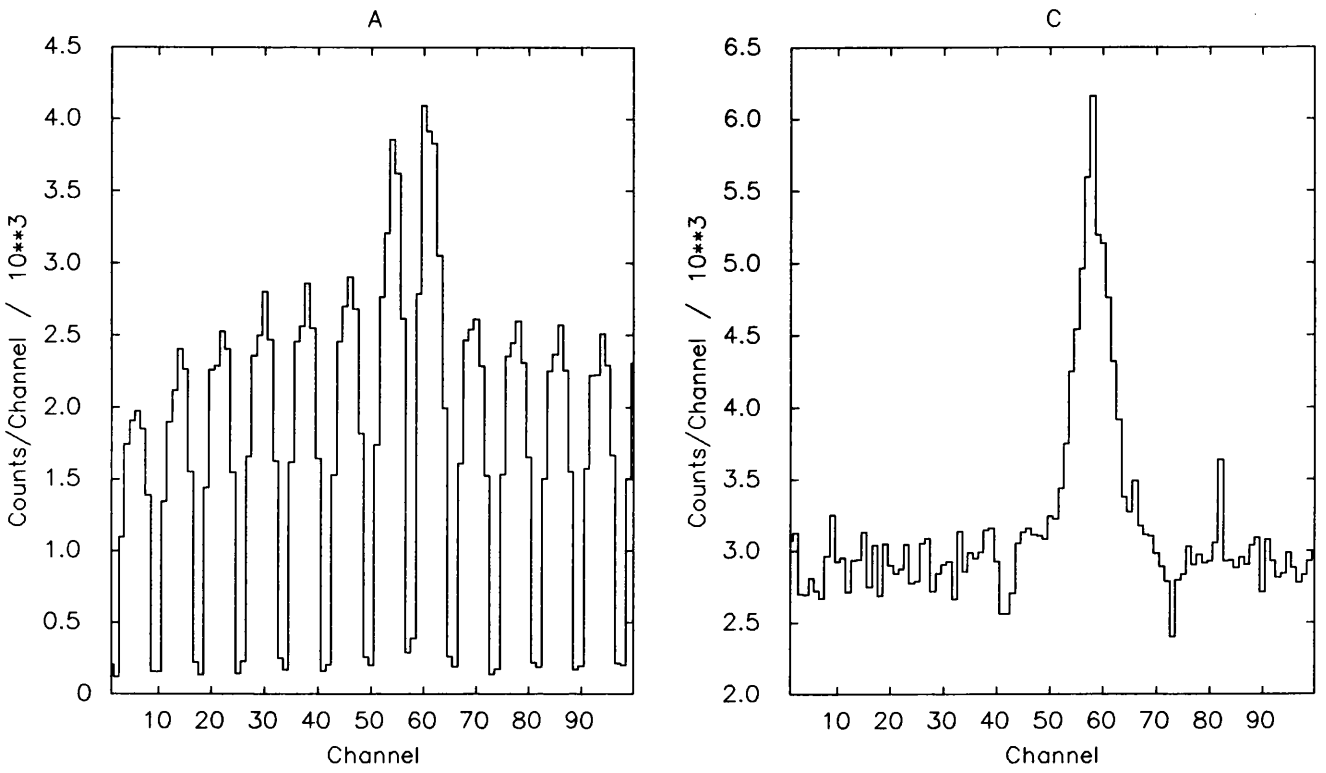

Fig 6.1. Pinhole profile with fixed pattern noise (A) and with the fixed pattern noise divided out (C)

The fixed pattern noise is then simply divided out. An example is shown in **Fig 6.1** for the image of a pinhole, where **Fig 6.1A** shows the cross section through a pinhole image with a faint background illumination, and **Fig 6.1C** shows an image of the same pinhole divided by an image of only the background illumination. Even after this method of correction, the effect of fixed pattern noise is still very noticeable due to an insufficient number of counts/subpixel with which to average over. Ideally, the affect of fixed pattern noise should be minimized at source.

The MIC detector reduces fixed pattern noise by changing the size of each subpixel in software such that the mismatch between event profiles and the centroiding algorithm is corrected for (Chapter 3). However, if the event width changes for any reason, the fixed pattern correction no longer applies and fixed pattern noise is re-introduced. So if there is a change in the number of coincident events for example, the average event profile changes and the level of fixed pattern noise increases.

6.2.1 Fixed Pattern Noise Analysis

An analysis of fixed pattern noise **vs** count rate was made by the author in order to more closely understand the relationship between fixed pattern noise and the rate of event coincidence loss. An experiment was carried out on the ground based detector using two CCD formats, one of size 384×256 CCD pixels, and the other with 384×64 CCD pixels, each event being centroided to $\frac{1}{8}$ of a CCD pixel. The analysis involved firstly carrying out a fixed pattern correction on a flat field image, in which an ND filter was placed between the source and detector. The level of fixed pattern noise was then measured in a fixed central region of the detector for different illumination intensities, by changing the ND filter. The number of events in each subpixel were summed and then divided by the total number of counts in all subpixels to find the fraction of events/subpixel for each subpixel (where for a perfect flat field, each subpixel would contain $\frac{1}{8}$ of the total number of counts). For each illumination intensity the sum of these fractional deviations were then summed over all eight subpixels to represent the deviation of the image from a flat field.

Fig 6.2 shows the results from using a 384×256 CCD pixel format (frame time 12ms), where the sum of all the subpixel count deviations from the mean is plotted against flat field intensity.

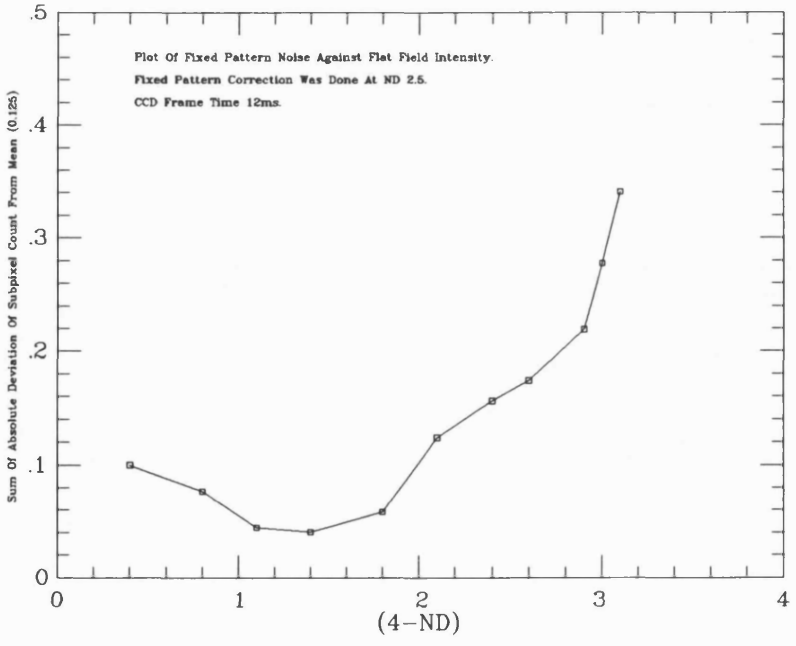

Fig 6.2. Sum of the fractional subpixel count deviations from the mean for different illumination intensities. Frame time 12ms.

The graph shows that for flat field intensities lower than those at which the fixed pattern correction was made (ND 2.6), the fixed pattern noise becomes slowly worse. This occurs mainly in two out of the eight subpixels. At ND 2.6, as expected, each subpixel has close to $\frac{1}{8}$ the total number of counts and so the subpixel count deviation is a minimum at this point on the graph. It then deviates rapidly from this at higher intensities.

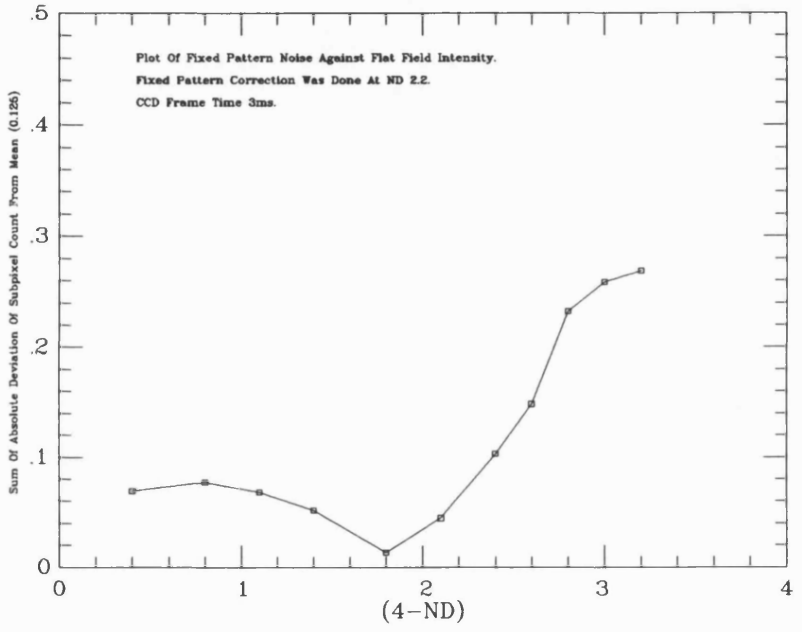

Fig 6.3. Sum of the fractional subpixel count from the mean for different illumination intensities. Frame time 3ms.

Fig 6.3 is the result of a similar experiment, this time using a 384×64 CCD pixel format. With this format, the fixed pattern correction was carried out at ND 2.2 and hence the minimum in the graph at this point. For intensities lower than that corresponding to ND 2.2, the curve is very similar to the one obtained with the 384×256 CCD pixel format, which has a longer frame time. However, at first glance the curves appear dissimilar in the region of the graph corresponding to very high count rates.

In order to try and explain the way in which fixed pattern noise changes with count rate we must firstly examine whether the observed changes are consistent for different CCD frame times. In order to directly compare the curves shown in **Figs 6.2** and **6.3**, we need to convert the x-axis to Counts/Pixel/Frame as this quantity determines the number of coincident events that occur. These curves are shown in **Fig 6.4**.

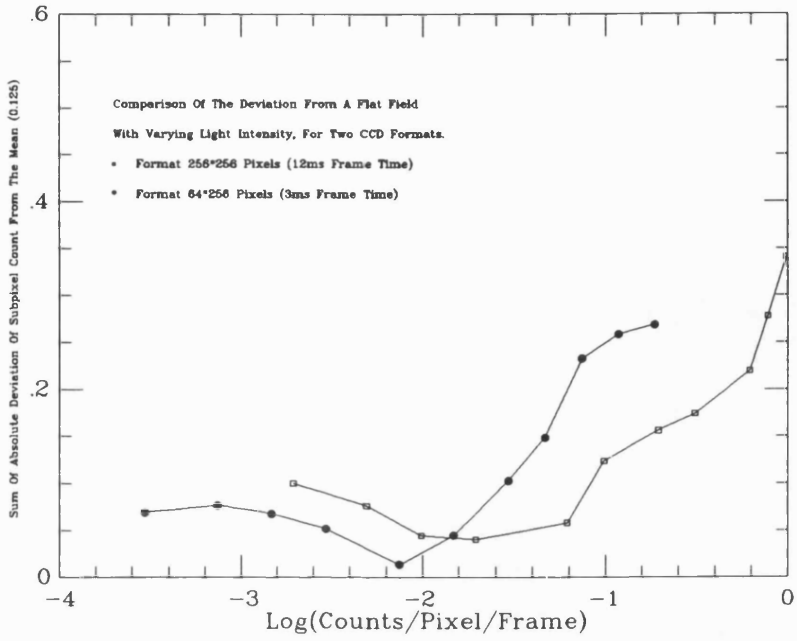

Fig 6.4. Variation in fixed pattern noise with the level of event coincidence

The shape of both curves is similar except that, because the fixed pattern corrections were carried out at different illumination intensities, there is an offset along the x-axis. The shape of the curves can be explained by dividing them into two sections, one in which the intensity is below that at which the fixed pattern correction was carried out (1), and the other in which the intensity is above that at which the fixed pattern correction was carried out (2).

1. The shape of the curves in this region can be explained by the fact that for both formats, the fixed pattern correction has been carried out at a low count rate (0.03 counts/CCD pixel/frame for the 256×256 CCD pixel format, and 0.007 counts/CCD pixel/frame for the 256×64 CCD pixel format). At these count rates there are very few coincidences taking place. As the count rate decreases further, the change in the rate at which coincidences take place (and hence the average event profile changes) varies slowly. This explains why, as the illumination intensity decreases, the fixed pattern noise increases but only at a slow rate. When eventually, at $\sim 5\times10^{-4}$ counts/pixel/frame no further decrease in the number of coincident events is detected, the curve levels off and no further increase in fixed pattern noise occurs.

2. The level of fixed pattern noise at higher count rates tends to increase quickly first of all, then slow down, and finally for very high count rates, increase at a high rate again.

   At first, fixed pattern noise increases rapidly as the number of coincidences between two events increases. At higher light intensities the fixed pattern noise continues to increase, but at a lower rate than before. At these intensities, there are still a large number of non-coincident events, but there are also an increasing number of coincidences between groups of three or more events. The event profiles caused by coincident groups of three or more events are not significantly different from those between groups of only two coincident events. In addition, because there are coincidences between increasing numbers of events in a group, only one peak in the data may be associated with large numbers of coincident events. This means that the number of single events becomes a higher proportion of the total number of events detected and therefore the average event profile changes at a slower rate than before.

   For intensities approaching 1 count/pixel/frame saturation is reached, where virtually every event counted is in a coincident group of three or more individual events. At this point the number of events detected actually decreases as the illumination intensity increases. Not only is the effective width of every event in a coincident group increasing, but the number of detected single events is decreasing. The rate at which the level of fixed pattern noise occurs is therefore increased further.

These results indicate that the change in fixed pattern noise due to a variation in the number of coincident events, is dictated by a change in the number of counts/pixel/frame, not simply the count rate/pixel. They also indicate the necessity of doing the fixed pattern correction with a flat field intensity close to that expected from the object being observed, and that if the frame time is changed between exposures of the same object, another fixed pattern correction should preferably be done. During the XMM-OM mission, MIC is expected to be exposed to a likely background count rate of 1×10^5 counts/second over the full 256×256 pixels of the CCD camera. If we were to apply these results to the XMM mission, then we would expect on average 0.018 counts/pixel/frame background counts incident on 256^2 pixels of the CCD. If the fixed pattern noise is corrected at this count rate, we would expect the count rate dependency to lie between the two curves in **Fig 6.4** as

one curve represents a fixed pattern correction carried out with 0.007 counts/pixel/frame and the other represents a fixed pattern correction carried out at 0.03 counts/pixel/frame.

6.3 Aliasing

In theory, there is no reason why events could not be centroided to a much greater accuracy than $\frac{1}{8}$ of a CCD pixel, for example, by centroiding to $\frac{1}{64}$ of a CCD pixel. But centroiding an event to a much greater accuracy than the resolution of the image intensifier gives us no additional information about the position of the original photon event. Instead, if the centroiding resolution is too high the CCD camera samples the front channel plate pore structure and the detector resolution remains limited by the pore to pore spacing of the front MCP and the intensifier front gap [*Carter* [2]].

This affect is called *aliasing* and can be seen directly when the intensifier is illuminated with an extended image, like a flat field, as opposed to a point source. Aliasing is similar to Moire fringing which is caused by sampling the hexagonally packed pore structure of the intensifier front MCP with square pixels. It can be explained by considering an extended or flat field image as a series of point sources packed in an hexagonal array whose centroids are one pore spacing apart (as each is effectively a point source derived from a single pore).

The smallest FWHM of a point source image that can be obtained with the MIC detector is $\sim 13\mu$m, as shown in **Fig 5.9**. This relates to nearly all the point source primary photoelectrons going down a single, front channel plate pore. When an extended source is sampled, this subtends to a number of hexagonally packed pores which are then sampled by the 8.8μm pixels as is illustrated in **Fig 6.5**.

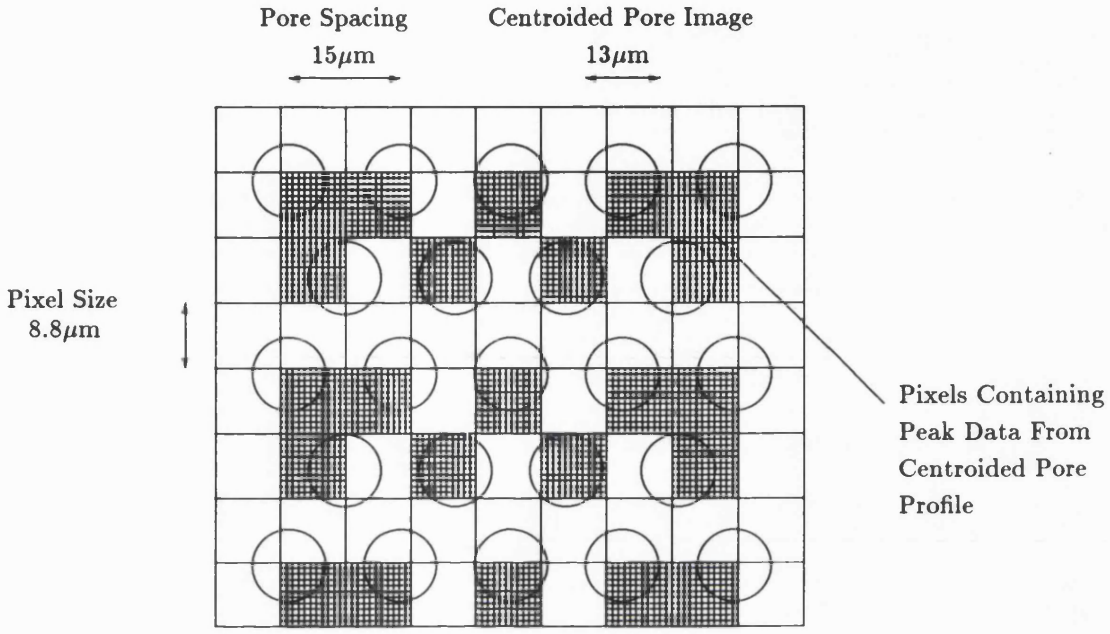

Fig 6.5. Schematic of how the channel plate pores are sampled by the centroiding electronics

This diagram shows the centroided pore structure superimposed on 8.8μm pixels, where the hashed pixels are those containing the peak data from each pore. Because the pixel size is small compared to the pore spacing, some pixels have low numbers of counts whereas others have high numbers of counts, introducing an aliasing whose form is dependent upon the orientation of the pores with the CCD.

6.3.1 The Degree To Which Aliasing Affects The MIC Detector

In order to quantify the degree to which aliasing is taking place with the XMM-MIC detector, a long flat field image was acquired in order to analyse any patterning which might be taking place. The total duration of the integration was 157000 secs and a low count rate of 0.15 counts/pixel/sec was used in order to minimize the affects of coincidence.

The maximum 256×256 CCD pixel format was used for data acquisition, and the events were centroided to $\frac{1}{8}$ of a CCD pixel, giving a format of 2048×2048 pixels and a pixel size of 8.8μm. Any low level fixed pattern noise was removed by dividing the image by an average through the fixed pattern, in both x and y to produce **Fig 6.6a**.

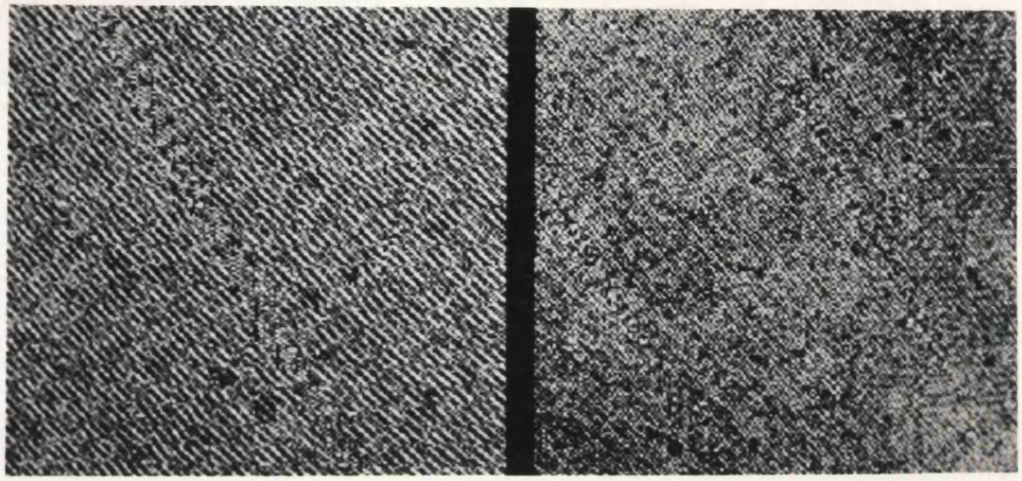

Fig 6.6a - Flat field image 8.8μm pixels

Fig 6.6b - Flat field image 17.6μm pixels

A single slice through **Fig 6.6a** is shown in **Fig 6.7** and shows the modulation associated with aliasing.

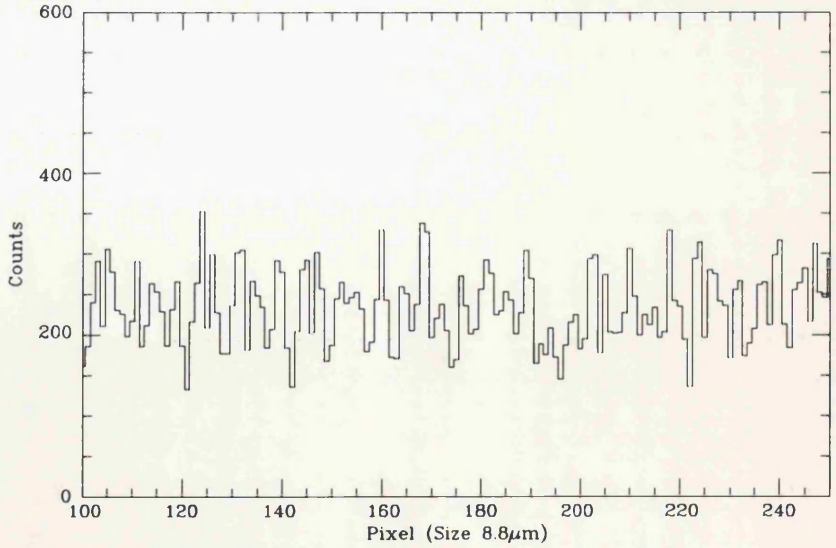

Fig 6.7. Slice through the flat field image with pixel size 8.8μm.

A histogram of the number of pixels containing a given data value was built up in

order that the modulation effect of any aliasing could be measured. This is shown in **Fig 6.8** (Plot 4) and in more detail in **Fig 6.9.**

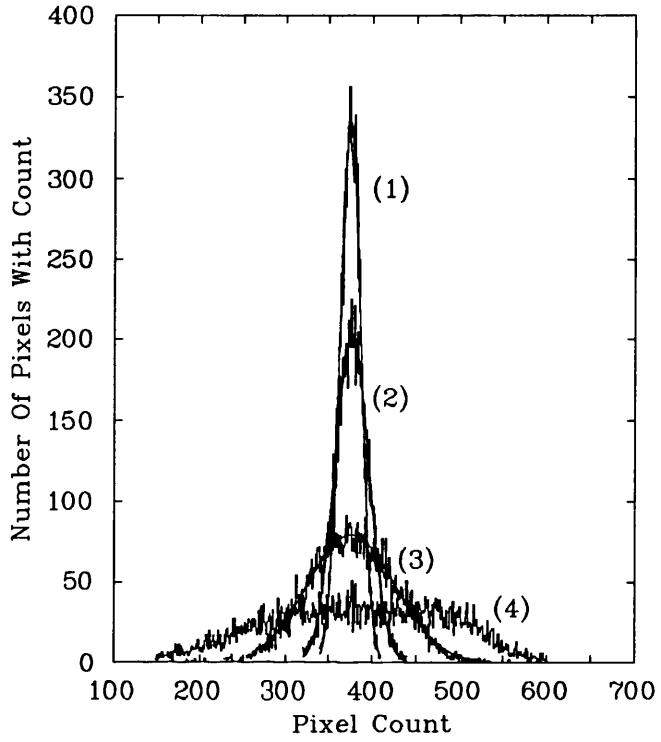

Fig 6.8. Pixel count distribution for a flat field image using four centroiding resolutions.

By averaging 4 pixels together and binning into larger pixels, the result for a 17.6μm pixel size can be extrapolated. An image of the flat field using 17.6μm pixels is shown in **Fig 6.6b**, and the corresponding histogram of count modulation is shown in Plot 3 of **Fig 6.8**. Similarly, 16 and 64 pixels were averaged and binned together in order that the level of aliasing for pixel sizes of 35.2μm and 70.4μm, respectively, could be found. These are shown in Plots 2 and 1 of **Fig 6.8**. Histograms **1,2** and **3** show the spread in data values associated with having detector centroiding resolutions of 1, $\frac{1}{2}$ and $\frac{1}{4}$ a CCD pixel respectively. The standard deviation (SD) of each distribution decreases with increasing pixel size as expected, because the sampled data is the binned average of successively greater numbers of 8.8μm pixel data. A gaussian distribution describes each histogram very well (to within 3%), and is also shown in **Fig 6.9**. Because histograms **1** and **2** are so symmetrical and gaussian, this suggests that aliasing is not evident at these sampling frequencies.

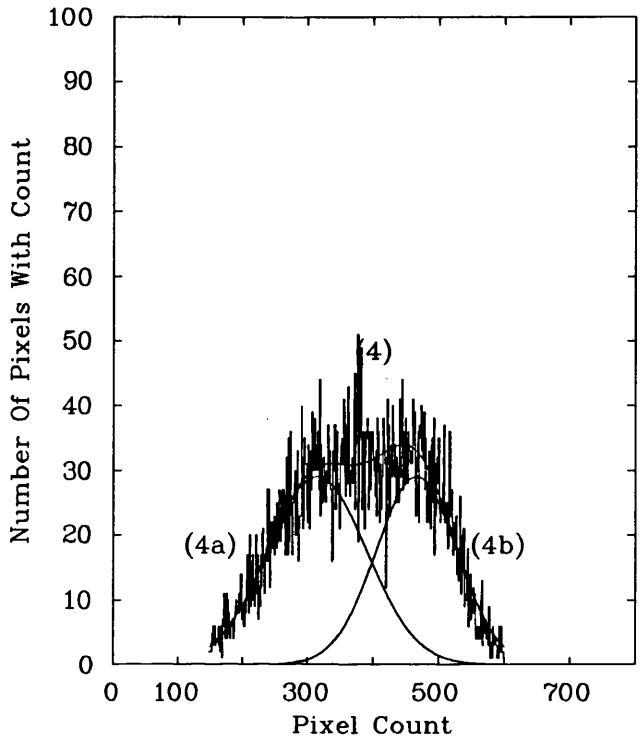

Fig 6.9. Pixel count distribution for a flat field image. Pixel size 8.8μm, pore spacing 15μm.

Histogram 4 in **Fig 6.9** is the count distribution when a pixel size of 8.8μm is employed. The distribution is non-gaussian, but does have the shape of two such profiles added together, where it can be assumed that the lower curve applies to the count distribution in the troughs introduced by aliasing and the upper curve to the count distribution introduced by the peaks. The curves in **Fig 6.9** show a best fit to the histogram distribution and their sum. A similar method was used to quantify the degree of aliasing for a pixel size of 17.6μm with the gaussian fits being shown in **Fig 6.10**. The attributes of each fit are given in **Table 6.1** for each of the four different pixel sizes.

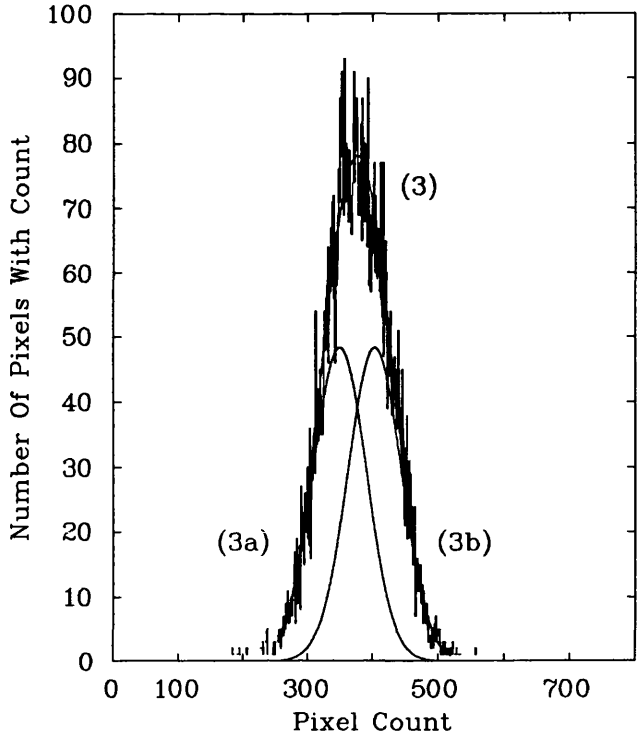

Fig 6.10. Pixel count distribution for a flat field image. Pixel size 17.6μm, pore spacing 15μm.

Curve Number	Pixel Size (μm) At Photocathode	Mean Pixel Data Value	Standard Deviation Of Histogram (Data Units)
1	70.4	374±1	11.4±0.3
2	35.2	376±1	19.5±0.1
3a	17.6	348±4	41±4
3b	17.6	402±4	41±4
4a	8.8	314±5	75±5
4b	8.8	466±5	61±5

Table 6.1 Count modulation due to aliasing

In order to quantify the average count modulation due to aliasing, the difference in the peak positions of fits **3a,3b** and **4a,4b** were taken from that of the average count/pixel. The average modulation is then

$$\text{Average Modulation} = \frac{(C-D_b)+(D_a-C)}{2C}\ \%$$

$$\text{So for curve 3, } = \frac{(375-348)+(402-375)}{2\times 375}\ \% = 7\%$$

$$\text{and for curve 4, } = \frac{(375-314)+(466-375)}{2\times375}\ \% = 20\%$$

where D_a is the peak position of fit (a) and D_b is the peak position of fit (b), and C is the peak position of distributions (1) and (2).

In order to quantify the maximum count modulation due to aliasing, the same calculation can be applied. This time instead of using the peak positions of curves **3a,3b** and **4a,4b** the position of the data value 3 SD's from the mean of each curve, can be taken.

$$\text{Max Modulation (curve 3)} = \frac{(375-89)+(652-375)}{2\times375}\ \% = 40\%$$

$$\text{Max Modulation (curve 4)} = \frac{(375-89)+(652-375)}{2\times375}\ \% = 75\%$$

6.3.2 Affect Of Aliasing On Detector Performance

Aliasing has a significant effect on MICs' image quality. For XMM-OM this will primarily manifest itself in the following ways.

- On the star tracking capability of the detector where the distortion to the star image profiles introduced by fringing, will adversely affect the results. By tracking several stars simultaneously the OM pointing error introduced by aliasing is expected to be greatly reduced.
- On the scientific quality of imaging data, in particular on faint stars, where the signal to noise ratio is not high.
- On the scientific quality of spectroscopic data.

The level of aliasing, $\sim$ 75% in the worst case, can only be reduced (without changing the pixel size) by utilizing channel plates with smaller pores. For XMM-MIC, the intention is to utilize 6μm pores on 7.5μm centres (i.e. half the size used in the trial) to increase resolution. In terms of aliasing, this is equivalent to using 12μm pores on 15μm centres with a pixel size of 17.6μm - i.e. the situation shown in **Figs 6.6b** and **6.10**. This will reduce the maximum modulation to $\sim$ 40% which is still significant. However, it is believed that aliasing will not be a great problem because tracking errors associated with the XMM satellite will inherently smooth through through it. As star images move with

respect to the detector they will subtend different pore profiles. The star movement is then corrected for by re-positioning (providing an X/Y offset) in memory. Thus, each integration will provide the summation of a number of sub-images with different degrees of aliasing and hense provide a smoothing function. For ground-based spectroscopy, no problems are expected as the spatial dimensions of each pixel will be limited to $\sim 40\mu$m due to the seeing conditions.

6.4 Affect Of Photocathode Defects On Image Quality

Occasionally, during the process of manufacture, small specks of dirt or dust can become trapped within the body of the intensifier and attach themselves to the inside surface of the photocathode. If the intensifier is powered up, the local electric field around the speck of dust becomes distorted and greatly increases in that region of the photocathode. There is a subsequent reduction in the localized work function of the photocathode, which becomes a field emission point continuously emitting electrons from the surface. The spot brightness is proportional to the applied voltage across the front gap and the electric field can become so strong as to evaporate the surrounding photocathode area. Usually this defect can be treated by carefully dislodging the dust grain into a region where there is no photocathode, but the grain can, in theory, return at any time during operation.

Areas of greatly reduced photocathode sensitivity can also occur for the following three reasons:

- Due to there being a gross non-uniformity in a low work function constituent of the photocathode. eg the non-uniform evaporation of a surface layer of caesium on a multialkali photocathode.

- Evaporation of the photocathode by positively charge ions. The ions are released from the surface of MCP pores when bombarded by electrons. A small percentage of ions are accelerated back towards the photocathode with a high energy and produce a decrease in the photocathode sensitivity.

- A localized evaporation of the photocathode due to an electrical breakdown between the photocathode and the front MCP.

The first of these is reduced by following a selection procedure, only accepting a pho-

tocathode which has been manufactured correctly and in which the caesium layer has been evaporated uniformally. The second problem only comes about when the MCPs have not been correctly scrubbed (Chapter 2) of hydrogen and is again just a matter of selecting an intensifier whose MCPs have been highly scrubbed during their manufacture. The third problem only occurs when the voltage between the photocathode and the first MCP has been increased above $\sim$ 500V (for a 300μm gap), ie 1.5×10^4 V/cm, at which point electrical breakdown occurs. So long as the intensifier is powered up correctly, no breakdown should occur. **Fig 6.13** shows a flat field image taken with an intensifier which has a small photocathode defect. This region (located in the upper left hand corner of the image) is irregular in shape and far larger than that subtended by a CCD pixel. It was probably formed during manufacture and has come about due to chemical or dirt/dust contamination during deposition of the photocathode.

6.5 Affect Of Fibre Taper Defects On Image Quality

There are three main types of image distortion common to fibre optic tapers. These are mainly caused by the processes involved in their manufacture. These are:

- A global pincushion distortion.
- Localized shear distortion between fibres (discussed earlier).
- Regions of low transmission efficiency between hexagonal fibre bundles which give rise to a 'chickenwire' pattern.

In order to obtain a good quality fibre optic taper for use with XMM-MIC, a batch of 5 fibre tapers were purchased from Schott Ltd. The taper with the least pincushion distortion was analysed in detail by *Bellis*, who examined straight line images through the taper and calculated the upper limit of pincushion distortion to be 5% (which occurred at the edge of the taper). **Fig 6.11** shows the shape of the distortion as viewed from the end with the largest aperture. Consequently the distortion is barrel shaped instead of pincushion.

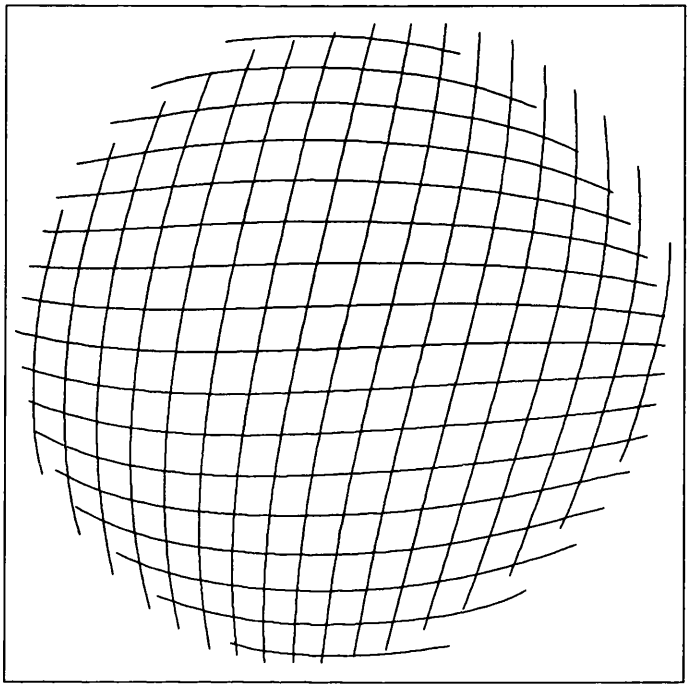

Fig 6.11. 10-fold exaggeration of the fibre taper distortion

The greatest effect that pincushion distortion has on the MIC detector is related to the star tracking capabilities of the OM. A global pincushion distortion alters the relative position of stars with respect to one another as viewed by the detector. *Bellis* concluded that the effect of the fibre taper distortion was small due to the maximum expected tracking errors (300μm over a period of 10000 secs). Only at the extreme edge of the taper was the distortion high enough to affect the star tracking capabilities of the detector. During this analysis no evidence of shear distortions were found.

The 'chickenwire' distortion is seen most clearly by illuminating the detector with a flat field image **Fig 6.12.** The fibre taper is constructed from hexagonal bundles of fibres. Events passing through the taper at the boundary between two fibre bundles are incorrectly centroided. There are fewer fibre bundles per unit area along the hexagonal shaped boundaries and as a result an event profile becomes distorted after passing through it. The events become centroided away from the boundary region and so the boundary is marked by an area of relatively few counts. The effect of 'chicken wire' can be simply

removed by flat fielding the image.

Fig 6.12. Flat field image taken with the MIC detector

6.6 Affect Of CCD Defects On Image Quality

The particular Thomson7863A CCD which has been used during all these tests has very few defects associated with it. **Fig 6.13** shows the image of a flat field in which each event is centroided to $\frac{1}{8}$ of a pixel. Only one iteration of the fixed pattern noise correction was carried out before imaging this flat field. As a consequence fixed pattern noise is present at a low level.

The defect labeled **(a)**, is caused by the 1:1 fibre block, which is bonded onto the face of the CCD. The block is formed by stitching together several smaller blocks. At the stitch boundaries there are fewer fibres than elsewhere in the block and this leads to a change in the event profile of any event passing through it at this point. These events are not lost altogether, they are merely centroided into positions away from the boundary. Like the 'chicken wire' defect in the fibre taper, this can simply be removed by flat fielding the

image.

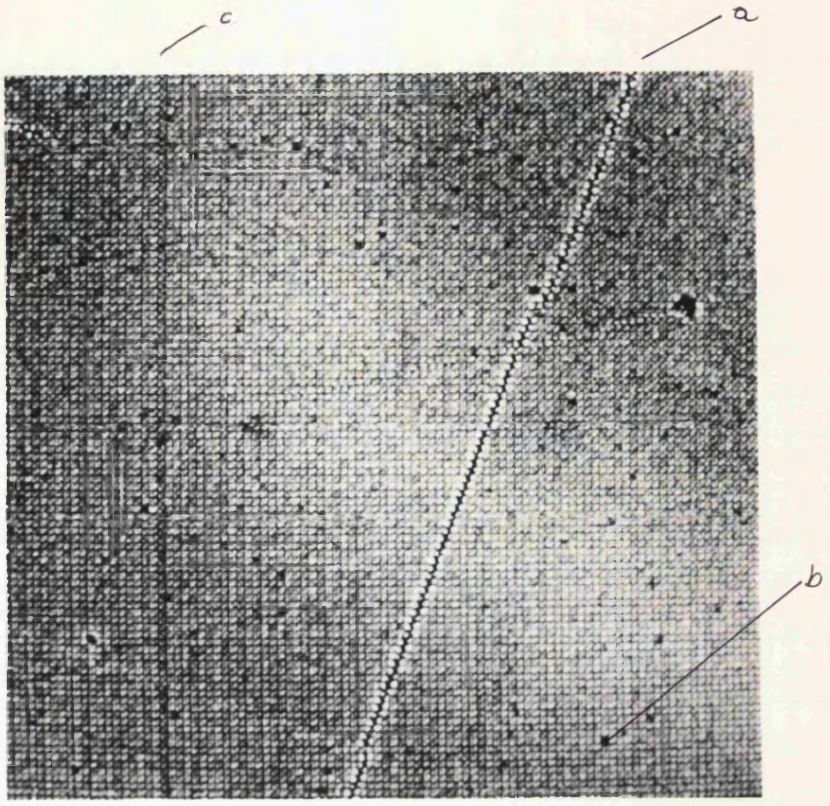

Fig 6.13. Image defects associated with the Thomson7863A CCD

Defect (**b**) is a CCD pixel whose QE is lower than those surrounding it. As a result, fewer counts are centroided into this pixel which is why it appears darker in the picture. Defect (**c**) corresponds to a CCD column whose charge transfer efficiency is lower than those surrounding it. Fewer counts are centroided in this column because events become slightly smeared during charge transfer and are therefore more likely to fall below the event detection threshold. These defects can also be removed by flat fielding and are not expected to affect the quality of scientific data taken with MIC.

Chapter 7

The DQE Of The MIC Detector

7.1 Introduction

Astronomers are continually demanding better performance from the instruments they use not only in terms of resolution and dynamic range but also in terms of the spectral range over which there is a high Detective Quantum Efficiency (DQE). The DQE of a detector is a measure of its ability to record a signal of amplitude S_i against that of background noise of amplitude N_i, where the DQE is defined as;

$$\mathrm{DQE} = \frac{\frac{S_o}{N_o}}{\frac{S_i}{N_i}} \tag{7.1}$$

$\frac{S_o}{N_o}$ being the detector output signal to noise ratio, and $\frac{S_i}{N_i}$ being the incident photon signal to noise ratio. A detector which introduces sources of noise in addition to the incident photon noise will have a DQE of less than 100%.

In order to obtain good quality data, an observer requires the output signal to be well above that of the background noise (typically a signal 3σ above that of the mean background is taken as the minimum detection limit). In cases where the input S/N is small the observer needs to integrate for long time periods in order to observe an object above the background noise. If the detector introduces further sources of noise then not only does the observer need to integrate for a long time in order to realize the input S/N ratio but also to average through the detector noise. As a result, the observer has to integrate for longer time periods in order to observe an object above the minimum detection limit. Therefore, by increasing the DQE of a detector the time taken to reach the required output S/N ratio can be reduced. This has the effect of:

- making the observation of much fainter objects possible.
- decreasing the time of observing programs.
- if the DQE is increased over a wide range of wavelengths, increasing the spectral range over which the detector can be used.

If a detectors' DQE approaches 100% then the output signal to noise ratio approaches that of the incident photon signal to noise ratio and no increase in photon noise is introduced by the detector itself. Because of the nature of photon counting where only the presence of an event is measured and not its size, the DQE of a photon counting detector is determined wholly by its *counting efficiency* providing that the rate at which noise, e.g. dark noise, produced by the detector is << than the input signal.

As mentioned in Chapter 4, the typical dark noise of a photon counting detector is dependent upon the type of photocathode used. For example, a bi-alkali photocathode typically has a dark count of 3 counts/cm^2/sec at 283K while an S20 photocathode typically has a dark count of 40 counts/cm^2/secs at 283K [*Fordham*[3] *et al*]. These count rates are much smaller than the background count rates expected by the XMM-OM for example, where the average white light background will be as high as 1×10^5 counts/sec over the whole active imaging area. Where the output S/N is limited purely by the input S/N as will be the case during observations with the XMM-OM, *Equ* 7.1 simplifies to:

$$\text{DQE} = \frac{\text{Number Of Detected Events}}{\text{Actual Number Of Events Incident On The Detector}} \tag{7.2}$$

which in the case of the MIC detector is:

$$\text{DQE} = (\text{Window Transmission} \times \text{Photocathode RQE}) \times \text{OAR} \times \text{Camera Efficiency} \tag{7.3}$$

where the **OAR** is the Open Area Ratio of the intensifiers' front MCP and the photocathode RQE is the photocathodes' photon to photoelectron conversion efficiency. Together, these four components determine the counting efficiency of the MIC detector.

7.2 Components Affecting The Detector DQE

7.2.1 The Intensifier Input Window

The percentage of photons having a wavelength λ, which successfully pass through the intensifier input window, depends upon the transmittance of the window material T_λ at

that wavelength. This is a function of both the degree to which a window material reflects and absorbs photons of light, as

$$T_\lambda = 1 - (R_\lambda + A_\lambda) \tag{7.4}$$

where R_λ is the reflection coefficient and A_λ is the absorption coefficient of the window material. The most important of these two quantities is the absorption coefficient, as materials possessing a highly reflective front surface would not even be considered as window materials. **Fig 7.1** shows the transmission curves for five materials which could potentially be used as an intensifier input window.

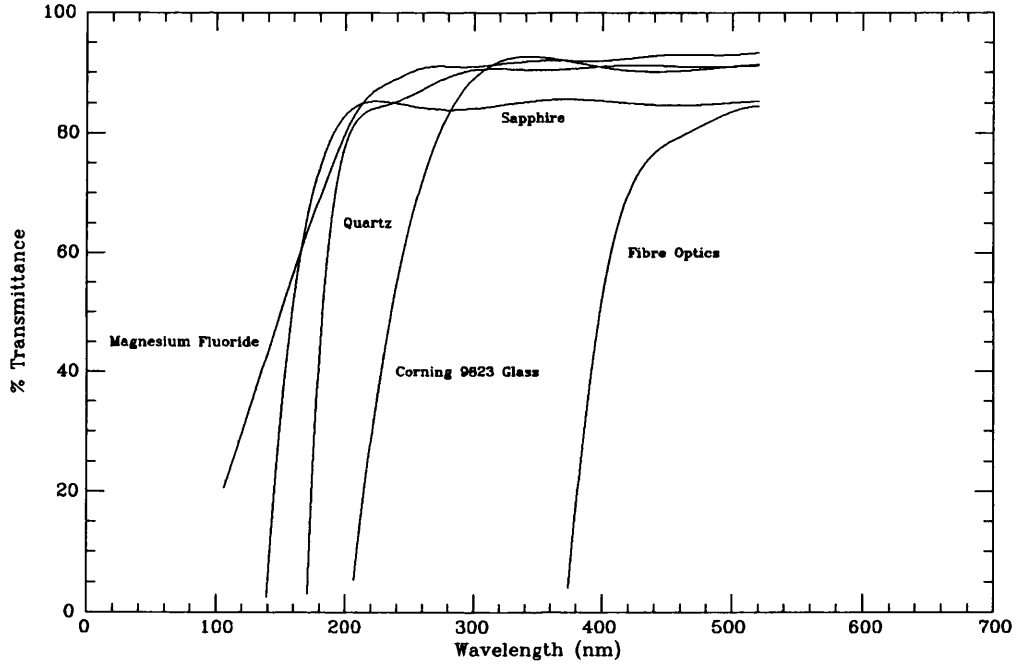

Fig 7.1. Transmission characteristics of five input window materials

All of these materials have a peak transmission of between 80-90% somewhere in the visible/UV region of the EM spectrum. The major difference between them is their lower wavelength cutoff. The input window generally defines the high frequency DQE cutoff of a photon counting detector because of the increased interaction between higher energy photons and the intensifier window material. A fibre optic window for example, has a wavelength cutoff at $\sim$ 400nm, most of the light with wavelengths shorter than this are unable to pass through it. [1]

[1] However, a fibre optic window can be butted to the MIC CCD as light from the intensifier output phosphor has a wavelength of $\sim$ 520nm at which point the fibre optic element has a transmittance of $\sim$ 80%.

One of the requirements of the XMM-OM is that it have a spectral range from 150-650nm and so the intensifier input window is required to have a high transmission over this range. **Fig 7.1** shows that out of the five window materials presented here, only quartz, sapphire and M_gF_2 can be considered for use with the MIC intensifier. However, as MIC is the blue/UV detector, as high a transmittance as possible is especially required in this spectral region. Because the absolute transmittance of quartz is negligible below 170nm there is a strong preference towards sapphire and M_gF_2.

Both these window materials have been tested in high radiation environments and used in previous space missions. It has been reported [*Swyler et al*] that exposure of certain window materials to high doses of radiation causes *browning* to occur in them. Browning is an effect whereby the window appears stained due to the production of colour centres within the window lattice. The low wavelength cutoff moves towards longer wavelengths, preferentially absorbing the blue/UV photons. This causes a degradation in the transmission properties of the window. Sapphire is one of the window materials in which browning can occur and this must be taken into account when considering which one of the two window materials should be chosen for the MIC intensifier. However, *Pellicori et al* reports that in pure sapphire, virtually no transmission losses occur after exposure to high doses of radiation and so the effect may only be a result of impurities within the sapphire lattice. Further radiation testing is required to verify this fact and to deduce how pure a sapphire window needs to be in order to meet the XMM-OM lifetime specifications. *Pellicori et al* also report no browning in M_gF_2 windows when exposed to high levels of radiation.

In terms of window transmittance alone, M_gF_2 appears to be the most suitable window material for the MIC intensifier as it has a transmittance some 10% higher than sapphire in the visible region and a slightly extended transmission into the UV. A M_gF_2 window may also have better lifetime qualities over that of a sapphire window. However, window transmittance is not the only factor which has to be taken into account when considering the choice of intensifier window.

Sapphire is known to phosphoresce (Chapter 4) if it contains radioactive impurities but, because of its more regular lattice structure, could potentially provide a substrate upon which can be grown photocathodes with QEs some 10-20% higher than previously achieved [*Dubovoi et al*].

7.2.2 The Intensifier Photocathode

In order to convert photons at optical and near UV wavelengths into photoelectrons, a photoemissive material is required. In closed intensifier systems, a photocathode is grown on the inner surface of the input window through which photons travel before reaching the photocathode surface. The optimum photocathode thickness is dependent upon its chemical constituents. If the photocathode is too thin then it becomes almost transparent to incident photons, most of which will simply pass straight through it. If the photocathode is too thick, then an electron liberated close to the front photocathode surface is likely to become absorbed back into the photocathode material. In practice, the optimum photocathode thickness is found by irradiating the photocathode with white light during deposition and adding further layers to it, during which the photocurrent from its rear surface is measured. When the photocurrent falls slightly below its maximum value the process is stopped. Because the maximum sensitivity of a photocathode does not occur when it is opaque to incident photons, these photocathodes are semi-transparent (typically allowing 20% of photons to pass through it) which is one reason why their QE is less than 100%.

Once a photoelectron has been produced within the photocathode itself, there is only a 50% probability that it will travel towards its rear surface. Only if a photoelectron is liberated from the rear photocathode surface can it be accelerated towards the front MCP and take part in the amplification process. This is the main limitation on the photocathode QE. If we combine this inefficiency with the losses associated with the photocathode being optically semi-transparent then the maximum theoretical photocathode QE will typically be 40% but depends greatly upon the photon wavelength and the type of photocathode.

The production of a photoelectron has three steps associated with it [*Csorba*],

- The excitation of an electron from the valence to the conduction band.
- The excitation of the electron from the conduction band level to that of the vacuum level.
- The excitation of the electron into the vacuum.

All these excitations require a quantity of energy dependent upon the size of each band gap which is in turn dependent upon the chemical constituents from which the photocathode is made. The photocathode sensitivity is therefore photon energy and hence photon

wavelength dependent. The nature of this dependency varies from photocathode to photocathode due to the inconsistencies involved in their manufacture, so in order to optimize the DQE performance of the detector for a particular application, the correct choice of photocathode has to be made in terms of the spectral range and peak QE required over that range.

Increased understanding of photoemissive materials has led to the production of photocathodes with progressively wider spectral ranges and greater sensitivity responses. Improvements made to the first photocathode, the S1 (Ag.O.Cs), and later the S11 (Cs.Sb) which was greatly used in early magnetically focused image tubes, has led to the production of the now widely used, multialkali S20 (Na_2KSb)Cs) and bi-alkali (K_2CsSb,Na_2KSb) photocathodes. **Fig 7.2** shows the absolute sensitivity response of five such photocathodes over a spectral range of 10nm to 1000nm [*Csorba*].

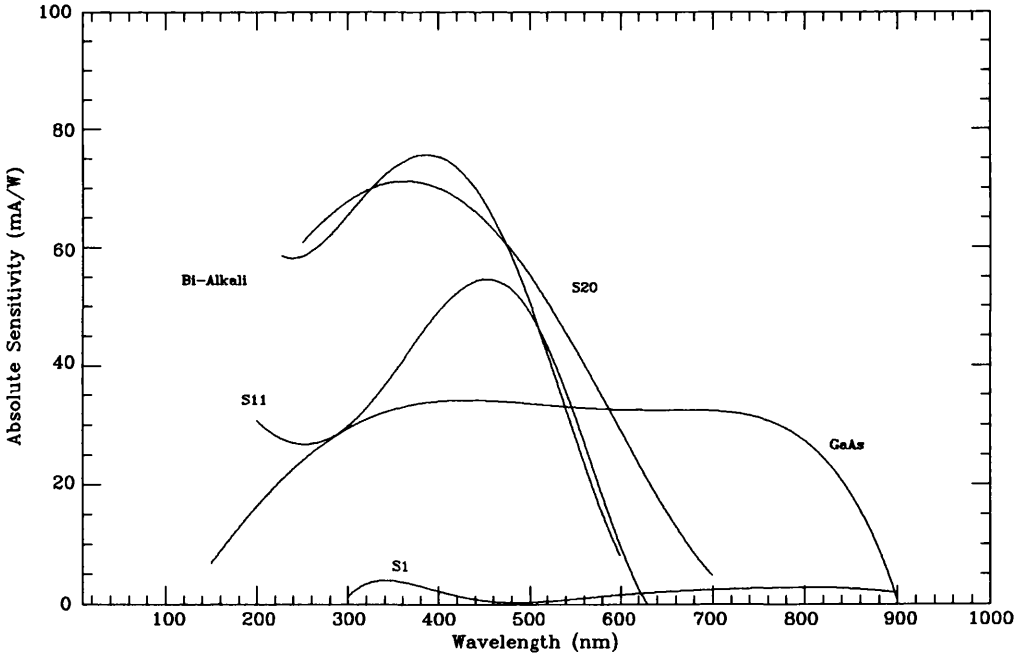

Fig 7.2. Typical photocathode sensitivity responses for five types of photocathode

Most photon counting detectors are primarily designed to cover the blue/UV regions of the EM spectrum because they are more efficient compared to CCDs in this region. In the red/infra-red CCDs can have RQEs as high as 85% or more and are best suited for work in this region. Photocathodes, like those mentioned above, allow photon counting detectors to compete with CCDs in the blue/UV region because although blue coated CCDs can have RQEs as high as 50% in the blue, their readout noise makes them less

attractive for faint light applications.

As mentioned previously, one of the requirements of the XMM-OM is for the MIC detector to have a spectral range from 150nm to 650nm. Therefore, the photocathode chosen for the MIC intensifier must have a high QE over this range, especially in the blue/UV region. **Fig 7.2** shows that there are only three choices of photocathode that could possibly satisfy this requirement. These are the bi-alkali, the S20 and the S11 photocathodes. However, the S11 only has a peak sensitivity of 55mA/W in the blue (QE of 15%), and although it does extend far into UV it has far too low a QE in the blue/UV. The S20 photocathode typically has a peak sensitivity of 70mA/W (QE of 23%) and maintains a high sensitivity over the whole wavelength range required by the XMM-OM. It also has an extended red response into the red/infra-red which although not a requirement of the OM means that its sensitivity is far higher than a bi-alkali photocathode at 650nm. The bi-alkali photocathode has a peak sensitivity of 75mA/W at 400nm (QE of 24%) and a response that extends over the whole required wavelength range. It does however have a low sensitivity in the red, dropping below 10mA/W (QE of 2%) at 600nm.

The bi-alkali and S20 photocathodes have very similar sensitivity responses in the blue, but the S20 has three times the sensitivity in the red making it more attractive for use with XMM-OM. The extended red response of the S20 causes it to have a higher dark current than a bi-alkali photocathode but this is not a consideration in the choice of photocathode for the space version of MIC because of the high sky background level.

The bi-alkali photocathode is favoured for the ground based applications of MIC because in most cases, both the objects and background are very faint so that the photocathode dark current is a more significant source of background noise. This is why a bi-alkali photocathode possessing a dark current some 14 times lower than an S20 photocathode is more suitable for ground based work.

7.2.3 The Front Channel Plate Open Area Ratio

Photoelectrons produced by the photocathode are accelerated across the intensifier front gap where they either strike the inconel electrode covering the front channel plate or enter a channel plate pore. The percentage of the front channel plate area subtended by the pore entrances, determines what is called the Open Area Ratio (OAR). The OAR affects the counting efficiency of the intensifier by determining the percentage of photoelectrons

which go on to take part in the charge amplification process. The intensifiers used with the MIC detector have pores which are placed in a hexagonally packed structure, minimizing the 'dead space' between each one. Intensifiers with two different pores sizes have been used to date:

1. having 10μm diameter pores and inter-pore spacings of 12μm.

2. having 12μm diameter pores and inter-pore spacings 15μm.

Both these configurations have an OAR of 63%, meaning that 37% of the front channel plate area is 'dead space'.

In some types of channel plate the OAR has been increased by 'funneling' the input to the front MCP pores, and coating them with a material possessing a high secondary emission coefficient. This increases the collecting area of each pore and hence the counting efficiency of the intensifier. Funneling the input to a pore can increase the effective OAR from 63% to as much as 75%.

The effective OAR is thought to be slightly larger than that calculated by means of geometry, due to a small percentage of photoelectrons 'bouncing' off the inconel electrode on the front face of the first channel plate, and into a pore [*Read at al*]. However, this affect is thought to be a small one, because the counting efficiency of the front channel plate is close to its theoretical value [*Norton*[1] *et al*].

Another type of MCP, examined by *Frazer*[1] *et al* has square shaped pores arranged in a square packing structure. This pore configuration has advantages over the non-funneled hexagonally packed pores as it decreases the dead space between each one. In this case the OAR is as high as 72%, but because of the difficulty in manufacturing these MCPs, the pore sizes are much larger as are the spacings between each pore centre (this particular MCP having square pores whose sides were 85μm and whose centre to centre spacing was 100μm). Unfortunately, large pores have the effect of greatly reducing the intensifier resolution (Chapter 5).

7.2.4 The CCD Camera Efficiency

The counting efficiency of the MIC detector is mainly governed by losses in the intensifier, which occur prior to charge amplification i.e. in the intensifier input window and at the photocathode and front MCP. After charge saturation in the rear MCP, a charge cloud

of typically $1 \times 10^5 e^-$ strikes the P20 output phosphor which has an electron to photon conversion of about 1:100. After passing through the fibre taper, which has a transmission of 6% [*Ref*[6]], $\sim 6 \times 10^5$ photons are incident on the CCD. The P20 phosphor emits light with a wavelength of 520nm and therefore, because the CCD has a QE of $\sim$ 15% at this wavelength (**Fig 7.3**), an event produces $\sim 9 \times 10^4$ e^- within the silicon lattice.

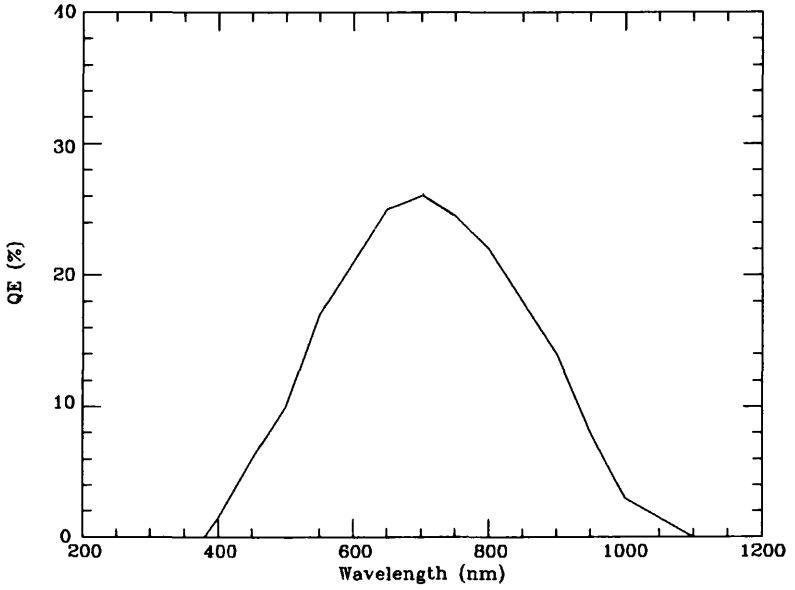

Fig 7.3. Quantum efficiency of the Thomson TH7863A CCD

The analog to digital converter is typically set such that 1 ADU (Analog to Digital Unit) corresponds to $400e^-$ and so in terms of ADUs the average event energy is 225 ADU. In the worst case where the event is spread almost equally over nine pixels the average energy in each pixel over which the event extends is $1 \times 10^4 e^-$ or 25 ADU. This is well above both the thermal noise ($50e^-$/pixel/12ms at 300K [*McLean*], 12ms being the maximum time taken to read out a whole frame of CCD data) and the CCD readout noise (of $\sim$ 300-$400e^-$/pixel). The combination of both these sources of noise is at a level of $\frac{350+50}{1 \times 10^4}\% = 4\%$ that of the average event signal/CCD pixel. This means that an event is easily detectable above the CCD noise, but because the CCD is sometimes run at high temperatures (up to 330K) and the event shape has to be maintained to a high accuracy, *black level clamping* is used in order to reduce the thermal noise contribution.

Once an event has been sampled by the CCD camera there are two circumstances in which that event may not be treated as a real event. These come about due to the following:

The Lower Event Detection Threshold

In order to distinguish between a real event (i.e. that derived from a photon event incident on the front face of the intensifier) and a noise event (that deriving from within the intensifier or on the CCD itself), MIC uses an event height detection threshold, events with heights above the threshold being treated as real. Simply relying on an event detection threshold to distinguish between real and noise events has its problems, the most important of these is knowing at which height to set the threshold. Its' minimum value must be that required to accurately centroid each event i.e 20 ADU.

Fig 7.4 shows the event height distribution of a 25mm diameter MCP intensifier (whose operating voltages are V_1 = 200V, V_2 = 870V, V_3 = 2840V, V_4 = 4550V), coupled to a CCD.

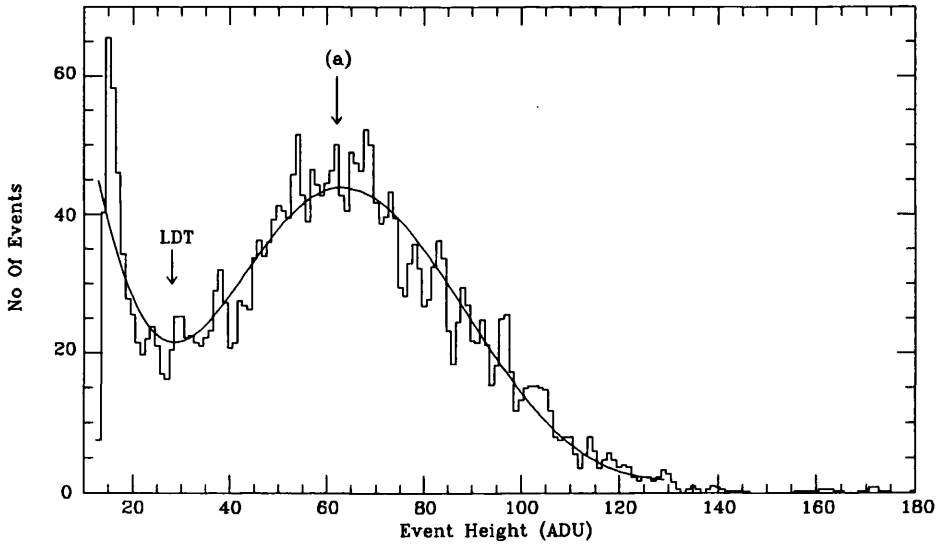

Fig 7.4. Event height distribution for a 25mm MCP intensifier

The event height distribution is made up of two separate components. These are

- Those being due to real events, whose distribution is roughly gaussian and whose mean height for these intensifier voltages is (a). The intensifier produces charge saturated events whose mean height (a), is large and whose height distribution (the gaussian FWHM) is relatively narrow.

- Those being due to noise events. These have a height distribution which is a negative exponential shaped curve. The noise components of this curve derive from three sources:

1. The CCD readout noise of 300-400 e^-.
2. Phosphor decay events where, due to the slow decay components of the P20 phosphor, events arriving close to the end of one frame period, can dump some of their energy into the next contiguous frame of the CCD. The amount of energy deposited in the next frame is dependent both on the intensity of the primary event in the first frame, and its arrival time with respect to the end of a frame period.
3. Events which are not charge saturated within the intensifier due to unfavorable electron ballistics [*Ref*[3]] e.g. a photoelectron whose trajectory is almost parallel to a pore wall, will strike the wall close to the end of the pore and the event gain will be lower than normal.

If the intensifier produces a tight event height distribution then the lower detection threshold is placed in the valley of the distribution, marked '*LDT*' in **Fig 7.4.** In this position, most of the real events lie above the threshold and most of the noise events lie below the threshold.

The event height distribution produced by a typical 4-stage EMI intensifier (**Fig 7.5**), which was the intensifier used with the CCD-IPCS, is very different from that of a MCP intensifier.

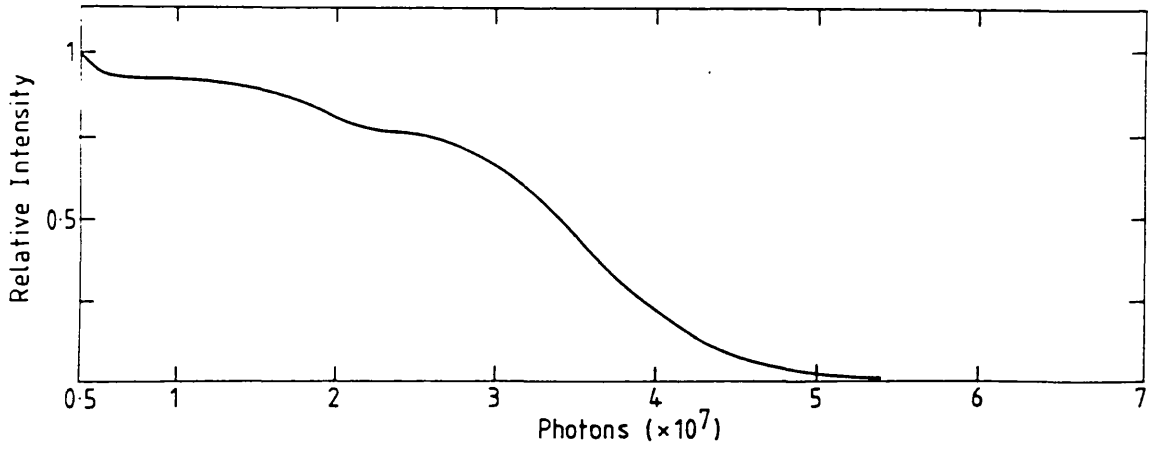

Fig 7.5. Event height distribution for a typical 4-stage EMI intensifier

The EMI intensifier does not produce a saturated event height distribution but in order to preserve resolution, the lower detection threshold is placed at 20 ADU (the height

below which events have unacceptable errors when centroided, Chapter 5). Placing the threshold at this height means that a number of real events are rejected, decreasing the camera efficiency in order to preserve resolution. Although a significant number of real events are rejected if the threshold is set at 20 ADU, placing the threshold at this height ensures that the number of real events lying above the threshold is kept to a minimum.

The CCD Frame Sync Period

During each frame period, events are integrated in the image area and then transferred to the storage area. The time taken to transfer a frame of data to the storage area is called the *frame sync period.*

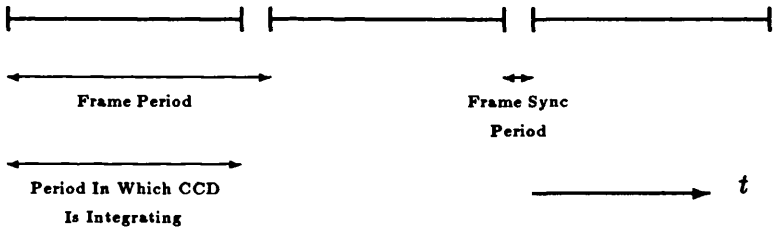

Fig 7.6. Time diagram of a fast scan frame transfer CCD

Because the intensifier output phosphor decays in a finite amount of time, the energy from any event deposited on the CCD during the frame sync period, is smeared out over several pixels in the direction of frame transfer. As a result, the peak height associated with such an event is very small because its energy is spread out over so many pixels. Typically, its peak height will fall below the lower counting threshold and the event is treated as a noise event (although, as explained in Chapter 4, it may produce a secondary (phosphor decay) event in the next CCD frame).

The length of the frame sync period is simply a function of the CCDs' vertical clock speed t_v (3MHz), and the total number of pixel rows, r in the image area, where:

$$\text{Frame Sync Period} = r \times t_v \tag{7.5}$$

which for the Thomson TH7863A having 288 rows of pixels in the image area, is 96μs.

The affect of having a *frame transfer period* on the camera efficiency is dependent upon the total frame time, which is in turn dependent upon the number of rows used for data

acquisition. The fraction of events which arrive during the frame sync period is:

$$\text{Fraction Of Events Arriving During The Frame Sync Period} = \frac{\text{Frame Sync Period}}{\text{Frame Period}} \qquad (7.6)$$

A scientific requirement of the XMM-OM is that the blue detector have a 2048×2048 pixel format which can be obtained by using a 256×256 CCD pixel format and centroiding events to $\frac{1}{8}$ of a CCD pixel. If all 256 rows are used for data acquisition then the fraction in *Equ* 7.6 is $\sim$ 0.0086 and when partially scanning the CCD for example, reading out only 32 rows, the fraction increases to $\sim$ 0.072. If a small data acquisition format is used then the frame sync period becomes a larger fraction of the frame time, and a higher proportion of events arrive during a frame sync period. As a result the camera efficiency is, to a small degree, dependent upon the data acquisition format.

7.3 Measured DQE Of The MIC Detector

In order to determine the wavelength dependent DQE of the MIC detector, an experiment was carried out with the aid of a UV monochromator (made by Acton Research) based at the Mullard Space Science Laboratories (MSSL). A schematic of the experimental set up together with a layout of the monochromator is shown in **Fig 7.7.**

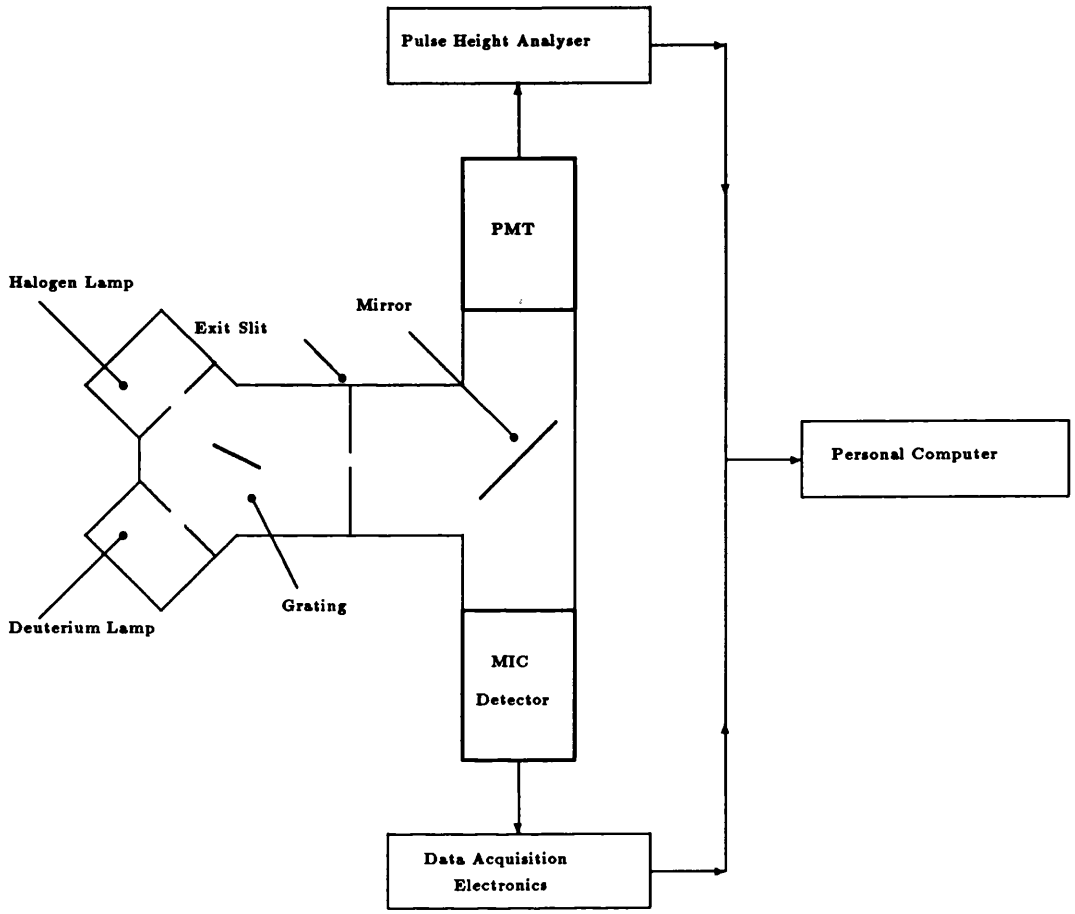

Fig 7.7. Experimental setup for the DQE tests

The monochromator consisted of two calibration lamps, one Deuterium lamp for the blue/UV region, and one Halogen lamp for the optical/near infra-red region. A grating was used to project a monochromatic beam of light, onto the exit slit of the monochromator. Light emerging from the slit was then deflected by a mirror onto one of two detectors, either a photomultiplier tube (PMT) or MIC. In order to prevent the atmospheric absorption of UV light, the inside of the monochromator was kept in vacuum at a pressure of $\sim 3 \times 10^{-5}$ Torr, with both detector mounts engineered to be vacuum tight.

The aim of the experiment was to quantify the counting efficiency of MIC by a comparison with the PMT tube, whose absolute DQE had previously been calibrated by EMI. A circular aperture of 6mm diameter was placed in front of the PMT window both of whose centres were in the optical axis of the monochromator. Events detected by the PMT were recorded using a high time resolution pulse height analyser. This was connected to a personal computer which was used to increment the count totals of both MIC and the PMT

during the experiment. The MIC detector employed a 25mm diameter intensifier having an S20 photocathode and a quartz input window. The combined QE response (provided by DEP *Ref*[7]) of this photocathode and window is shown in **Fig 7.8.**

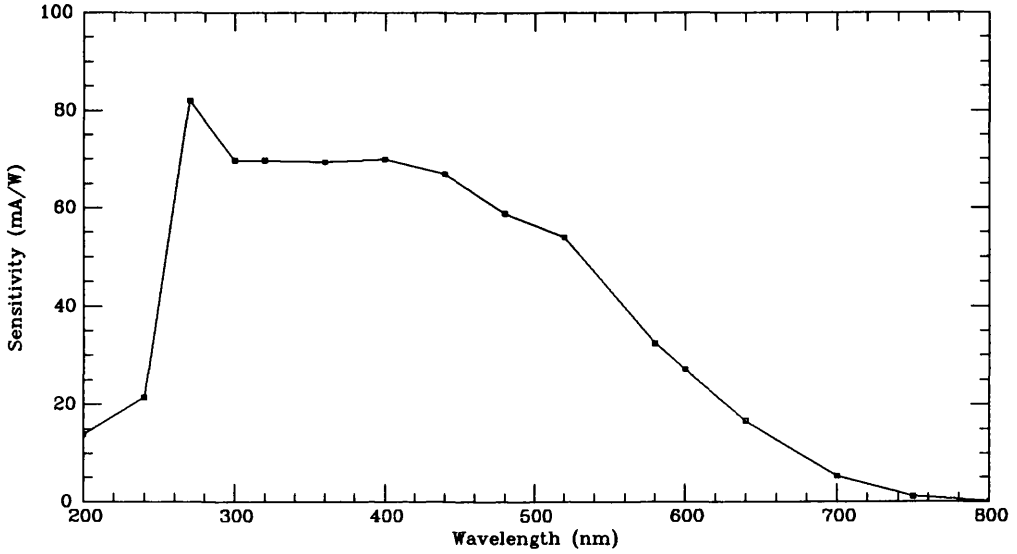

Fig 7.8. Measured RQE of an S20 photocathode and Quartz input window

The MIC detector, instead of using an aperture in front of the intensifier defined the area in which events were recorded by creating a software generated data acquisition window, whose size corresponded to a 6mm×6mm at the input to the intensifier. This window was centred on the optical axis of the monochromator and in an area of the photocathode free from defects.

7.3.1 Experimental Method

The experiment was set up so that the position of the deflecting mirror was such that the projection of the exit slit onto both detectors was the same. This position was found for the PMT tube by illuminating the exit slit and rotating the mirror until the PMT recorded the highest count rate. Because the rotation axis of the mirror is perpendicular to the optical axis of the monochromator, the slit image was then assumed central on the PMT tube. This procedure was repeated for the MIC detector this time observing the position of the broad slit image and rotating the mirror until it was central on the intensifier.

In order to compare the counting efficiency of the PMT and MIC, both the PMTs' pulse counter and the output of MICs' event recognition circuit (the event recognition flag) were connected to and analysed by the PC. Coincidence events were avoided by decreasing the exit slit width of both lamps until the brightest illumination intensity (over

the wavelength range at which the experiment was carried out) was below that at which a significant number of coincidence events would take place.

The experiment was started by firstly switching on the deutrium lamp and allowing it to stablize. The first wavelength was selected and the mirror rotated such that the image of the entrance slit illuminated the PMT. Three, ten second integrations and a dark current measurement were then taken. The mirror was then rotated such that the image of the entrance slit illuminated MIC. Once more, three, ten second integrations and a dark current measurement was taken. These readings were repeated for each detector making six measurements/wavelength in all, and the whole process repeated for wavelengths between 150nm and 550nm, in steps of 10nm. A correction was applied to the data to allow for the difference in aperture sizes used with the PMT tube and MIC.

7.3.2 Results

The measured DQE of the MIC detector is shown in **Fig 7.9**. The large error on each point of the graph is due to errors in the DQE calibration of the PMT. EMI quote errors of ± 35% on DQE measurements at wavelengths smaller than 240nm, and errors of ± 15% on DQE measurements at wavelengths longer than 240nm.

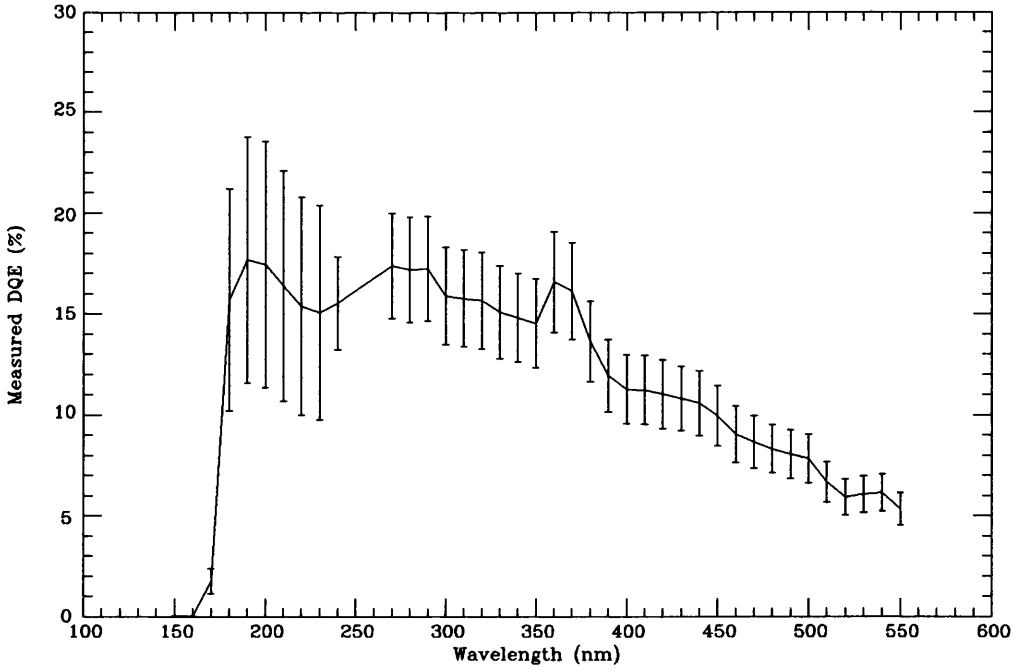

Fig 7.9. Measured DQE of the MIC detector with S20 photocathode and Quartz input window

The curve indicates that below 190nm there is a dramatic fall in the detector DQE. This is due to the transmission cutoff of the intensifiers' quartz input window. The DQE curve peaks in three places, at 190nm, 280nm and 360nm reaching close to 17.5% at each point. The peak at 270nm corresponds to a peak in the photocathode QE curve shown in **Fig 7.8** but there is no corresponding peak at 360nm as one might expect. This may be due to the way in which the photocathode RQE was measured by DEP. The step between each RQE measurement was 40nm and it is possible that the peak at 360nm was not sampled by them.

Below 300nm the DQE steadily decreases until at 550nm it falls to 6%. This photocathode/window combination provides a broad sensitivity response but does not extend down to 150nm. The peak DQE is also lower than that required by the space version of the MIC detector which ideally requires a peak DQE of above 20% in the blue/UV.

If we divide the DQE curve by the RQE curve for the same photocathode and input window, **Fig 7.8**, then we can estimate the combined value of the OAR and camera efficiency from *Equ* 7.3. For the wavelengths at which the photocathode/window QE measurements were made, the average value of the OAR and camera efficiency is 55%. Because the OAR for the intensifier will be close to the theoretical OAR of 63% the results suggest a camera efficiency of $\sim$ 87%.

7.3.3 Summary

The combination of the S20 photocathode and quartz window used in the experiment described above, indicates that by swapping the quartz window for a M_gF_2 window, the DQE requirements placed on the MIC detector by the XMM-OM will be realized. M_gF_2 is the best choice of intensifier window material because of its high optical transmission which extends below 150nm (see **Fig 7.1**), and as importantly because of its resistance to radiation damage. The S20 photocathode is a photoemissive material whose QE response is high both in the UV and red, and although it has 14 times the dark current of a bi-alkali photocathode this is unimportant so far as space observations are concerned.

For ground based work, where the detector is used for either faint object direct imaging or for the detection of high resolution spectra, both object and background signals are very small. In this case the photocathode dark current is significant compared to the image background signal and so a low dark current bi-alkali photocathode is the best choice of

photocathode.

7.4 Future Improvements To The MIC DQE

One of the most promising ways of improving the DQE of future intensifiers is to use photocathodes grown not by the traditional method of depositing the photocathode onto a substrate one element at a time, but by the method of Molecular Beam Epitaxy (MBE) [*Dubovoi et al*]. This is a method in which compounds are firstly formed in a vapour state by co-evaporation, and then evaporated onto the substrate. For example, a bi-alkali $(Na,K)_3$ Sb photocathode is traditionally grown by the evaporation of an Sb layer, which is then activated by the the evaporation of both alkali metals. Using the method of MBE, K_3Sb is formed by coevaporation of Sb and K vapours, and then activated by the evaporation of both alkali metals. MBE produces photocathodes with RQEs' some 20-30% higher than those produced using the traditional method, and their response is far more uniform and reproducible from photocathode to photocathode. The process also takes only $\frac{1}{10}$ the time to complete and can also be automated. In their initial trials, *Dubovoi et al* have grown a bi-alkali photocathodes onto sapphire substrates, the combined quantum yields of which are consistently higher than those of bi-alkali photocathodes grown in the traditional way.

Another way in which the DQE can be increased is by improving the OAR of the intensifier front channel plate. At present, current manufacturing techniques can only produce large sized, square shaped pores. As the fibre optics manufacturing process (from which MCPs take their technology) becomes more refined, there should follow a decrease in the size of square shaped pores. MCPs with closely packed square pores (especially if they are funneled) will have OARs' greater than those presently attainable with cylindrical shaped pores.

Chapter 8

Comparison Of Photon Counting Detectors

8.1 Introduction

There are two broad types of photon counting detector, those whose readout cameras are charge sensitive and those whose readout cameras are photon sensitive, where MIC whose readout camera is a CCD, falls into the second of these categories. In most modern photon counting detectors event amplification is provided by a microchannel plate image intensifier of the type described in Chapter 2. The intensifier architecture may vary between detectors but the fundamental way in which events are charge amplified, is similar to all. For this reason, photon counting detectors vary little in DQE for example, as the DQE of a photon counting detector is governed to a large degree not by the type of readout camera employed but by the intensifier (the photocathode QE and the OAR of the front MCP being the dominant factors (Chapter 7)). Different designs of intensifiers can be used in conjunction with each readout camera providing the output event is in the appropriate form (i.e. a charge event for charge sensitive readouts or a scintillation of light for photon sensitive readouts) and is run at a sufficiently high gain. This is why most photon counting detectors are mainly described in terms of their readout camera alone.

8.2 Charge Sensitive Readout Detectors

Unlike the MIC intensifier, intensifiers used in conjunction with charge sensitive readouts do not have an output phosphor. In these cases (e.g. Resistive anodes, Spiral anodes) the event capture device is sealed directly inside the intensifier body. Amplified events emerging from the rear MCP are accelerated directly onto an anode where their presence and position can be determined. At present there are three different ways in which the event position can be determined.

8.2.1 Event Detection Using Charge Division

In 1930, *Schottky* proposed that the position of a charge cloud (an event) could be determined by capturing it on a resistive anode around which several charge collecting electrodes are placed. By comparing the ratio of charge collected by each electrode a measure of the event position was made. In this case the charge associated with each event is divided between different electrodes the ratio of the charge on each electrode being unique for every event position.

These types of anode produce an output which varies continuously with event position and hence the event position is determined by analog means. There are several types of detector which use this analog ratio technique for determining the event position, three of which, the *Resistive anode*, the *Wedge and Strip anode* and the *Spiral anode* (SPAN) are described below.

The Resistive Anode

The resistive anode is a single anode of resistance, r_0, where r_0 is typically $2\times10^5\Omega$ across its imaging area [*Lampton et al*]. Anodes which have square or rectangular geometries tend to produce large degrees of barrel distortion but the anode geometry shown in **Fig 8.1** has been shown to produce theoretically distortionless images [*Gear*].

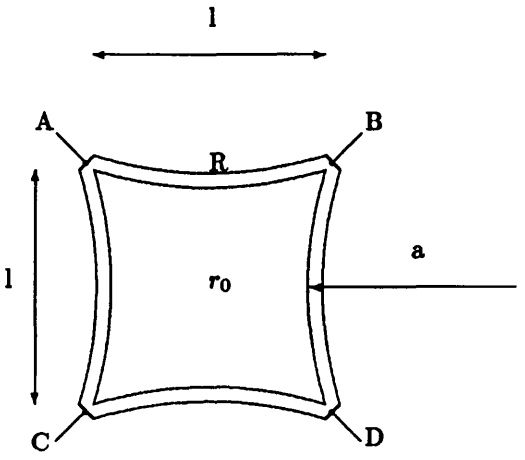

Fig 8.1. Schematic of a Resistive Anode

Electrodes connected to each corner of the anode are in turn connected to a separate amplifier circuit and then to a set of event positioning electronics. The anode has curved edges each edge being terminated with a material of resistance, R, where $R=\frac{r_0}{a}$ (**Fig 8.1**). The event position is found from the ratio of charge on each of the four electrodes where the x position is found using the algorithm;

$$\frac{x}{l} = \frac{(I_B + I_D)}{(I_A + I_B + I_C + I_D)} \tag{8.1}$$

where l is the anode length, and the y position is similarly found from using the algorithm;

$$\frac{y}{l} = \frac{(I_A + I_B)}{(I_A + I_B + I_C + I_D)} \tag{8.2}$$

These simple algorithms determine the centroid position of each event and so no additional event centroiding electronics are required to increase the anode resolution. The event position can be determined to a typical accuracy of 200μm limited by the thermal noise of the anode and the amplifier noise.

Typical characteristics for a resistive anode readout system are shown in **Table 8.1**

Format	100x100 pixels
Anode Size	25 mm x 25 mm
Anode Resolution	200 μm
Image Distortion	3% over the anodes' central region
Number Of Amplifiers	4
Event Processing Time	10μsec

Table 8.1. Typical characteristics of a Resistive Anode

The Wedge And Strip Anode

Instead of having a single resistive anode the Wedge and Strip anode is made up of three or four independently insulated electrodes (depending upon the anode geometry) each of which is connected to a different amplifier circuit. Most Wedge And Strip anode geometries have two electrodes which resemble resistive strips while another two resemble a wedge type pattern like that designed by [*Anger*] and shown in **Fig 8.2.**

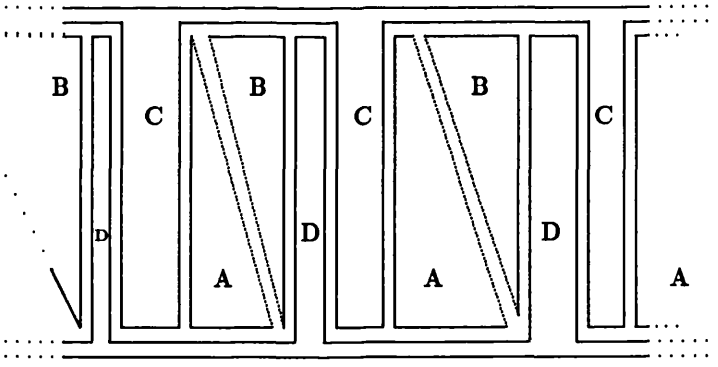

Fig 8.2. Schematic of the Wedge and Strip Anode

At the centre of the anode array each electrode takes up 25% of the total imaging area but these percentages change with increasing distance from the centre. The position of each event is found in x using electrodes C and D. The width of electrode D increases for increasing values of x while the width of C decreases for increasing values of x. An event captured by the array produces charge on electrodes C and D in a ratio which depends

upon its x position along the array length. For each x position electrodes C and D make up a different proportion of the array area and hence sample different fractions of the event charge. The same is true in the y direction where electrodes A and B vary in width along the y axis.

The x position of each event is found using the algorithm;

$$x = \frac{I_D}{(I_C + I_D)} \tag{8.3}$$

and the y position is found from;

$$y = \frac{I_B}{(I_A + I_B)} \tag{8.4}$$

By allowing the event to spread over at least two periods of the electrode pattern, the event charge is sampled with sufficient accuracy in both x and y to produce a resolution that is better than the Resistive Anode. It also requires a lower event gain in order to realize this spatial resolution [*Timothy*].

The Wedge and Strip anode has several other advantages over the resistive anode;

- It has a lower level of image distortion.
- It shows greater image stability with variations in temperature.
- They are very easy and inexpensive to make.

Typical characteristics for a Wedge and Strip anode are given in **Table 8.2**

Format	up to 1000×1000 pixels
Anode Size	25 mm × 25mm
Anode Resolution	25 μm
Number Of Amplifiers	3-4
Event Processing Time	10μsec

Table 8.2. Typical characteristics of a Wedge and Strip Anode

The Spiral Anode (SPAN)

The Spiral Anode developed by *Lapington et al* uses six electrodes, three per axis, to determine the presence and position of each event. The electrode structure, shown for simplicity in one dimension only, is given in **Fig 8.3.**

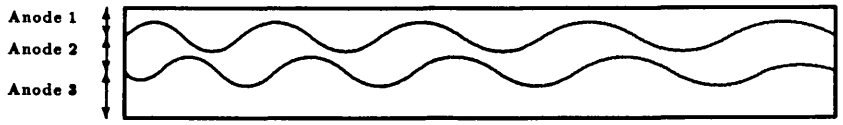

Fig 8.3. A 1-dimensional representation of the SPAN readout system

Three electrodes vary in width sinusoidally along both axes and at each position along the axis the pattern made by each electrode is unique [*Breeveld*]. An event deposits a quantity of charge onto each electrode, the amount of charge depending upon the event position along the axis. Encoding algorithms are used to find the event position (in $r\theta$ space) with respect to both axes, hence the name Spiral Anode.

SPAN displays a high image uniformity the maximum positional deviation being $<$ 30 μm across the whole imaging area and possesses a high spatial resolution. Typical characteristics of a spiral anode is given in **Table 8.3**

Format	512x512 pixels
Anode Size	25 mm x 25mm
Anode Resolution	10 μm
Number Of Amplifiers	6
Event Processing Time	4μsec

Table 8.3. Typical characteristics of a Spiral Anode

8.2.2 Event Detection Using Coincidence Encoding Anode Arrays

The readout cameras described above determine the position of each event by measuring the ratio of charge deposited on different charge sensitive electrodes. Another way in which the event position can be determined is by using arrays of coincidence electrodes. In this case the event position is determined by the event triggering certain electrodes and not others. The combination of triggered electrodes is related to a unique position on the array and so the event position can be found from a knowledge of which electrodes have been triggered. In this case, the variation in detector output with event position is not an analog quantity but a digital one as an electrode is either triggered or it is not triggered.

There are many photon counting detectors which employ coincidence encoded anode arrays, the Codacon and the MAMA detector being just two. Only the MAMA detector is discussed here as it has a superior set of performance characteristics.

The Multi-Anode Microchannel Array (MAMA)

The MAMA detector developed by *Timothy et al* consists of a MCP intensifier and an encoded anode readout camera. The anode can take several forms but all are similar to that shown in **Fig 8.4.** This diagram represents those electrodes required to detect the position of events in just one dimension. In order to form a 2-dimensional detector, two sets of electrodes are placed orthogonal to and insulated from each other.

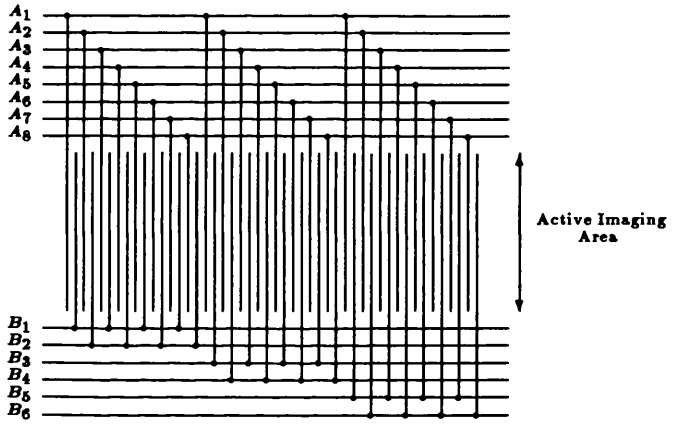

Fig 8.4. One electrode configuration for the MAMA readout system

Using this electrode configuration a total of (m×n) pixel elements in each dimension can be formed from (m+n) amplifier and discriminator circuits. This allows the MAMA detector to potentially have a very large image format and yet have relatively simple electronics associated with it. Because the event is digitally sampled, the anode resolution does not depend upon the intensifier gain but upon the anode to anode spacing which is typically 25μm. This means that the intensifier can be run at gains of 10^6 instead of the 10^8 required for most anodes which employ analog positioning techniques.

Typical performance characteristics for a photon counting detector employing a MAMA readout system are given in **Table 8.4**

Format	256×1024 pixels
Anode Size	6.4×26 mm
Anode Resolution	25 μm
Number Of Amplifiers	120
Event Processing Time	1μsec

Table 8.4. Typical characteristics of the MAMA detector

8.2.3 Event Detection Using The Rise Time Method

Another method of capturing and determining the position of charge events emerging from a MCP intensifier is the *rise time method* [*Siegmund* [2] *et al*][*Williams* [2] *et al*]. In this case events fall onto a conducting *delay line*, whereby the time difference in the charge reaching each end of the delay line is a measure of the 1D event position. By using two orthogonal delay lines, an estimate of the event position can be made in two dimensions.

The Delay Line Readout

A typical delay line anode is composed of an orthogonal pair of electrically independent conducting wires which are wound around a rectangular substrate, like that developed by [*Williams* [2] *et al*] and shown in **Fig 8.5.**

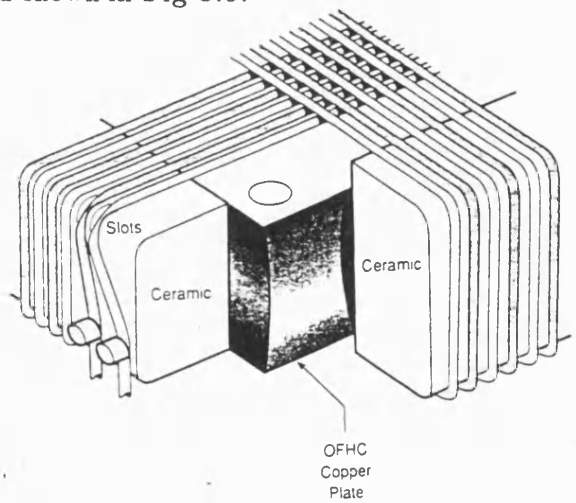

Fig 8.5. Schematic of a Delay Line readout system

The anode shown above consists of two, 200μm thick, delay lines each made of copper zirconium wire and wound around (but electrically separated from) a copper substrate with a pitch of 1mm. The two delay lines are separated from each other by a gap of 1.5mm

and each is held at such a potential that the event charge is divided equally between both of them. The charge associated with an event is then collected on one winding of each of the two delay lines.

When an event is captured on the anode, the charge dissipates towards both ends of a delay line and the time difference between the charge reaching each end is measured. This time difference is converted into digital form using a time-to-digital converter (TAC) having a typical conversion speed of 1μs. If another event arrives within this processing time both events are discarded and so the conversion speed of the TAC determines the dynamic range of the anode.

Delay line anodes can have very large active imaging areas and high resolutions provided the intensifier gain is high (2-3x10^7) and the pre-amplifier noise is kept to a minimum. In order to determine the event position to the highest accuracy the anode is designed such that each event produces a signal whose leading edge is sharp and whose width is narrow. These anodes typically have a low degree of barrel distortion associated with them introducing a maximum positional inaccuracy of 100μm over the whole field.

Typical performance characteristics for a photon counting detector employing a delay line anode readout is given in **Table 8.5**

Format	2500 FWHM per axis
Anode Size	130x130 mm
Anode Resolution	50 μm
Number Of Amplifiers	4
Event Processing Time	1μsec

Table 8.5. Typical performance characteristics of a Delay Line Anode

8.3 Photon Sensitive Readout Detectors

Apart from detectors such as MIC, that employ cameras for event capture [*Carter*], the only other known photon counting detector which has a photon sensitive readout is the PAPA (Precision Analog Photon Address) detector [*Papaliolios et al*].

8.3.1 The PAPA Detector

The PAPA detector employs a MCP intensifier with a P47 output phosphor and, instead of using a CCD camera to capture each event, it uses an array of photomultipliers, **Fig 8.6.**

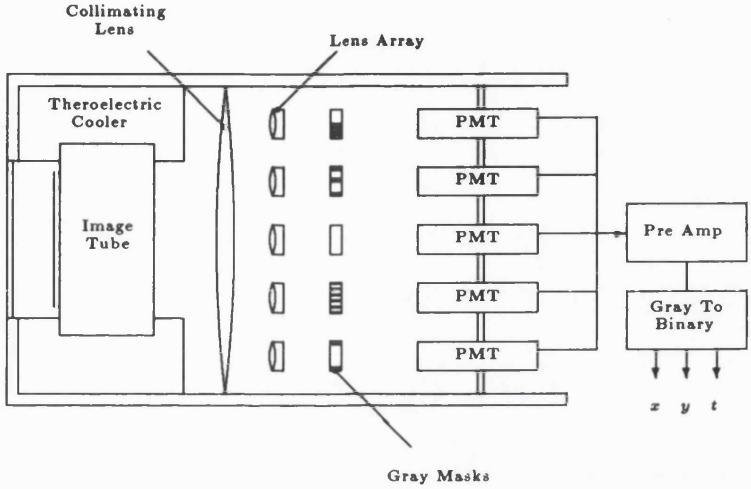

Fig 8.6. Schematic of the PAPA photon counting detector

A mask is placed in front of each photomultiplier which would otherwise see an image of the intensifier output phosphor. Each individual mask is made up of a different pattern of transparent and opaque areas each pattern representing one element of a gray code. The presence of an event is only detected by a photomultiplier if the event position is such that it corresponds to a transparent area of the mask placed in front of it. From knowing which photomultipliers in the array have detected an event, the event position can be determined. An array of 2×9 photomultipliers (producing a 9-bit address in both the x and y dimension) and masks will produce a detector format of 512×512 pixels. Once an event has been detected its position is translated from gray code into binary code and is then stored directly on magnetic tape.

The P47 output phosphor possesses a rise time of 20nsec and a decay time of 200ns [*Papaliolios et al*]. This decay time is far faster that of the P20 phosphor whose fastest decay component has a typical decay time of 2μs.

The detector format is limited by a combination of the intensifiers' active imaging area and the size of the photomultiplier array. Because the optical elements placed between the intensifier and the photomultipliers are imperfect, and there are small misalignments in the coded masks, pixel to pixel count variations of 30% rms can arise. However, these

imperfections tend to be stable over long time periods and so their effects can be reduced by flat fielding.

Typical performance characteristics for a PAPA photon counting detector are given in **Table 8.6**

Format	512×512 pixels
Active Imaging Area	Limited By Intensifier
Resolution	30 μm
Event Processing Time	1μsec

Table 8.6. Typical characteristics of a PAPA Detector

8.4 Comparing The DQE Of Each Detector

As stated in Chapter 7, the DQE of a photon counting detector is a product of the intensifier DQE and the readout camera DQE. The readout camera invariably has a very high DQE because the intensifier is set up such that most events have sufficient gain to lie above the event discrimination threshold. The DQE of a photon counting detector is therefore mainly dependent upon the intensifier DQE.

There are only a few factors which determine which intensifier is most suitable for use with which readout camera. Firstly, each event output from the intensifier must be of the correct form i.e. a charge event for charge sensitive readout detectors and a scintillation of light for photon sensitive readout cameras. Secondly, an intensifier must provide a sufficiently high gain to ensure that events are amplified well above the cameras' readout noise, ensuring it is detected and accurately positioned. The intensifier components which affect the different forms of output event and gains are not responsible for changing the intensifier DQE. Providing that each detector employs an intensifier with a similar input window, photocathode and front channel plate Open Area Ratio they will each have very similar DQEs (Chapter 7). Thirdly, the intensifier must have a sufficiently broad spectral range and its photocathode have a sufficiently high sensitivity to ensure a high performance from the detector in the application to which it is put. Photon counting detectors used for different applications (e.g. requiring the detection of photons over a different wavelength range) are unlikely to have the same DQE.

Photon counting detectors used in a vacuum environment, for example, for the direct

detection of soft X-rays and extreme UV light, require an intensifier with no input window or photocathode i.e. it is an open window intensifier. The intensifier RQE will depend upon the front channel plate OAR and the probability with which these energetic photons can liberate a photoelectron from the front MCP [*Vallerga et al*]. If the same detector is used outside a vacuum environment, an input window is required, together with an X-ray scintillator. In conclusion, the DQE of each detector is virtually the same for a fixed intensifier input configuration.

8.5 Comparing The Spatial Resolution Of Each Detector

The first types of resistive anode were disk shaped and suffered from a large degree of image distortion. As a consequence the image uniformity was worse than 500μm. The anode geometry suggested by [*Gear*] and shown in **Fig 8.1** produces images with virtually no distortions associated with them. However, this geometry does introduce a higher degree of thermal noise over the anode which means that MCP gains as high as 10^8 are required in order for the anode to have a spatial resolution of 200μm.

Conducting anodes such as the Wedge And Strip Anode, and the Quadrant Anode [*Lampton* [2] *et al*], do not suffer from thermal noise in the same way as resistive anodes do. Their main two sources of anode noise, both of which affect the event position, are a) noise associated with the front end of each pre-amplifier and b) partition noise caused by statistical variations in sampling a limited number of electrons per event with more than one electrode [*Lapington* [2] *et al*]. The typical spatial resolution of a Wedge And Strip anode is 25μm and is achieved with intensifier gains of 10^7 [*Timothy* [3]].

By allowing each event to extend over several sampling elements of the anode readout, the Spiral anode is theoretically able to determine the position of each event to an accuracy as high as 10μm [*Smith et al*]. In order to achieve these results the intensifier is set up to produce a charge gain of $10^7 e^-$ which is 10^2 times greater than that required by MIC.

Because the MAMA detector does not employ any type of event centroiding, the anode resolution is determined solely by the spacing between each charge collecting electrode [*Morgan et al*]. This spacing is typically 25μm and so the pixel size of the MAMA anode is typically 25μm square with the pixel centre lying midway between two electrodes. If the MAMA is used in conjunction with an intensifier employing 12μm pores on 15μm spacings

the overall spatial resolution of the MAMA detector would be close to 32μm.

The spatial resolution of a delay line anode is mainly dependent upon the event shape as presented to the timing electronics (i.e. the distribution of event charge with time) and the pre-amplifier noise. The timing electronics ideally require the temporal distribution of event charge to have a fast rise time and a narrow width. This is best achieved by increasing the intensifier gain. By cooling both the preamplifiers and the TAC (Time to Analog Converter) electronics and employing an intensifier gain of 3×10^7, a delay line resolution as high as 18μm has been obtained [*Williams et al*]. This still compares poorly to the centroiding resolution of the MIC detector which is only 2μm (Chapter 5).

The PAPA employs a series of gray coded masks in order to determine the position of each event, the precision of which depends upon the number of photomultipliers and masks per axis [*Papaliolios et al*]. Nine photomultipliers along each axis produces an image format of 512 pixels in both the x and y dimensions, but for each additional photomultiplier/mask per axis the image format can be doubled. Ultimately the camera resolution is determined by the precision to which the masks can be aligned and the quality of the imaging optics placed in front of each mask. There are significant image distortions associated with obtaining a 512^2 camera format and so increasing the format further becomes difficult.

Apart from the resistive anodes which have very poor resolution most readout cameras have very similar resolutions. Many of the cameras have been able to resolve their intensifiers MCP pores suggesting that the resolution of the SPAN, MAMA and Wedge and Strip Anodes are limited not by the readout camera but by their intensifiers.

8.6 Comparing The Dynamic Range Of Each Detector

The dynamic range of these photon counting detectors is limited at the faint limit by either the photocathode dark current, for closed intensifier systems, or by the MCP dark current for open intensifier systems [*Siegmund*]. The bright limit of dynamic range is governed by coincidence losses within both the intensifier and the readout camera.

8.6.1 Event Coincidence Within The Intensifier

Two events are coincident within the intensifier if:

- an event arrives within a time, T_i, of a previous event, where T_i is the intensifier dead time.

- the same event is located within a radius R_i of the previous event. R_i is the radius over which each event depletes sufficient charge from the surrounding pores that a second event arriving within a distance R_i and a time T_i is not amplified above the noise discrimination threshold of the readout camera (as described in Chapter 7).

The readout cameras described above can all be used in conjunction with MCP intensifiers and so the way in which coincidences take place within the intensifier of each detector is similar in all detectors. .

8.6.2 Event Coincidence Within The Camera

Two events cannot be processed simultaneously without one affecting the signal produced by the other, except in the case of the MAMA and PAPA detectors where all coincident events are rejected. After capturing an event, electronic readout cameras must firstly process that event before a following event can be evaluated. Typically, once captured, each event is sampled, processed and ultimately stored in computer memory. These processes take a time T_e, dependent on the type of readout camera used. When one event arrives within a time T_e (referred to as the *electronic dead time*) of a previous event both events are said to be coincident and depending upon the readout camera only one, the combined event, (for the Resistive Anode, Wedge and Strip Anode and the Spiral Anode) or in some cases neither (for the MAMA and PAPA) of the events are recorded. One event is coincident with another event if they arrive within the electronic dead time of one another independent of their spatial positions.

If events are coincident on the Resistive Anode, the Wedge and Strip Anode or the Spiral Anode then it is the event position corresponding to the mean position of all the associated events that is recorded. This causes what is called a 'ghost' event to be recorded at a position where there is no real event. For example, if there are two very intense point source images in the field of view, a ghost image will appear half way between them.

If two events are coincident on the MAMA or PAPA readout cameras then both events are rejected in which case no 'ghosting' occurs and the image quality is improved. Coincident events can be rejected by these cameras due to the coincidence encoding method

by which an event position is determined. In reality this method of rejecting coincident events makes little difference to the detectors' dynamic range but improves the image quality considerably.

The problem of 'ghosting' is minimised in the MIC detector because two events are only spatially coincident with each other on the CCD camera if their profiles overlap. The FWHM of an event is typically 1.3 CCD pixels and so only events separated by less than 1.3 CCD pixels ($\sim$ 90μm at the intensifier) in the same CCD frame produce a 'ghost' event. When this does occur the resulting 'ghost' event is detected very close ($\sim$ 0.7 CCD pixels) from both the real events and so the decrease in image quality is far smaller than for most electronic readout cameras.

8.6.3 Dynamic Range Simulations

In order to model the bright limit of dynamic range for photon counting detectors which use the readout cameras described above, a number of computer simulations have been created by the author. These simulations are intended to predict the upper limit of dynamic range for each detector and observe the affect that changes to the intensifier dead time and the readout cameras' electronic dead time T_e, make.

There are two types of model, one which simulates the variation in point source dynamic range for different intensifier and electronic dead times, and one which does the same but for simulated flat field illuminations.

Point Source Dynamic Range Simulations

The readout cameras described above have electronic dead times of typically between 1μs and 10μs. Even an electronic dead time of 10μs is one hundred times shorter than the dead time of the MIC intensifier which is estimated to be close to 1ms. The point source dynamic range of an electronic readout detector is therefore expected to be limited by the intensifier and not the readout camera.

Each dynamic range model simulates coincidence losses between photons in the intensifier in exactly the same way as that carried out for the simulations of the MIC detector (described in Chapter 4). In these point source dynamic range simulations all events are assumed to be spatially coincident within both the intensifier and the readout camera. This is a valid assumption because:

- the area over which an event depletes charge from the intensifier (the *dead area*) is greater than the FWHM of a narrow 'point source' image [*Edgar et al*].

- As stated previously, spatial coincidence is independent of event position and so two events arriving within a time T_e of one another will be coincident on the camera.

Given this assumption, if two or more events are coincident in time within the intensifier, only one of these (the first) is detected by the readout camera. If two or more events are coincident in time on the readout camera then, because all these events are spatially coincident, just one event is recorded.

Fig 8.7 shows the simulated point source dynamic range curves describing the photon counting detectors discussed in this chapter.

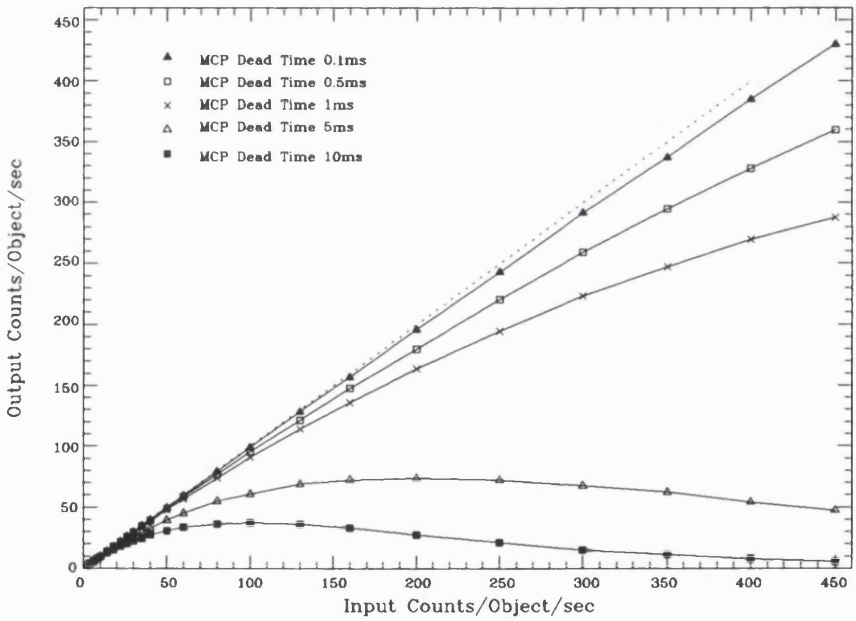

Fig 8.7. Simulated point source dynamic range curves for electronic readout photon counting detectors

The curves represent the dynamic range response of a MCP intensifier (whose dead times are labeled on the diagram) and a readout camera possessing a fast electronic dead time of 0.5μs. Identical simulations have been carried out for electronic dead times in the range of 0.1μs and 10μs. There was found to be virtually no difference between these curves and those shown in **Fig 8.7**, and hence the curves shown in **Fig 8.7** represent the response of all the detectors described in this chapter.

The simulations indicate that the point source dynamic range of a photon counter whose electronic dead time is far smaller than the intensifier dead time, is determined not

by the readout camera but solely by the intensifier. For example, for an intensifier dead time of 0.1ms, 10% coincidence occurs at a count rate as high as 1100Hz while for a dead time of 10ms 10% coincidence takes place at a count rate of only 14Hz. It is therefore highly desirable to run the intensifier with as small a dead time as possible.

Intensifiers run at gains of $10^5 - 10^9$ are thought to have a dead times of between 1ms and 100ms depending upon the gain [*Cho et al*]. Given this range of intensifier dead times the point source simulations in **Fig 8.7** predict that all the photon counting detectors described above are not expected to have a bright limit of point source dynamic range which exceeds 25Hz as even in the best case condition (i.e. for MAMA) the intensifier gain is still greater than 10^6. This is in contrast to the MIC intensifier which is believed (Chapter 4) to have an intensifier dead time of 1ms made possible by running at a charge gain of only 5×10^4. In this case the bright limit of dynamic range is limited by the CCD camera and not the intensifier, being 200Hz for a CCD frame time of 1.5ms and 25Hz for a frame time of 10ms.

Timothy et al have been able to increase the point source dynamic range of the MAMA detector to as high as 100Hz. This is higher than that predicted by the simulations, where a MCP dead time of 5ms was assumed. In these experiments they used an intensifier employing 'hot' channel plates (very low resistance MCPs) [*Siegmund* [4] *et al*]. Once charge is depleted from a 'hot' channel plate the pore is replenished at a faster rate than that experienced from normal channel plates so the effective dead time of the intensifier is smaller. Extrapolating from **Fig 8.7** the dead time of this 'hot' channel plate intensifier can be extrapolated. The intensifier is estimated to have a dead time of only 1ms, some 5-10 times higher than intensifiers possessing normal channel plates.

In conclusion, although the electronic dead time of charge readout cameras is extremely fast (it can be made as small as $0.1\mu s$ for the MAMA detector) their point source dynamic range is limited not by the camera but by the intensifier. An intensifier which produces charge gains of 10^6-10^8 has a dead time of between 5ms and 10ms, much larger than the dead time associated with the camera. The MIC intensifier requires a charge gain of only 5×10^4 and is thought to have a dead time of only 1ms. The point source dynamic range of the MIC detector is limited by the CCD camera and not the intensifier and can be up to 8 times greater than for detectors employing high gain intensifiers.

Flat Field Dynamic Range Simulations

Dynamic range simulations were also carried out in order to model the response of each detector to a flat field illumination. In this case events are assumed coincident if:

- Two or more events are spatially coincident within the intensifier i.e. one event arrives within a distance R_i (the dead radius) of a previous event, and it does so within a time T_i (the intensifier dead time) of that previous event [*Edgar et al*].
- One or more events arrive anywhere on the readout camera within a time T_e (the electronic dead time) of a previous event [*Timothy et al*].

In order to directly compare the response of each detector with that of MIC the simulations have been carried out also assuming:

- That each detector employs the same sized intensifier whose active imaging area is 25mm in diameter. This is the same size as the intensifier used in the dynamic range simulations of the XMM-MIC and described in Chapter 4.
- Each event passing through the intensifier fully depletes charge from an area, known as the dead area, (Chapter 4) whose radius, R_i, is three pore spacings from the event centre. For all but the last simulation, the dead area is assumed to be the same for the MIC intensifier and intensifiers used with charge readout cameras. This assumes that intensifiers producing events with different gains have a similar dead area and represents the best case condition for charge readout detectors.
- Each camera is assumed to have a square format whose size is 17.6mm^2 (the maximum square format which can be imaged by the 25mm diameter intensifier).

Fig 8.8 shows the simulated flat field dynamic range response of a photon counting detector of the type described above, whose electronic dead time is 10μs. The simulations were carried out for intensifier dead times of 0.1ms, 0.5ms, 1ms and 10ms. The Resistive Anode and the Wedge And Strip Anode typically have an electronic dead time of 10μs and are therefore represented by these curves.

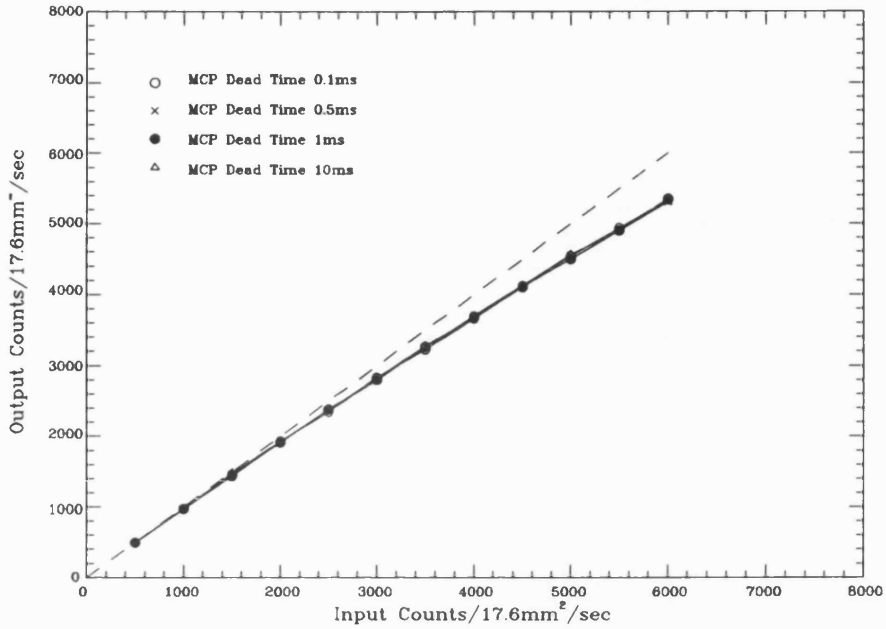

Fig 8.8. Simulated flat field dynamic range curves for a photon counting detector with an electronic dead time of 10μs and a MCP dead radius of 45μm.

The flat field dynamic range response appears to be virtually independent of the intensifier dead time (over the range of dead times displayed here) as the curves follow each other closely. Instead, most coincidence losses occur on the anode itself because, although the electronic dead time is some 10-1000 times less than the intensifier dead time, two events are spatially coincident on the anode independent of their position. Because the electronic dead time is relatively large compared to, for example, the MAMA and PAPA detectors, the bright limit of flat field dynamic range is very small, typically 5000 counts/sec over the whole area.

Fig 8.9 shows the simulated flat field dynamic range response for a similar electronic readout detector whose electronic dead time is this time only 5μs. These simulations were also carried out for intensifier dead times of 0.1ms, 0.5ms, 1ms and 10ms. The Spiral Anode (SPAN) has an electronic dead time close to 5μs and is therefore represented by these curves.

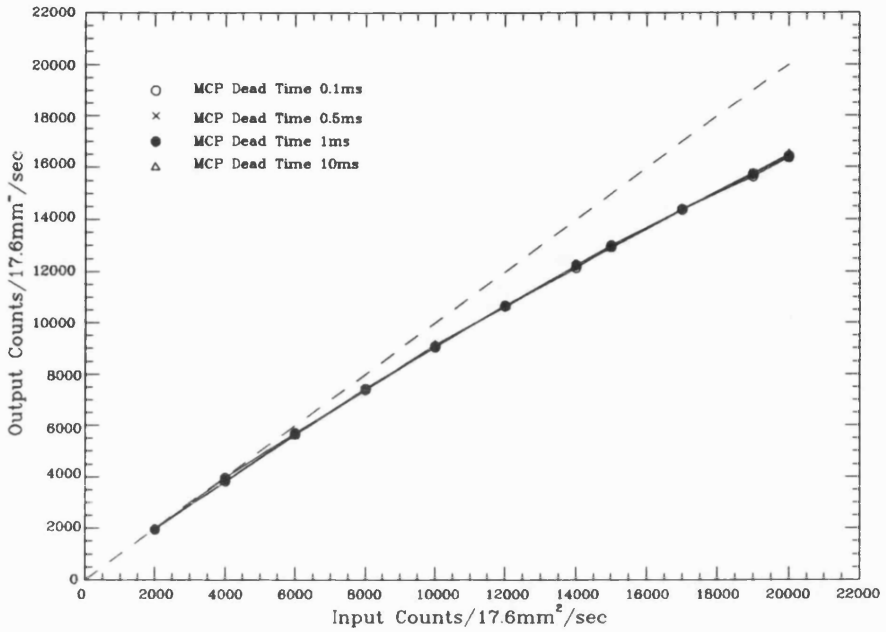

Fig 8.9. Simulated flat field dynamic range curves for a photon counting detector with an electronic dead time of 5μs and a MCP dead radius of 45μm.

Once again, the flat field dynamic range response for this detector is virtually independent of the intensifier dead time. 10% coincidence occurs at a count rate of 15000 counts/sec over the whole area. This is three times greater than for the Resistive Anode and Wedge and Strip detectors whose electronic dead times are only twice as large. The flat field dynamic range is therefore very sensitive to changes in the electronic dead time.

Fig 8.10 shows the simulated flat field dynamic range response expected from a photon counting detector whose electronic dead time is 0.1μm. Versions of the MAMA, PAPA and Delay Line detectors, optimized in terms of their event processing speed can have electronic dead times as small as 0.1μs.

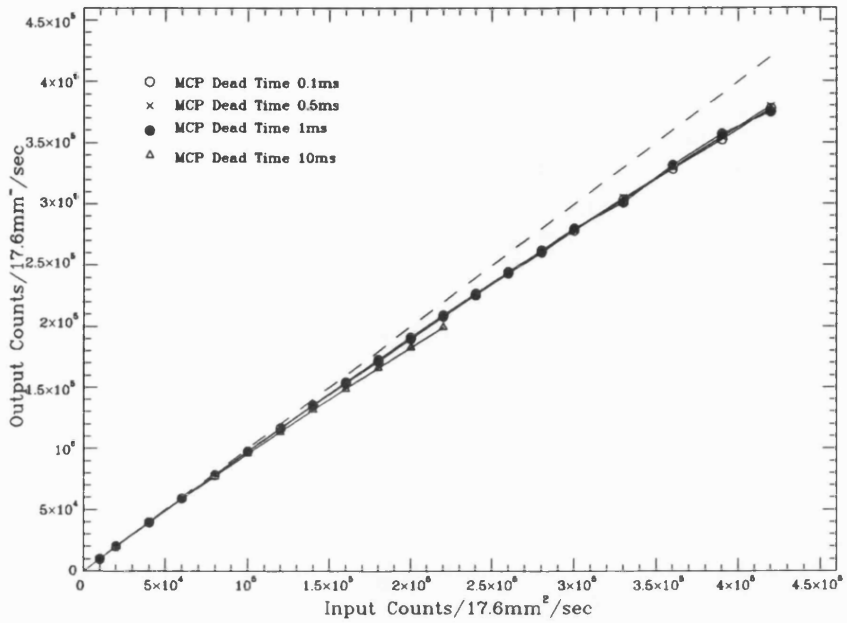

Fig 8.10. Simulated flat field dynamic range curves for a photon counting detector with an electronic dead time of 0.1μs and a MCP dead radius of 45μm.

In this case the electronic dead time is so low that for MCP dead times between 0.1ms and 1ms, 10% coincidence occurs at a far higher count rate of close to 4.2×10^5 counts/sec over the whole area. A MCP dead time of 10ms is large enough to cause a significant number of coincidence losses within the intensifier itself. For a MCP dead time of 10ms, 10% coincidence occurs at only 2.4×10^5 counts/sec over the whole area. A dead time of 10ms is close to that expected for any intensifier which produces high gain events (including the PAPA detector which employs a charge gain of typically 10^7) and so we expect the intensifier to have a significant affect on the flat field dynamic range of a real detector of this type.

So far these simulations have been used to compare the flat field dynamic range of the MIC detector with that of other detectors assuming the intensifier used with both types of detector to be the same. The final simulation models the flat field dynamic range response of the readout cameras above with simulation parameters most appropriate for each detector.

Firstly, intensifiers with high charge gains are known to amplify events which deplete larger areas of the MCP than events amplified by intensifiers with small charge gains. It is therefore reasonable to simulate this effect by doubling the dead radius of the intensifier

(to 90μm) [*Edgar et al*] making the simulation more realistic. The flat field dynamic range of each detector was then modeled by assuming:

1. For the Resistive Anode, a MCP dead time of 10ms (because charge gains of 10^7-10^8 are used, and an electronic dead time of 10μs [*Lampton et al*].

2. For the Wedge And Strip Anode, a MCP dead time of 10ms for the same reason as above, and an electronic dead time of 5μs [*Siegmund* [3] *et al*].

3. For SPAN, a MCP dead time of 5ms and an electronic dead time of 5μs [*Ref* [4]].

4. For the PAPA and Delay Line Anode, a MCP dead time of 5ms and an electronic dead time of 1μs [*Papaliolios et al*][*Williams* [2] *et al*].

5. For the MAMA, a MCP dead time of 5ms and an electronic dead time of 0.1μs [*Timothy* [3] *et al*].

Fig 8.11 shows the simulated flat field dynamic range response for all six detectors.

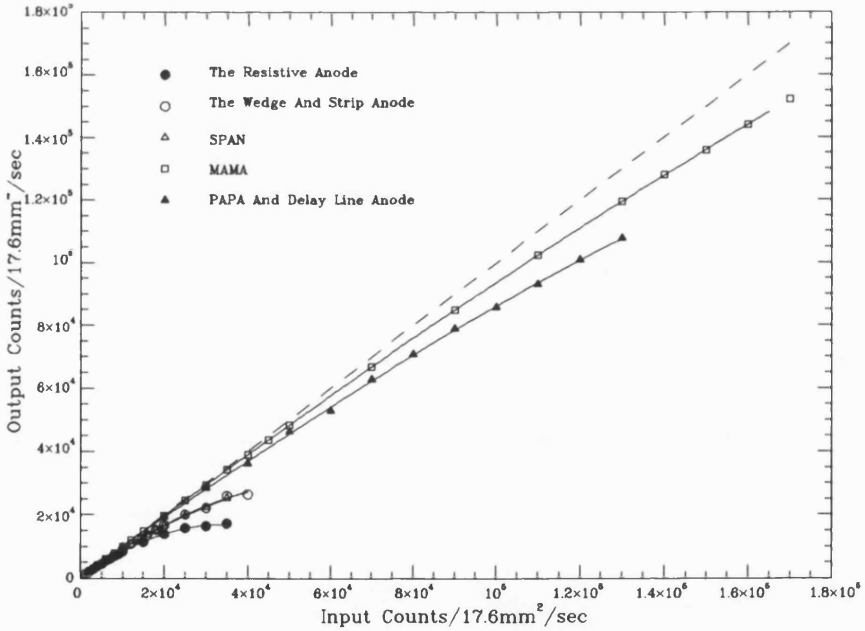

Fig 8.11. Simulated flat field dynamic range response of the Resistive Anode, Wedge and Strip Anode, SPAN, MAMA, PAPA and Delay Line photon counting detectors.

The results of this flat field simulation and the point source simulations given in **Fig 8.7** are summarized in **Table 8.7**.

Detector	Point Source Dynamic Range Counts/Object/Sec	Flat Field Dynamic Range Counts/17.6mm^2/Sec
MIC	25 (10ms frame time) 200 (1.5ms frame time)	3.2×10^5 (10ms frame time). (equiv) 2.3×10^6 (1.5ms frame time)
Resistive Anode	14	6×10^3
Wedge And Strip Anode	14	1.2×10^4
SPAN	25	1.2×10^4
PAPA	25	7×10^4
MAMA	25	1.7×10^5

Table 8.7. Comparison of MICs dynamic range with simulated data for several other photon counting detectors

The simulation results predict the dynamic range response of each detector system as a whole, both intensifier and readout camera. Although the electronic dead time of all these photon counting readout cameras is extremely fast ($<10\mu s$) these type of detectors are limited in dynamic range by two factors:

- The point source dynamic range is limited by the intensifier dead time. The detectors require a high internal gain which causes the intensifier dead time to increase.
- Because events are spatially coincident within the readout camera independent of their position, the flat field dynamic range of these detectors is greatly dependent upon the electronic dead time.

For these two reasons both the point source and flat flat dynamic range of the MIC detector is expected to be equal to or in most cases greater than the other types of photon counting detector described here. MICs' point source dynamic range is limited not by the intensifier, which is run at a low gain, but mostly by the CCD camera. By only partially reading out sections of the CCD the frame time can be made smaller thus increasing both the point source and the flat field dynamic range over sections of the CCD.

8.7 Summary

The DQE of all photon counting detectors is determined by the type of intensifier used. Most modern detectors use MCP intensifiers whose DQE are dependent upon the input window transmission properties and photocathode sensitivity (if there is one) , and the front channel plate open area ratio. Detectors which are used for similar applications will

have very similar DQEs as the type intensifier input window and photocathode will be chosen in order to maximize the DQE over the wavelength range required.

The resolution of Resistive Anode and Wedge and Strip type detectors is limited by thermal noise and noise associated with the pre-amplifiers. Its effect is best reduced by increasing the event gain (and hence the event signal to noise) with the effect increasing the intensifier dead time. The Delay Line Anode, the SPAN, MAMA and PAPA detectors require less event gain to achieve high anode resolutions but their overall detector resolutions, like MIC, are limited by the intensifier pore to pore spacing and the primary electron spread across the intensifier front gap.

The most significant way in which photon counting detectors differ is their dynamic range. The detectors described in this chapter all require events gains of typically 10^6-10^8, at least ten times higher than that required by MIC. As a result both the intensifier dead time and the area over which an event depletes charge is increased. This has a detrimental effect on the detectors' point source dynamic range which is limited to 25 counts/object/sec despite having electronic dead times as low as 100ns.

The flat field dynamic range of these detectors is limited by the electronic dead time of the readout camera. Because events are spatially coincident with each other no matter what their positions, events have to be processed in as small a time as possible in order to reduce the probability of event coincidence. Because a CCD camera has a pixelated structure and events are only spatially coincident if their profiles overlap, two events can be captured by the same CCD frame of the MIC detector and not be spatially coincident.

Tests carried out on the MIC detector over the last few years seem to indicate that the DQE and resolution performance of the detector can at least match those of other photon counting detectors currently available. The simulations carried out in this chapter indicate that MICs' dynamic range performance is superior to that of other photon counting detectors but because no real dynamic range curves (known to the author) have been published by other groups the simulations can only give a reasonable estimate of their actual dynamic range performance.

Chapter 9

Summary And Future Work

9.1 The XMM-OM

XMM is an ESA 'Horizon 2000' space observatory due for launch in 1998. Its primary scientific goal is to carry out astronomical observations in the X-ray wavelength range but in addition, the XMM-OM will carry out simultaneous observations in the optical and ultra-violet wavelength ranges. The OM will have two detectors, a CCD camera (the red camera) for the 650nm to 1000nm wavelength region and a photon counting detector (the blue camera) for the 150nm to 650nm wavelength region.

Initially, the choice of blue cameras for XMM-OM was between the prototype versions of XMM-MIC and SPAN. The SPAN detector was later withdrawn from these considerations and so the blue camera will be XMM-MIC. The required performance of XMM-MIC is that given in **Table 1.3** and reproduced here in **Table 9.1.**

No		White Light (150-650nm)	B-Band
1	Zodiacal Light Background (cnts/sec/arcsec^2)	0.2	0.04
	Count Rate from B=15th mag star (cnts/sec)	200	60
2	Maximum Point Source Count Rate (cnts/sec/object)	1000	
3	Detector Dark Count (cnts/sec/arcsec^2)	4×10^{-4}	
4	Brightest Star Observable (Mag)	13.2	12.0
5	Brightest Star Observable With Electronic Defocussing		~ 9
6	3σ detection limit in 1000s (equiv. B mag.)	24.0	23
7	Magnitude At Which 10% Variation Detectable in 1000s	20.5	19.5
8	Spectral Range	150-650nm	
9	Detector Lifetime	10 years	

Table 9.1 Performance characteristics required for XMM-MIC

These performance characteristics were set by taking into account two major factors:

- the typical number of photons per wavelength range emitted by stars of different magnitudes.
- the DQE of the OM telescope and detector by taking into account the aluminium reflectance, the dichroic reflectance, the filter transmittance and the DQE of MIC.

Because the DQE of the MIC detector was not known at the time at which these performance characteristics were being decided, a typical DQE response for the detector was assumed. This was done by assuming an intensifier OAR of 65% and using an RQE curve from a sample ITL tube with the response. As a result, the performance characteristics were set assuming the DQE response of XMM-MIC shown in **Fig 9.1.**

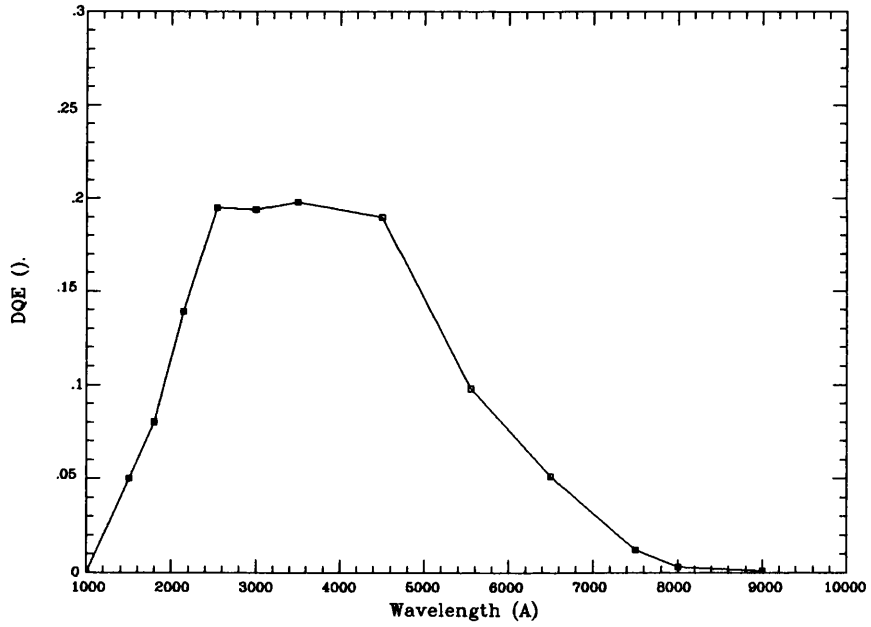

Fig 9.1. Assumed DQE curve of XMM-MIC on which the performance characteristics are based.

The DQE response shown in **Fig 9.1** is expected to be close to that obtained with the Space qualifiable 25mm intensifier tube (similar to that shown in **Fig 7.10**) and so this set of performance characteristics is valid for XMM-MIC.

9.2 Performance Of The XMM-MIC Detector

An estimate of how close XMM-MIC comes to meeting the performance requirements of the XMM-OM can be made by considering XMM-MICs performace characteristics as

summerized in **Table 9.2.**

Active imaging area	18mm×18mm
Maximum format	2048×2048 pixels
Pixel size	8.8μm
Spectral Range	170 nm - >550 nm
DQE	18%
Detector Resolution	18μm (White light)
Point Source Dynamic Range	> 25 cnts/pix/sec on full format 2048×2048 pixels > 25 cnts/pix/sec on full format. Double Counting Enabled (600 ADU). > 200 cnts/pix/sec on spectroscopic format 2048×256 pixels > 200 cnts/pix/sec on spectroscopic format. Double Counting Enabled (600 ADU).
Flat Field Dynamic Range	> 5 cnts/pix/sec on full format 2048×2048 pixels > 13 cnts/pix/sec on full format. Double Counting Enabled (600 ADU). > 35 cnts/pix/sec on spectroscopic format 2048×256 pixels > 70 cnts/pix/sec on spectroscopic format. Double Counting Enabled (600 ADU).
Dark Count (S20)	30-50 cnts/cm^2/sec

Table 9.2 Performance characteristics of the XMM-MIC detector

This is best carried out by discussing each requirement listed in **Table 9.1** individually.

1. Zodiacal Light Background. The expected zodiacal background count rate is $\sim$ 0.2 counts/arcsec^2/sec which is equivalent to 2.81 counts/CCD pixel/sec.

   The flat field dynamic range of the XMM-MIC detector is 5 counts/CCD pixel/sec over the maximum CCD format which can be increased to 16 counts/CCD pixel/sec if the double counting threshold (MCT) is enabled. If the MCT is disabled then XMM-MIC is able to count linearly on an extended object whose (white light) detected count rate is (5-2.81) counts/CCD pixel/sec. If the MCT is enabled then XMM-MIC can count linearly on extended objects whose count rate is as high as (16-2.81) counts/CCD pixel/sec.

   If a spectroscopic format is used then XMM-MIC is able to count linearly on extended objects whose count rates are as high as 32 counts/CCD pixel/sec (if the MCT is disabled) and 67 counts/CCD pixel/sec (if the MCT is enabled).

2. Point Source Dynamic Range. The point source dynamic range of the prototype XMM-MIC detector is 200 counts/sec using a spectroscopic format of 256×32 CCD pixels and 25 counts/sec using the maximum format of 256×256 CCD pixels. Enabling the MCT has no effect on the point source dynamic range at low count rates but increases detector linearity at high count rates.

   A count rate of 200 counts/object/sec is far smaller than the 1000 counts/sec required by XMM-OM but one way of increasing the dynamic range further is by using the dynamic range curve to extrapolate the input count rate from the detected count rate. In theory this method can be used up to count rates of > 500 counts/object/sec.

   The problem of any photon counting detector being able to count linearly on a point source count rate of 1000Hz is made more difficult when the MCP intensifier dead time is considered. Even the MIC intensifier which is run at a charge gain of only 5×10^4 typically produces 10% coincidence at only 700Hz for a point source.

3. Dark Current. The XMM-MIC intensifier is expected to employ an S20 photocathode. A typical S20 photocathode has a dark current of between 10-50 counts/cm^2/sec at temperatures between 15°C and 25°C, the operating temperature range of the intensifier. This corresponds to a dark current of 1.7×10^{-4} counts/sec/arcsec^2 in the worst case, more than two times lower than the requirements set by XMM-OM.

4. Brightest Observable Star Is 13.2 Magnitude. XMM-MIC is expected to record 200 counts/sec from a 15^{th} magnitude star. Using Pogsons Law (*Equ 9.1*) a 13.2 magnitude star is expected to produce 1050 events/sec. XMM-MIC is therefore required to count linearly up to 1050Hz. This is similar to requirement 2 (described above) and can only be achieved, at present, by extrapolating from a dynamic range curve, or by electronic defocussing (see below).

5. Brightest Star Observable With Electronic Defocussing. XMM-MIC is required to count linearly on a 9^{th} magnitude star. A 9^{th} magnitude star is expected to produce 15000 detectable events/sec which cannot be acheived unless the star is defocussed before reaching the detector.

   If the flat field dynamic range of the detector is 35 counts/CCD pixel/second (using a spectroscopic format) the star can be imaged by defocussing it over an area of

typically 21×21 CCD pixels. If the maximum image format is used then the star must be defocussed over an area of 55×55 CCD pixels.

6. <u>3σ Detection Limit In 1000 Seconds</u>. Let us consider a 24.0 magnitude star being observed in white light. If XMM-MIC detects 200 counts/sec from a 15^{th} magnitude star then using Pogsons' Law

$$m_1 - m_2 = -2.5log\frac{E_1}{E_2} \tag{9.1}$$

where m_1 and m_2 are the apparent magnitudes of stars 1 and 2, and E_1 and E_2 are the energies from each star [1], XMM-MIC will detect 0.05 counts/sec from a 24.0 magnitude star. So in 1000 seconds XMM-MIC will have detected $\sim$ 50 counts from the star.

The white light sky background count is expected to be $\sim$ 2.7 counts/CCD pixel/sec and so, if the detector dark current is 2.5 counts/CCD pixel/10^3 secs, the total background count will typically be 2700 counts/CCD pixel in 1000 seconds.

A star will typically subtend 10μm at the input to the detector and if the intensifier pore spacing is 7.5μm (as expected) then the star will have a FWHM of typically 20μm at the back of the intensifier. The best way of observing this star is to make the pixel size as close as possible to the star FWHM in order to increase the signal to noise ratio in that pixel. If events are centroided to $\frac{1}{4}$ of a CCD pixel then most of the star will be captured in a single subpixel. This sized subpixel will typically contain 40 counts from the star and 170 background counts.

Because a photon counting detector has no other sources of background noise we can use Poissonian statistics to determine the standard deviation (σ) of the background count, where

$$\sigma = \sqrt{\text{Background count}} \tag{9.2}$$

In this case, the number of counts/subpixel from the star is almost exactly 3σ and so a 24.0 magnitude star can be detected provided events are centroided to $\frac{1}{4}$ of a CCD pixel in both x and y.

If events are centroided to $\frac{1}{8}$ of a CCD pixel then the 3σ detection limit in 1000 seconds is only a 22.7 magnitude star.

[1] here we assume the stars are of the same type, with energies E_1 and E_2 being proportional to the number of photons/sec emitted from each star.

7. Magnitude At Which 10% Variation Is Detectable In 1000 Seconds. The calculations given above indicate that in 1000 seconds we expect 170 background counts/subpixel (when centroiding to $\frac{1}{4}$ of a CCD pixel). From Pogson's Law, XMM-MIC will detect 1260 counts/subpixel from a 20.5 magnitude star in 1000 seconds, most of which will be centroided into just one subpixel. A 10% variation in the stars count rate corresponds to $\sim$ 130 counts in 1000 seconds. This is well above the 3σ detection limit and so a 10% variation in a 20.5 magnitude star can be detected by XMM-MIC.

8. Spectral Range. The spectral range of the prototype XMM-MIC detector is dependent upon the transmission properties of the intensifier window and the spectral sensitivity of the intensifier photocathode. The DQE results presented in Chapter 7 were for a 25mm diameter intensifier (DEP Tube 1) which was found to have a long wavelength cutoff wavelength > 550 nm. The short wavelength cutoff at 170nm was caused by the quartz input window whose transmission at 160nm falls below 1%. The quartz window will, in future versions of the detector, be replaced by a MgF_2 window having a transmission cutoff below 150nm. This will ensure that the XMM-OM specifications in terms of spectral range (between 150-650nm) can be met.

9. Lifetime. The lifetime properties of the detector is a subject of future work (Section 9.3.1). The CCD is expected to be subject to radiation damage while the intensifier will be subject to long term gain depression [*Frazer*[4]] and a possible reduction in spectral sensitivity [*McMullan et al*].

The other performance characteristics of XMM-MIC are summarized below:

- DQE. Different intensifiers of the same design differ in their DQE response which is due to variations in photocathode sensitivity. Even photocathodes of the same type have slightly different chemical compositions and the way in which they are manufactured cannot be precisely reproduced. The DQE curve presented in **Fig 6.10** represents the DQE response of the XMM-MIC detector used in conjunction with DEP Tube 1. Although for this tube the peak DQE does not exceed 18%, by simply employing a higher sensitivity photocathode the detector DQE can be improved by at least 5%.

- Resolution. The prototype XMM-MIC has a resolution of $\sim 18\mu$m. The resolution is currently limited by the MCP pore spacing which for the DEP 25mm intensifiers is 15μm. Future versions of the detector may employ microchannel plates whose pores are 6μm in diameter with the distance between each pore being 7.5μm. This is not only expected to increase the detector resolution to 15μm but also reduce the degree to which *aliasing* takes place.

- Image Quality. Because a CCD has pixels which are physically fixed with respect to one another the MIC camera possesses a high degree of spatial stability. The detector does suffer from a small degree of global pincushion distortion introduced by the fibre taper coupling the intensifier to the CCD. However, the distortion is not expected to affect the tracking capability of the detector provided the satellite drift is small over each integration period and several stars are used for tracking at any one time.

  The intensifier photocathode, CCD and fibre taper all have regions of low sensitivity associated with them. These cause defects in an otherwise flat field image whereby some regions have less counts than others. These defects, which are stable over an integration period, can simply be compensated for in software during the data reduction stage.

  The most serious problems associated with the detectors' image quality is the affect of *aliasing* and *fixed pattern noise* both of which introduce unpredictable count modulations in an otherwise flat field image. The focus of future work is to try and reduce both these effects.

The performance characteristics of the XMM-MIC detector in most cases meet or come very close to the specifications set by the XMM-OM. XMM-MIC has demonstrated that it is suitable for Space applications and that later versions of the detector are expected to have a superior set of performance characteristics.

9.3 Future Work

To transform the prototype XMM-MIC detector into a space qualifiable detector further testing is to be carried out in the following areas:

9.3.1 The Detector Lifetime

One of the requirements of the XMM-OM is that it have an operational lifetime of 10 years. The main problem with predicting whether XMM-MIC can operate over this time span, is the lack of lifetime data presently available. Very few lifetime tests have been carried out with this kind of photon counting detector but the component that is expected to degrade most rapidly is the intensifier.

The lifetime of the intensifier photocathode is governed by outgassing from the microchannel plates (described in Chapter 2). Positively charged ions are accelerated towards the photocathode, evaporating small regions of the surface and greatly decreasing its red response.

Accelerated lifetime tests were carried out on a 40mm intensifier incorporating an S20 photocathode [*Norton*]. The photocathode was exposed to a photon flux equivalent to that expected from 3 years operation at a ground based observatory. The tests revealed that after exposure the S20 photocathode increased its QE in the blue by 1%, in this case from 21% to 22%. However it lost all its red response (due to evaporation of the surface cesium layer), causing it to have a QE response similar to that of a bi-alkali photocathode. Further lifetime tests have to be carried out under more realistic operating conditions. This means using intensifiers with highly scrubbed plates, to reduce outgassing, and a photon flux closer to that expected in a space environment.

In addition, the intensifier gain characteristics are expected to vary over the 10 year lifetime of the detector [*Pearson et al*][*Frazer*[3] *et al*]. This problem can be solved by remotely controlling the potential applied across each intensifier channel plate.

There are several other problems which XMM-MIC has to overcome in order to be safely deployed and operated in Space. These are:

1. **Mechanical Shock**

    - During both deployment and operation of the XMM-OM, XMM-MIC will be subjected to mechanical shocks. In the prototype version of XMM-MIC, the most vulnerable component expected to be affected by mechanical shock is the bonding between the fibre optic components these being between the intensifier and fibre taper, and the fibre taper and CCD. This should not be a problem

for the space qualifiable version of XMM-MIC which will employ a single fibre optic component, bonded directly into the intensifier and onto the surface of the CCD.

- The intensifier MCPs and electrical connection tags are vulnerable to mechanical shock. If they are housed and sealed correctly this is not expected to be a problem.

2. **Radiation Damage** There are two sources of radiation which will be encountered by the XMM-OM whilst in Space. These are:

   - The 'inner' proton belt which extends to an altitude of $\sim$ 15000km above the equatorial plane.
   - The 'outer' electron belt which extends to an altitude of 60000km above the equatorial plane.

   Radiation affects the OM by either causing permanent damage to the detectors or by producing radiation induced background noise. Several components of the detector are susceptible to radiation damage.

   (a) **The Intensifier Input Window.** When MgF_2 and Sapphire windows are exposed to high levels of radiation there is a degradation in their transmission properties [*Fowler et al*]. The materials appear to turn a brown colour as their short optical wavelength transmission (in the UV/blue) decreases at the fastest rate. The affect of radiation on the transmission properties of these windows is currently being evaluated.

   (b) **The CCD** is prone to radiation damage especially from protons [*Ref*[2]]. High energy protons interact with the silicon semi-conductor promoting electrons into the conduction band which are then stored in a pixel. This produces an additional source of noise. Because MIC is a photon counting detector each proton will typically give rise to only one count and only if sufficient numbers of electrons are released in order to produce an event above the noise threshold. Tests to be carried out on Thomson CCDs are expected to show that they are prone to permanent damage from radiation. EEV CCDs on the other hand,

are thought to be more resistant to large doses of radiation and so EEV CCDs are being considered for use with future versions of the detector.

(c) **The fibre optic taper** also suffers from 'browning' when exposed to high levels of radiation, decreasing its transmission performance. The affect of radiation on the transmission properties of the fibre taper is currently being evaluated but is not expected to be a problem as the intensifier gain can be increased to compensate for it.

(d) **The Electronics** are vulnerable to radiation. Each component has a radiation hard version of it except the analog to digital converter (ADC) for which a radiation hard version is currently unavailable.

3. **Thermal Damage** The thermal operating range for the XMM-OM, is from -15°C up to +55°C. The intensifier is expected to operate within a temperature range of 15°C to 25°C while the operating temperature range for the electronics and CCD is -30°C to +60°C. The CCD and electronics must be able to operate over this temperature range.

9.3.2 Fixed Pattern Noise

Once a fixed pattern noise correction has been carried out any change in the event rate leads to an increase in the level of fixed pattern noise (Chapter 6). This produces a degradation in the image quality which could otherwise only be partially corrected for in the data reduction stage.

The problem arises because as the event rate changes so does the average event width presented to the centroiding electronics. A change in event rate causes a change in the number of coincidences which cause events to be incorrectly centroided if the appropriate fixed pattern correction is not applied. Future work has to be carried out on producing a centroiding algorithm which can adapt to the various event profiles presented to it. This work is currently being carried out at UCL.

9.3.3 New Microchannel Plate Intensifier

Aliasing as described in Chapter 7 is produced by the MIC detector when the intensifier pore structure is oversampled by the CCD camera producing a count modulation in the

output image of a flat field illumination. For example, if the MCPs have a pore spacing of 15μm and events are centroided to $\frac{1}{8}$ of a CCD pixel (each subpixel being 34μm at the intensifier) an average count modulation of 20% is produced.

In order to reduce the degree of aliasing it has been proposed that XMM-MIC employ an intensifier whose MCPs have a pore to pore spacing of only 7.5μm and a pore diameter of 6μm. In this case, for a subpixel size of 34μm the average level of fixed pattern noise decreases to 7%.

The effect of using MCPs with smaller pore diameters and spacings has not yet been determined. An intensifier employing these types of plate may have different dead time characteristics to the types of plate used during initial detector tests. The detector resolution should also decrease but with unknown consequences. In order to discover the characteristics of a detector employing such an intensifier extensive new tests will have to be carried out in the future.

9.4 Other Applications Of The MIC Detector

Because of its small size and ease of use it is possible to develop different versions of the MIC detector to suit different applications. Of these, three main applications have been persude, two of which are outside the field of astronomy.

9.4.1 BIGMIC

A 75mm diameter version of the MIC detector, called BIGMIC, is currently being developed at UCL. It is expected to have:

- An active imaging area of 61mm×46mm.
- Pixel size options of 10μm,20μm,40μm and 80μm square.
- A maximum format of 6100×4600 pixels.
- A resolution $< 25\mu$m.
- A (full format) frame time of 50ms.
- Quantum Efficiency of $> 14\%$

- Bright limit of dynamic range > 100,000 counts/sec over the whole detector area
  ~ 6 counts/pixel/sec on narrow emission line on full format
  ~ 50 counts/pixel/sec on narrow emission line on spectroscopic format

BIGMIC has primarily been developed with three main applications in mind:

For Large Telescopes

The next generation of large telescopes will be designed to have a maximum throughput i.e. demagnifying optics will not be employed to make the image plane smaller unless absolutely necessary as these introduce additional losses. The typical image plane of a large telescope is therefore expected to be 70-80mm in diameter and so in order to image the whole field a detector possessing a 70-80mm diameter is required, making BIGMIC ideal for this application.

2 Degree Field

The AAT will in the near future be able to image a 2° star field. This will have a fibre optic feed which will take data from individual stars within the field. The larger the detector used to image this data , the greater the number of stars that can be imaged at any one time.

For The ECHELLE Spectrograph

An echelle spectrograph splits a light spectrum into a number of orders (echellogram) covering a relatively large spatial area. A large detector area is therefore required to maximize the observed spectral range. Recently, at the AAT, a very high resolution facility (UHRF) with a resolution of 10^6 has been incorporated. This takes just one order from the echelle and provides a high resolution 1D spectrum. The spectrum would be undersampled by directly imaging it with a CCD camera (whose pixels are typically $23\mu m \times 23\mu m$) and so a large format, high resolution photon counting detector is required instead.

9.4.2 X-Ray Crystallography

The MIC detector has been used in trials at the Daresbury X-ray synchrotron facility in order to assess the X-ray detection performance characteristics of the detector. X-ray

photons were down converted into optical photons using a Gadox screen placed in front of the detector. MIC was required to produce relatively low resolution images of Bragg spots in time slices of a few seconds. MIC was successful in imaging Bragg spots of both very high and low intensity whilst producing uniform Bragg spot profiles [*Oldfield et al*].

Ideally MIC requires a higher DQE in order to detect faint Bragg spots in such small integration times. It also requires a high dynamic range in order to avoid coincidence losses at the high count rates encountered while imaging intense Bragg spots. Whilst not too much valid data was taken during these initial trials (due mainly to saturation of the calibrating photographic images) these trials have proved that MIC, which is primarily used for optical applications, can be used for X-ray applications.

9.4.3 Bio-Medical Imaging

There are many applications in bio-medicine in which florescent dies are used to mark biological material. In the field of genetics individual genes are identified with the use of different dies which mark specific gene materials. These images currently takes several hours to analyse because they are simply scanned with a single channel photomultiplier. This process is very time consuming and because hundreds of these tests should take place in a single week, a faster alternative would be extremely beneficial.

The MIC detector is ideal for these applications because it is a faint light imaging detector which can scan a whole image in the same time it takes a photomultiplier to scan a few small sections of the same image. Because data can be stored and analysed by MIC the process of data retrieval and data reduction is also made very much simpler.

A prototype version of the MIC detector designed specifically for bio-medical applications is currently under construction at UCL.

References

Anger.H.O, Martin.C, Jelinsky.P – "Wedge And Strip Anodes For Centroid-Finding Position Sensitive Photon And Particle Detectors" – Rev Sci Instrum 52(7), Jul 1981

Beaver.E.A,Acton.L,Wenzel.H. – "S-20 Photocathode Stability Considerations" – 9th Symposium On Photoelectronic Images Devices. Imperial College London. September 1987.

Bellis.J.G. – "Fibre Taper Distortion Associated With The MIC Detector" – Report To XMM-OM 10-Oct-91

Beynon, Lamb – "Charge Coupled Devices And Their Application" – McGraw-Hill Book Company (UK) Ltd (1980)

Boksenburg.A. – "Astronomical Use Of Television-Type Image Sensors" – Proc Symp At Princeton University (NASA SP-256) (1970)

Boutot.J.P,Delmotte.J.C,Mieke.J.A. – "Impulse Response Of Curved Microchannel Plate Photomultipliers" – Rev Sci Instum 48 (1977) P 1405

Breeveld.A.A, Edger.M.L, Smith.A, Lapington.J.S, Thomas.P.D. – "A SPAN MCP Detector For The SOHO Coronal Diagnostic Spectrometer" – SRI-91 Conference Proceedings

Carter.M.K, Cutler.R, Patchett.B.E, Read.P.D. – "Transputer Based Image Photon Counting Detector" – Internal Paper RAL

Carter.M.K. – "Data Processing Requirements In A Centroiding Photon Counting System" – Internal Paper RAL Jan 1991

Cho.D.J, Morris.M.G. – "Local dead Time Effects In Microchannel Plate Imaging Detectors" – SPIE Vol 976 Statistical Optics (1988)

Csorba.I.P. – "Image Tubes" – Published By Howard W. Sams and Co, Inc (1995)

Dick.J.S.B, Jenkins.C.R, Ziabicki.J. – "Design Fundamentals Of Algorithms For Photon Counting Systems" – PASP Vol 101:684-689,1989

Dubovoi.I.A, Chernikov.A.S, Prokhorov.A.M. – "Multialkali Photocathodes Grown By The MBE Technique" – General Physics Institute, USSR Academy Of Science, Moscow. (1992)

Eberhardt.E.H. – "An Operational Model For Microchannel Plate Devices" – IEEE Trans On Nuclear Science Vol NS-28 No 1 Feb 1981

Eberhardt.E.H. – "Image Transfer Properties Of Proximity Focused Image Tubes" – Applied Optics Vol 16 No 8 Aug 1977

Eberhardt.E.H. – "Gain Model For Microchannel Plates" – Applied Optics 18,1418 (1979)

Eccles.M.J, Tritton.K.P. – "Low Level Light Detectors In Astronomy" – Cambridge University Press (1983)

Edgar.M.L, Lapington.J.S, Smith.A. – "The Spatial Extent Of Gain Depression For MCP Based Photon Detectors" – Rev Sci Instrum SRI 91 Proceedings (1991)

Fordham.J.L.A, Bone.D.A, Oldfield.M, Bellis.J, Norton.T.J. – "The MIC Photon Counting Detector" – BFSD MIC Technical Report No.1

Fordham.J.L.A, Bone.D.A, Jordan.A.R. – "The UCL CCD-Based Image Photon Counting System"

Fordham.J.L.A, Bone.D, Oldfield.M, Bellis.J. – "MIC/SPAN Review" – XMM-OM/MSSL/RV/0003.01 21-Mar-1991

Fordham.J.L.A, Hook.R.N. – "Interpolative Centroiding In Photon Counting Detectors"

Fowler.W.B, Reed.E.I, Blamont.J.E. – "Effects Of Energetic Particles On Photomultipliers In Earth Orbits Up To 1500Km" – Applied Optics vol 14,No 9 Sept 1975

Fraser.G.W, Lees.J.E, Pearson.J.F, Barstow.M.A. – "The Operation Of Microchannel Plates With Square Pores" – IEEE Trans Nuclear Instruments And Methods In Physics Research A310 (1991)

Fraser.G.W , Hill, Pollehn. – "The electron Detection Efficiency Of MCPs" – IEEE Trans Nuclear Instruments And Methods In Physics Research 206 (1983)

Fraser.G.W, Pearson.J.F, Lees.J.E. – "Evaluation Of Long Life (L^2 Microchannel Plates For X-Ray Photon Counting" – IEEE Trans On Nuclear Science Vol. 35 No 1 Feb (1988)

Fraser.G.W, Pain.M.T, Lees.J.E, Pearson.J.F. – "The Operation Of Microchannel Plates At High Count Rates" – IEEE Trans Nuclear Instruments And Methods In Physics Research A306 (1991)

Garcia.R.N. – "Investigations Of Pore Paralysis In Microchannel Plates" – Msc Thesis Dept Physics And Astronomy, University College London (1990)

Gatti.E, Oba.K, Rehak.P. – "Study Of The Electric Field Inside Microchannel Plate Multipliers" – IEEE Trans On Nuclear Science Vol NS-30 No 1 Feb (1983)

Gear.C.W. – Proc for the Skytop Conf on Computer Systems in Experimental Nuclear Physics, (1969) USAAEC Conf-670301

Hect,Zajac. – "Optics" – Addison Wesley Publications (1974)

Hill.G.E. – "Secondary Electron Emission And Compositional Studies On Channel Plate Glass Surfaces" – Mullard Research Laboratories, Redhill, Surrey, England.

Hodgman.C.D. – "Handbook Of Chemistry And Physics" – The Chemical Rubber Publishing Company Ohio USA (1960)

Jaanimagi.P.A, Hestdalen.C. – "Streak Camera Phosphors: Response To Ultra-Short Excitation" – Laboratory For Laser Energetics, University Of Rochester, 250 East River Road, Rochester (1990)

Jordan.A.R, Fordham.J.L.A. – "Reducing The Granularity Noise Of An Image Photon Counting System Using Magnetic Scanning" – Q.J.R.Astr Soc (June 1986)

Lampton.M, Carlson.C.W. – "Low Distortion Resistive Anodes For 2-Dimensional Position Sensitive MCP Systems" – Rev Sci Instrum 50(9) Sept (1979)

Lampton.M, Malina.R.F. – "A Quadrant Anode Image Sensor" – Rev. Sci. Instrum Vol 47, P1360, (1976)

Lapington.J.S, Breeveld.A.A, Edger.M.L, Trow.M.W. – "A Novel imaging Readout With Improved Speed And Resolution" – Nuclear Instruments And Methods A310(1991) P299-304

Lapington.J.S, Kessel.R, Walton.D.M. – "Spatial Resolution Limitations Of Microchannel Plate And Conductive Charge Division Readout Devices" – Nucl Instrum And Methods A273(1988) 663-666

McLean.I.S. – "Electronic And Computer Aided Astronomy- From Eyes To Electronic Sensors" – Ellis Norwood, Chichester

McMullan.D,Powell.J.R. – "Residual Gasses And The Stability Of Photocathodes" – Conf Proc

Morgan.J.S, Slater.D.C, Timothy.J.G, Jenkins.E.B. – "Centroid Position Measurements And Subpixel Sensitivity Variations With The MAMA Detector" – Applied Optics/ Vol 28, No 6 / 15 Mar (1989)

Niescmidt.E.B, Lawrence.R.S, Gentillon.C.D. – "Count Rate Performance Of A Microchannel Plate Photomultiplier" – IEEE Trans On Nuclear Science Vol NS-29 No 1 Feb (1982)

Norton.T.J, Airey.R.W, Morgan.B.L, Fordham.J.L.A, Bone.D.A. – "An Intensifier With High DQE For Astronomical Photon Counting" – Conf On Photoelectronic Imaging Devices. London. Sept (1991)

Norton.T.J, Airey.R.W, Morgan.B.L. – "A 40mm MCP Intensifier For Photon Counting" – Electronics And Electron Physics Vol 74.

Oldfield.M.K, Fordham.J.L.A, Bone.D.A, Bellis.J.G, Norton.T.J,Nave.C. – "Protein Crystallography Trials With The MIC Photon Counting Detector At The Daresbury Lab" – Internal Report (1992)

Papaliolios.C, Niesenson.P, Ebstein.S. – "Speckle Imaging With The PAPA Detector" – Applied Optics Vol 24, No 2 Jan (1895)

Pearson.J.F, Lees.J.E, Fraser.G.W. – "Operating Characteristics Of Sandwich Microchannel Plates" – IEEE Trans On Nuclear Science Vol 35, No 1 Feb (1988)

Pellicori.S.F, Russell.E.E, Watts.L.A. – "Radiation Induced Transmission Loss In Optical Materials" – Applied Optics/ Vol 18 No 15 (1979)

Read.P.D, Van Breda.I.G, Norton.T.J, Airey.R.W. – "Properties Of A 40mm Micro-Channel Plate Intensifier" – SPIE Conf. Santa Cruz July (1987)

Sharma.A, Walker.J.G. – "Effect Of Deadtime In Imaging Detectors" – Quantum Optics 1 (1989)

Siegmund.O.H.W, Vallerga.J , Wargelin.B. – "Background Events In Microchannel Plates" – Space Astrophysics Group Contribution No 321 Proc IEEE (1987)

Siegmund.O.H.W, Lampton.M, Raffanti.R, Herrick.W. – "High Resolution delay Line Readouts For Microchannel Plates" – Nuclear Instrums And Methods In Physics A310(1991) 311-316

Siegmund.O.H.W, Clothier.S, Thornton.J. – "Application Of The Wedge And Strip Anode To Position Sensing With Microchannel Plates And Proportional Counters" – IEEE Trans on Nuclear Science NS-30 No 1 Feb (1993)

Siegmund.O.H.W, Stock.J. – "Performance Of Low Resistance Microchannel Plate Stacks" –

Smith.A, Edgar.M.L, Kawakami.H, Lapington.J.S. – "The SPAN Photon Counting Detector For The BFSD" – Boresight Faint Star Detector Final Report Part 2 Sept (1992)

Smith.S.R, Lowrance.J.L. – "Single Photoelectron Excitation Of Phosphors" – PASP P154 (1972)

Swyler.K.J, Hardy.W.H, Levy.P.W. – "Radiation Induced Colouring Of Glasses Measured During And After Electron Irradiation" – IEEE Trans On Nuclear Science, Vol NS-22, No 6, Dec (1975)

Timothy.G.J. – "Photon Counting Detector Systems" – SPIE Conf. Santa Cruz July (1987)

Timothy.G.J, Bybee.R.L. – "Photon Detector Arrays" –

Timothy.G.J. – "Electronic Readout Systems For Microchannel Plates" – IEEE Trans On Nuclear Science, Vol NS-32, No 1 Feb (1985)

Treadaway.M.J, Passenheim.B.C, Kitterer.B.D. – "Luminescence And Absorption Of Electron Irradiated Common Optical Glasses, Sapphire and Quartz" – IEEE Trans On Nuc Sci, Vol NS-22 (1975)

Vallerga.J, Lampton.M. – "Charged Coupled Devices vs Microchannel Plates In The Extreme And Far UV: A Comparison Based On The Latest Laboratory Measurements" – Proc. SPIE/ANRT, 868, (1987)

Viemann.W, Eubanks.A.G, Pieper.G.F, Bredekamp.J.H. – "Photomultiplier window materials under electron irradiation: Fluorescence and Phosphorescence" – GSFC Rep (1968)

Viemann.W, Eubanks.A.G. – "Noise Limitations Of Multiplier Phototubes In The Radiation Environment Of Space" – NASA Technical Report TN D-8147 (1976)

Walker.G. – "Astronomical Observations: An Optical Perspective" – Cambridge University Press (1987)

Williams.F.E, Eyring.H. – "The Mechanism Of The Luminescence Of Solids" – Journal Of Chemical Physics Vol 15 No 5 May (1947)

Williams.M.B, Sobottka.S.E, Shepherd.A. – "Delay Line Readout Of Microchannel Plates In A Prototype Position Sensitive Photomultiplier Tube" – Nuclear Instrums And Methods In Physics A302(1991) 105-112

Wiza.J.L. – "Microchannel Plate Detectors" – Nuclear Instruments And Methods In Physics Research 162 (1979)

Worswick.S.P, Wynne.C.G. – "A Fast Relay Lens For The Next Generation Of Photon Counting Detectors" – The Observatory Vol 105, No 1066, pp. 95-96 June (1985)

Ref [1] Private Communications with ITL (1991)

Ref [2] EEV Technical Note – "Radiation Damage Effects In EEV CCDs" – Private Communications (1991)

Ref [3] Private Communications with Tim Norton, Imperial Collage London 1993.

Ref [4] Private Communications with H.Kawakami, MSSL (1993).

Ref [5] Private Communications with Francisco Diego (UCL)

Ref [6] Private Communications with Schott Fiber Optics Inc (1992)

Ref [7] Private Communications with Delft Electronische Production (DEP) Holland (1992)

List Of Publications

Oldfield.M.K. – "Background Count Rate Contribution Due To Fluorescence In MCP Intensifier Windows" – XMM-OM Technical Report (1991)

Oldfield.M.K, Fordham.J.L.A. – "Protein Crystallography Trials With The MIC Detector" – Internal Report To The Daresbury Laboratory (1992)

Oldfield.M.K, Fordham.J.L.A. – "Second Generation PDA For HST. Improvement In Dynamic Range And Resolution Of The MIC Detector" – Report From UCL To BAe (1991)

Oldfield.M.K, Fordham.J.L.A. – "The Affect Of Aliasing On The MIC Detector" – XMM-OM Technical Report (1992)

Fordham.J.L.A, Oldfield.M.K, Bellis.J.G, Bone.D.A. – "The Effect Of Phosphor Decay On The Dynamic Range Of The MIC Detector" – XMM-OM Technical Report (1990)

Bone.D.A, Oldfield.M.K, – "Evaluation Of The Prototype DEP MIC Intensifier" – XMM-OM Technical Report (1992)

Fordham.J.L.A, Bone.D.A, Oldfield.M.K, Bellis.J.G, – "Photoelectronic Imaging Devices" – Ed B.L.Morgan, IOP Publishing Bristol P105.

Fordham.J.L.A, Bone.D.A, Bellis.J.G, Oldfield.M.K, Polychronopulos.B. – "MIC Final report" –ESA Contract 8819/90/NL/US(SC) (1992)